

INVESTIGATION OF A THREE-PHASE FORCEDCOMMUTATION SERIES CAPACITOR OPERATING WITH VARIABLE-VOLTAGE AND VARIABLE-FREQUENCY SYSTEMS

Tahani Hamodi Mazher Al-Mhana B.Sc., M.Sc.

A thesis submitted for the degree of Doctor of Philosophy

April, 2016

School of Electrical and Electronic Engineering
Newcastle University
United Kingdom

Preface Abstract

Abstract

This thesis investigates the use of a three-phase forced-commutation series capacitor (FCSC) for power factor correction in stand-alone variable-voltage variable-frequency (VVVF) systems. Two environmentally-friendly applications are chosen to represent the VVVF systems. The first application is a renewable energy resource as a direct drive wave energy conversion (WEC) buoys. The second application is the more electric aircraft (MEA).

In such systems, permanent magnet PM generators are most commonly used. A generator-set generally consists of a three-phase generator connected directly to a conventional three-phase diode bridge rectifier for simplicity and cost reduction. Due to the high inherited inductance of the PM generators used in such applications, this configuration suffers from a poor power factor as a result of commutation overlap.

Several controlled series compensator (CSC) topologies have been employed for decades in power systems where the voltage levels and frequency are fixed. However, in applications such as WEC and MEA, the voltage and frequency vary. Therefore, in this work, a variable switched capacitor is used in order to inject a capacitive reactance and therefore compensate the inductive reactance of the generator, which prevents power factor degradation. In a VVVF system, it is important to inject variable capacitive reactance since the inductive reactance changes with frequency variations. Five commonly used CSC circuits are compared and the FCSC is considered as the most suitable circuit topology which is able to cope with a range of frequency variations.

This research mainly investigates the performance of the three-phase FCSC circuit when controlled by novel control strategy, in terms of power factor, output voltage, and output power under various load conditions, including constant and variable load. The harmonic content of the three-phase FCSC is also investigated in order to propose this topology for MEA power system. In an aerospace system, the power quality is required to meet high standards and harmonic distortion should not exceed the limited level set by aerospace industry authorities. Therefore, several types of conventional power factor corrector (PFC) are excluded from aerospace systems, due to the associated distortion levels.

Preface Abstract

In this thesis, a novel symmetrical duty cycle control (SDCC) scheme is proposed in order to qualify the three-phase FCSC converter to be employed in different ranges of frequency variation, including 1-3 Hz for wave energy and 50-500 Hz as part of aircraft frequencies. The approach is simple to implement, with no need for a sophisticated controller design. The switch duty cycle is a function of the supply frequency and this allows the FCSC circuit to cope with frequency variation.

The modes of operation for both single and three-phase circuit topologies are presented. The three-phase FCSC circuit is designed and tested in the laboratory environment. The performance of the three-phase FCSC circuit when using SDCC is tested experimentally and assessed by comparison of its performance with that of the conventional three-phase diode bridge rectifier. Experimental and simulation results validate the capability of the three-phase FCSC- rectifier to improve the power factor to approximately unity in addition to increasing the output voltage and power at higher voltage and frequency values. However, only limited improvements are achieved at the lower values of the frequency spectrum.

Preface Dedication

Dedication

To my loving parents and my beloved husband Faris

Preface Acknowledgment

Acknowledgement

First and foremost, I would like to thank Allah for giving me strength, patience and guidance to complete this thesis. Praise and gratitude to Allah.

I would like to express my utmost thanks towards all my supervisors. My sincere gratitude to my supervisor Prof. Volker Pickert for his valuable guidance, support, and encouragement during my doctoral research. Also, my deepest appreciation and thanks to Dr. David Atkinson for sharing his great practical and theoretical knowledge, and for useful discussions before and after supervisions. I would like to thank also my former supervisor, Dr. Bashar Zahawi, for his general guidance and the useful comments he made after reading my papers and part of the thesis. I am also very grateful to the rest of the Electric Power group academic staff for assistance and support in my research, particularly Dr. Nick Baker for providing the machine parameters.

I would like to acknowledge the support I have received from the technicians in the school of EEE during this research. In particular, Darrren Mackie who helped me in manufacturing the printed circuit boards and modification of the general interface board. I am also very grateful to James Richardson and Steve Mitchell for their valuable help in the UG lab during the experimental setup, also, Jack and Allan and Jeffrey for their help when needed. It is also my pleasure to thank all the administrative staff, particularly Gillian Webber, and Deborah Alexander for help in all administrative work.

Moreover, I would like to acknowledge the friendly collaboration of my colleagues in the Electrical Power group. Four years of hard work would be very difficult if there had not been an enjoyable place to work. I would like to thank them for their valued friendship and encouragement throughout my work, particularly, Musbahu Muhammad and Bassim Jasim. Also, I am very grateful to my dearest friends, Marina and Bryan Crossling for their valued friendship, kindness, encouragement, and supports during my time in Newcastle.

I would like to express my great appreciation to my sponsor, the Ministry of Higher Education and Scientific Research of Iraq, for granting me a scholarship for my PhD degree. Without their sponsorship, I would not have had the opportunity to study in the UK.

Finally, I would like to express my extreme and deepest appreciation to my dearest parents Hamodi and Alya. I am very grateful for their never-ending love, unconditional care and Preface Acknowledgment

support and the encouragement they have provided me with throughout my entire life. I am eternally grateful to them and wish that my father was still alive to see my achievement. Also, I owe my deepest gratitude to my brother, Alaa, and his family: many thanks for his unbelievable kindness, endless love and continuous support and for the love, and belief in me of his children. I would like also to thank my beloved sisters for their love and kindness. I thank my family for their patience at my studying abroad. It is also my pleasure to thank my relatives for their love, support and keeping in touch with me. Also, I acknowledge the encouragement of my friends in Iraq.

Last, but most important, my sincere deepest gratitude and appreciation to my husband, Faris. I cannot thank him enough for all his endless love, unconditional support and immense patience throughout my PhD study. I am extremely grateful for all his affection and moral support. I am very fortunate to have such a husband. Thank you Faris for everything as my research would not have started nor would it have been completed without your understanding support. You have always encouraged me in, and sustained my enthusiasm for my research. I am eternally grateful to you for sharing all the stress and frustration experienced during the research for my thesis.



Table of Contents

Abstrac	:t	iii
Dedicat	ion	v
Acknow	vledgement	vi
Table o	f Contents	ix
List of	Figures	xiii
List of	Tables	XX
Princip ¹	le Nomenclature	xxi
Chapter	1. Introduction	1
1.1	Introduction	1
1.2	Variable-Voltage and Variable-Frequency (VVVF) Applications	2
1.3	Research Motivations and Objectives	3
1.4	Contributions to Knowledge	7
1.5	Publications Arising From This Research	7
1.6	Thesis Overview	8
Chapter	2. Review of Controlled Series Compensator (CSC) Circuits	11
2.1	Series and Shunt Compensation	12
2.2	CSC Applications	12
2.3	Overview of Controlled Series Compensator Circuits	13
2.3	3.1 Variable Reactance Series Compensator (VRCSC)	15
2.3	3.2 Switching power converter series compensator (SPCSC)	25
2.4	Comparison of Different CSC Topologies	30
2.5	FCSC-Rectifier in Wave Energy Buoys	33
2.6	Summary	35

Chapt	er 3.	Single-Phase FCSC Converter	. 36
3.1	An	alytical Description	. 36
3	3.1.1	FCSC-rectifier topology	. 37
3	3.1.2	Electrical generator	. 37
3	3.1.3	Single-phase diode bridge rectifier	. 38
3	3.1.4	Principles of operation	. 38
3	3.1.5	Modes of operation of single-phase FCSC converter	. 39
3.2	Per	formance Consideration	. 44
3.3	Nu	merical Analysis and Simulation Results	. 48
3	3.3.1	Single-phase FCSC- rectifier in wave energy converter	. 48
3.4	SA	BER Model of the Single-Phase FCSC-Rectifier	. 50
3.5	Op	erations at Various Load Conditions	. 54
3.6	Sui	nmary	. 58
Chapt	er 4.	Three-Phase FCSC Converter	. 60
4.1	Pov	wer Electronics Converter Topologies for Aircraft Applications	. 61
4.2	Des	scription of the Three-Phase FCSC Converter	. 63
4	1.2.1	Three-phase FCSC-rectifier topology	. 63
4	1.2.2	Three-phase electrical generator	. 65
4	1.2.3	Three- phase six-pulse diode bridge rectifier	. 65
4	1.2.4	Principles of operation of the three-phase FCSC converter	. 69
4.3	Per	formance Consideration	. 70
4.4	Nu	merical Analysis and Simulation Results	. 72
4	1.4.1	SABER model of three-phase FCSC rectifier	. 72
4	1.4.2	Simulation results	. 74
4	1.4.3	Operation at various load conditions	. 86
4.5	Sui	nmary	89

Chaptei		Control of the FCSC Converter for Variable-Voltage Variable-Fr	equency
Applica			
5.1	Syn	nmetrical Duty Cycle Control (SDCC) for the FCSC Converter	92
5.1	1.1	Symmetrical duty cycle control for the single-phase FCSC converter	94
5.1	1.2	Symmetrical duty cycle control for the three-phase FCSC converter	109
5.2	Har	monic Analysis of Three-Phase FCSC Rectifier	132
5.3	Ass	essment of the Proposed Symmetrical Duty Cycle Control Strategy	135
5.4	Sun	nmary	137
Chapter	r 6.	Experimental Set up, Hardware and Measurement	139
6.1	Ger	neral Description of the Laboratory Test Platform	139
6.2	Zer	o Crossing Detection	141
6.3	Har	dware Modification of the General Interface Board of eZdsp TM F28335	142
6.4	Lab	oratory Test Bench Measuring Equipment	147
6.5	Sof	tware Development	147
6.6	Sun	nmary	148
Chapter	r 7.	Experimental Results and Analysis	151
7.1	Rea	lisation of the Programmable AC Power Source Distortion	152
7.2	Exp	perimental Results for a Three-Phase Diode Bridge Rectifier oper	ating at
Varia	able-V	Voltage and a Variable-Frequency Range of 50-480 Hz	156
7.2	2.1	Operating with constant load	156
7.2	2.2	Operating with variable load resistance	160
7.3	Exp	perimental Results for a Three-Phase FCSC-rectifier operating at V	/ariable-
Volta	age ar	nd a Variable-Frequency Range of 50-480 Hz	162
7.3	3.1	FCSC operating with constant load	162
7.3	3.2	Three-phase FCSC-rectifier under various load conditions	170
7.4	Har	monic Analysis of the Three-Phase FCSC-Rectifier	172
7.5	Cor	mparison between the Use of the Three-Phase Diode Rectifier and the	e Three-
Phase	e FCS	SC-Rectifier	175

7.5.1 Operating under constant load	175
7.5.2 Operating under variable load condition	179
7.6 Comparison of the Experimental and Simulation Results	182
7.7 Summary	184
Chapter 8. Conclusion and Future Work	186
8.1 Future Work	191
Appendix A. Variable-Voltage Variable-Frequency Applications	193
A.1 Wave energy converters (WEC)	193
A.2 More electric aircraft (MEA)	196
Appendix B. Three-phase six-pulse bridge rectifier with pure resistive load	201
Appendix C. Simulation Results of the Three-Phase Diode Bridge Rectifier Fe under Constant and Variable Load	_
C.1 Three-Phase Diode Bridge Rectifier Operating with Fixed Load	206
C.2 Three-Phase Diode Bridge Rectifier Operating with Variable Load	211
Appendix D. Harmonic Analysis of the Programmable AC Power Source	214
Appendix E. Hardware Development	217
E.1 Hardware Set-up	217
E.2 General purpose power interface board for eZdsp TM F28335	227
E.3 Current sensors	229
E.4 Voltage sensors	230
E.5 Design and construction of the zero crossing detection card	231
E.6 Protective features and safety	232
Appendix F. Schematic of the protection circuit	234
Appendix G. Selective Experimental Results for a Three-Phase Rectifier Variable-Voltage and Variable-Frequency	
Appendix H. Distorted Operating Voltages Impact on the system behaviour	239
References	241

List of Figures

Figure 2.1 Family tree of common static controlled series compensators	14
Figure 2.2 TSSC circuit diagram (only one-phase is shown)	16
Figure 2.3 TCSC circuit diagram (only one-phase is shown)	18
Figure 2.4 Impedance characteristics of TCSC [52]	20
Figure 2.5 GCSC circuit configuration (only one-phase is shown)	22
Figure 2.6 Line current and capacitor voltage waveforms as a function of γ during the	e positive
half cycle	23
Figure 2.7 Switched variable series capacitor circuit arrangement (only one-phase	is shown)
	25
Figure 2.8 MERS configuration (only one-phase is shown)	
Figure 2.9 Schematic description of dynamic voltage restorer (DVR)	28
Figure 2.10 Schematic of the SSSC circuit	29
Figure 2.11 Single-phase FCSC circuit	34
Figure 2.12 Switching pattern of the single-phase FCSC in wave energy buoys	34
Figure 3.1 Single-phase FCSC converter configuration in stand-alone system	37
Figure 3.2 Voltages and current in single-phase full-wave rectifier connected to sti	ff voltage
source and feeding RC load	39
Figure 3.3 Conventional turn-off angle control for FCSC converter	40
Figure 3.4 Schematic circuit diagram when S ₁ is OFF	41
Figure 3.5 Effective FCSC equivalent circuit; mode1/mode 3	42
Figure 3.6 Schematic circuit diagram when S ₁ is ON	43
Figure 3.7 Effective FCSC equivalent circuit; mode 2/mode 4	43
Figure 3.8 Supply voltage, supply current and first harmonic current relationship	46
Figure 3.9 SABER model of a single phase FCSC converter	52
Figure 3.10 Single phase FCSC converter waveforms, input voltage (Vs), input c	urrent (i_s)
and load voltage (V_L) when $\gamma = 0$ at F_s =3Hz	54
Figure 3.11 Frequency spectrum of peak input current harmonics	
Figure 3.12 Displacement, distortion and power factor as a function of R_L/R_S	56
Figure 3.13 Percentage current total harmonic distortion as a function of R_I/R_S	56

Figure 3.14 Distortion, displacement and power factor as a function of C_L/C_C	. 57
Figure 3.15 Current total harmonic distortion as a function of C_L/C_C	. 58
Figure 4.1 Three-phase FCSC-rectifier in stand-alone variable-voltage variable-frequency.	. 64
Figure 4.2 Commutation sequences in the three-phase six-pulse diode rectifier	. 66
Figure 4.3 SABER model of the three-phase rectifier with RL load	. 67
Figure 4.4 Voltage and current waveforms of the three-phase rectifier with RL load	. 67
Figure 4.5 Voltage and current waveforms of the three-phase rectifier with RC load	. 69
Figure 4.6 Circuit configurations as a function of line-line voltage polarity	. 70
Figure 4.7 SABER model for the three-phase FCSC converter	. 75
Figure 4.8 SABER model for the system without FCSC	. 76
Figure 4.9 Voltage and current waveforms for phase a when the system is working with	out
the FCSC circuit	. 77
Figure 4.10 Phase a current and diodes D_1,D_3 and D_5 currents during commutation interval	79
Figure 4.11 Diode current waveforms	. 79
Figure 4.12 Current and voltage waveforms in each phase	. 80
Figure 4.13 Voltage and current waveforms in phase a and load voltage	. 81
Figure 4.14 Average voltage and current in the DC output	. 82
Figure 4.15 Diode currents in all phases	. 83
Figure 4.16 Overlap commutation interval between diodes	. 84
Figure 4.17 Frequency spectrum of the current in phase a when employing three-phase FC	SC-
rectifier with PMA	. 84
Figure 4.18 Input current harmonics	. 86
Figure 4.19 Displacement, distortion and power factor as a function of R_L	. 87
Figure 4.20 FCSC converter efficiency and current total harmonic distortion	. 87
Figure 4.21 Input and output power and power losses in the three-phase system	. 88
Figure 4.22 Percentage input current harmonics as a function of load variations	. 89
Figure 5.1 Turn-ON periods of FCSC switching devices: (a) SDCC technique (b) Previ	ious
technique	. 93
Figure 5.2 Single-phase FCSC converter waveforms at a frequency of 5 Hz	. 97
Figure 5.3 Single-phase FCSC-rectifier waveforms and switches ON time at 4 Hz	. 99
Figure 5.4 Diodes current transitions in single-phase FCSC-rectifier	100
Figure 5.5 Single-phase FCSC-rectifier waveforms and switches ON time at 2.5 Hz freque	ncy
	101

Figure 5.6 Single-phase FCSC-rectifier waveforms and switches ON time at a 1 Hz102
Figure 5.7 Power factor, distortion factor and displacement factor as a function of frequency
variation of 1-5 Hz in a single-phase circuit
Figure 5.8 Single-phase converter total harmonic distortion as a function of frequency
variation of 1-5 Hz in single-phase FCSC circuit
Figure 5.9 Single-phase circuit waveforms and switch ON time at a frequency of $500~\mathrm{Hz}$ $105~\mathrm{Hz}$
Figure 5.10 Single-phase circuit waveforms and switches ON time at a frequency of 400 Hz
Figure 5.11 Single-phase circuit waveforms and switches ON time at a frequency of 250 Hz
Figure 5.12 Single-phase circuit waveforms and switches ON time at a frequency of 50 Hz108
Figure 5.13 Power factor, distortion factor and displacement factor as a function of frequency
variation of 50-500 Hz in single-phase circuit in single-phase FCSC circuit109
Figure 5.14 Total harmonic distortion as a function of frequency variation of 50-500 Hz in
single-phase circuit in single-phase FCSC circuit
Figure 5.15 Diodes and switching states for three-phase FCSC-rectifier assuming γ equal $\pi/12$
Figure 5.16 Equivalent circuit of three-phase FCSC converter as a function of V_{ab}
Figure 5.17 A simplified system model with the three-phase FCSC converter during model
Figure 5.18 A simplified system model with the three-phase FCSC converter during mode 2
Eigens 5 10 A simplified contain model with the three phase ECSC converted during model 2
Figure 5.19 A simplified system model with the three-phase FCSC converter during mode 3
Figure 5.20 A simplified system model with the three-phase FCSC converter during mode 4
116
Figure 5.21 Three-phase FCSC converter waveforms at a frequency of 5 Hz (phase-a only)
Figure 5.22 Three-phase FCSC converter waveforms at a frequency of 4 Hz (phase-a only)
Figure 5.23 Three-phase FCSC converter waveforms at a frequency of 2.5 Hz (phase-a only)

Figure 5.24 Three-phase FCSC converter waveforms at a frequency of 1 Hz (phase-a only)
Figure 5.25 Power factor, distortion factor and displacement factor as a function of frequency
Figure 5.26 Percentage total harmonic distortion of three-phase FCSC-rectifier operating in a
frequency range of 1-5 Hz
Figure 5.27 Three-phase FCSC converter waveforms at a frequency of 480 Hz (phase-a only)
Figure 5.28 Three-phase FCSC converter waveforms at a frequency of 400 Hz (phase a only)
Figure 5.29 Three-phase FCSC converter waveforms at a frequency of 240 Hz (phase-a only)
Figure 5.30 Three-phase FCSC converter waveforms at a frequency of 50 Hz (phase-a only
128
Figure 5.31 DC output voltage and input current under as a function of frequency in FCSC-
rectifier
Figure 5.32 Power factor, distortion factor and displacement factor as a function of frequency
in FCSC-rectifier
Figure 5.33 Efficiency and percentage total harmonic distortion of the three-phase FCSC-
rectifier operating in a frequency range of 50-480 Hz
Figure 5.34 DC output voltage of the FCSC converter as a function of supply voltage and
frequency variations under various loads
Figure 5.35 Load current of the FCSC converter as a function of supply voltage and frequency
variations under various loads
Figure 5.36 Input current of the FCSC converter as a function of supply voltage and
frequency variations under various loads
Figure 5.37 Input power factor of the FCSC converter as a function of supply voltage and
frequency variations under various loads
Figure 5.38 Input current harmonic spectrum as a function of V_S/F_S variations when $R_L=10$
Ω
Figure 5.39 Input current harmonic spectrum as a function of V_S/F_S variations when $R_L=20$
Ω

Figure 5.40 Input current harmonic spectrum as a function of V_S/F_S variations when $R_L=30$
Ω
Figure 6.1 Experimental test bench arrangement
Figure 6.2 Photograph of full workstation for the experimental test
Figure 6.3 Photograph of the designed ZCD board
Figure 6.4 Voltage waveforms of the zero crossing detection board
Figure 6.5 The modification in the voltage sensor interface
Figure 6.6 EPWM master and slave configurations
Figure 6.7 The PWM hardware modifications in gate drive interfaces
Figure 6.8 Six PWM pulses for IGBT switches at a frequency of 400 Hz146
Figure 6.9 National Instruments LabView panel
Figure 6.10 The CCS software structure
Figure 7.1 Three phase line-to-neutral voltage waveforms: (a) SABER voltage source
waveforms; (b) acquired experimental power supply voltage waveforms153
Figure 7.2 Current in phase-a shape in experimental and simulation tests; (a) phase-a current
in SABER; (b) acquired experimental phase-a current
Figure 7.3 Input voltage and current waveforms in SABER for all three phases155
Figure 7.4 Acquired input current and voltage waveforms from the experimental test155
Figure 7.5 Voltage and current waveforms under $F_s = 400 \text{ Hz}$, $V_s = 90 \text{ V}$ and $R_L = 30 \Omega \dots 158 \Omega$
Figure 7.6 Output voltage and current under constant load (R_L =30 Ω) (conventional rectifier)
Figure 7.7 Power factor under constant load (R_L =30 Ω)(conventional rectifier)160
Figure 7.8 DC output voltage as a function of supply voltage and frequency variations
(conventional rectifier)
Figure 7.9 Input current as a function of load resistance and supply voltage and frequency
variations (conventional rectifier)
Figure 7.10 Power factor as a function of load resistance and supply voltage and frequency
variations (conventional rectifier)
Figure 7.11 Circuit waveforms with $V_s = 100 \text{ V}$ and $F_s = 480 \text{ Hz}$ (FCSC circuit)
Figure 7.12 Circuit waveforms with $V_s = 90 \text{ V}$ and $F_s = 400 \text{ Hz}$ (FCSC circuit)
Figure 7.13 Circuit waveforms with $V_s = 75$ V and $F_s = 240$ Hz (FCSC circuit)
Figure 7.14 Circuit waveforms with $V_s = 50$ V and $F_s = 50$ Hz (FCSC circuit)

Figure 7.15 DC output voltage and input current under constant load (R_L =30 Ω)(FCSC-
rectifier)
Figure 7.16 Power factor under constant load (R_L =30 Ω)(FCSC-rectifier)
Figure 7.17 DC output voltage as a function of supply voltage and frequency variations
(FCSC-rectifier)
Figure 7.18 The output load current as a function of supply voltage and frequency variations
(FCSC-rectifier)
Figure 7.19 Input current as a function of supply voltage and frequency variations (FCSC-
rectifier)
Figure 7.20 Power factor as a function of supply voltage and frequency variations (FCSC-
rectifier)
Figure 7.21 Input current harmonic spectrum as a function of V_S/F_S variations when $R_L=10$
Ω
Figure 7.22 Input current harmonic spectrum as a function of V/F_S variations when $R_L = 20$
Ω
Figure 7.23 Input current harmonic spectrum as a function of V_S/F_S variations when $R_L=30$
Ω
Figure 7.24 Comparison of the average output voltage of the rectifier with that of the FCSC-
rectifier under constant load of $R_L = 30 \Omega$
Figure 7.25 Comparison of the average output current of the diode bridge rectifier with that of
the FCSC-rectifier under constant load of $R_L = 30 \Omega$
Figure 7.26 Comparison of the input current of the rectifier with that of the FCSC-rectifier
under constant load of $R_L = 30 \Omega$
Figure 7.27 Comparison of the output power of the conventional rectifier with that of the
FCSC-rectifier under constant load of $R_L = 30 \Omega$
Figure 7.28 Comparison of the input power factor of the conventional rectifier with that of
the FCSC-rectifier under constant load of $R_L = 30 \Omega$
Figure 7.29 Comparison of the average output voltage of the conventional rectifier with that
of the FCSC-rectifier under 90 V/400 Hz
Figure 7.30 Comparison of the average output current of the rectifier and that of the FCSC-
rectifier under 90 V/400 Hz
Figure 7.31 Comparison of the input current of the conventional rectifier and that of the
FCSC-rectifier under 90 V/400 Hz

Figure 7.32 Comparison of the output power of	the conventional rectifier and that of the
FCSC-rectifier under 90 V/400 Hz	181
Figure 7.33 Comparison of the input power fact	or of the conventional rectifier and that of
the FCSC-rectifier under 90 V/400 Hz	182

Preface List of Tables

List of Tables

Table 2-1 Comparison of VRCSC topologies in transmission systems network	30
Table 3-1 Single phase linear PM generator parameter	51
Table 3-2 Simulation circuit parameters for single-phase topology	53
Table 4-1 Performance requirement of PMA which feeds the FADEC engine control	73
Table 4-2 PMA parameters at a frequency of 300 Hz	74
Table 4-3 Simulation circuit parameters for three-phase system	74
Table 4-4 Current harmonic limits for balanced three-phase electrical equipment as imp	posed
by RTCA DO-160 [143]	85
Table 5-1 Scale factor as a function of frequency variations	95
Table 5-2 Circuit parameters at maximum frequency of 5 Hz	96
Table 5-3 Simulation circuit parameters for a frequency range 50-500 Hz	103
Table 5-4 Circuit parameters for frequency spectrum of 50 Hz-480 Hz	123

Principle Nomenclature

List of Acronyms

AC Alternating current

ADC Analogue to digital converter

AEA All electric aircraft

CCM Continuous current mode

CF Constant frequency

CPU Central processing unit

CSC Controlled series compensator

DC Direct current

DCM Discontinuous current mode

DF Distortion factor

DPF Displacement power factor

DSP Digital signal processing

DVR Dynamic voltage restorer

eCAN Enhanced controller area networks

EMI Electromagnetic interface

ESR Equivalent series resistance

FACTS Flexible AC transmission systems

FADEC Full authority digital electronic controller

FCSC Forced-commutation controlled series capacitor

GCSC GTO Thyristor-controlled series capacitor

FFT Fast Fourier transform

IDG Aircraft integrated drive generator

IGBT Insulated gate bipolar transistor

ISR Interrupt service routine

JTAG Joint test action group

MEA More electric aircraft

MERS Magnetic energy recovery switch

ML Multi-level

PCB Printed circuit board

PF Power factor

PFC Power factor correction

PM Permanent magnet

PMA Permanent magnet alternator

PTO Power take-off mechanism

PWM Pulse width modulation

RMS Root mean square

SCI Serial communication interfaces

SHEV Series hybrid electric vehicle

SPI Serial peripheral interface

SSR Sub-synchronous resonance

SSSC static synchronous series compensator

SVSC Switched variable series capacitor

SDCC Symmetrical duty cycle control

TBCLK Time base clock

TCSC Thyristor controlled series capacitor

TFPM Transverse-flux permanent-magnet

THD Total harmonic distortion

TL Transmission line

TSSC Thyristor switched series capacitor

VF Variable frequency

VRPM Variable reluctance permanent-magnet

VRCSC Variable reactance controlled series compensator

VVVF Variable-voltage variable-frequency

WEC Wave energy converter

List of symbols:

T	Period
η	Efficiency
ω	Angular frequency
γ	Turn-off angle
β	the phase delay of the switch
\mathcal{O}_m	The mechanical speed
D	Duty ratio
F	Frequency
GTO	Gate turn-off thyristor
I	RMS current
I_1	Fundamental current component
i_s	AC current in one phase of the three-phase system
i_L	Inductor current
L	Inductance
L_S	Machine inductance
P	Real power
P_{in}	Input power
P_{Loss}	The total losses
P_{out}	Output power
Q	Reactive power
R	Resistance
R_s	The stator resistor
S	Apparent power
V	RMS voltage

 V_{ab} , V_{bc} , V_{ca} Line-to-line voltages

 V_L DC load voltage

 X_C Capacitive reactance

 X_L Inductive reactance

C Capacitance

 φ Power factor angle

 φ_{in} Current phase delay angle

 φ_{vn} Voltage phase delay angle

Chapter 1. Introduction

1.1 Introduction

Climate change represents a significant environmental threat to the world. Such change can be observed in the rapid increase in global warming, which causes severe weather patterns such as extremely high sea levels and abnormal precipitation events including flooding, droughts, heat waves and wildfires [1]. These threats increase in proportion to the discharge of greenhouse gases such as carbon dioxide and methane. Many nations are devoting considerable effort to reducing the emission of greenhouse gases by developing new power and energy technologies. Moving toward carbon-neutrality for power and transport fuel plays a key role in the reduction of pollution and emission control.

Recently, the transition to renewable energy has dramatically accelerated and these sources of energy are replacing fossil fuels to provide services such as heating, cooling, electricity, transport fuel, and chemicals. Renewable energy provides secure energy supplies for many countries in two ways: firstly, due to the variety of renewable sources, including wind, solar, wave, tidal, hydro, and biomass; and secondly it is independent of imported oil [2]. Many governments are intensively investing in developing renewable energy industry to avoid fuel crisis and environmental problems.

The energy of the oceans is a massive untapped renewable energy source, and is considered to represent an infinite source of energy which can provide energy security. Different types of ocean energy systems are available, including wave energy, tidal energy, ocean thermal energy, and osmotic energy systems. Based on a report by the European Renewable Energy Council (EREC), ocean energy has been theoretically estimated to be able to satisfy the global demand for electricity of 16000 TWh/year, and wave energy could contribute 8,000-80,000 TWh/year [2]. In Europe, wave energy and marine currents are the best ocean energy resources which could satisfy an important part of electricity demand. In comparison with other renewable energy resources, wave energy offers significant advantages, including the highest energy density and limited environmental interference, since most converters are located offshore. Only small energy losses are typically observed, and power generation can

be expected up to 90 of the time [3, 4]. In addition, wave energy is more predictable and persistent than wind energy. However, ocean energy conversion systems face many technical challenges to achieving high reliability and maintain low costs, due to the harsh marine environment [5].

Another way of reducing carbon emissions is to improve the aerospace industry as a part of the overall automation industry. According to the Intergovernmental Panel on Climate Change (IPCC), the transportation industry contributes ~20% of the world's carbon emissions, and an estimated 2% of global CO₂ emissions are caused by commercial and military aviation. Commercial aviation is responsible for 80% of this total [1].

In order to achieve cleaner skies, several targets for air transportation have been set by the Advisory Council for Aeronautics Research in Europe, to be realised by 2020. These targets include reducing fuel consumption dramatically to 50% of present CO₂ emissions, reducing emissions of NO_x by 80%, and reducing external noise by 50%. In addition, a green life cycle for products is required, including for design, manufacturing, maintenance, and disposal. Therefore, a significant challenge faces the aerospace industry in order to reduce emissions and fuel dependency by moving toward more environmentally-friendly aircraft, such as the more electric aircraft (MEA) [6]. MEA can play an important role in reducing pollutant gases by reducing fuel burn. It also helps to improve the reliability of the aircraft, and reduce the operating and maintenance costs.

1.2 Variable-Voltage and Variable-Frequency (VVVF) Applications

In some applications, such as the wave energy converter (WEC) and MEA, the electrical generator provides an output with a variable-voltage and variable-frequency (VVVF). In direct drive WECs, the voltage levels, frequencies, and linear motion of the generator are related to the wave movements. The waves vary in height and period, and this produces a variable back EMF and variable frequency from the generator. In MEA, the voltage levels and frequencies are related to the thrust power of the turbine jet engine. In both applications, a conventional diode bridge rectifier is typically used to provide AC to DC rectification. The diode rectifier is considered to be the cheapest and simplest power electronics circuit, since there is no control requirement [7-9]. The electrical generator is commonly connected directly to a diode bridge rectifier to supply several DC loads, such as for electronic equipment and

DC drives [10, 11]. This general configuration is called the generator-set. A brief overview of WECs and MEA is provided in Appendix A.

Due to the long wavelength of water waves and the electrical machine design, WECs commonly produce low output frequencies in the range between 1-3 Hz. Due to fluctuating voltages and frequencies, the power produced varies accordingly. However, for MEA applications, higher frequencies in the range 360-720 Hz are achieved. This is because the generator output is a function to the thrust of the engine power. In aircraft electrical power systems, moving toward either variable frequency (VF) AC power systems, as an alternative to constant frequency (CF) three-phase AC power, or to a hybrid system seems to represent the future. The use of VF power in the MEA architecture has been proposed to improve overall efficiency and reduce volume and weight [12].

In both applications, the inherent inductance of the PM generator is very high due to the generator design. Therefore, the generator-set suffers from a poor power factor due to commutation overlap. This increases losses and consequently reduces the DC output voltage and output power over the full operational range.

1.3 Research Motivations and Objectives

Several existing power electronic converters can be used to adjust the load with wide speed/frequency variations. However, many of these power converters are not specifically optimized for these applications, and may pollute the power bus with harmonics [12, 13]. Harmonics can cause malfunctions in some avionics and marine equipment, especially when using an uncontrolled rectifier to supply electronic and other DC loads. Therefore, it is important to develop power electronic converters which meet the realistic requirements of electrical equipment for aircraft and marine buoys, such as the direct interfacing with a VVVF source, with a high power factor and high DC output voltage level. In addition, one of the most challenging issues in aerospace power systems is developing a power electronic converter which can meet the regulatory requirements for commercial aircrafts, such as the Radio Technical Commission for Aeronautics (RTCA) DO-160 [14]. RTCA DO-160 defines a strict operational capacity for the power converter, and includes tight limits for current harmonic distortion [12, 15].

Different types of power electronics conversion and control methods have been investigated and compared in aircraft systems and WECs. These include the 12-pulse rectifier, and two-

level and three-level active three-phase pulse width modulation (PWM) rectifiers [10, 16]. However, the commonly used PWM converter, which already uses a complex control strategy, can cause unstable operation in high voltage AC and DC power systems which are considered to be the likely future trend in the aerospace industry [17, 18].

In order to reduce harmonic distortion by compensation, an active power filter (APF) has been proposed for non-linear loads. However, this requires a sophisticated control scheme. Full details have been presented elsewhere of the modelling and characterisation of the variable speed constant frequency (VSCF) cyclo-converter aircraft system and the supply of non-linear load [19-22].

Moreover, many conventional power factor correction (PFC) topologies have been excluded from employment in aircraft systems due to the resulting high levels of distortion which arise from zero crossing distortion. Therefore, a new PFC topology with no zero-crossing distortion is a crucial requirement for such systems [23-26].

In power systems where frequency and voltage are fixed, series compensators based on power-electronics have been employed for decades in order to control the current in the transmission line network. The series compensation is implemented in the power system network using one of two approaches: either a variable reactance impedance implemented using a controlled series capacitor, or controlled voltage source using a static synchronous series compensator (SSSC) [27].

In VVVF systems, the supply frequency varies and hence the machine's inductive reactance varies accordingly. Therefore, variable capacitive reactance is needed to compensate for the effect of inductive reactance. As a result, in this research, the CSC is proposed for use as a compensation approach in the VVVF system.

The forced-commutation controlled series capacitor (FCSC) circuit (named GCSC when using the GTO-thyristor) is one of the existing CSC circuits in power transmission networks where the frequency is fixed at 50 Hz [28]. In the transmission network, the compensation level is limited to be less than 30% due to concerns about the occurrence of sub-synchronous resonance (SSR) [27]. This will be further explained in Chapter 2. The FCSC circuit is controlled by adjusting the GTO switches off-time governed by the value of the turn-off angle γ . A transcendental equation is used to express the relationship between this angle and the

effective capacitive reactance of the GCSC circuit. In such a fixed frequency system, and because of the compensation level limitation, the value of γ does not need to vary continuously. Different control strategies have been used to control the FCSC capacitive reactance by predicting a suitable value of angle γ according to the operating condition. Moreover, a simulation-only evaluation of the FCSC circuit has been presented for another fixed frequency three-phase system where the operating frequency is higher and fixed at 300 Hz, such as in series hybrid electric vehicles (SHEVs). This simulation is based on a comparison between system performance when employing the FCSC circuit and when using conventional rectifiers, including uncontrolled and fully controlled diode bridge rectifiers; the diode rectifier with a boost DC-DC converter, and a PWM voltage source current-controlled rectifier [29].

In 2009, the FCSC circuit was used at Newcastle University for a stand-alone wave energy conversion buoy where the frequency varied between 1-3 Hz. By interfacing the single-phase linear generator with FCSC circuit, the overall power factor of the system improved. The circuit is controlled using the same transcendental equation used for transmission networks. Therefore, the IGBT switches are kept ON for a period equivalent to $\pi/2+\gamma$ [30], which means that the switch will be ON for most of the time where the switch is active, thus limiting the range of variation in γ , and consequently capacitive reactance. This limitation does not affect the use of the FCSC in wave energy conversion buoys, since the frequency variation is limited in the range between 1-3 Hz (i.e. the frequency range is 3 p.u).

Furthermore, since the value of the turn-off angle is based on the transcendental equation, which requires significant processing time, real-time calculation of γ is not possible in systems where the operating frequency is continually changing. For this reason, the value of γ must typically be pre-calculated and stored in a look-up table.

Therefore, this thesis contributes to current knowledge by proposing symmetrical duty cycle control (SDCC) to control the FCSC circuit in a VVVF system with a wide frequency range. The proposed control method should provide continuous variation in the capacitive reactance required for each operating condition by controlling the duty cycle of the switches in accordance with operating frequency variations. In addition, it is better to avoid the need to perform a pre-calculation process and storing the data in a large look-up table, as used previously in WECs. This helps avoid the need for a large memory sized microcontroller.

Furthermore, since a three-phase generator is commonly used in VVVF systems, it is important to investigate the performance of the three-phase FCSC circuit compared to the single-phase circuit topology. This is because there is no previous academic research that has yet assessed the behaviour of the three-phase FCSC circuit in a VVVF system.

The aims of this research are to propose, investigate, evaluate, simulate, and build a suitable CSC circuit with a novel control strategy to be employed in low-and medium-frequency applications such as wave energy converters and more electric aircraft. The performance evaluation in this work focuses mainly on power factor correction.

The main objectives of this research are to:

- Provide a general overview of certain stand-alone variable-voltage variable frequency systems, especially the wave energy converter and more electric aircraft.
- To review common series compensators. In particular, the thesis will review in detail the controlled series capacitor circuit topologies employed in power transmission systems, in relation to their advantages, disadvantages, and limitations.
- Propose the most suitable CSC circuit for stand-alone variable frequency systems, including a low frequency range of 1-5 Hz, and a medium to high frequency range of 50 Hz up to 800 Hz.
- Determine whether or not the FCSC circuit can be used in VVVF systems with a wide range of frequency variation.
- Investigate numerically the performance of the FCSC circuit in its single-phase and three-phase form, including an assessment of power factor, output voltage, and total harmonic distortion.
- Identify the effect of load variation on the performance of the single-phase and threephase topologies for the FCSC circuits.
- Propose a new control strategy for single-and three-phase FCSC circuit topologies to cope effectively with both small and wide frequency ranges and to validate the strategy both numerically and experimentally. This is one of the key contributions to knowledge within this thesis.
- Investigate numerically and experimentally the harmonic distortion level of the converter to determine its suitability for employment in MEA applications.

1.4 Contributions to Knowledge

The key contributions to knowledge from this research are as follows:

 Proposing a variable reactance CSC circuit for the first time to be employed in aircraft systems.

- Identifying a CSC circuit for both low and medium frequency applications, with a wide range of frequency variation. The range of frequency variation in this thesis is believed to be much higher than that considered by existing literature; here, 10 p.u, frequency changes are investigated.
- Proposing a novel control technique so that the FCSC circuit can effectively cope with low and high frequency ranges in both single-and three-phase topologies.
- Examine the ability of the proposed control technique in controlling the FCSC circuit with a wide range of frequency variation such as 50-500 Hz (i.e 10 p.u. of frequency variation range).
- Investigating the employment of SDCC on both single-phase and three-phase circuit topologies and highlighting the difference between both topologies in terms of the commutation overlap and output voltage.
- Investigating comprehensively the performance of the three-phase FCSC circuit in terms of power factor, output voltage, and harmonic level, under different variable frequency systems such as wave energy converter buoys (1-5 Hz) and more electric aircraft (50-500 Hz).
- Introducing the FCSC converter behaviour according to the duality principle.
- Identifying and analysing the impact of load variation on the behaviour of the FCSC circuit in both single and three-phase circuit topologies in a VVVF system.
- Simulating and experimentally validating the performance analysis of the three-phase
 FCSC circuit with a widely varying operating frequency and voltage, in addition to various load conditions.

1.5 Publications Arising From This Research

The research conducted in this thesis has resulted in three international conference papers listed below:

1- T. Al-Mhana, V. Pickert and B. Zahawi, "Impact of load variations on the operating PF of an FCSC converter applied to wave energy systems," in *IEEE Energytech 2013*, Cleveland, Ohio, United States of America, May 2013, pp. 1-6.

- 2- T. Al-Mhana, V. Pickert and B. Zahawi, "FCSC converter with symmetrical short duty cycle for variable frequency applications," in 7th IET International Conference on Power Electronics, Machines and Drives (PEMD), Manchester, United Kingdom, April 2014, pp. 1-5.
- 3- T. Al-Mhana, B. Zahawi and V. Pickert, "Symmetrical duty cycle control for FCSC converter for wave energy applications," in 9th International Symposium on Communication Systems, Networks & Digital Signal Processing (CSNDSP), Manchester, United Kingdom, July 2014, pp. 56-60.

1.6 Thesis Overview

The thesis consists of eight chapters and eight appendices. A brief description of each chapter is given below:

Chapter 1 provides a general introduction to stand-alone variable-voltage variable-frequency (VVVF) applications and focuses on wave energy converters and more electric aircraft. It explains the terminology used for both applications, and presents a general overview of series compensation techniques. The research objectives and contributions to knowledge are presented, and a thesis overview is also provided.

Chapter 2 reviews the common controlled series compensator (CSC) configurations described in the literature. This includes the CSC circuit topologies employed in power systems. It presents a theoretical comparison of several common CSC circuit configurations in terms of their advantages, disadvantages, and limitations, with a particular emphasis on limitations in cases of frequency variation. The chapter proposes the FCSC circuit as the most promising types of CSC circuit to serve in stand-alone variable-voltage variable-frequency applications.

Chapter 3 presents details of the performance analysis of the single-phase FCSC circuit in terms of power factor, output voltage, output power, efficiency, and the total harmonic distortion (THD). The power factor is investigated in terms of displacement factor (DPF) and distortion factor (DF). Details are provided of the single-phase FCSC-rectifier's principle of operation and various modes of operation. A SABER-based model is developed and the

behaviour of the single-phase FCSC converter is tested by simulation at a low frequency value of 3 Hz which is a typical wave energy application frequency. The chapter also describes the impact of load variations on the performance of the single-phase FCSC circuit. The chapter concludes with the idea that there is a minimal impact of load capacitance variation on circuit performance.

Chapter 4 investigates the behaviour and performance of the three-phase FCSC circuit topology to be proposed for stand-alone three-phase systems. It describes the three-phase FCSC converter and the principle of operation. The chapter also analyses circuit performance numerically by simulation in terms of power factor, efficiency and THD. The simulation analysis covers two rectifier circuit topologies: the three-phase six-pulse diode-bridge rectifier and the three-phase FCSC-rectifier operating at 500 Hz. It also describes the ability of the three-phase FCSC-rectifier to correct the power factor to almost unity and to reduce the effect of current commutation. An in-depth harmonics analysis is also provided in order to assess circuit performance according to the power quality requirements of aerospace systems. Simulation results are presented for both fixed and variable load. An overview of the DC load types which can be supplied by the rectifier output and its effect on the AC side of the circuit is also provided.

Chapter 5 presents the novel symmetrical duty cycle control (SDCC) technique which is proposed to enable the FCSC-rectifier to cope with frequency variations. The chapter explains the technique for both single and three-phase topologies. The simplicity of the IGBT switching pattern is also explained. The relationship between the switch duty cycle and the supply frequency is formulated, and the new control scheme is tested and validated by simulation. The FCSC-circuit operation under this approach is simulated at various frequency ranges, including 1-5 Hz and 50-480 Hz for both topologies. A description of different modes of operation is also presented. The current harmonics components are analysed to evaluate the distortion level of the three-phase FCSC-rectifier under fixed and variable load. The simulation results show how the three-phase FCSC is capable of correcting the power factor and maintaining low current distortion between the maximum frequency and half of its value.

Chapter 6 briefly describes the experimental set-up for testing the performance of the three-phase FCSC-rectifier with SDCC and operating in VVVF system.

Chapter 7 presents and analyses the experimental results achieved from testing the effect of applying the proposed control scheme on the three-phase FCSC converter. The results are recorded at various voltage and frequency values. It concentrates on providing a practical evaluation of the employment of the SDCC for the three-phase FCSC-rectifier in a variable voltage and frequency system. To evaluate converter performance, the experimental results are presented for both the three-phase conventional diode bride rectifier and the FCSC-rectifier under the same operating conditions. The results are compared for both circuit topologies in terms of output voltage, output current, output power, power factor and the total harmonic distortion under both fixed and variable resistive load. The ability of the three-phase FCSC-rectifier to improve the power factor, output voltage and output power against the diode bridge rectifier is validated.

Chapter 8 presents the conclusions of this research. It highlights the main findings described in this thesis and the concordance between simulation and experimental results. Possible suggestions for the future work are also summarised in this chapter.

Chapter 2. Review of Controlled Series Compensator (CSC) Circuits

In variable-voltage, variable-frequency applications, it is important to employ a power electronics converter that is able to cope effectively with the variable input voltages and input frequencies generated by power sources such as electric generators operating in stand-alone systems. In addition to the efficient operation of the power converter, a power converter should also optimise the power flow from the source to the load at all source and load conditions. An efficient power flow is measured in terms of the power factor. An electrical system that operates with a poor power factor requires higher currents to deliver to the load. With a system which has a low power factor, the generator efficiency is reduced due to the increase in the copper losses. If the power converter is able to operate the generator system with a unity power factor, the generator kW capacity will increase. Therefore, the electric machine can be smaller and lighter for the given active power rating [31].

This work investigates the use of controlled series compensator (CSC) circuits applied to stand-alone generator-set known for their variable output voltages and frequencies. In such a system, the CSC is normally positioned between the generator and a conventional diode bridge rectifier, where the latter is considered to be the simplest and cheapest rectifier solution.

This chapter introduces the basic configurations of common types of controlled series compensators, after providing a brief description of the role of series and shunt compensation techniques in power transmission networks. In order to achieve a better understanding of compensator operation, a comprehensive comparison between the different topologies of CSCs is also carried out based on the available literature, including consideration of the effectiveness and drawbacks of each type of series compensator. In addition, the limitations of these topologies are highlighted to determine their suitability for different applications. The results of this comparison will help in the selection of the most suitable CSC topology to be used in VVVF systems with a wide variation of frequency range. It will also help determine the extent to which the FCSC circuit, which has been proposed for a very small range of

frequencies, is the most suitable CSC topology for use in such systems or if there is a need to propose another type of series compensator.

2.1 Series and Shunt Compensation

Flexible AC transmission system (FACTS) devices are used in power transmission systems for reactive power compensation using electronically controlled reactive devices [32]. Series and shunt compensation methods have a long history as important techniques in electrical power systems. Shunt compensators are highly effective in regulating the desired voltage at a substation node under various loads, by injecting/drawing current into the transmission line [7]. However, actual transmittable power cannot be controlled effectively using a shunt compensator, since it is governed by the series impedance of the transmission line and the angle between the sending and receiving end voltages. On the other hand, a series compensator controls reactive power by merely supplying or consuming VARs in electrical systems, and so it functions as controlled voltage source. Therefore, series compensation is more powerful than the shunt controller in controlling the current and power flow and damping oscillation in the transmission network [27]. Series compensation techniques were introduced several decades ago in power transmission systems to control power transfer capability by reducing line impedance and the phase angle between the sending and receiving end voltages. The transmittable power can be increased by series capacitive compensation, which reduces the reactive line impedance. In general, controlled series compensation is considered to be an effective technique to control the power flow in the transmission lines and to improve system stability [33]. Therefore, in this research, the series compensation technique is adopted in order to correct the power factor through controlling the line current in the system.

2.2 CSC Applications

CSCs have been employed in different power networks, including in power transmission systems where the amplitude of voltage and frequency are constant [27, 34]. One CSC circuits has also recently been introduced to applications where the supply voltages and supply frequencies varies. For example, Pickert *et al.* [30] proposed an FCSC with a single-phase stand-alone wave energy conversion buoy, where the amplitude of voltage and its frequency vary with wave movements. In such a system, the frequency is very low and varies within a small range between 1-3 Hz. In addition, CSCs have been also proposed for wind farm applications [35-41].

CSCs have been well established to operate for fixed input voltages and frequencies. However, fewer advances in development have been undertaken so far for CSCs with variable input voltages and frequencies. In these cases, the power is usually generated from a standalone generator as described in [30, 35-38]. Due to the design of stand-alone electric generators, most variable-voltage, variable-frequency systems suffer from poor input power factors, which cause a reduction in output power and efficiency. One possible solution is to propose a power electronic converter which is able to offer better utilization of the electric generator with different supply voltages and frequencies. This means that such a converter will be able to achieve a high power factor at various frequencies and increase the output power and efficiency of the system. Therefore, the need to find a proper converter to interface the generator and load to improve the power factor is crucial.

2.3 Overview of Controlled Series Compensator Circuits

Controlled series compensators can be classified in two different categories based on the basic approaches used. The variable reactance controlled series compensator (VRCSC) determines the capacitive reactance of the compensator using specific switching patterns to control a passive element. At the same time, the switching power converter series compensator (SPCSC) represents a controllable synchronous voltage source in series with the transmission line [27].

The VRCSC controls the capacitive reactance of the compensator using specific switching patterns. These can be split into two sub-categories based on the passive components used: the C-group and LC-group. The LC group is represented by the so-called thyristor-controlled series capacitor (TCSC) circuit, whilst the C-group comprises three different topologies: the forced-commutation controlled series capacitor (FCSC; also called the GCSC or gate-controlled series capacitor); the thyristor switched series capacitor (TSSC); and the switched variable series capacitor (SVSC)). However, the converter-based series compensators can control reactive power by circulating current in the system without a need for an energy storage element [27]. These include the magnetic energy recovery switch (MERS), which dumps the reactive power using a DC capacitor, the static synchronous series compensator (SSSC), and the dynamic voltage restorer (DVR). A family tree of the most common controlled series compensators is illustrated in Figure 2.1.

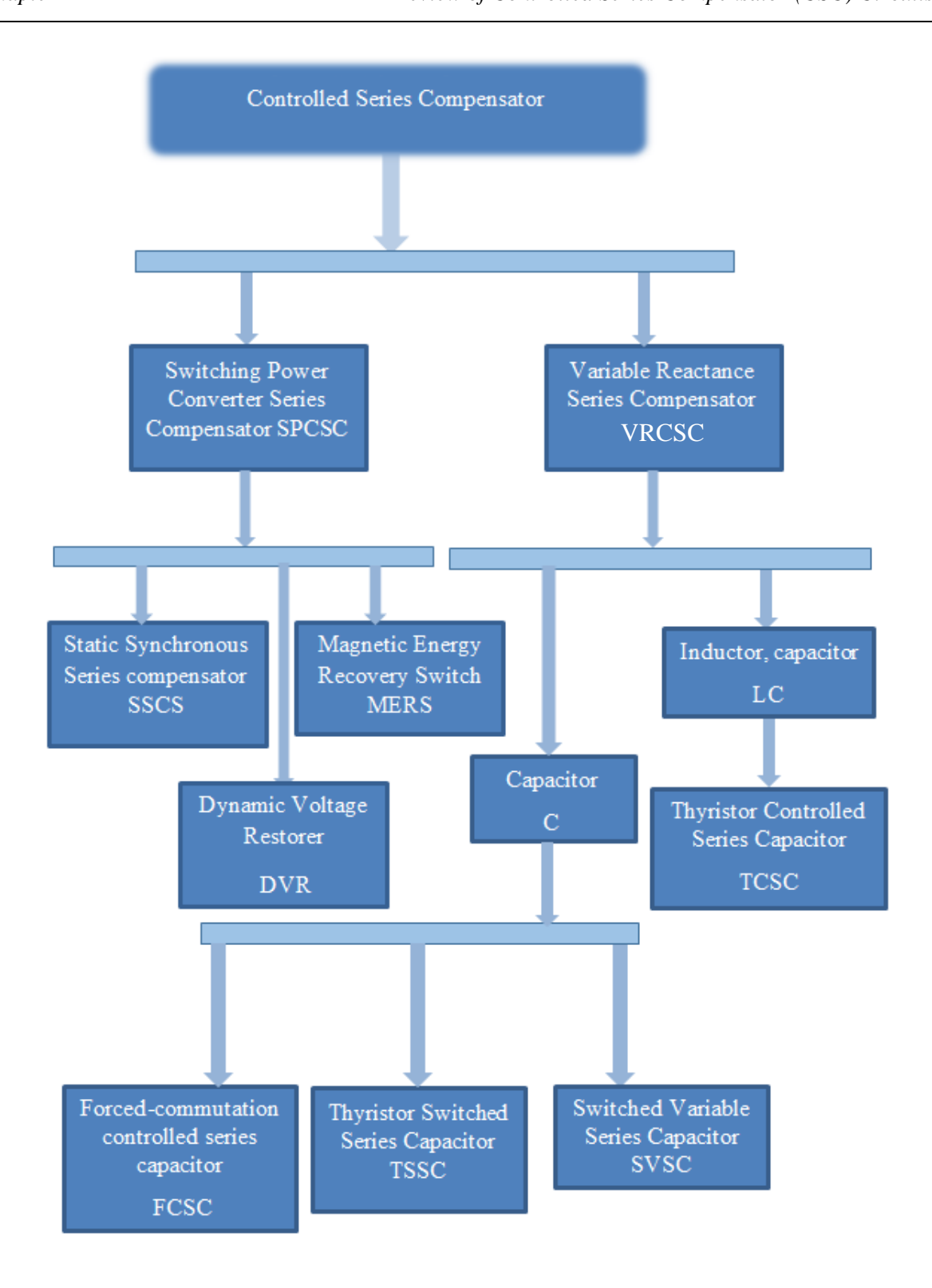


Figure 2.1 Family tree of common static controlled series compensators

Most of the common VRCSCs employ an AC capacitor connected in series with the system, which is needed to control the reactive power by using a fundamental frequency switching (FFS) pattern where the switching devices are turned ON and OFF once in one cycle. This reduces switching losses and, therefore, it is a preferred approach with higher utilization of

the switches. However, the SPCSC compensators generally employ a DC capacitor as energy storage and control of the reactive power is achieved using various switching modulation techniques, such as PWM techniques, which cause high switching losses in the system [32].

It is worth mentioning that, based on the concept of converter-based series compensation (SPCSC), the impedance-frequency relationship plays no role in achieving the desired compensation level in the transmission system since it controls the system's voltage amplitude and phase. In contrast, the concept of VRCSC depends on the relationship between frequency and impedance which characterises the system by improving the transient stability and providing it with immunity to SSR [27]. It is important to note that the use of VRCSC is the preferred technique in this research for two reasons. Firstly, the present work focuses mainly on correcting the power factor at wide frequency variations by cancelling the inductive reactance. Secondly, the ability of the CSC capacitor to work at a fundamental frequency over PWM switching frequency promises a reduction in losses. Hence, a wide-ranging investigation of comparing various VRCSC types is carried out in this chapter. However, a description of the most common SPCSC is presented later to provide a complete picture of controlled series compensators.

Furthermore, Kalpaktsoglou and Pickert [42, 43] conducted a simulation which was limited in comparing MERS and other different VRCSC circuits, to be employed for power factor correction in a single-phase wave energy conversion buoys. In WEC, the frequency is very low between 1-3 Hz. This means that the range of frequency variation is very narrow. The comparison showed that MERS is not considered to be the most effective device to implement with this scale of frequency variations. Based on their findings, MERS will not be proposed as a power factor correction circuit for this work.

2.3.1 Variable Reactance Series Compensator (VRCSC)

The most common types of VRCSC can be categorized as follows:

1) Thyristor Switched Series Capacitor (TSSC)

The basic TSSC configuration consists of a number of identical capacitors (C_{TSSC}) connected in series, as shown in Figure 2.2. Each capacitor is connected in parallel with a switch which consists of two anti-parallel thyristors, where each thyristor will be active for half of the cycle of the line current.

The degree of series compensation and the value of effective capacitance are controlled by decreasing or increasing the number of bypassed capacitors. This is achieved by turning ON or OFF the corresponding thyristor switch. By turning the appropriate switch ON, the capacitor is short-circuited, while it is inserted with the line when the switch is in blocking state.

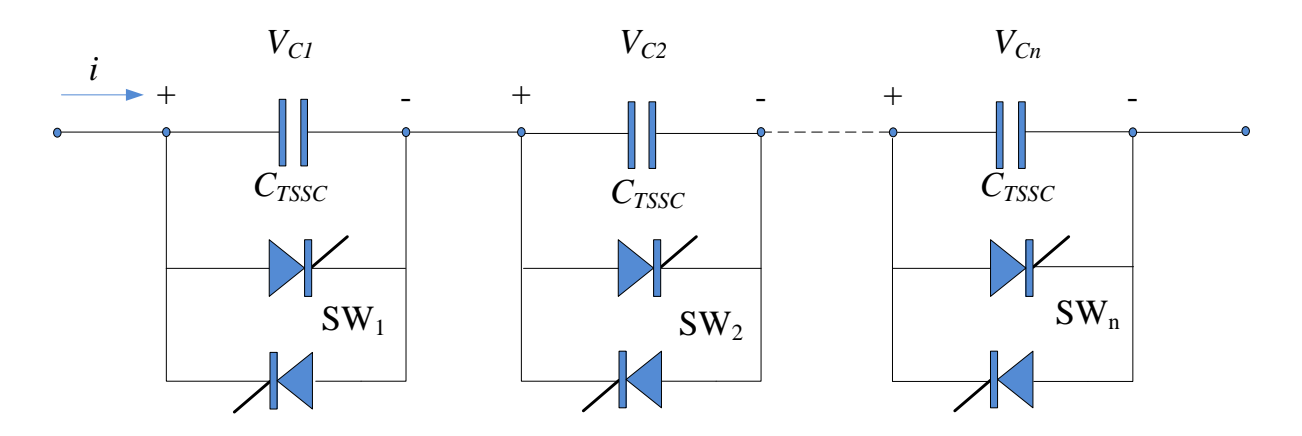


Figure 2.2 TSSC circuit diagram (only one-phase is shown)

If all thyristor switches are conducting, the total equivalent capacitance is $(C_{eq}) = 0$ F. However, when all the switches are blocking, the total equivalent capacitance can be determined from equation (2-1):

$$C_{eq} = \frac{C_{TSSC}}{n} \tag{2-1}$$

where n represents the number of inserted capacitors.

The TSSC uses the thyristor as a switch. When the line current crosses zero, all the thyristors turn OFF naturally, because thyristors are natural commutated switches. The capacitor can be inserted into the line only at the moment when the line current is at the instant of zero crossing, which means only at zero current switching (ZCS). As a result, the inserted capacitor can be charged to its maximum voltage during the full half cycle of line current. For the opposite polarity half cycle of the line current, the capacitor discharges its voltage from the maximum value to zero [7, 27].

The thyristor should be ON only when the capacitor voltage is zero, to reduce the initial surge current and transient voltage which can be calculated as:

$$i_C = C \frac{dv_C}{dt} \tag{2-2}$$

The main problem in this configuration is the possible occurrence of sub-synchronous resonance (SSR) which is similar when employing a fixed capacitor [44]. SSR is a phenomenon induced in the system due to the interaction between the mechanical system and the electrical system in the power generation, as represented by the turbine-generators set and series capacitors. It occurs as a reaction to any change in the electrical power system which leads to a response from the mechanical system at a given frequency. This includes any system variations, which can affect the energy at certain sub-synchronous frequencies such as the series capacitor in the compensated transmission lines. This sub-synchronous frequency can interact with the specific torsional mode of the turbine-generator shaft which results in damage to the shaft [45]. In 1973, Ballance and Goldberg reported the sub-synchronous resonance SSR phenomenon in a compensated transmission line with a fixed capacitor due to resonance in the series transmission line coupled with a synchronous generator. A photograph of the failure of the shaft at the MOHAVE generating station in Southern Nevada caused by SSR has been published in [46]. A detailed analysis of solutions in dealing with SSR was introduced within a NAVAJO project in 1977 [47].

An additional drawback of this arrangement in practice is the necessity of connecting a current limiting reactor in series with the TSSC in order to hold the high current; this is due to the physical constraints of the thyristor such as di/dt and the magnitude of the surge current [27].

Furthermore, an adaptive controller with a continuous approach has been proposed for a power system network to achieve continuous reactance control [48]. This controller attempts to damp power oscillations to improve transient stability without the limitation of the common linear control approach by using a generic system model. In general, most power system control models with a linear control approach lose their power damping when the system's operating point is changed. This occurs after a large disturbance in the system, and a controller can also be used to control a system with a TCSC compensator [48].

2) Thyristor Controlled Series Capacitor (TCSC)

In 1988, Vithayathil *et al.* proposed a basic arrangement of the TCSC which was introduced as an approach for "rapid adjustment of network impedance" [49, 50]. An analytical study of

the control interaction between TCSC and an existing device in the power system, such as the Static Var Compensator (SVC), was produced in [51]. In 1999, the first TCSC was established in Sweden for 400 kV grids to mitigate the (SSR) problem. Figure 2.3 shows the basic scheme of the TCSC. It consists of a series of fixed capacitors shunted with a thyristor controlled reactor (TCR) circuit. The TCR circuit is comprised of an inductor connected in series with a switch (SW) which includes two anti-parallel thyristors.

The TCSC is the only VRCSC which is able to supply the line with inductive or capacitive reactance as needed. This depends on the conduction and blocking intervals of the thyristors through their firing angle α . The TCSC can be modelled as fixed capacitive impedance X_C in parallel with variable inductive impedance $X_L(\alpha)$.

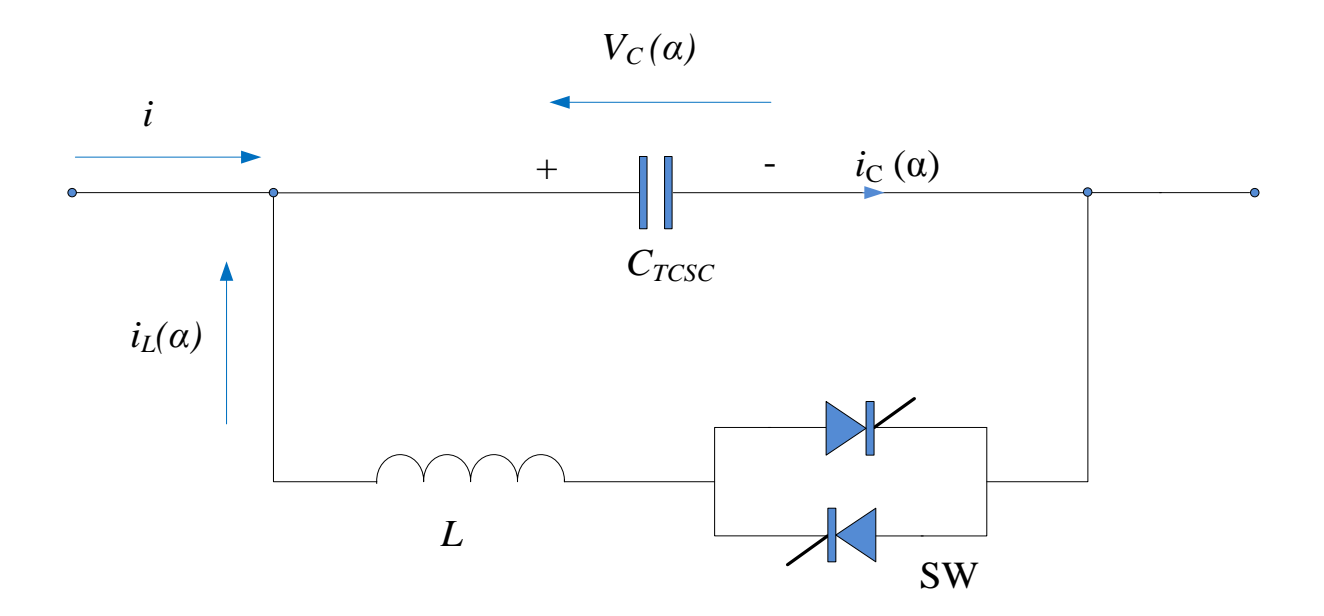


Figure 2.3 TCSC circuit diagram (only one-phase is shown)

Equation (2-3) represents the effective impedance of the TCSC ($X_{TCSC}(\alpha)$) as:

$$X_{TCSC}(\alpha) = \frac{X_C \times X_L(\alpha)}{X_L(\alpha) - X_C}$$
 (2-3)

where $X_L(\alpha)$ represents the variable inductor of TCR which can be calculated as follows [27, 52]:

$$X_L(\alpha) = X_L \times \frac{\pi}{(\pi - 2\alpha - \sin \alpha)}$$
 for $X_L \le X_L(\alpha) \le \infty$ (2-4)

where α is the delay angle which can be measured from the zero crossing point of the line current or equivalently the instant of peak capacitor voltage, and:

$$X_L = \omega L = 2 \times \pi \times f \times L \tag{2-5}$$

$$i_{C}(\alpha) = i + i_{L}(\alpha) \tag{2-6}$$

Depending on the delay angle α , X_L is varied between a minimum value ($X_L(\alpha) = \omega L$) and a maximum value. Therefore, $X_{TCSC}(\alpha)$ will behave as a tuneable LC circuit to compensate for the line with the required reactance passing through internal resonance. Internal resonance occurs when X_c is equal to $X_L(\alpha)$, which leads to $X_{TCSC}(\alpha)$ theoretically being infinity, as expressed in equation (2-3). Therefore, α needs to be within certain limits to avoid the occurrence of internal resonance [7, 27]. Figure 2.4 illustrates the dependency of the TCSC impedance to the firing angle α and demonstrates the modes of operation. In general, TCSC has three modes of operation [52-54]:

- 1. Bypassed-thyristor mode: In this mode, the thyristors continuously conduct the current with a firing angle of 180°. This leads the effective reactance X_{TCSC} to be a function of parallel L and C. However, based on the typical values of reactor and capacitor susceptances, the current is inductive.
- 2. Blocked-thyristor mode: This mode occurs when the thyristors are not conducting at all since the valve is turned OFF when their current is reduced to zero. The line current only flows through the series capacitor. Therefore, the effective TCSC reactance X_{TCSC} is capacitive and equal to X_C .
- 3. Vernier mode: TCSC behaviour is a function of the phase control of the thyristors delay angle α in this mode. Therefore, the TCSC can operate either as controllable inductive reactance or controllable capacitive reactance. There are two basic regions for TCSC operation, the capacitive and inductive regions. When α is large, the TCSC operates as capacitive reactance, while a lower firing angle delay makes TCSC behave as inductive reactance. α is measured from the crest of the capacitive voltage, as shown in Figure 2.4.The figure also shows that the smooth transition between the capacitive and the inductive region is not permitted because of the internal resonance.

Different models for the TCSC were derived to improve power system stability and design a proper controller for this purpose, as well as develop a better understanding of

this compensator during its operation. The steady state and dynamic characteristics of TCSC have been analysed for all three modes of operations [55-59].

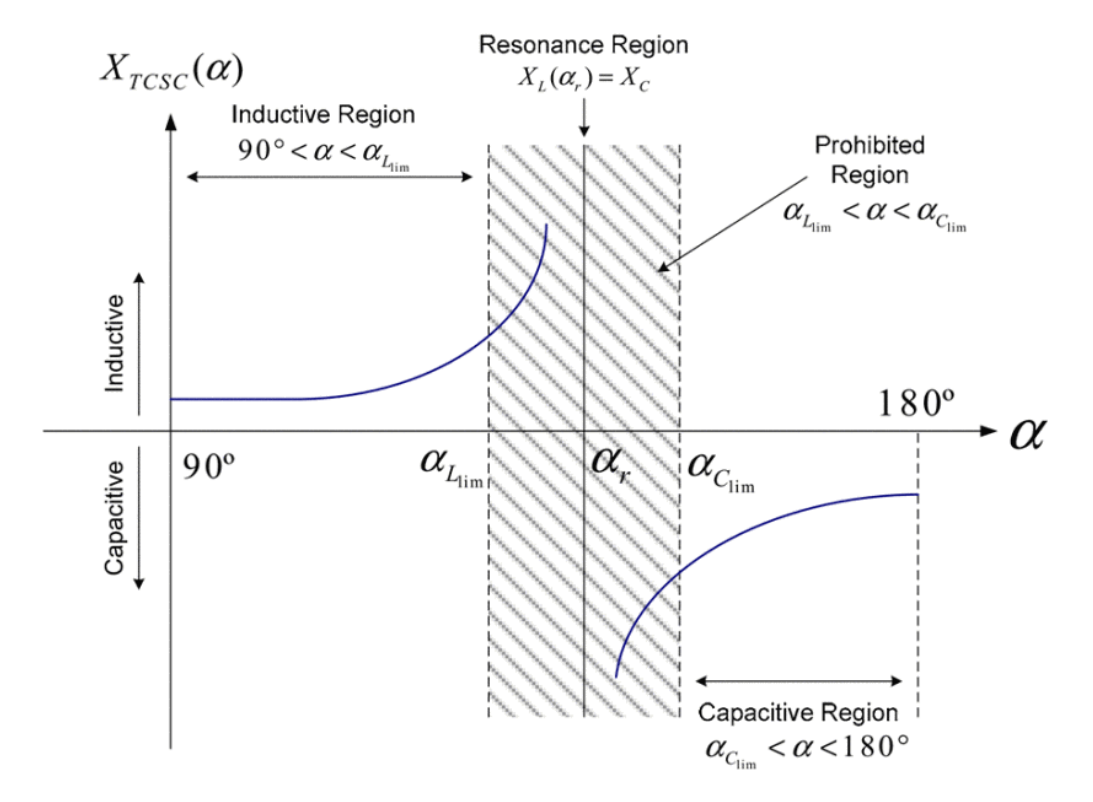


Figure 2.4 Impedance characteristics of TCSC [52]

A controller for the TCSC has been designed based on mathematical modelling and the transfer function [60]. Optimized values of the capacitor and inductor of the TCSC have been selected as a function of the degree of series compensation to avoid the occurrence of the SSR problem and series and parallel resonance [61].

In 1966, Kimbark [62] analysed the improvement of transient stability in long transmission lines by using a switched series capacitor for the first time. His analysis controls the degree of series compensation according to fault occurrence in the transmission system such as a three-phase fault.

The TCSC is able to improve power quality by applying a specific arrangement for poles and zeros [63]. It is also able to enhance power quality by preventing voltage sag and limiting the current during faults by changing the TCSC mode to bypass mode during a disturbance [64, 65]. Furthermore, the TCSC is considered to be one of the most effective FACTS devices for use in mitigating the risk of SSR, that is why the TCSC is referred to as SSR neutral [66, 67]. A detailed analysis of the TCSC performance when used in long transmission lines showed that the TCSC is free of the risk of SSR when a 60% compensation ratio is added [68]. The

SSR in the system can be suppressed by the appropriate selection of the thyristor delay angle α so that the power damping becomes zero [69]. Several other control methodologies have also been proposed to mitigate SSR. Pillotto *et al.* [70] analysed the system with the three control methodologies of constant current control, constant power control and constant impedance control, using a first IEEE benchmark model in their investigations in addition to the effect of firing control techniques. The IEEE benchmark is a benchmark model used to study and simulate the SSR in a transmission network with two tests [71]. It was concluded that TCSC power control loops respond slowly to oscillation, while the current controller responds quickly to any disturbances.

Different control strategies have also been proposed to control the effective reactance of the TCSC, improve transient stability and damp power oscillations. An adaptive controller using backstepping methods based on second and third order non-linear system models has been introduced and the derivation of system models discussed in several studies [72-75].

3) Forced-Commutation Controlled Series Capacitor (FCSC)

A forced-commutation controlled series capacitor can be described as a series fixed capacitor in parallel with a switch, as shown in Figure 2.5. The switch is bidirectional and consists of two anti-parallel forced commutation type devices such as a GTO or an IGBT. The only difference between FCSC and TSSC circuit configuration is the use of the forced commutation switch type to control the instant at which the device is turned OFF. This configuration is called GCSC when the switches are GTOs. By using the phase control technique with this arrangement, the voltage across the capacitor Vc, can be controlled by varying the turn OFF angle of the GTO switch at a specific line current. The major advantage of FCSC over TCSC is that the former offers the fast and continuous control of series compensation by using one passive component only, C_{FCSC} .

Figure 2.5 illustrates clearly that the capacitor is bypassed when the switch is turned ON and Vc is zero. Conversely, the voltage across the capacitor is at its maximum value when the switch is turned OFF [44]. The capacitor voltage, Vc, is controlled by closing and opening the switches in each half cycle in synchronism with supply frequency. In addition, the forced commutated switch is turned ON whenever the capacitor voltage crosses zero to avoid emerging current or voltage transient, and it is turned OFF at a certain turn OFF delay angle (γ) , which indicates the turn OFF instant. The turn OFF angle (γ) , is referenced to the crest of

the line current and can be varied within the range $0 \le \gamma \le \pi/2$. Figure 2.6 demonstrates the relationship between the line current and the capacitor voltage with the turn OFF angle γ .

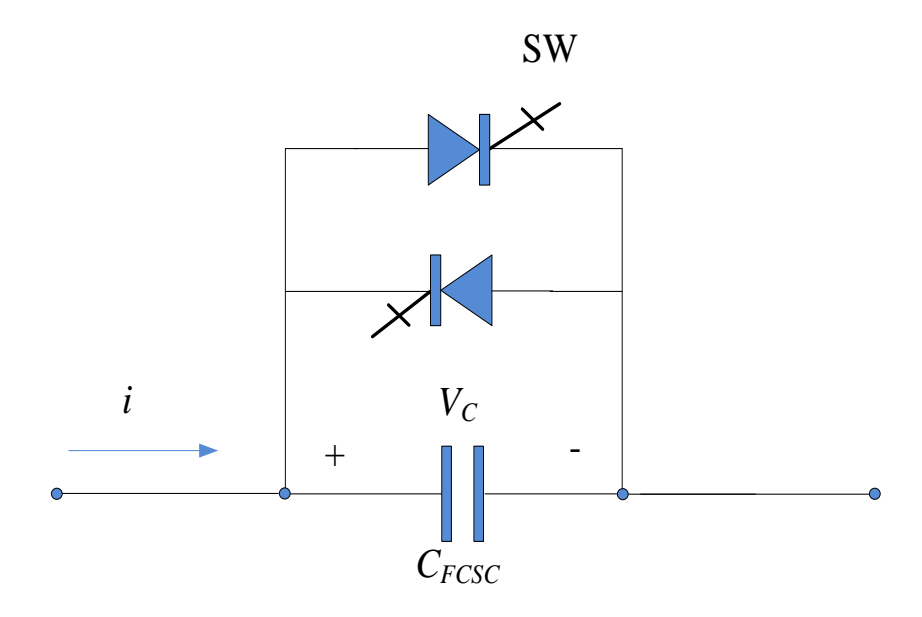


Figure 2.5 GCSC circuit configuration (only one-phase is shown)

During the positive half cycle of the supply voltage, when γ equals zero, the voltage across the capacitor, and hence the capacitor reactance will be at its maximum value. However, V_c is reduced to a minimum value when the switch is turned OFF at a certain γ value. The current will pass through the capacitor when the switch is OFF for the duration of δ . Identical behaviour occurs during the negative half cycle with the corresponding switch ON and OFF.

As the capacitor voltage is non-sinusoidal, the fundamental capacitor voltage can be expressed in the following equation:

$$V_{C1}(\gamma) = \frac{I_m}{\omega C_{FCSC}} \left(1 - \frac{2\gamma}{\pi} - \frac{\sin 2\gamma}{\pi}\right) \tag{2-7}$$

where I_m is the maximum of the line current and ω is the angular supply frequency.

The effective capacitive impedance X_{FCSC} is a function of γ :

$$X_{FCSC} = \frac{V_{C1}(\gamma)}{I_m} = X_C (1 - \frac{2\gamma}{\pi} - \frac{\sin 2\gamma}{\pi})$$
 (2-8)

Equation (2-8) shows that the FCSC is considered to be variable capacitive impedance. X_{FCSC} is varied from a maximum value ($X_{FCSC} = X_C = 1/\omega C$) when γ equals zero to a minimum value of zero when γ is at its maximum value (i.e $\gamma = \pi/2$) [27, 76].

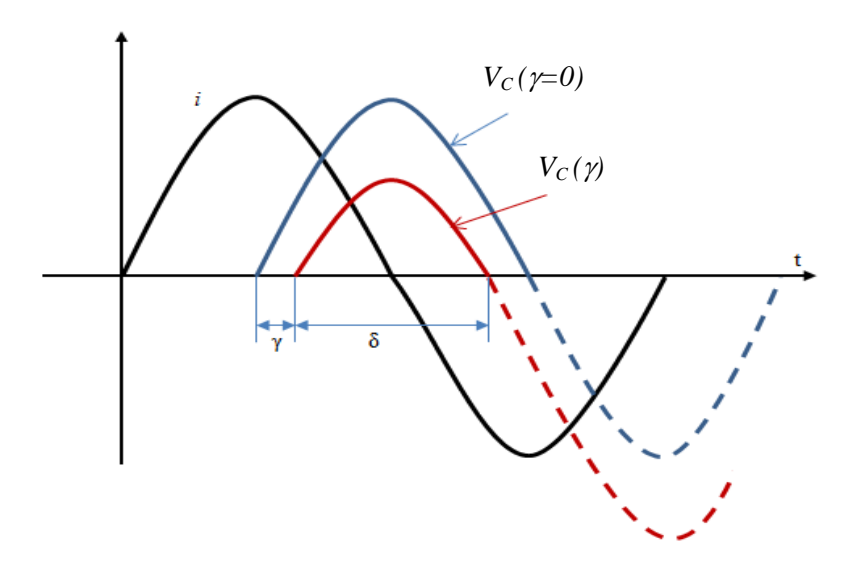


Figure 2.6 Line current and capacitor voltage waveforms as a function of γ during the positive half cycle

Therefore, the control of γ leads to continuous variation of the capacitive reactance X_{CFCSC} . The switch transition between the OFF and ON states occurs only when the voltage is zero, which means that it is a zero voltage switching (ZVS) device. ZVS is a significant advantage for the device in series connection systems, especially in high power applications [77-79].

The GCSC was introduced for the first time in 1973, by Karady *et al.* [80]. A new method was proposed for the smooth variation of series compensation in a transmission network, by employing a bi-directional switch with anti-parallel connection such as GTO and controlling the ON and OFF time of the GTO switches with two different arrangements. One arrangement is by series connections of switch pairs with a bank capacitor, while the second arrangement is by parallel connection of the switches with a bank capacitor. Fault performance and a snubber design circuit, along with its advantages with the GTO-CSC, were subsequently investigated [81].

One of the main advantages of the GCSC is that it is able to mitigate SSR effectively without any specific control system or with a simple controller. It was shown through simulation and using the IEEE First Benchmark model that, by adjusting the generation of turn OFF angle γ as a function of zero crossing detectors, SSR can be naturally avoided in addition to power oscillation being damped [82-84].

From the available literature, the TCSC and GCSC are highly competitive regarding the power system since they share many advantages. Both devices are employed in power transmission systems to control power flow in long transmission lines. Therefore, a

comparison between both FACTS devices in terms of sizing and capacitor rating has been conducted [79], and it was concluded that the capacitor megavolt-ampere in the TCSC is higher than that in the GCSC because the current flowing in the capacitor in the latter is always lower than in the TCSC. With regards to the switch rating, the forced commutated switch current rating is lower than the thyristor rating in the TCSC. It has been argued [79] that the GSCS promises to be the most effective solution for series compensation. However, for Power Oscillation Damping (POD) (where the FACT device is used to damp the low frequency power oscillation initiated for different reasons, including any sudden change in the output of the generators or transmission line fault), each capacitor's rating in either device is approximately the same. Nonetheless, the TCSC is considered to be a desirable device for POD since circuit protection is simpler.

Furthermore, the major crucial feature of FCSC that enables it to be considered as an effective FACTs device is the capability to improve dynamic stability at high efficiency when using a damping controller [85]. Moreover, different modern control methodologies have been proposed to overcome the risk of SSR and in the design of a damping controller such as a fuzzy logic controller [86, 87].

In addition, the FCSC is capable of mitigating the effect of low frequency power system oscillations to enhance the stability margin by using Particle Swarm optimization (PSO) algorithm to design a damping controller [88, 89]. This algorithm attempts to find the optimized value of the parameters of the damping controller through Eigenvalue analysis of different operating conditions.

4) Switched Variable Series Capacitor (SVSC)

The basic arrangement of the SVSC circuit consists of two capacitors C_1 and C_2 connected in parallel through two bidirectional switches S_1 and S_2 , as shown in Figure 2.7. The value of C_2 is larger than that of C_1 . The average capacitor value C_{av} is a function of a duty factor. The switches S_1 and S_2 alternate with each other. This can lead to the production of an interval where both switches are in the OFF state. Therefore, the resistor R_{SVSC} is connected in parallel with the capacitors to ensure the continuity of current during the transition period between the ON and OFF state of the switches. The value of R_{SVSC} is chosen to be larger than the capacitors impedance [90, 91].

It is important to maintain the alternating operation of the switches S_1 and S_2 within a specific control scheme, such as those utilizing PWM control. The PWM technique should ensure that S_1 and S_2 are not working simultaneously. At high frequency, the controller allows the current to pass through S_2 and C_2 only (with S_1 in the OFF position). However, S_2 is in the OFF state at low frequency and S_1 and C_I carry the current at this frequency. Both capacitors are switched alternately with a specific PWM technique for frequencies in between these values [29, 92].

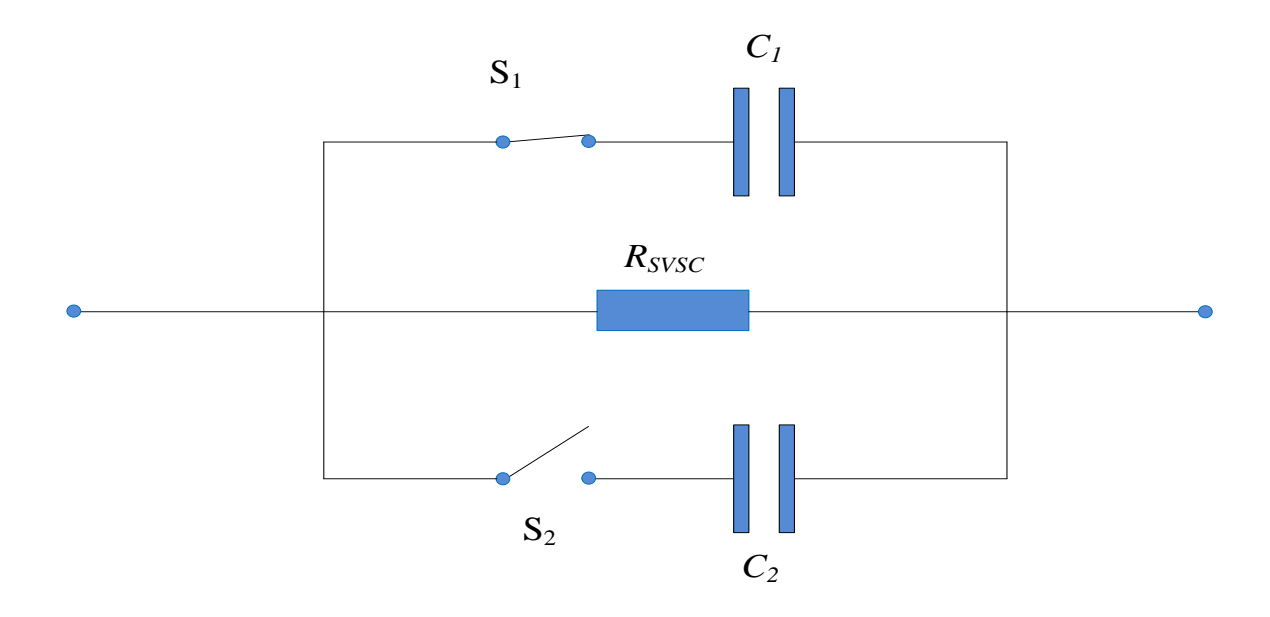


Figure 2.7 Switched variable series capacitor circuit arrangement (only one-phase is shown)

2.3.2 Switching power converter series compensator (SPCSC)

Common types of the SPCSCs are as follows:

1) Magnetic Energy Recovery Switch (MERS)

The magnetic energy recovery switch (MERS) is considered variable series compensation. Figure 2.8 illustrates the MERS circuit configuration, which is similar to a single phase full bridge. It consists of four forced commutation switches such as IGBT or MOSFET, four antiparallel diodes and a DC capacitor. Each switch is shunted by a diode. This arrangement therefore has the highest number of switches in comparison with VRCSC compensators.

The MERS implies a different approach to reactive power compensation. In this approach, the system can be compensated without any variation in the reactive impedance, but instead by

the absorption of the inductance stored magnetic energy. The DC capacitor is positioned in the middle of the two legs.

The small DC capacitor absorbs the magnetic energy stored in system inductance through forced LC resonance in the system [43, 93]. The MERS is normally located between the voltage supply and the load.

Generally, the control method for MERS depends on the application. However, the typical control method is by turning a pair and another pair of switches ON/OFF. There are three modes of operation. When S_1 and S_3 are ON while S_2 and S_4 are OFF, the charging current passes through the capacitor and there is a voltage across the capacitor; this mode is called non-continuous. The DC-offset mode occurs during the conduction of S_2 and S_4 and the blocking of S_1 and S_3 when there is an offset in the capacitor voltage. When the capacitor is by-passed for a certain interval (because the current flows through the switches only), this mode is named the by-pass mode [94].

It has been suggested that the MERS improves synchronous generator output power, by injecting series voltage, which is able to compensate the voltage drop across synchronous reactance. This series voltage is produced by absorbing the magnetic energy stored in the generator reactance.

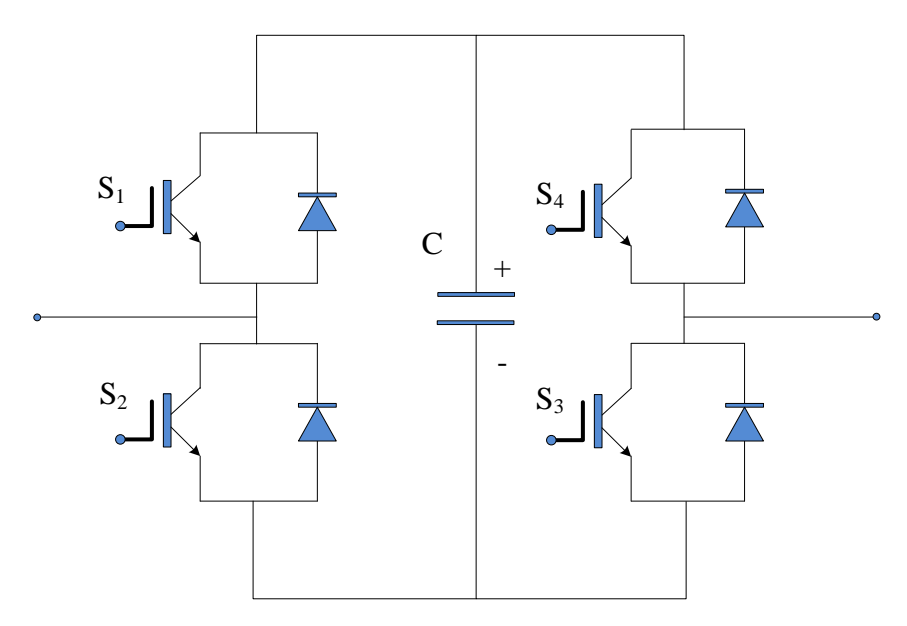


Figure 2.8 MERS configuration (only one-phase is shown)

The direction of current flowing through the DC capacitor is controlled by turning a pair of switches ON and OFF. S_1 and S_3 represent the first pair while the second pair are S_2 and S_4

[95]. By turning the first pair (S_1 and S_3) ON, the current flows from the supply to the load. When S_1 and S_3 are turned OFF, the stored magnetic energy in the inductance is recovered to the capacitor. The capacitor discharges its energy through the load when S_2 and S_4 are turned OFF. To achieve a unity power factor, the switching phase angle of S_1 and S_3 is advanced by 90°, which can make the inductive generator voltage fully compensated by the capacitor voltage [93, 96].

As mentioned earlier, by applying different switching techniques, the MERS is able to generate a pulse current for a pulsed power supply in certain applications, such as magnetizers and synchrotron accelerator bending magnets [97].

Nevertheless, a major drawback of the use of the MERS is the high number of switches needed. For a single-phase system, four forced commutated switches with four anti-parallel diodes are required. For three-phase system, 24 switches are needed, 12 forced commutated switches (such as IGBTs) and 12 anti-parallel diodes. This also requires a more complicated control algorithm to adjust the switching pattern for this high number of switches in synchronism with the supply frequency. Furthermore, the switching losses will be very high. For the above reasons, the MERS compensator will not be discussed in any detail in this thesis.

2) Dynamic voltage restorer (DVR)

This is a static VAR device used to inject an AC voltage into the power distribution grid to overcome some power quality issues such as voltage sags and swells and harmonic currents when a disturbance or voltage dip occurs in the power network [32, 98]. Voltage sag is considered to be a common voltage disturbance which is caused by a fault and leads to a phase angle jump in the distribution system. A DVR is often used to protect a sensitive load from voltage sag, a transient current and any disturbance in converter operation caused by the phase jump [99, 100]. However, the use of the DVR requires the employment of a large DC link capacitor to satisfy the requirements for high active power, which eventually leads to a substantial increase in the cost and the size of the compensator [101].

Basically, the DVR is comprised of four parts: a voltage source converter (VSC) with at least six IGBT switches; a DC link capacitor as energy reservoir; a harmonic filter to prevent the harmonics generated by the converter switching being injected with the injected voltage into the power grid; and finally, a connecting transformer to connect the DVR to the system as

shown in Figure 2.9 [32, 101]. When the system is healthy, the DVR will remain in stand-by mode, whereas it will inject an AC series voltage when a voltage dip occurs, to maintain the required voltage level.

Recently, a two-cascaded three-phase inverter instead of one VSI has been proposed for the regulation of the voltage at the load side, using a specific PWM control approach. This configuration has the benefit of reducing harmonic distortion, the power switch voltage rating, and converter losses. A comparison with other conventional VSI has also been presented [102]. Based on the purpose of using the DVR, different control strategies have been proposed. A fast and effective DVR response to compensate for voltage sag has been achieved by controlling the amplitude of the injected voltage and the phase angle of each phase separately without the need to use phase lock loop (PLL) method [103].

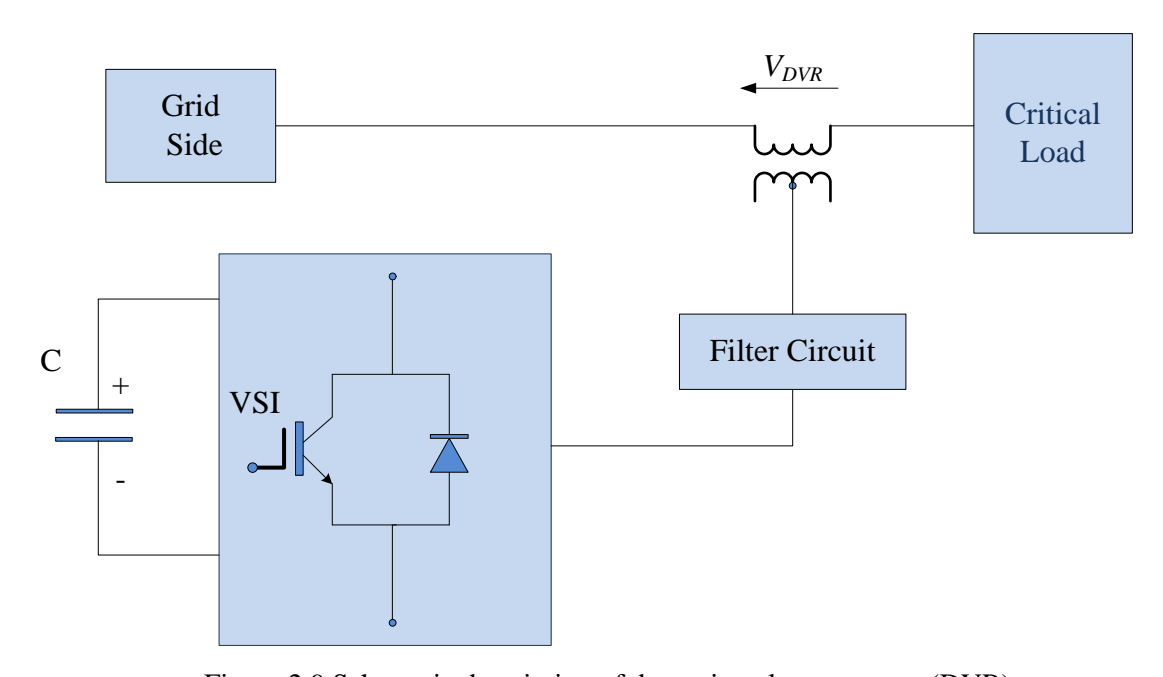


Figure 2.9 Schematic description of dynamic voltage restorer (DVR)

On the other hand, to mitigate the voltage sag and swell, an in-phase method has been adopted [104]. A multifunctional DVR control method has also been presented using a closed-loop control system to prevent steady state error and enhance the transient response by employing a Posicast and P+Resonant controllers [105].

It can be concluded, therefore, that the DVR is mainly used for voltage regulation and load protection purposes in a distribution network with a complex control and circuit topology.

3) Static synchronous series compensator (SSSR)

In 1989, the static synchronous series compensator was proposed for the first time by Gyugyi as a converter-based series compensator [27]. It mainly consists of a voltage source inverter (VSI), which can employ different switches controlled by a controller, a DC capacitor for energy storage, and a coupling transformer, as shown in Figure 2.10. The basic function of the SSSC is similar to most converter-based series compensators which control the amplitude and phase of the voltage across the transmission system [106, 107]. The SSSC is also able to mitigate SSR phenomena in the transmission system by implementing a controller which is able to increase the damping of the network at the frequencies which induce the SSR [108]. In addition, a combination of the SSSC and a passive series capacitor has been presented for faster power flow control, increasing the transmittable power and reducing the risk of SSR occurrence [109]. In addition, the SSSC has also been introduced into wind farms for the same purpose [110].

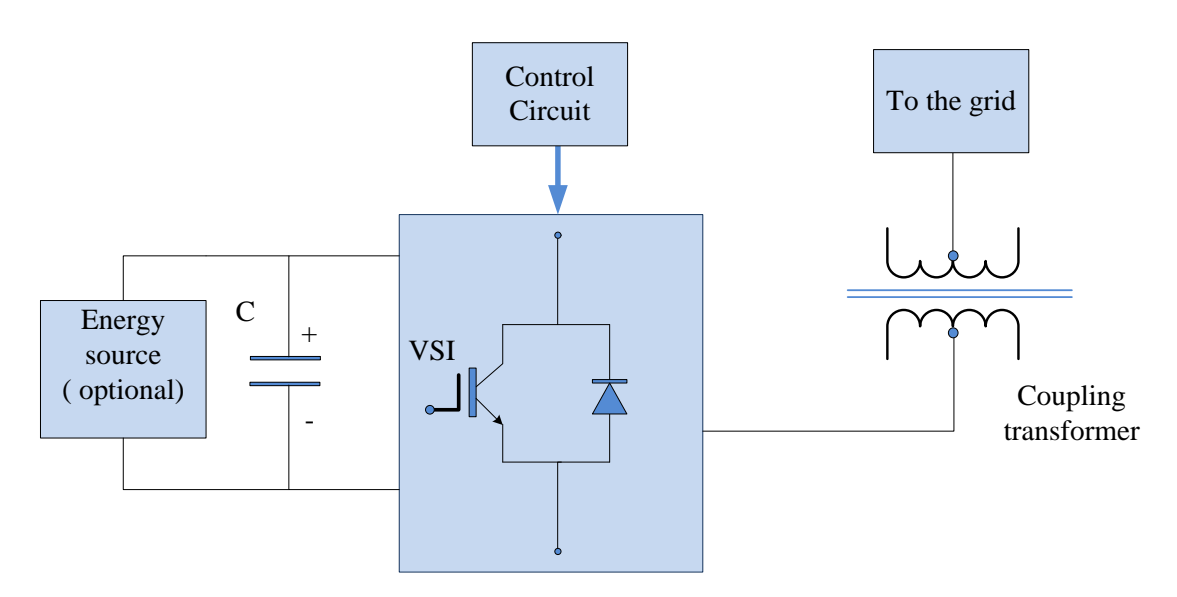


Figure 2.10 Schematic of the SSSC circuit

Based on the above information, it seems that the converter-based series compensators have the highest numbers of switches and circuit components and large DC link capacitors (such as in the DVR) and mostly need an interfacing transformer to be used. In addition, the control methods associated with employing various PWM techniques are very complex and have the drawbacks of high switching losses and electromagnetic interference (EMI) problems. This will lead to the increased size, cost, and complexity of a converter to be employed in a VVVF system. In addition, these compensators are mainly used for series compensation based on a voltage regulation approach rather than the dependency of the impedance-frequency

relationship. Therefore, the present study focuses on the most promising circuit topology of CSCs that is able to cope effectively with a wide range of frequency variations at acceptable complexity and cost, without a corresponding increase in size associated with the use of large circuit components and system protection.

2.4 Comparison of Different CSC Topologies

This section presents a comprehensive comparison of the most common VRCSC circuit topologies based on the available literature, to highlight the general performance levels, and advantages and disadvantages of different circuit topologies in power transmission systems, as shown in Table 2-1.

Table 2-1 Comparison of VRCSC topologies in transmission systems network

TSSC	TCSC	FCSC	SVSC				
General Specifications							
Consists of a number of identical capacitors, each shunted by two thyristors	Uses fixed single capacitor and single inductor with two thyristors	Consists of fixed single capacitor with two anti-parallel switches (GTO or IGBT)	Consists of two AC capacitors with four switches and a resistor				
Number of thyristors equal to double number of capacitors	Employs two thyristors only	Two forced commutated switches only	Four forced commutated switches				
Control is a function of firing angle	Capacitance is fixed while inductance can vary by controlling the firing angle	Control is a function of turn OFF angle γ	Capacitors are connected depending on the frequency range. C_2 and S_2 will be ON at high frequency, while C_1 and S_1 are ON for low frequency				
Due to thyristor constraint, the capacitor is inserted only at the zero crossing of the line current	The use of thyristor leads to restrictions on the ON time intervals	The use of forced commutated switches provides flexible control for varying ON and OFF intervals	Use of forced commutated switches provides flexible control for varying ON and OFF intervals				

TSSC	TCSC	FCSC	SVSC		
Advantages					
Higher power ratings and lower cost due to use of thyristors	Higher power ratings and lower cost since it employs thyristors	Fast and continuous control of the degree of series compensation	Can be employed for high and low frequency applications		
Is able to control the power flow and oscillation damping with moderate speed response	The capacitor reactance can be controlled smoothly by varying the delay angle α	Has a unique ability for the direct control of capacitor reactance by controlling the turn OFF angle γ			
	Continuous control of the degree of series compensation	Has been proposed as an economic and simple solution for series compensation in power control applications			
	Can provide the transmission line with inductive or capacitive compensation	Component ratings for capacitors and switches are lower than for the TCSC			
	Has the ability to mitigate SSR problems	Has the ability to prevent SSR without a controller or with a simple controller			
	Increases energy transfer, and improves transient stability in long transmission lines by damping the power oscillation	Increases energy transfer, and improves transient stability in long transmission lines (TL) by damping power oscillation with a simple controller			
	Is capable of controlling power flow in TL and limiting fault currents as well as enhancing power quality	Effective in controlling the power flow in long TL where it is considered a simpler and more economical solution			
		Can improve the system stability margins by mitigating power system low frequency oscillations.			
		A ZVS device which can be used in high power applications			

	Able to improve dynamic stability due to its high efficiency
--	--

TSSC	TCSC	FCSC	SVSC				
	Disadva	ntages					
Disacranages							
Offers discrete control of the degree of series compensation	Indirect control of X_C value, since X_C varies as a function of $X_L(\alpha)$	In POD applications, the scheme of GCSC protection is important	Care needs to be taken to ensure alternative operation of the switches				
The need to connect a current limiting reactor in series due to the thyristors physical constraints	The major drawback is the probability of parallel resonance between its L and C, which leads to infinite reactance		It is challenging to decide appropriate values of capacitors C_1 and C_2				
Use the thyristor, which is naturally commutated switch			R _{SVSC} is added to provide the current path during switch transitions				
Not suitable for high compensation levels because of the risk of SSR			Many components, two capacitors and four switches				
The characteristics of SSR are similar to those of a fixed capacitor							
The degree of compensation varies in a step-like way							

The aforementioned comparison clearly shows that the TCSC and FCSC can be considered the most significant FACTS devices used so far, and they have been employed effectively and successfully in power transmission systems. Furthermore, the availability of many detailed investigations of these devices in terms of performance analysis and modelling, in addition to the actual deployment of both types of device, increases the likelihood of them being proposed for employment in stand-alone systems.

It is obvious from the above comparison that selecting the most suitable series compensator circuit which can cope effectively with a wide range of voltage and frequency variation

requires the exclusion of the TCSC circuit from employment in any system where the frequency is expected to vary over a wide range, which is the case with the system proposed in this thesis. The reason for this is the increased risk of dangerous intrinsic parallel resonance occurring between L and C in the TCSC, which requires the frequency range in the operating region to be limited, as mentioned in Table 2-1. Furthermore, this table shows that, in general, the advantages of the FCSC outnumber those of the TCSC.

The SVSC may also be considered a promising circuit which can deal effectively with various frequencies. However, the large numbers of switches and capacitors, which would be even more numerous in the three-phase topology, makes it an inappropriate choice for such systems. This is due to the higher switching losses which would be involved and the greater complexity of the control method required which would increase the cost of the converter.

Although many studies have investigated the behaviour of CSC circuits in power systems with a fixed frequency and voltage amplitude, only a limited number have demonstrated the use of the CSC with generator-set systems [29, 43, 76]. An example of the application of a CSC to a generator-set is described in the next section.

2.5 FCSC-Rectifier in Wave Energy Buoys

In stand-alone wave energy conversion buoys, the frequency is very low due to the nature of the long wavelength of water waves which vary over a small range between 1-3 Hz. Generally in such systems, the generator is connected to a diode bridge rectifier to achieve AC to DC conversion.

A single-phase FCSC circuit for wave energy conversion buoys has been introduced to improve the overall power factor of the system [42]. In this work, a single-phase FCSC circuit is connected to the single-phase linear generator to improve the power factor. The FCSC output is then fed to an uncontrolled single-phase diode bridge rectifier, as shown in Figure 2.11. Two IGBT switches were used in this configuration. As explained earlier, each switch is ON for half of the supply voltage cycle. In the control scheme used in this work, the switch is ON when the voltage crosses zero and is kept ON until the delay angle γ is reached which is measured from the current waveform peak, as illustrated in Figure 2.12. Therefore, each switch is ON for $\pi/2 + \gamma$ and OFF for the rest of the half cycle of the generator voltage. This means that each IGBT switch will always be ON for $\pi/2$ before any control action and,

therefore, each of these switches has already lost half of its active region. As a consequence, the ability of the controller is limited to a small change in the operating conditions.

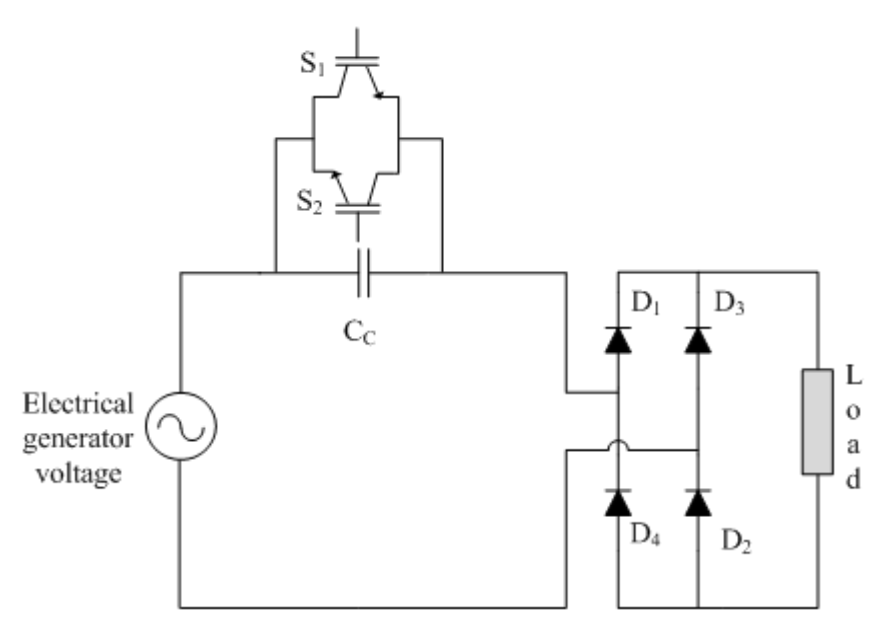


Figure 2.11 Single-phase FCSC circuit

Although the three-phase generator is commonly used in such systems, the investigations in previous research were carried out only for a single-phase FCSC topology and without any consideration of load variation [30, 92]. The control method used for the single-phase FCSC-rectifier in wave energy buoys with a small range of frequency variations 1-3 Hz is illustrated in Figure 2.12.

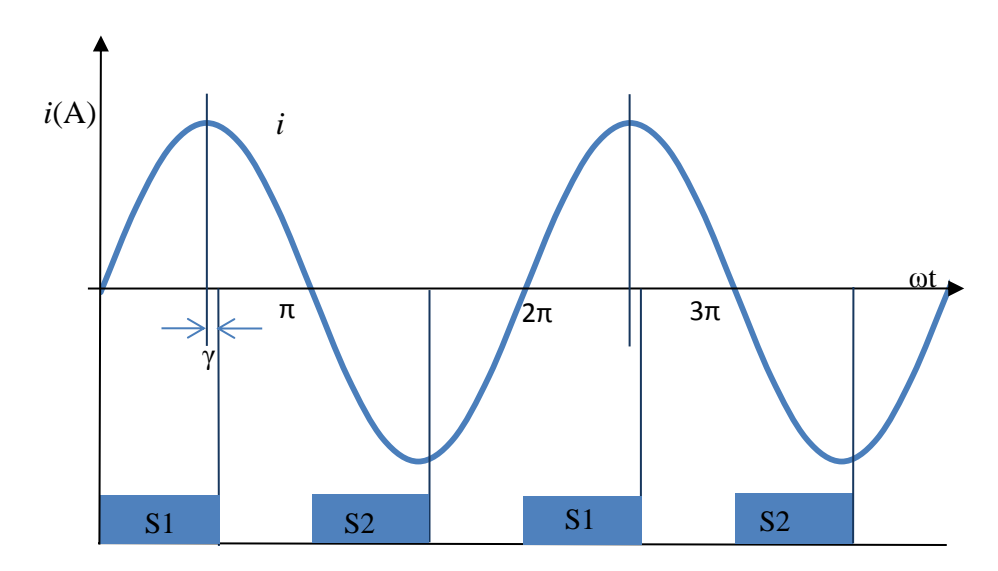


Figure 2.12 Switching pattern of the single-phase FCSC in wave energy buoys

Therefore, it is important to investigate the three-phase topology of the FCSC circuit to examine its operating performance and behaviour during wide range of voltage and frequency variations in a three-phase system. The limitations of considering a small range of frequency variation should be overcome and, thus, it is crucially important to find a new control method to be able to control the circuit in single and three-phase FCSC circuits to cope with the wide operating frequency values.

2.6 Summary

The above sections have investigated the available CSC circuit topologies for different applications. Generally, CSCs are mainly used in power transmission systems where the amplitude of voltage and frequency are fixed. CSCs used in power transmission are considered FACTS devices. In such systems, the CSC is able to increase the transferred power, improve system stability and enhance power quality. This chapter has provided an overview of the family tree of VRCSCs. A theoretical comparison between different circuit configurations is presented to provide a better understanding of the strengths and weaknesses of each type of configuration. This helps in selecting the most suitable compensator circuit topology able to cope effectively with variable-voltage variable-frequency systems. Based on the above investigation and comparison, it is concluded that the FCSC circuit is the most suitable circuit topology for implementation in such systems.

Generally, in many stand-alone variable-voltage, variable-frequency systems such as wave energy converters, the high inductance of the generator-set leads to deterioration in the overall system power factor. It is one important target of this research to develop a power electronic converter able to improve the power factor over wide frequency and voltage variations. This requires an investigation into whether combining the FCSC circuit with a simple uncontrolled diode bridge rectifier, and developing a new control technique for the FCSC converter that allows wide frequency variations, is able to correct the operating power factor with low harmonic levels. A high power factor ensures a better utilization of electric generator output, which will enhance the power transferred to the load.

The next two chapters describe the implementation and performance behaviour of both singlephase FCSC converter and three-phase FCSC converter by simulations.

Chapter 3. Single-Phase FCSC Converter

In Chapter 2, it was concluded that the FCSC circuit represents the most promising CSC circuit topology to be employed in stand-alone systems operating at variable-voltage and variable-frequency with wide ranges of frequency variations, to achieve a high power factor and high output power. This chapter investigates the behaviour of the single-phase FCSC-rectifier. Firstly, the system is described analytically, including various modes of operation, as presented in Section 3.1.5. Secondly, a numerical simulation for the converter is carried out (in Section 3.3) using SABER as a circuit simulator for modelling and simulation. A SABER model for the single-phase topology is developed to provide a better understanding of how the converter behaves in a stand-alone system. The operation of the single-phase FCSC under different load conditions is also investigated and simulation results are presented in this chapter. Furthermore, system performance in terms of the power factor and total harmonic distortion (THD) is also described in the final section.

The major concerns of this thesis mainly lie in proposing and developing a new control strategy to be employed for the three-phase FCSC-rectifier which is able to cope effectively with wide variations of supply voltages and frequencies. Circuit performance when employed in a three-phase stand-alone system is described in Chapter 4. Therefore, in this chapter, the single-phase topology is investigated merely to develop a basic understanding of both the performance of the FCSC converter and the novel control strategy presented in Chapter 5. Moreover, the single-phase FCSC circuit has been investigated previously, as mentioned in Chapter 2, for a very small range of frequency variations. However, previous work has not considered the impact of load variations on the behaviour of the single-phase FCSC-rectifier and therefore it will be covered in this chapter.

3.1 Analytical Description

In a stand-alone system, a single-phase FCSC converter is positioned between a single-phase variable-voltage variable-frequency electrical generator and a single-phase diode bridge rectifier feeding a DC load, as shown in Figure 3.1.

3.1.1 FCSC-rectifier topology

As explained in Chapter 2, the FCSC circuit employs a series compensation capacitor, C_c , connected in parallel with two anti-parallel forced commutated IGBT switches, S_1 and S_2 . Each switch will be ON for half a cycle of the voltage supply waveform, depending on the voltage polarity of the electrical generator through two driving circuits.

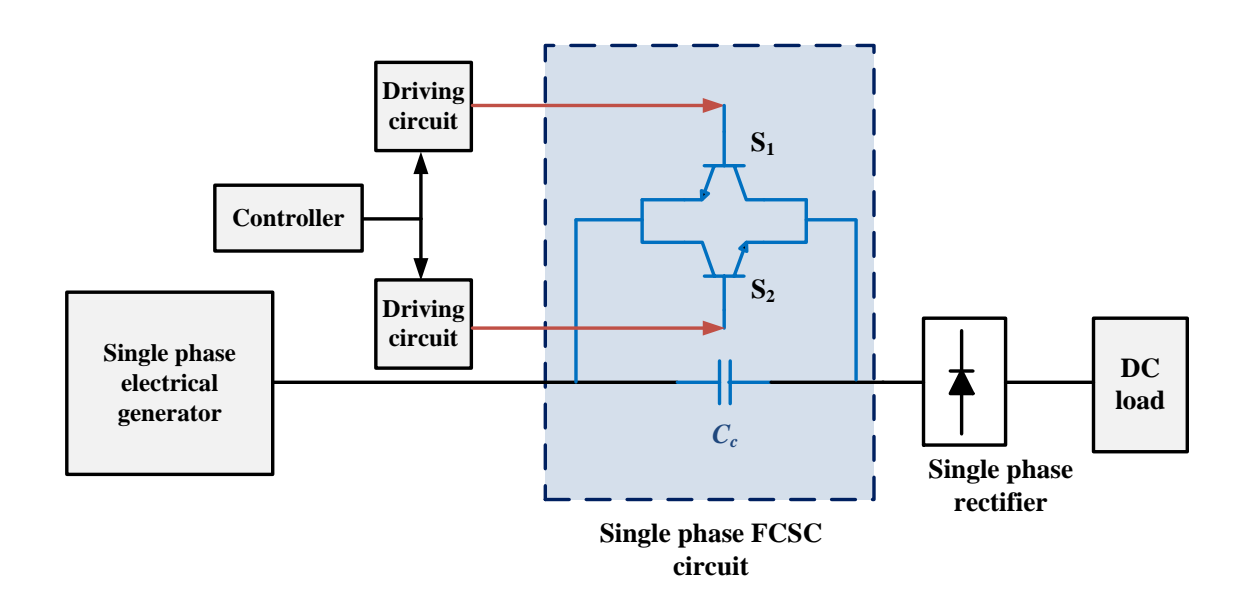


Figure 3.1 Single-phase FCSC converter configuration in stand-alone system

These driving circuits are controlled to vary the ON and OFF times of switches S_1 and S_2 . During each half cycle of the generator output voltage, S_1 and S_2 are controlled to vary the effective capacitive reactance by controlling the turn-off angle γ of the two switches, as expressed in equation (2-8). This means that the FCSC represents a controllable reactance compensator which can be used to compensate for the reactive power in electrical power systems.

3.1.2 Electrical generator

The electrical generator is represented by its back EMF, V_s , the internal machine resistance, R_s , and the internal machine inductance, L_s . In this chapter, a single-phase linear permanent magnet generator is utilised to supply the variable amplitude of the back EMF with a variable frequency.

3.1.3 Single-phase diode bridge rectifier

In many stand-alone systems, the electrical generator output is fed to a rectifier circuit. A single-phase diode bridge rectifier is used to rectify the AC power to DC power and keep cost and complexity at a minimum. However, the use of conventional diode rectifiers has a deleterious effect on the source power quality, since it pollutes the AC power supply with harmonics. Therefore, it is important to employ a high-quality rectifier which ensures a high power factor, high efficiency and low harmonic generation [111, 112].

This thesis investigates the performance of the FCSC-rectifier to determine if it can qualify as a high quality rectifier. The load consists of a parallel RC circuit, with R_L and C_L representing the load resistance and load capacitance respectively. The load is fed from a single-phase full-wave diode bridge rectifier (D_I to D_4). In the conventional diode bridge rectifier, C_L is used as a DC filter to reduce the ripple in the output voltage. This ripple will be very small when the time constant (R_L C_L) is sufficiently larger than the line voltage period. At a very large value of C_L , the circuit operates in the discontinuous current mode (DCM). This is because, when the instantaneous rectifier input voltage is higher than the capacitor voltage, the current passes through the conducting diode and charging C_L to the peak of the input voltage. However, when the instantaneous input voltage falls to a value lower than V_L , the diodes are reverse-biased, no current passes through them, and the capacitor discharges through the load resistance [113, 114], as shown Figure 3.2. This figure shows the input voltage and the voltage across the capacitor when the diode rectifier is connected to a sinusoidal voltage source and feeding R_LC_L load with a very high C_L (neglecting any inductance in the circuit), and the current in the circuit is in discontinuous mode.

In this thesis, the DC load is modelled as a resistance which is defined by Ohm's law ($R_L = V_L/I_L$). The actual DC load may include not only the resistive load, but also non-linear loads, switching converters and regulators which, at certain operating points, can be defined by the ratio between the average voltages to the average currents which represent R_L .

3.1.4 Principles of operation

In stand-alone variable-voltage variable-frequency systems, the role of the FCSC is to compensate the inductive reactance of the electrical generator by matching its capacitive reactance to cancel out the effect of machine inductance, which otherwise causes a reduction in output voltage and a poor power factor (PF).

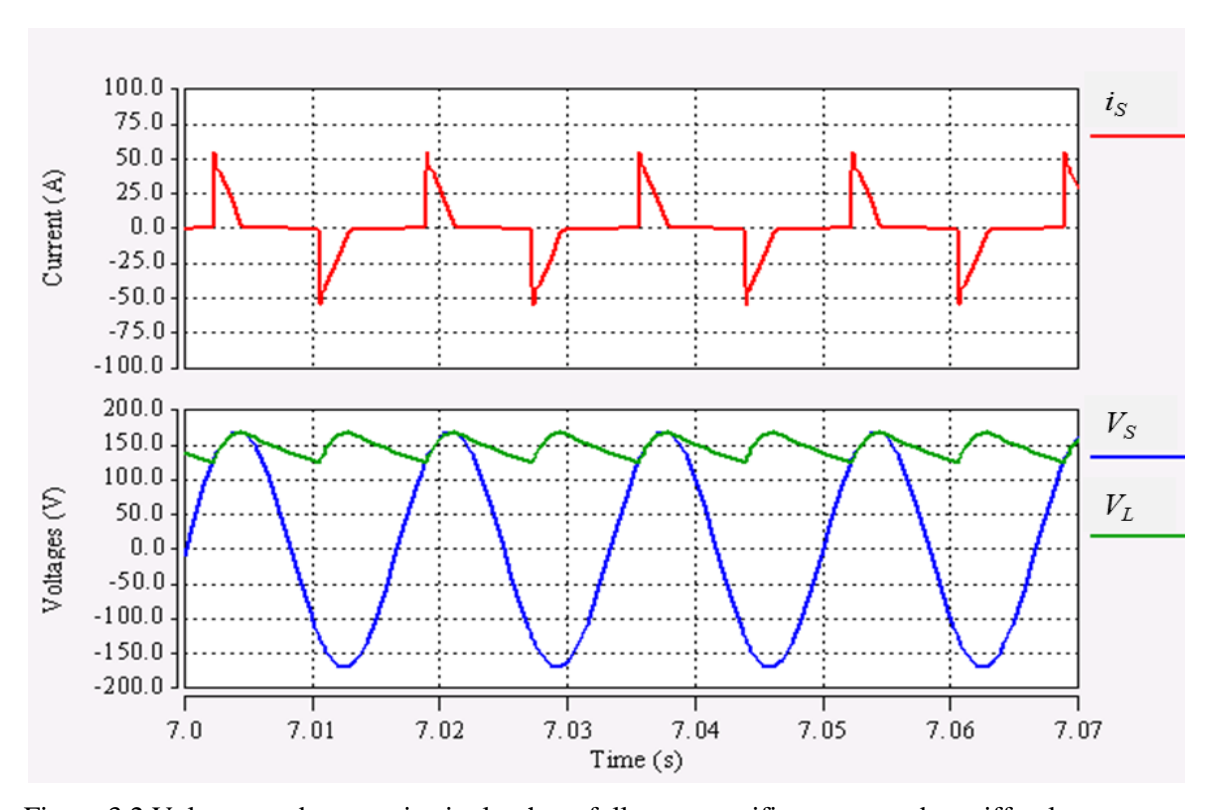


Figure 3.2 Voltages and current in single-phase full-wave rectifier connected to stiff voltage source and feeding RC load

In essence, as explained previously, the FCSC capacitor voltage and hence capacitive reactance can be varied by controlling the turn-off angle (γ) of the two switches. This angle corresponds to the peak input current value and the zero crossing point of the capacitor voltage. By controlling (γ), the capacitive reactance of the FCSC can be controlled. Theoretically, when $X_c = X_L$, the voltage waveform is in phase with current waveform, this means that the system is operating at unity power factor. Therefore, if the controller is capable of adjusting the system reactance, in this case the FCSC-rectifier will operate with a power factor of unity because there will be no phase difference between the current and voltage waveforms.

3.1.5 Modes of operation of single-phase FCSC converter

As the FCSC circuit employs two IGBT switches, the circuit configuration changes periodically according to the switch states. Assuming the utilized circuit is a pure inductor and

capacitor and only two rectifier diodes will conduct in each half cycle, which means that the commutation period is zero.

As explained earlier, each IGBT switch is ON for a half voltage waveform cycle. S_1 represents the only active switch which controls the voltage and current during the positive half cycle of the generator's back EMF, while S_2 will be the active switch during the negative half cycle. Figure 3.3 illustrates the conventional IGBT's switching pattern in terms of turn-off angle for a power transmission system. This means that during each half cycle of the generator back EMF, one switch will be permanently OFF. There are two subintervals during the half cycle of the voltage waveform regarding to the switching state. This leads to four modes of operation per generator frequency cycle. Each two modes are identical due to the identical switches ON and OFF state per half cycle. Therefore, two different circuit configurations describe the system during one switching cycle of CCM. S_1 and S_2 are driven by two driving circuits which are controlled to vary values of γ , as illustrated in Figure 3.1.

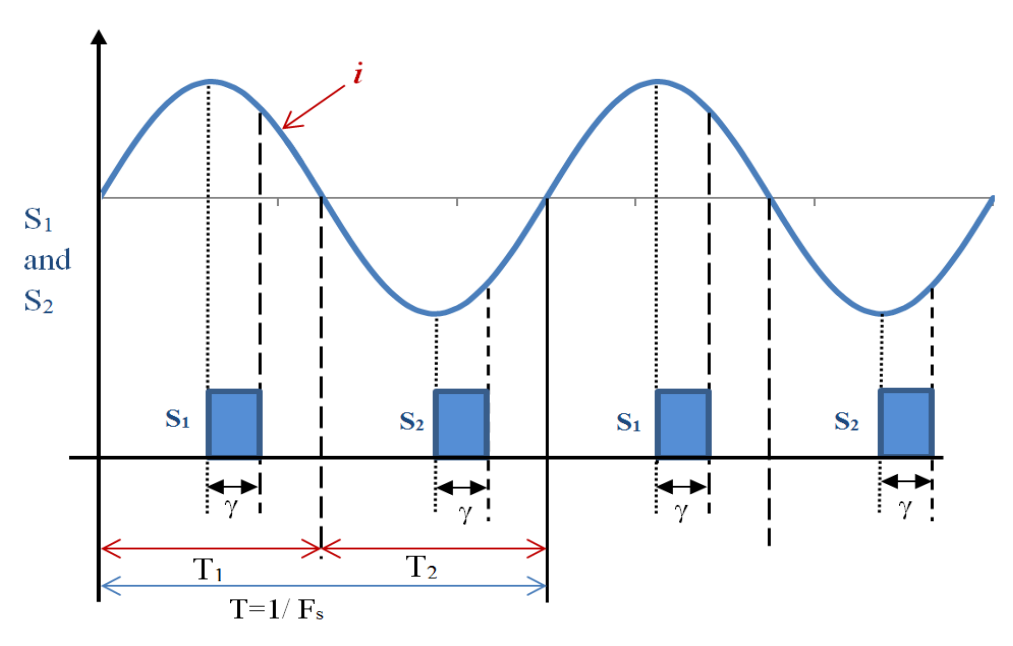


Figure 3.3 Conventional turn-off angle control for FCSC converter

Figure 3.3 shows the conventional control method when the GTO switches are turned off at a value of γ . In this figure,

$$T = \frac{1}{F_S} \tag{3-1}$$

where F_s is generator frequency; and

$$T_{ON} = D T (3-2)$$

$$T_1 = T_2 = \frac{1}{2} T \tag{3-3}$$

1) Mode 1: S_1 OFF, S_2 OFF, D_I and D_2 conducting at $t=T_{OFF}$

During the positive half-cycle of the generator back EMF, T_1 , S_1 is opened permanently until the controller provides the required pulse to turn S_1 ON for a certain time through a driving circuit, and returning to OFF for the rest of the period T, and S_2 is permanently OFF in this interval. A representative diagram for the current path flow when S_1 is OFF during the positive half cycle is shown in Figure 3.4. The current path is highlighted by the red line.

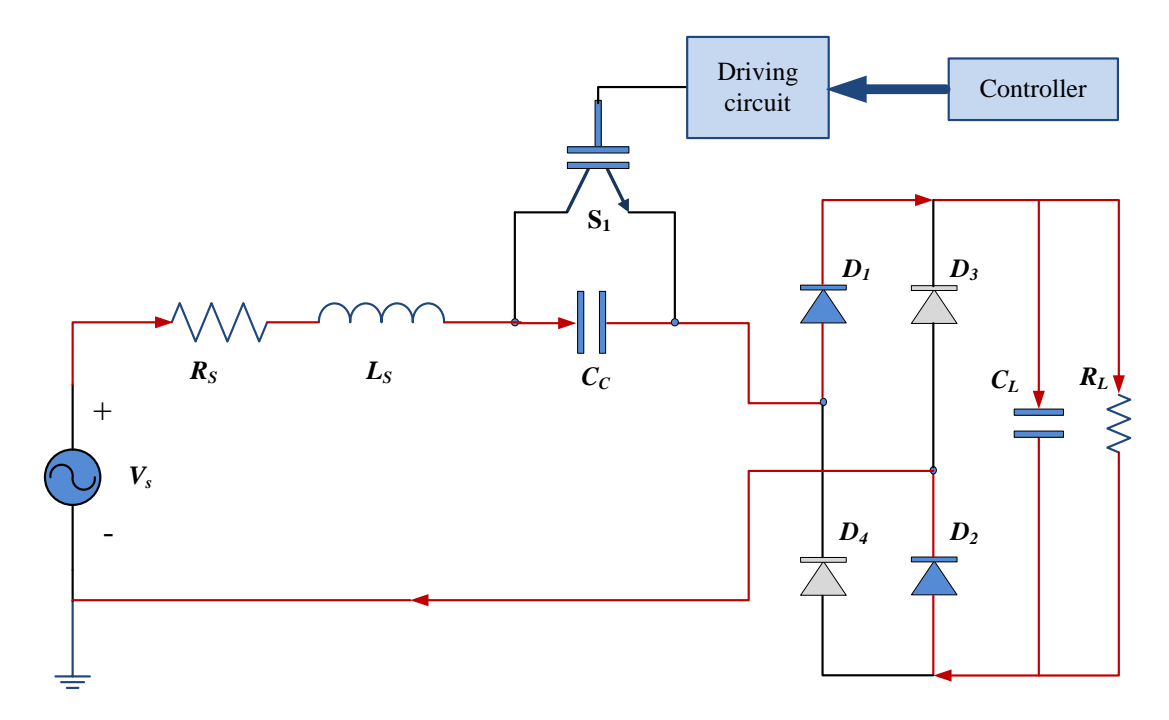


Figure 3.4 Schematic circuit diagram when S₁ is OFF

For this interval when both switches are in their OFF state during time $t = T_{OFF}$, the equivalent circuit configuration is given in Figure 3.5. As the switch S_I across the capacitor C_C is opened, the capacitor is able to fully compensate the inductor voltage with a certain voltage value. This voltage is a function of the switch OFF time. The two conducting diodes in the rectifier circuit are simply regarded as short-circuit and named DT in the equivalent circuit diagram. The generator voltage polarity changes during each half cycle in addition to the active switch which alternates with its polarity. Therefore, the generator back EMF is represented by $|V_S(t)|$ to indicate the generator voltage regardless of its polarity.

In this mode, two capacitors are present in the circuit with two different functions. The output capacitor (C_L) works as a smoothing capacitor, while the series capacitor acts as a

compensator by resonating with the generator's inductor. The equations which can describe the system in this mode are based on Kirchhoff's voltage and current laws as follows:

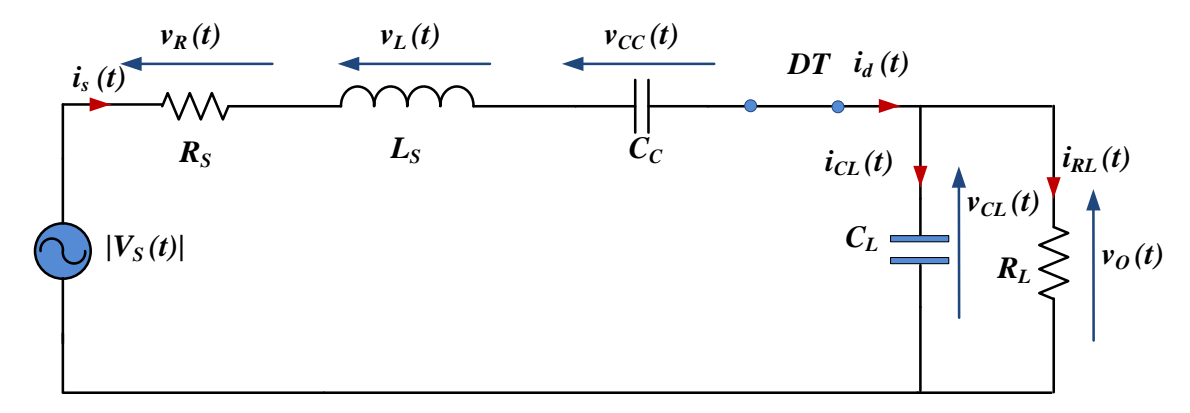


Figure 3.5 Effective FCSC equivalent circuit: mode1/mode 3

$$|V_S(t)| = v_R(t) + v_L(t) + v_{CC}(t) + v_{CL}(t)$$
(3-4)

Rewriting equation (3-4) gives

$$|V_S(t)| = i_S(t)R_S + L_S \frac{di_S(t)}{dt} + v_{CC}(t) + v_{CL}(t)$$
(3-5)

From Figure 3.4 we can write:

$$i_s(t) = i_d(t) \tag{3-6}$$

$$v_o(t) = v_{CL}(t) (3-7)$$

$$i_d(t) = i_{CL}(t) + i_{RL}(t)$$
 (3-8)

Referring to equation (3-6), this yields:

$$i_S(t) = C_L \frac{dv_{CL}(t)}{dt} + \frac{v_{CL}(t)}{R_L}$$
 (3-9)

2) Mode 2: S_1 ON, S_2 OFF, D_1 and D_2 conducting at $t = T_{ON}$

During the second interval of the positive half-cycle of the generator back EMF, T_I , S_1 is closed at $t = T_{ON}(S_2)$ is always opened during T_I) and remains ON for a period of γ which is adjusted by the controller.

Figure 3.6 illustrates the current flow (shown in red) during the γ period of time when S_1 is in its ON state. The capacitor C_c is shorted by closing S_1 for a γ period; again the two conducting

diodes in the rectifier circuit D_1 and D_2 are simply represented by a short circuit DT, giving the equivalent circuit configuration as shown in Figure 3.7. During this subinterval of T_{ON} , the circuit is configured differently as shown in the figure.

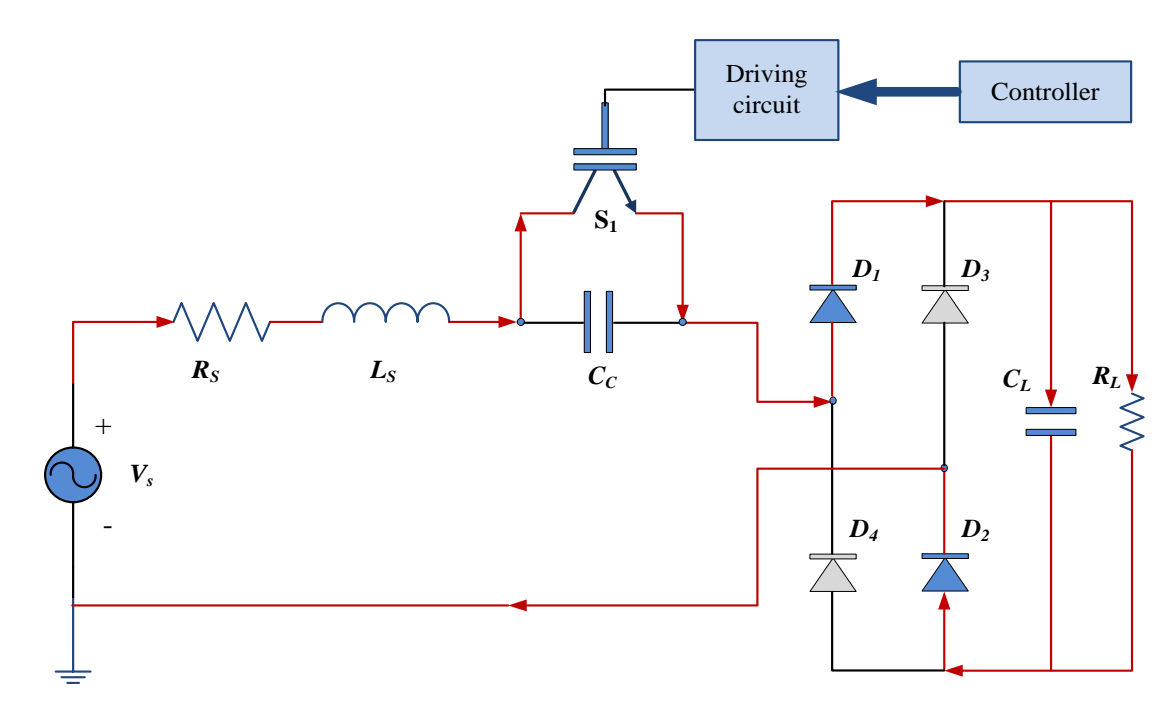


Figure 3.6 Schematic circuit diagram when S₁ is ON

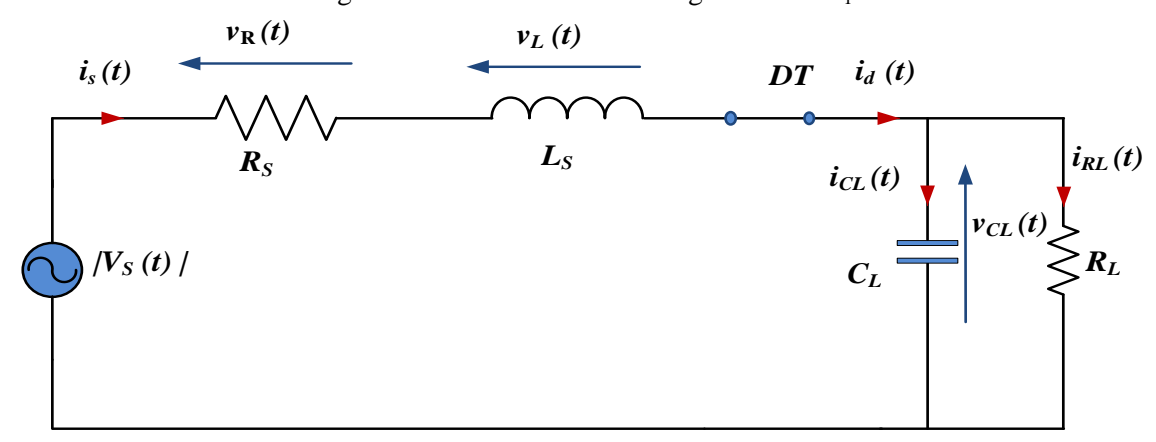


Figure 3.7 Effective FCSC equivalent circuit: mode 2/mode 4

From Figure 3.7:

$$i_s(t) = i_d(t) \tag{3-10}$$

$$|V_S(t)| = v_R(t) + v_L(t) + v_{CL}(t)$$
(3-11)

Re-writing equation (3-11) produces

$$|V_S(t)| = i_S(t)R_S + L_S \frac{di_S(t)}{dt} + v_{CL}(t)$$
(3-12)

And

$$i_d(t) = i_{CL}(t) + i_{RL}(t)$$
 (3-13)

Re-arranging (3-13) gives:

$$i_S(t) = C_L \frac{dv_{CL}(t)}{dt} + \frac{v_{CL}(t)}{R_L}$$
 (3-14)

3) Mode 3: S_2 OFF, S_1 OFF D_3 and D_4 are conducting at $t = T_{OFF}$

During the negative half cycle of the voltage waveform, S_2 is closed (S_1 opened) at $t = T_{OFF}$, giving the equivalent circuit shown in Figure 3.5. Circuit operation is again described by equations (3-4) to (3-9).

4) Mode 4: S₂ ON, S₁ OFF, D₃ and D₄ conducting

For the remainder of the negative voltage half cycle, the system equivalent circuit is as shown in Figure 3.7 and operation is described by equations (3-10) to (3-14).

The above equations show that the variation in load voltage is a function of load resistance in all modes of operation. Therefore, the effect of load variation on the FCSC-rectifier behavior is investigated in this research and verified in the next section by simulation.

3.2 Performance Consideration

I. Power factor (PF)

The operating power factor of a circuit is a measure of the effectiveness of drawing real power from the supply and transferring it to the load. In other words, it is an indicator of the effective utilization of an electric power supply. Therefore, the power factor can be defined as the ratio of real power (P) to apparent power (S) as expressed in the following equation [112]:

$$Power Factor(PF) = \frac{Real Power}{Apparent Power} = \frac{P}{S} = \frac{\frac{1}{T} \int_{0}^{T} v(t) i(t) dt}{VI}$$
(3-15)

In a linear sinusoidal single phase system, real power (P), apparent power (S) and the reactive power (Q) can be computed using the following equations:

$$P = V I \cos \emptyset \tag{3-16}$$

$$S = V I \tag{3-17}$$

$$Q = \sqrt{S^2 - P^2} \tag{3-18}$$

where V and I represent the RMS values of voltage and current.

The angle ϕ is the phase angle between the sinusoidal current and voltage waveforms. Unity power factor load reduces the losses caused by the current drawn from the electrical power source, as the current is inversely proportional to the power factor, shown in equation (3-15). For non-sinusoidal waveforms, a Fourier series may be used to express the voltage and currents as:

$$v(t) = V_0 + \sum_{n=1}^{\infty} V_n \cos(n\omega t - \varphi_{vn})$$
(3-19)

$$i(t) = I_0 + \sum_{n=1}^{\infty} I_n \cos(n\omega t - \varphi_{in})$$
(3-20)

where φ_{vn} , φ_{in} represent the phase delay of voltage and current waveforms respectively.

By substituting equations (3-19) and (3-20) in equation (3-15), the power factor can be calculated. However, since the voltage source is purely sinusoidal in the simulation analysis, equation (3-15) can be re-written to calculate the power factor with non-sinusoidal current as follows:

$$PF = \frac{P}{S} = \frac{V_1 I_1 \cos(\varphi_{v1} - \varphi_{i1})}{V I} = \frac{I_1}{I} \cos \varphi$$
 (3-21)

where I_I is the RMS value of the fundamental current component. The angle φ_{iI} is the phase angle between I_I and the voltage. The power factor can be re-formulated as:

$$PF = DF \times DPF \tag{3-22}$$

$$DF = \frac{I_1}{I} \tag{3-23}$$

$$DPF = \cos \omega \tag{3-24}$$

where *DF* and *DPF* are the distortion and displacement power factor, respectively. The *DF* is defined as the ratio of the RMS fundamental current to the RMS current. Equation (3-21) shows that large distortion in the current waveform yields a small distortion factor and, hence, a low power factor even with a high DPF. The *DPF* represents the phase shift between the

fundamental current (I_I) and supply voltage, as shown in Figure 3.8. This is unity when the fundamental current is in phase with the voltage waveform [115, 116].

II. Efficiency

The efficiency of an electrical system can be defined as a ratio of the output power (P_{out}) to the input power (P_{in}) as follows:

$$\% \, \eta = \frac{P_{out}}{P_{in}} \times 100\% \tag{3-25}$$

It is an indicator of the amount of power dissipation in any power system. Low efficiency means a large amount of heat resulting from dissipated power [113].

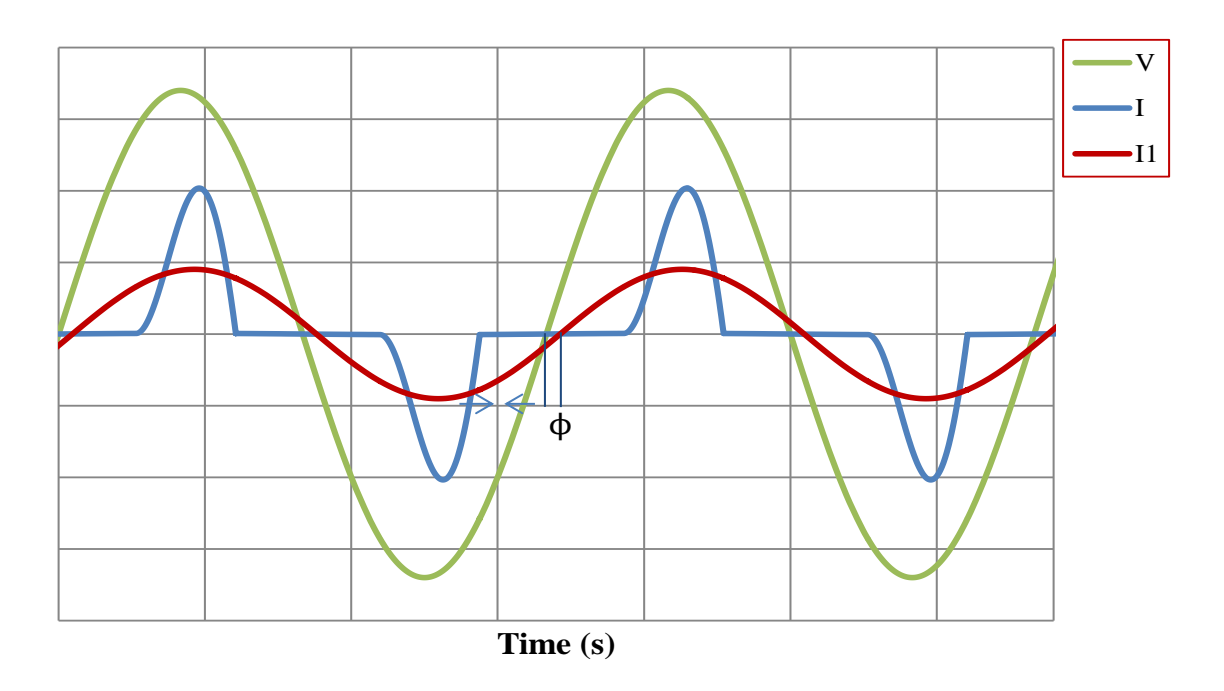


Figure 3.8 Supply voltage, supply current and first harmonic current relationship

Therefore, the total power loss (P_{loss}) can be defined as:

$$P_{loss} = P_{in} - P_{out} (3-26)$$

The switch total losses (P_{st}) are a part of the total system losses, and P_{st} can be divided into switching losses (P_{sw}) , conduction losses (P_{cond}) and fixed losses (P_{fix}) as expressed by the following equations:

$$P_{st} = P_{sw} + P_{cond} + P_{fix} ag{3-27}$$

The switching losses are comprised of turn-ON losses ($P_{turn-ON}$) and turn-OFF losses (P_{turn_OFF}), which are both a function of switching frequency. They can be expressed as:

$$P_{sw} = P_{turn-ON} + P_{turn-OFF} (3-28)$$

$$P_{turn-ON} = \frac{1}{2} V_{CE} I_C f_S(t_{c(ON)})$$
 (3-29)

where V_{CE} is the voltage appearing across the switch before the transition to the ON state or after transition to the OFF state. I_C represents the current flowing through the IGBT switch during its ON state and $t_{C(ON)}$ is the switch transition interval to ON state.

$$P_{turn-OFF} = \frac{1}{2} V_{CE} I_C f_S(t_{c(OFF)})$$
(3-30)

 $t_{c(OFF)}$ represents the switch transition time to be in OFF state. Substituting equations (3-29) and (3-30) in equation (3-28) leads to:

$$P_{sw} = \frac{1}{2} V_{CE} I_C f_S (t_{c(ON)} + t_{c(OFF)})$$
 (3-31)

However, the conduction loss can be expressed as:

$$P_{cond} = V_{ON}I_C \frac{T_{ON}}{T} \tag{3-32}$$

where V_{ON} is the voltage across the switch during the (ON state) and the ratio of T_{ON}/T is the duty ratio D. According to this equation, the conduction loss is a function of duty cycle. On the other hand, P_{fix} is classified as a constant loss because it is not affected by load and switching frequency variations. P_{fix} includes the switch control circuit power requirement, which is typically small. Therefore, it is neglected here [112, 114].

III. Total harmonic distortion (THD)

Essentially, harmonic analysis is a technique that can be useful to analyse voltage and current waveforms arising in the presence of non-linear loads [117].

THD is an index of the distortion of the waveforms which can be used to describe the deviation of non-sinusoidal waveforms from a sinusoidal form. Therefore, THD is the ratio between the RMS values of the harmonics to the RMS value of the fundamental component [111, 112]:

$$\% THD_i = \frac{\sqrt{I^2 - I_1^2}}{I_1} \times 100 \tag{3-33}$$

The aforementioned information shows that both power factor and THD are functions of distortion in the waveform, which helps in formulating the relationship between them as:

$$PF = \frac{DPF}{\sqrt{1 + \left(\frac{\% THD}{100}\right)^2}}\tag{3-34}$$

It is always required to keep the waveform distortion at a minimal level. A high current distortion has deleterious effects in electrical power systems, including utility power loss.

3.3 Numerical Analysis and Simulation Results

In this section, the numerical analysis is carried out using a simulation package. In this thesis, the SABER from Synopsys is employed as a simulation platform to perform the numerical analysis and model the system. SABER version I-2013-12 is used in this work. SABER is a powerful platform which is able to simulate physical systems. For a power electronic converter, SABER is an effective platform which is able to model different semiconductor switches in ideal and non-ideal cases. This helps the designer to predict the performance of the power converter, including the switching losses. In addition, it has a huge number of datasheets for actual devices from different manufacturers which are modelled in a MAST language to achieve a proper estimation by the designer of system performance. Furthermore, the user can characterize different semiconductor switches such as IGBT, MOSFET and DIODE through its modelling tool to provide accurate predictions of switch behaviour in terms of switching speeds, losses and thermal impedance if needed. Therefore, it was decided to use SABER as a platform for simulation to model, simulate and analyse the single-phase FCSC-rectifier in this chapter and the three-phase FCSC-rectifier in the next chapter.

In the following subsections, a general overview is presented to highlight major performance measurements which can characterise system behaviour, followed by relevant circuit simulations.

3.3.1 Single-phase FCSC- rectifier in wave energy converter

The single phase operation is investigated for low frequency applications only, such as wave energy conversion.

With wave energy converters (WECs), it is required to capture and convert mechanical power into electrical power as efficiently as possible. Therefore, the mechanisms of power take-off (PTO) represent a main focus of much research into wave energy because it plays an

important role in cost, including infrastructure costs and energy efficiency in terms of output power.

The PTO mechanisms can be categorized into four different types as follows [118-120]: oscillating water column (OWC); hydraulic-pump converters, including Pelamis [121]; overtopping devices such as the wave dragon [122]; and direct drive converters. Different electrical generator topologies exist in these categories which are classified mainly as fixedspeed and variable-speed electrical generators. The generator selection and design have been investigated by many researchers to improve system efficiency in addition to reduce cost and size, which are considered as major concerns in marine technology. The direct drive converter has been proposed as a promising PTO technique in terms of efficiency and reliability, since the mechanical parts are removed. Polinder el al. [123] compared different generator topologies, such as the conventional three phase PM generator, switched reluctance generator and induction generator. Electric generators from the variable reluctance permanent-magnet VRPM family, such as the transverse-flux permanent-magnet generators (TFPM) have been proposed as a promising generator topology suitable for employment in such applications due to their high efficiency, small size and lower cost [123-125]. However, these generators have the significant major drawback of poor power factor due to the high inherent inductance of the generator, which has a deleterious effect on power factor. The power factor has been calculated to be as low as 0.31 [123-125]. Therefore, the need to provide the required reactive power is crucially important to improve the power factor. Due to frequency variations, Muller [124] described the necessity of using a variable capacitance during one wave cycle to maintain high output power and achieve optimum performance. As the frequency and induced voltage vary in wave energy applications, the use of fixed capacitor assisted excitation for voltage regulation proposed by Chen in [126] will not be effective.

In general, in direct drive wave energy conversion schemes, the output of the electrical generator is a variable-frequency, variable-amplitude voltage waveform, as the generator is directly coupled with the reciprocating motion of the waves. Due to the nature of the long wavelength of water waves, linear electric generator topologies generate low electric frequencies between 1-3 Hz [92].

Moreover, the electrical generation system in a wave energy converter consists generally of an electrical generator and a power converter. Different rectifier topologies form the interfaces between electric generator and the load in such a system. Common rectifier circuits include the diode bridge rectifier, PWM rectifier and DC-DC boost rectifier. A comparison of these topologies has been published [29, 127] for series hybrid vehicle (SHEV) applications with a constant frequency of 300 Hz. The authors therein addressed the weaknesses and strengths of each topology in terms of power flow, power factor and output voltage control. They highlighted that the PWM rectifier has the best performance, at the expense of high cost and complex control circuitry. On the other hand, the diode bridge rectifier represents the simplest topology with the downside of it having no control on power flow and power factor. In addition, a small change in the DC output ripple voltage results in large variations in the AC current waveforms [112].

The single phase FCSC-rectifier is used to interface the linear generator in wave energy buoys, to overcome the degradation of the power factor in such systems; this will be demonstrated in the following sections. Beside the ability of stand-alone wave energy buoys to generate energy, they are used as a navigation-warning device in addition to having the ability to monitor any seismic activity. The electric generator is employed in order to power up the buoy's electronic parts. Several electronic devices are included in the buoy, such as a central processing unit (CPU), lights, and transmitters to send a warning signal when sea conditions change during activity such as a tsunami.

3.4 SABER Model of the Single-Phase FCSC-Rectifier

The simulation is carried out using the SABER platform. In this simulation, parameters of the linear generator, shown in Table 3-1, have been taken from a previous study [42]. This linear generator was introduced and tested originally by Ran *et al.* [128] for direct drive wave energy conversion as a three phase generator. A 2.8 kW single-phase linear PM generator feeds a single phase FCSC-rectifier which provides the load with DC power. This generator has 16 air-cored coils per phase which are configured to have only eight active coils at any moment, while the other eight coils are inactive. The maximum induced voltage in each coil is 60 V, which provides a maximum back EMF voltage of 480 V per-phase with a maximum current of 75 A. The coil inductance and resistance are 24 mH and 0.4Ω , respectively, which gives a total inductance of 384 mH per phase and a resistance of 6.4Ω per phase.

Figure 3.9 illustrates the model developed for the system, where the linear generator is represented by its back EMF (V_s), and the generator internal resistance and inductance are R_s and L_s , respectively.

 Back EMF (Vs)
 Inductance (L_S)
 Resistance (R_S)

 480 V
 384 mH
 6.4 Ω

Table 3-1 Single phase linear PM generator parameter

The same representation will be used later on a per-phase basis for a three-phase generator. The FCSC circuit is modelled as series capacitor C_c , with two anti-parallel IGBT switches available in the SABER library of components. A fast speed IGBT from International Rectifier (irgpc20f) is employed, which is represented as S_1 and S_2 in the figure. The IGBTs were characterized on physical devices by performing laboratory measurements within the software library. This helps to develop a proper understanding of the circuit behaviour with non-ideal IGBT switches.

Power diodes D_5 and D_6 are used in series with S_1 and S_2 , respectively. D_5 is forward-biased during the positive half cycle of back EMF, which ensures that the current is passing through S_1 only when S_1 is in its ON state, D_6 is reverse biased. The DC load is modelled as a resistor R_L in parallel with the smoothing capacitor C_L as explained in section (3.1.3). During the negative polarity of the back EMF, D_6 conducts, which ensures that the current flows through S_2 when it is in the ON state. Both switches are driven by a classic driving circuit to provide the required pulses for turning the switches ON and OFF for certain intervals.

In order to provide S_1 and S_2 with the required pulses for ON and OFF intervals, two driving circuits are modelled. Each consists of a gate resistor, R_g , connected in series with a programmable square wave generator, V_g . The numbers 1 and 2 in indices refer to the driving circuits for S_1 and S_2 , respectively. A simple single phase full-diode bridge rectifier is connected to the FCSC output to perform AC to DC conversion. Diodes D_1 and D_2 are conducting during the back EMF's positive half cycle, while D_3 and D_4 conduct during the negative half cycle as usual. The smoothing capacitor C_L (sometimes called the reservoir capacitor) is connected in parallel with the load resistor R_L to store energy when the rectifier voltage is around its maximum value, and it supplies the load for the rest of the time. A high capacitance is important to reduce the ripple component in the output voltage [7, 129]. All of the simulation circuit parameters are listed in Table 3-2. Same diodes and IGBTs are used to simulate the three-phase FCSC circuit in the next chapters.

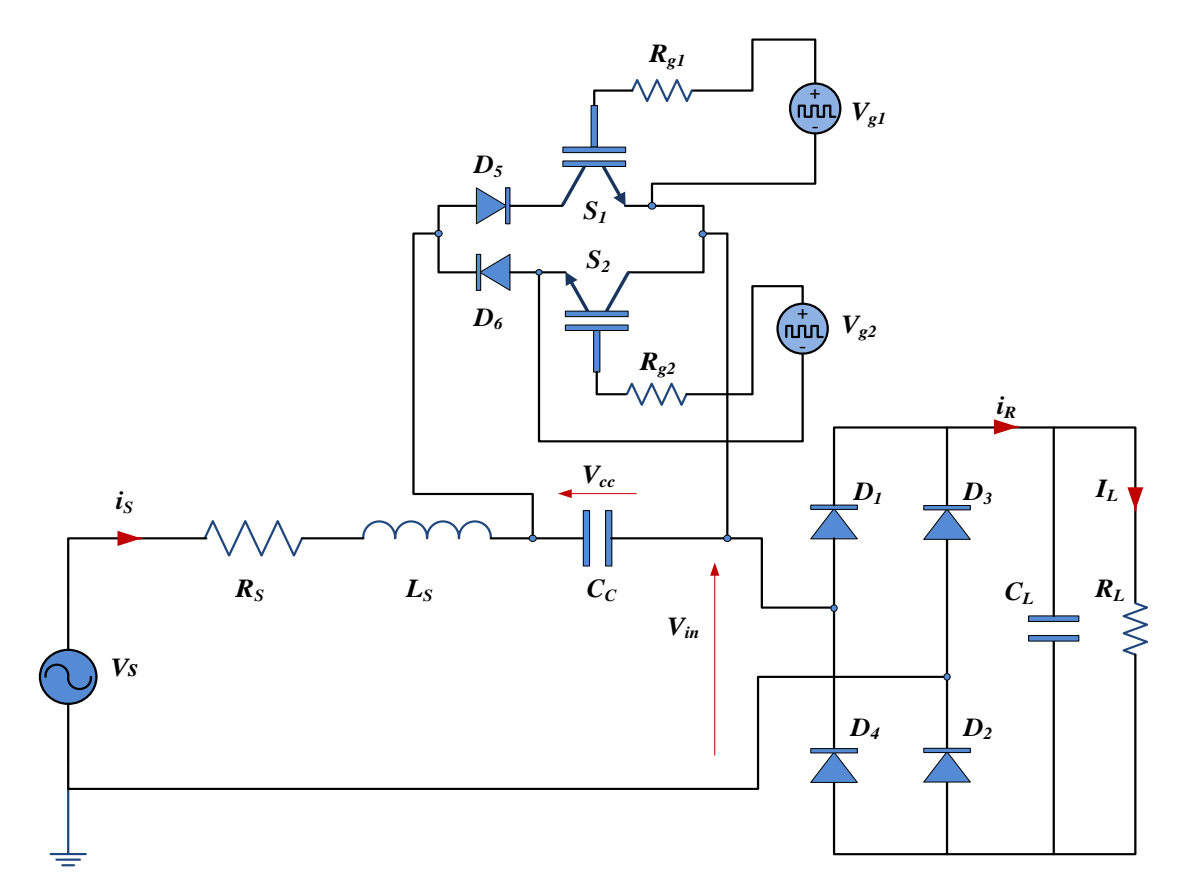


Figure 3.9 SABER model of a single phase FCSC converter

All simulation results assume that the controller is continuously adjusting the FCSC reactance to match the machine inductive reactance $X_{cc} = X_{LS}$, implying that γ =0 at a frequency of 3 Hz. The simulation results clearly show that, by using the FCSC, the power factor is high at 0.986 as the current waveform is approximately sinusoidal and almost in phase with the machine voltage waveform, as shown in Figure 3.10.

The output voltage is 243 V with an RMS ripple value of 1.356 V. It is always recommended that the time constant of C_LR_L should be much larger than the duration of the line frequency cycle, to reduce output voltage variations (i.e. to reduce the ripple) [7, 114].

It should be mentioned that, to fully compensate the generator inductance, a single-phase FCSC circuit needs to use a high capacitance value of 7 mF. This means that, in the single phase topology, both the compensation capacitor and smoothing capacitor are large.

The power factor is calculated in two ways in this simulation; firstly, in terms of real and apparent power as expressed in equation (3-21); and by using SABER measurement tools to measure P and S, the power factor is high with a value of 0.986.

Table 3-2 Simulation circuit parameters for single-phase topology

	Circuit parameter	Value	
	V _S max	576 V	
	F_s	3 HZ	
	R_S	6.4 Ω	
	$L_{\mathcal{S}}$	384 mH	
	Cc	7 mF	
	$R_{gI}=R_{g2}$	50 Ω	
	$V_{gI} = V_{g2}$	15 V	
	C_L	300 mF	
	R_L	10 Ω	
	V_{on}	0.7 Ω	
Diode	g _{on} = 1/R _{on}	10 kmho	
	$g_{ m off}$ = 1/ $R_{ m off}$	0.001 mho	
	V _{CES}	600 V	
	V _{CE (sat)}	≤ 2.8 V	
BT	I_{c}	9 A	
0f -IC	Pd _{max} _Ja	60 W	
Irgpc20f -IGBT	Ia _{max}	64 A	
II	Vgk _{max}	20 V	
	rth_ja	40 Ω	
	Rth_jc	2.1 Ω	

Secondly, the power factor is calculated for the distortion and displacement factor. As the current is not purely sinusoidal, as shown in Figure 3.10, it is important therefore to calculate the distortion in the input current waveform. Using Fast Fourier Transform FFT analysis will

help in identifying the contamination of the input current waveform by harmonics. The results show that the total power factor is high as both DF and DPF are high (DF=0.991, DPF= 0.995, PF = 0.985) as given by equations (3-23), (3-24) and (3-22), respectively. Both methods result in approximately the same values of power factor.

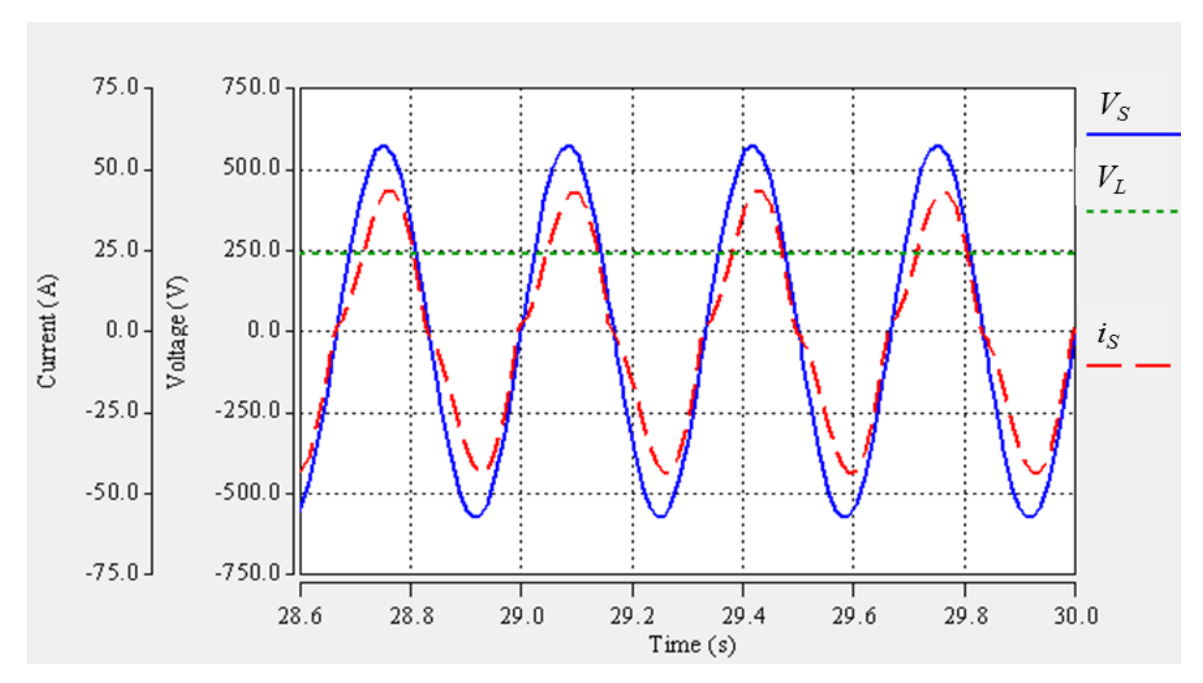


Figure 3.10 Single phase FCSC converter waveforms, input voltage (V_s), input current (i_s) and load voltage (V_L) when $\gamma = 0$ at $F_s = 3$ Hz.

In order to calculate the current harmonic contaminations in the system, FFT (Fast Fourier transform) analysis is carried out by using SABER. The harmonic content of the current waveform is shown in Figure 3.11. This figure demonstrates the peak value of each harmonic. It is clear that the dominant harmonic is the third order harmonic. The percentage current at this frequency is 13.048% with the harmonic order until the 11th harmonic order included in the THD calculation.

The efficiency is calculated as the ratio of the DC output power to the AC input power to the FCSC-rectifier (η =93%) using equation (3-25). In this case, the conduction loss and switching loss are zero as γ =0.

3.5 Operations at Various Load Conditions

This subsection investigates the behaviour of a single-phase FCSC-rectifier at different load conditions to assess converter performance during load variations [130]. The investigation is divided into two parts.

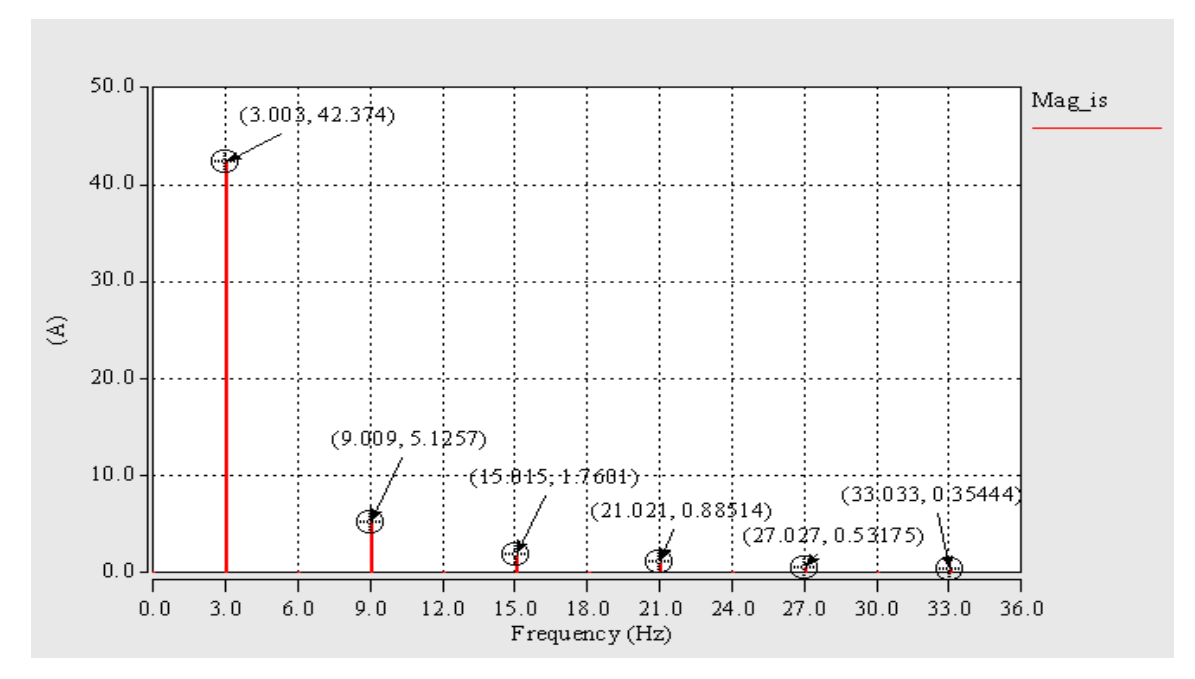


Figure 3.11 Frequency spectrum of peak input current harmonics

The load resistance R_L is varied in part A, while the load capacitance C_L is kept constant at a value of 300mF. Conversely, in part B, only the load capacitor is changed with a fixed value of R_L at 10 Ω . It is assumed that the controller is continuously tuned in such a way as to keep the phase angle between the voltage waveform and the fundamental component of the current waveform at zero. The simulation results have been taken with an initial voltage of 209V on the reservoir capacitor.

The results show that the variations in load resistance have an impact on the performance of the FCSC which verifies the equations which describe the system during each modes of operation. However, a minimal effect on FCSC-rectifier behaviour occurs during variations in C_L . The distortion factor in the FCSC-rectifier will be affected by load variations as a result of the dependency of the input current on the load, as stated earlier in (3-9) and (3-14).

A. Variation of load resistance (R_L)

The circuit is simulated with increasing ratios of R_L/R_S from 0.1 to 50, by varying R_L only and maintaining R_s at 6.4 Ω . Figure 3.12 shows that the power factor drops slightly as the load resistance is increased.

The distortion in the input current waveform and the phase shift between the back EMF and the fundamental component of the machine current are lower at higher values of R_L , decreasing the overall value of the power factor. The DPF is maintained at a high level at

different values of load resistance, which leads to improvements in the power factor value even when the distortion in the input current is high. This shows that both factors affect the total power factor.

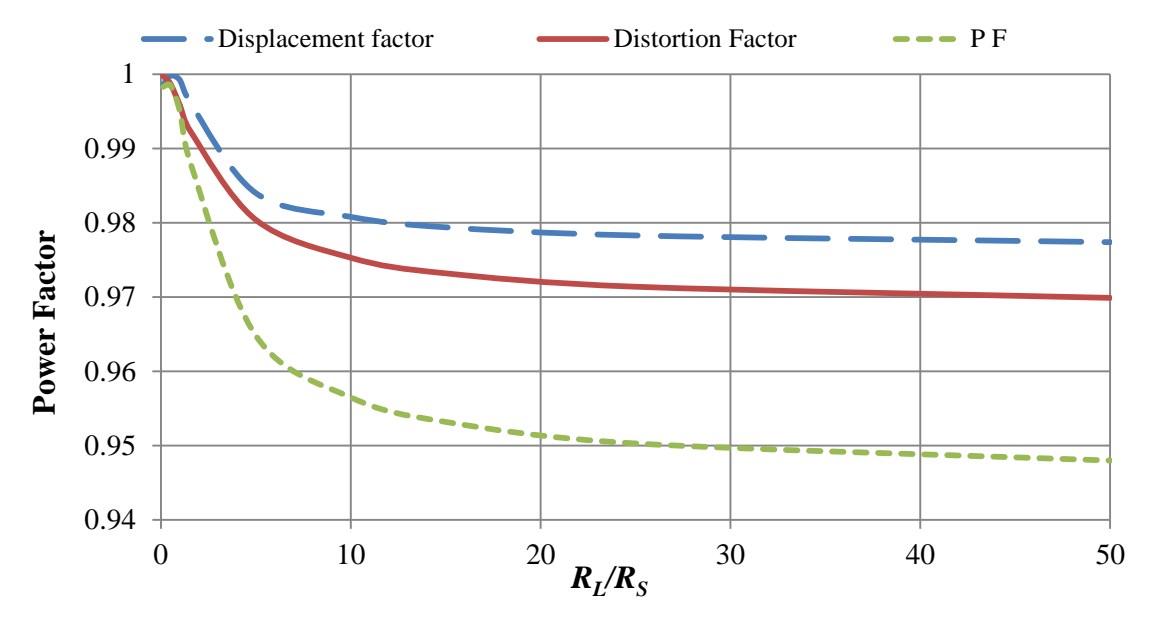


Figure 3.12 Displacement, distortion and power factor as a function of R_L/R_S

When the converter load is changed to be a light load, the percentage current total harmonic distortion THD_i is affected. As shown in Figure 3.13, the THD_i is higher at higher values of load resistor. However, at heavy loads, there is a dramatic reduction in THD_i .

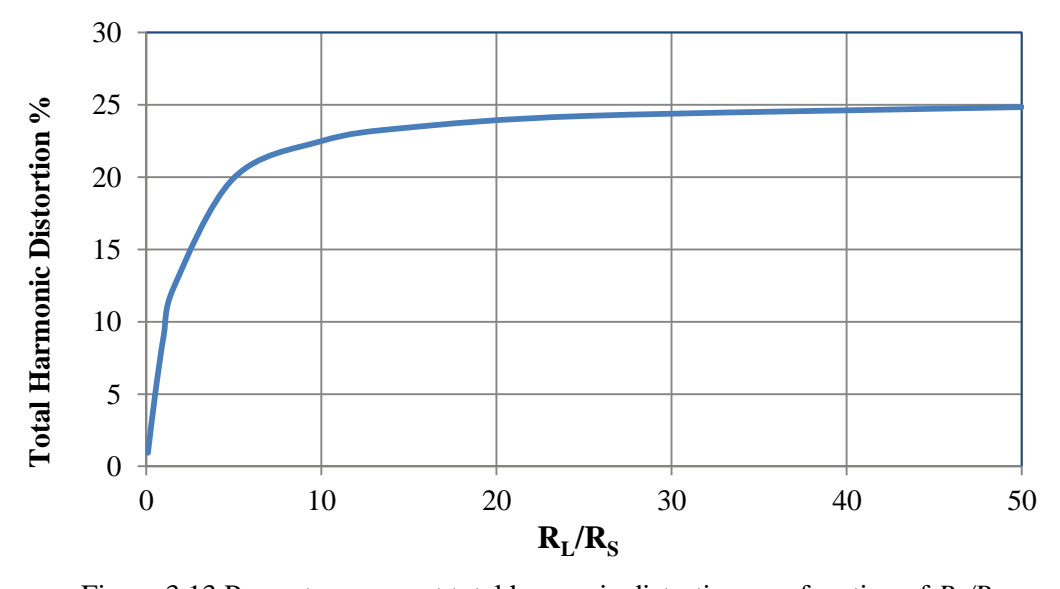


Figure 3.13 Percentage current total harmonic distortion as a function of R_L/R_S

B. Variation of load capacitance

By following the same procedure and increasing the ratio between load capacitor C_L and C_C by keeping C_C at 7 mF and increasing C_L from 70 μ F to 700 mF, the simulation results demonstrate that C_L has a slight effect on FCSC-rectifier performance. Figure 3.14 illustrates the total power factor, the distortion factor and the displacement factor as a function of C_L/C_C .

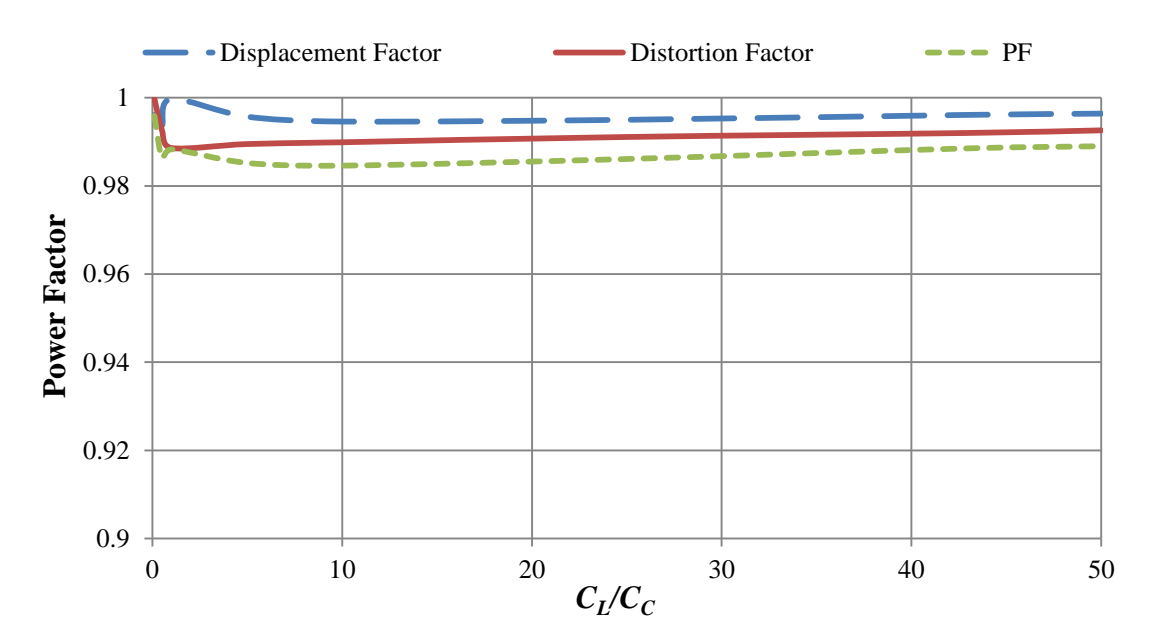


Figure 3.14 Distortion, displacement and power factor as a function of C_L/C_C

The high displacement factor is a result of the controller adjusting the back EMF in phase with the machine current. The distortion factor is also high for all C_L values. Although the value of C_L varies, the power factor is almost constant at about 0.99 with a slight drop at low capacitance values. This drop can be ignored in practice as the output voltage is highly unstable in this region.

Figure 3.15 describes the variation in the current total harmonic distortion when C_L is varied. As the value of C_L increases, the ripple content in the system waveforms is reduced, improving THD.

The results clearly show that although the controller is able to maximize the value of DPF, the power factor is still affected by the value of DF. The results also demonstrate that the power factor of the FCSC converter is reduced with increasing load resistance but is hardly affected at all by changes in load capacitance. This is because the input current is affected by variation in load resistance and less so when changing C_L . Overall, it can be concluded that changes in

the power factor are relatively small when the load is varied within a certain practical range of values.

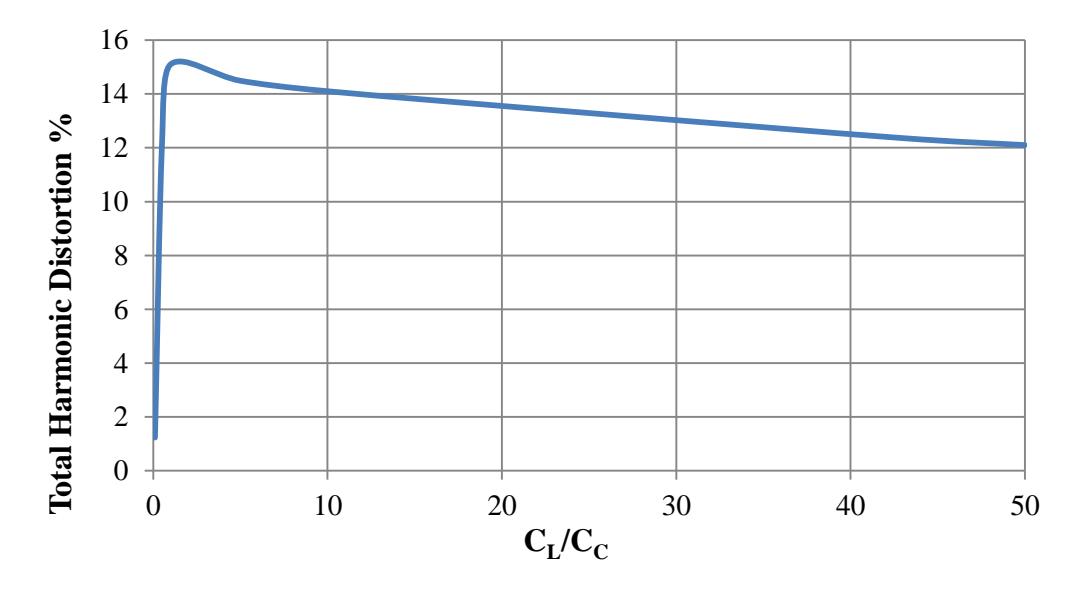


Figure 3.15 Current total harmonic distortion as a function of C_L/C_C

3.6 Summary

This chapter describes the use of a single-phase FCSC-rectifier in a wave energy converter. As water buoys operate at low frequencies in addition to the high generator inductance value, the effects of commutation overlap in the rectifier circuit is significant, reducing the operating power factor of the system. Several generator topologies and designs have been presented in the literature. However, this cannot prevent the degradation of the power factor in such applications. Therefore, the need to employ a power electronic converter which is able to provide better generator utilization is important.

The modes of operations of the FCSC converter are also described and its performance is analysed numerically using SABER. Simulation results show that the FCSC is effective in improving the power factor in such systems to a high value of up to 0.99.

The impact of variation in load on power factor is also investigated. The simulation results show that the increase in load resistance will reduce the operating power factor of the circuit, driven by a drop in the distortion factor. This effect appears despite the capability of the controller to stipulate a zero phase shift between the machine voltage and machine current. It is also shown by simulation that changes in load capacitor value have a minimal impact on the total power factor.

From the results presented in this chapter, it can be concluded that the turn-off angle (γ) corresponding to the maximum total power factor of the FCSC circuit is not only a function of generator inductance (i.e. the phase angle between machine voltage and fundamental current as a result of rectifier commutation overlap), but is also influenced by the loading of the circuit, including the resistance of the load. Nonetheless, the variation in power factor is very limited with a maximum change of around 2%.

As mentioned earlier, the main focus of this research is the three-phase of FCSC converter; thus no further investigations will be performed for the single-phase circuit topology. However, the novel proposed control technique presented in Chapter 5 is initially tested on the single-phase FCSC circuit to achieve a basic understanding before implementing it in the three-phase FCSC circuit configuration.

In the next chapter, the same procedural approach as that used for the single-phase FCSC-rectifier will be followed for the three-phase FCSC-rectifier circuit. However, based on the simulation results in Chapter 3, only load resistor variations will be investigated in the next chapter.

Chapter 4. Three-Phase FCSC Converter

This chapter describes the performance and behaviour of the three-phase FCSC circuit in stand-alone variable-voltage variable-frequency systems, which are typically three-phase systems. Based on the principles and simulation results for a single-phase FCSC circuit which were presented in Chapter 3, this converter is able to maintain a high input power factor and high output power in its single-phase topology. Similarly, the operation of the three-phase FCSC circuit is investigated in this chapter to assess its performance.

The suitability of the three-phase FCSC circuit for employment in a variable-voltage variable-frequency stand-alone system is investigated in this thesis. One such application is an aerospace system where the operating frequency is varied between 350-800 Hz (named the wild frequency [11, 131]). This chapter investigates the three-phase FCSC converter in a stand-alone system with an operating frequency of 500 Hz, which is considered to be within the more electric-aircraft (MEA) frequency range. All simulation results in this chapter assume that the resonant frequency is 500 Hz, which is equal to the maximum frequency. This means that in this investigation the maximum frequency of the aircraft application is reduced to 500 Hz in order to be compatible with practical constraints, as discussed later in Chapter 6. The frequency variation range is investigated in the next chapter.

As explained in earlier chapters, the three-phase FCSC-rectifier has only been simulated previously in comparison with certain PFC converters and some CSC circuits when operating at a fixed frequency of 300 Hz [29]. However, this previous work did not investigate the operation of the three-phase FCSC converter at the various operating conditions of a VVVF system. Therefore, this chapter analyses the converter topology by introducing the circuit principle of operation in order to understand the circuit behaviour in such system at a resonance frequency, followed by numerical investigations of the system with and without employing the FCSC circuit in order to evaluate the impact of using three-phase FCSC converter in such a system. The investigation is also including a discussion for the circuit behaviour based on the duality concept, which has not been discussed before for either single-phase or three-phase FCSC circuit. Furthermore, as this converter is proposed for employment in an aerospace application, an overview of existing PFC converters employed in aerospace

applications is also presented, and the problem of zero crossing distortion in different converters is highlighted.

The system is modelled and simulated in order to observe the performance of the three-phase FCSC converter at a medium frequency of 500 Hz. In addition, the simulated model will be used in the design and implementation of the three-phase FCSC-rectifier. The other advantage of the simulation is that its results are used as a base in order to compare it with the practical implementation results in Chapter 6. The simulation results show that the three-phase FCSC-rectifier is capable of improving the power factor in addition to being able to comply with the current distortion requirements in such application.

The impact of load variations on the performance of three-phase FCSC is also investigated in this chapter. However, as a result of the findings in Chapter 3, where it was demonstrated that the load capacitor has a minimal impact on the behaviour of a single-phase FCSC converter in a stand-alone VVVF systems, the investigation is limited to variation in the load resistance only.

In this thesis, as the three-phase system (a, b and c) is assumed to be a balanced system, most of the results will be presented for one phase such as phase a, because the other phases are assumed to be identical.

4.1 Power Electronics Converter Topologies for Aircraft Applications

AC to DC conversion plays an important role in MEA power systems, and is important as it provides DC power for different DC loads and electrical drives. Power quality, size, weight, cost and reliability are trade-offs for different aerospace applications. In airborne applications, on-board equipment should be strictly compatible with the manufacturer's guidelines and regulatory limits such as DO-160 (environmental conditions and test procedures for airborne equipment). DO-160 is a guideline for the standard procedures and criteria of environmental tests for airborne hardware, including electrical and electronic avionics and mechanical systems, published by the Radio Technical Commission for Aeronautics (RTCA). This document also defines the input harmonics distortion limits caused by various loads, due to the recognition of the negative impact of harmonics on aircraft power systems caused mainly by the intensive use of uncontrolled rectifiers in airborne systems. Therefore, one of the most important requirements for an on-board converter is the maximum allowance of the input current harmonic distortion [10, 12]. In general, different power electronics converter

topologies are proposed to interface the aircraft power grid, including the permanent magnet alternator (PMA), with different electrical loads. Therefore, the employment of a power factor correction (PFC) converter is very important. However, the selection of a suitable converter is very challenging, because most conventional PFCs pollute the input current with harmonics. The active PFC technique is able to improve the power factor and reduce the harmonics; however, it causes distortion in the input current at the zero crossing point of the input voltage, which becomes higher at medium frequencies of 360-800 Hz [26, 132]. For example, the boost PFC AC-DC topology suffers from zero crossing distortion (also called crossover distortion), which is low at a frequency of 50 or 60 Hz, but much higher at a frequency of 400 Hz or higher. The latter is the frequency range of commercial aircraft, especially when the aircraft adopts a variable frequency range such as wild frequencies [133]. Sun [23, 24] summarized the limits for the even, triplen and non-triplen harmonics set by the RTCA DO-160G for a single phase system, and showed clearly that this topology had a high distortion level when employed in a system at a frequency of 400 Hz. Furthermore, this distortion increased proportionally with frequency at aircraft frequencies, which means that the topology exceeds the allowable harmonic level set by RTCA DO-160G and thereby it cannot be employed in airborne applications. The high current distortion levels of the boost PFC topology are mainly caused by cusp distortion and the discontinuous conduction mode (DCM) of the boost inductor. Cusp distortion arises as soon as input voltage crossover occurs with a limited voltage across the inductor. This distortion is a function of boost inductor size [25]; however, reducing the inductor size affects the DCM interval. The input current distortion due to DCM occurs before the zero crossing point and is mainly related to the phase displacement between the current and the input voltage. The low frequency input current distortion can be avoided by increasing the ratio between the switching frequency and line frequency, at the expense of the power level. However, a good current loop design can reduce the DCM distortion. Therefore, different approaches have been proposed by many researchers to overcome this problem in the single-phase topology in the higher frequency range of 350-800 Hz. Sun [23] proposed a phase delay technique for a single-phase topology to reduce or cancel the distortion from the existing phase lead according to DCM distortion, while Xiaohui and Xinbo [133] proposed a single-phase boost multi-level (ML) converter to reduce this problem at the wild aircraft frequency. Comparisons between different existing converter topologies have also been performed by several researchers. In 2011, Zhang et al. [25] presented a comparison of different single-phase PFC topologies, including the traditional

single-phase PFC, the diode-assisted single-phase PFC, three level single-phase PFC, and bridgeless single-phase PWM rectifier. They concluded that the PWM rectifier with a bi-directional current is able to eliminate zero-crossing distortion, with the downside of high switching losses, a large boost inductor and a complex control loop, which meant increasing the cost of the system. ML-PFC and diode-assisted PFCs are able to reduce the zero-crossing distortion to the different levels at the expense of complex control circuity. Furthermore, a switched capacitor scheme using two directional switches to minimize the zero-crossing distortion has also been presented [25]. Brombach *et al.* [10] analysed and tested three conventional PFC topologies, including a PFC with boost converter, a PFC with a flyback converter and a PFC with passive filters. They concluded that none of them fulfilled the requirements of aircraft power quality. On the other hand, an evaluation of the three-phase PFC converter topologies according to efficiency, volume and weight has also been published [16].

The aforementioned information clearly shows that the need to employ high performance PFC converters is crucial in aircraft applications.

4.2 Description of the Three-Phase FCSC Converter

In three-phase stand-alone VVVF systems, the three-phase FCSC circuit is located between the AC variable-voltage and variable-frequency electrical generator and the three-phase six-pulse diode bridge rectifier which feeds the DC power to a DC load, as shown in Figure 4.1.

4.2.1 Three-phase FCSC-rectifier topology

Similar to the single-phase FCSC-rectifier, the three-phase FCSC-rectifier also employs a series capacitor C_C shunted by two anti-parallel IGBTs in each phase. In order to feed the DC load, a three-phase six-pulse diode bridge rectifier is used. The DC load is modelled as a resistor for simplicity in this research and shunted by a filtering capacitor as explained earlier in Chapter 3. Any unregulated DC load which obeys Ohm's law could be used as a load, such as heating equipment and certain types of DC-DC converter. For clarity, the DC load is modelled as an equivalent resistor in this thesis.

In order to maximize the utilization of the PM generator, the power factor should be approximately unity. Therefore, the FCSC circuit is used to cancel out the effect of generator

inductance by the effect of the FCSC series capacitor C_C . The effective capacitive reactance is a function of the ON time of IGBT switches.

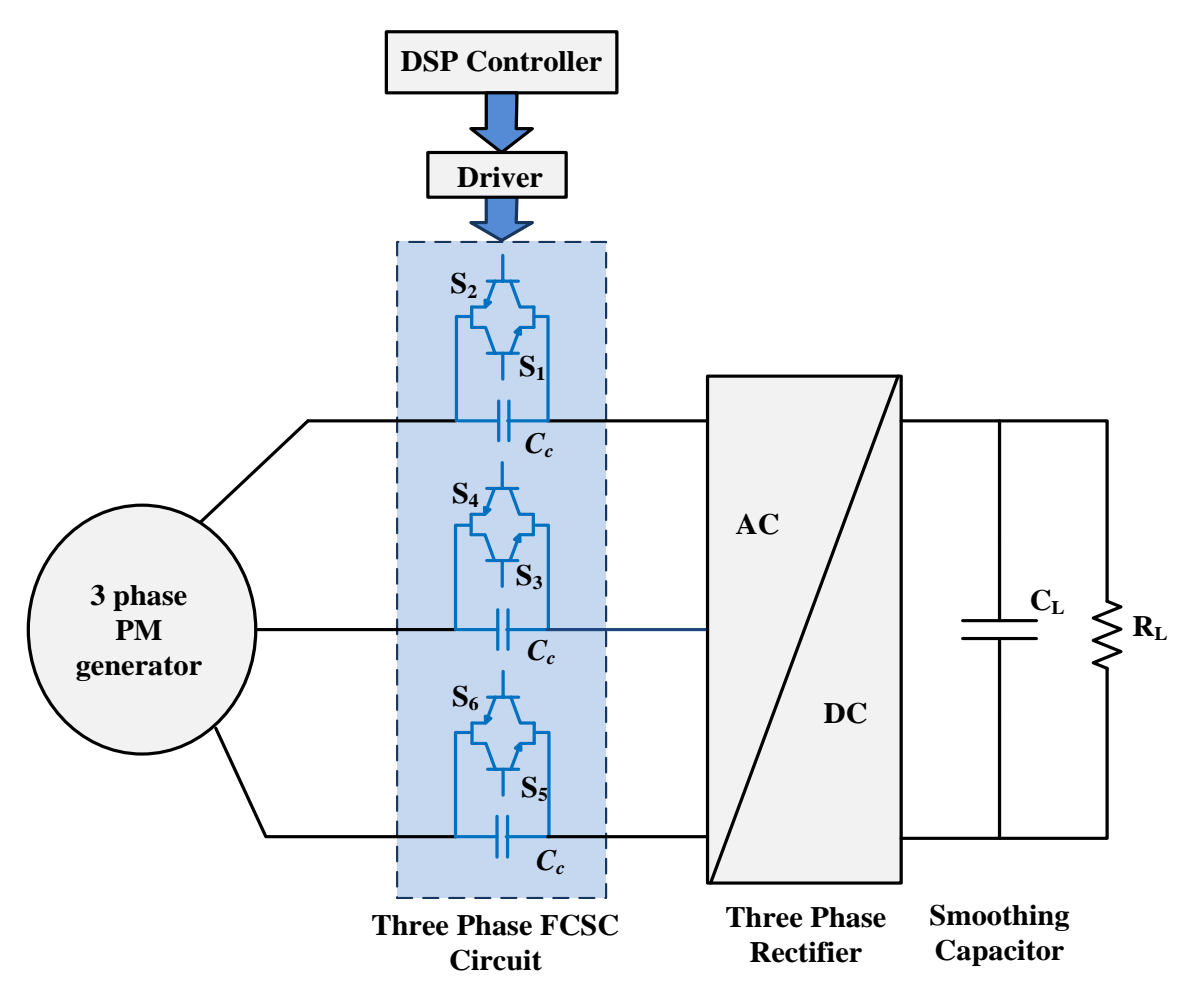


Figure 4.1 Three-phase FCSC-rectifier in stand-alone variable-voltage variable-frequency

The IGBT switches are controlled using a DSP digital controller. The pulse is generated to turn the switch ON and OFF for certain periods during each half-cycle of the generator's back EMF. Each IGBT switch will be ON for an interval of γ and OFF for the rest of the half-cycle of the generator voltage waveforms. There is a phase shift of 120° between each IGBT pair of phase, which is compatible with the phase shift between the phase voltage waveforms. In other words, the switches S_1 , S_3 and S_5 are phase shifted by 120°, and similarly S_2 , S_4 and S_6 are also shifted by 120°. However, the anti-parallel switches in each phase have a phase difference of 180° between them. This means, that there is a 180° phase shift between each pair such as S_1 - S_2 , S_3 - S_4 and S_5 - S_6 , while the phase shifts between S_1 - S_3 , S_3 - S_5 , S_2 - S_4 , and S_4 - S_6 are 120°.

It is worth mentioning that, in commercial aircraft, the load can be classified as AC and DC loads supplied by either constant-frequency (CF) or variable-frequency (VF), according to recent developments in aircraft power systems, which reduces the costs [12]. The AC loads, include the galley, electric motors and turbo-fans, whereas various DC loads are distributed in the aircraft which can be categorized as constant power, constant voltage, and constant current loads. These include the avionic systems, heating, and various controllers and actuation systems [20].

4.2.2 Three-phase electrical generator

In general, a three-phase permanent magnet (PM) synchronous generator is used in VVVF systems, such as in aerospace applications. In this thesis, an aero engine generator presently under development at Newcastle University is used for simulation and practical implementation. As the inductance of this generator is considerably high, it has a poor power factor [134, 135]. In this research, the PM generator is represented as a series connection of a sinusoidal voltage source and stator inductance and resistance, on a per-phase basis.

4.2.3 Three- phase six-pulse diode bridge rectifier

The three-phase six-pulse diode bridge rectifier is used in the system to perform AC to DC conversion. In general, the modes of operation of the three-phase rectifier supplied by three-phase balanced AC source are conceptually illustrated in Figure 4.2. In this figure, for the sake of simplicity, commutation overlap is neglected. In one AC supply cycle, commutation occurs every 60° [136]. At each commutation interval, the current passes through a different diode. This means that for every 60° the circuit configuration changes according to the line-line voltage.

The operation of the uncontrolled three-phase rectifier differs according to the type of DC load connected to the rectifier output [112]. For various applications, three common types of load are generally fed by the rectifier: including pure resistive load (R), series inductive load (RL), and parallel RC load. It is important to mention that, in this work, the load is parallel RC; however, RL load is described to provide an understanding of the duality principle of the circuit as described later.

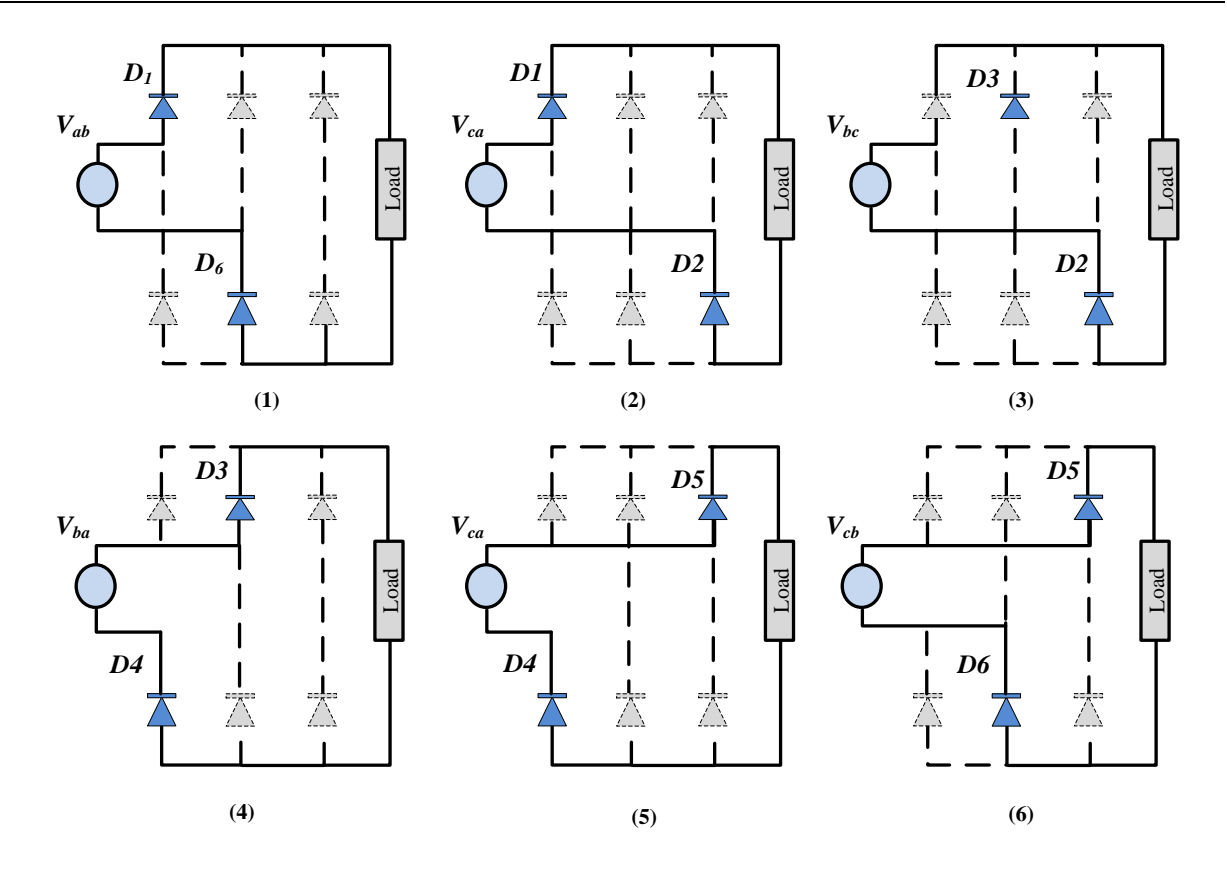


Figure 4.2 Commutation sequences in the three-phase six-pulse diode rectifier

I. Resistive load

The ideal operation of the three-phase six-pulse rectifier supplied by a three-phase balanced AC source and feeding a pure resistive load is presented in Appendix B. This shows that when the load is a resistive load, the output voltage and current of the rectifier are comprised of six pulses during one AC frequency cycle, while the AC input current contains two pulses in each half-cycle of the phase current frequencies. The AC currents are symmetrical and shifted by 120 degrees.

II. RL load

Figure 4.3 shows that the three-phase rectifier is connected to a stiff sinusoidal three-phase supply, and feeds a series connection of RL. The filter inductor on the DC side is capable of absorbing the pulses (ripples) from the input AC current and also smooths the DC load current as shown in Figure 4.4. The figure also shows that the output voltage consists of six pulses per one AC frequency. Each ripple is in accordance with the AC line-line voltage, which varies every 60°. The load voltage can be calculated in a similar way to the resistive load case as:

$$V_{DC} = 1.35 V_{LL} (4-1)$$

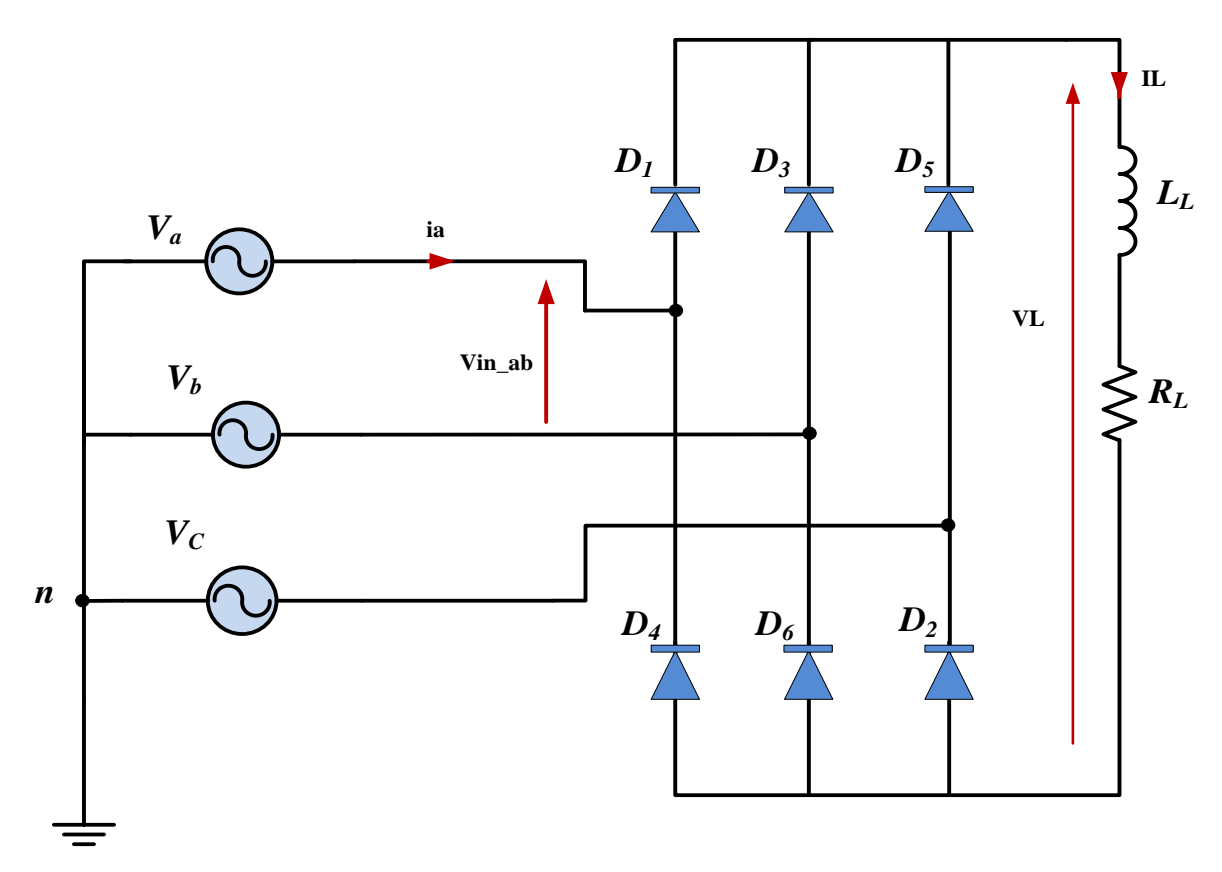


Figure 4.3 SABER model of the three-phase rectifier with RL load

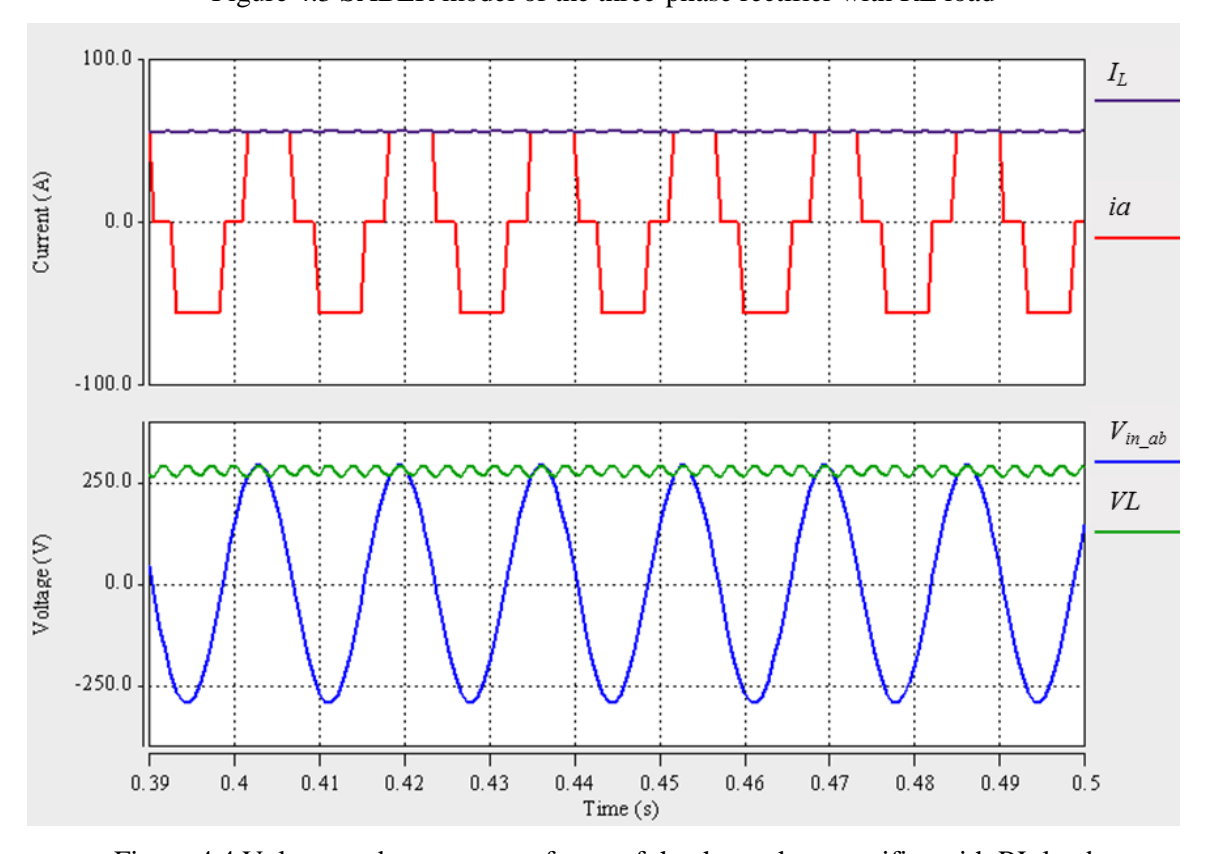


Figure 4.4 Voltage and current waveforms of the three-phase rectifier with RL load

In Figure 4.4, the average output voltage is measured using SABER measurement tools as 279.1 V, and this agrees with the above expression, since the RMS of *Vin_ab* is measured as 206.5 V after adding the two diode voltage drop.

Based on the basic relationship of the inductor voltage, the slope di(t)/dt can be very small if the value of the inductor is large enough at a given voltage (the slope is zero when L is infinite), and the rectifier will operate in continuous current mode (CCM) and each diode conducts for 120° [112]. Therefore, if the value of the inductance in the rectifier circuit is sufficiently large, the load current has negligible ripple and is considered as a DC current.

III. RC load

When the rectifier output is connected to the capacitor-filter in parallel with a DC load (represented by equivalent resistor), it operates differently. This type of rectifier circuit is commonly used in various applications such as battery chargers and adjustable speed drives [137]. However, unlike the conventional inductor filter rectifier, limited literature analyses this rectifier comprehensively [138].

The value of the filtering capacitor determines the value of the output voltage ripple. For a sufficiently large capacitor, the output voltage (V_L) become a constant DC voltage based on the definition of capacitor current and the slope dv(t)/dt. Hence, if C_L tends to infinity, the output voltage will be pure DC. Furthermore, as soon as the line-to-line input voltage (V_{LL}) becomes larger than the load capacitor voltage, two diodes conduct (one from the top and one from the bottom). This forms one pulse from the six pulses in the output current, and two positive pulses and two negative pulses in the AC input current in accordance with the peak of the line-line voltage. During this interval, the capacitor will be charged to the peak of the input voltage. On the other hand, when V_{LL} is lower than the capacitor voltage, the two conducting diodes are in blocking mode and the capacitor discharges its voltage through the load resistor so that the circuit will operate in a discontinuous current mode (DCM). In addition, the load resistance current (I_L) is proportional to the load voltage (V_L) [112, 139]. In such a case, the rectifier operates in discontinuous current mode and starts to peak-detect, as shown in Figure 4.5.

4.2.4 Principles of operation of the three-phase FCSC converter

As explained earlier, the FCSC circuit is used to cancel out the effect of the generator inductance via the FCSC series capacitor C_C .

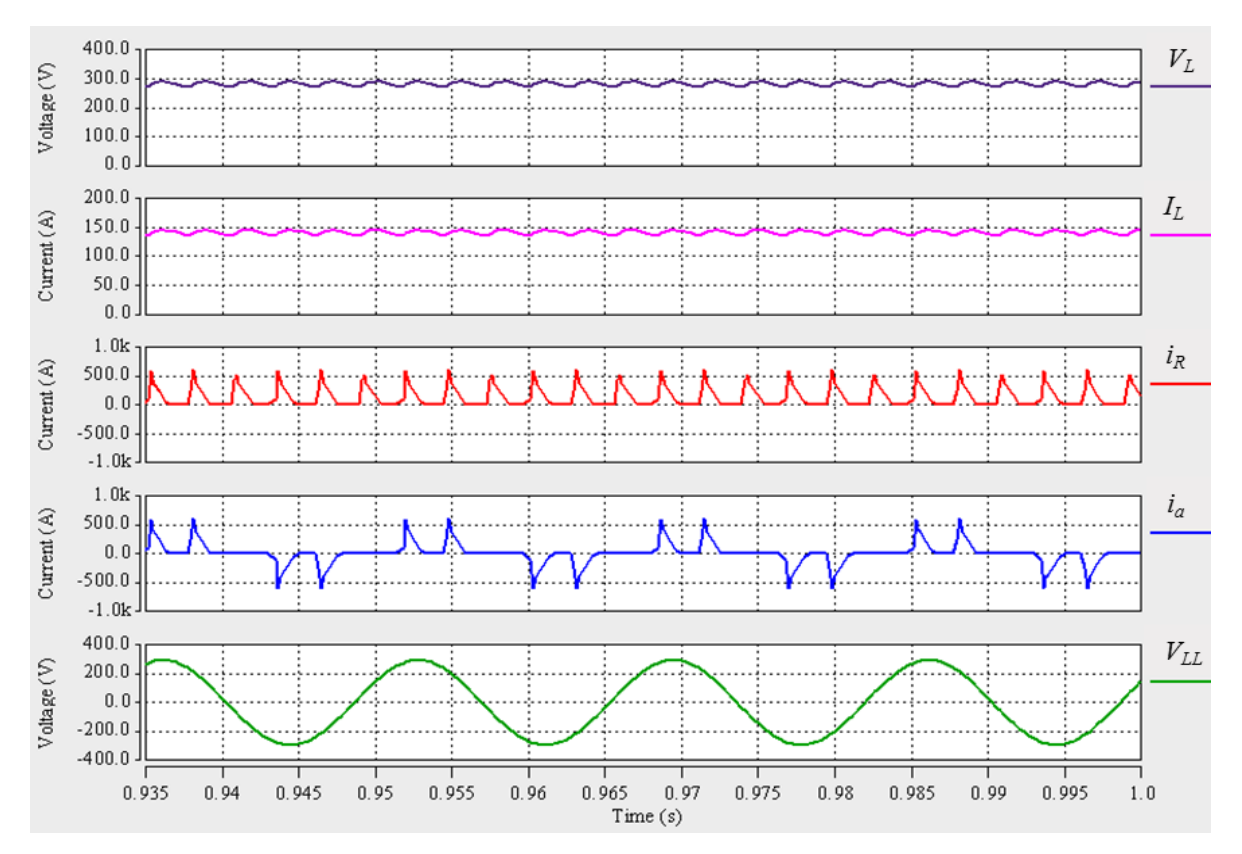


Figure 4.5 Voltage and current waveforms of the three-phase rectifier with RC load

The same principle as in the single-phase case is applied for the three-phase system. All switches in all phases will be ON for an interval, while maintaining a phase difference between each other according to the phase sequences. Each phase is controlled by two IGBT switches, and each IGBT is active for a half-cycle of the PM generator voltage waveform. Figure 4.6 illustrates the circuit configuration every 60° . The figure shows that the active switches and the conducting diodes change as a function of the V_{LL} polarity. In each mode, two phases are connected together and the equivalent circuit includes circuit resistance and inductance with values of 2 R_s and 2 L_s , respectively. The grey colour in this figure represents the IGBT switches which have no effect on circuit behaviour in this interval, and the non-conducting diodes in addition to the phase hold no current. Based on Figure 4.6, which shows the six circuit configurations, there are in addition two IGBT switching states in each half of the line-line voltage. Therefore, there are 12 modes of operation that can describe the circuit behaviour for one frequency cycle.

However, the circuit configurations are identical in several modes, except for the location of the active switches and conducting diodes.

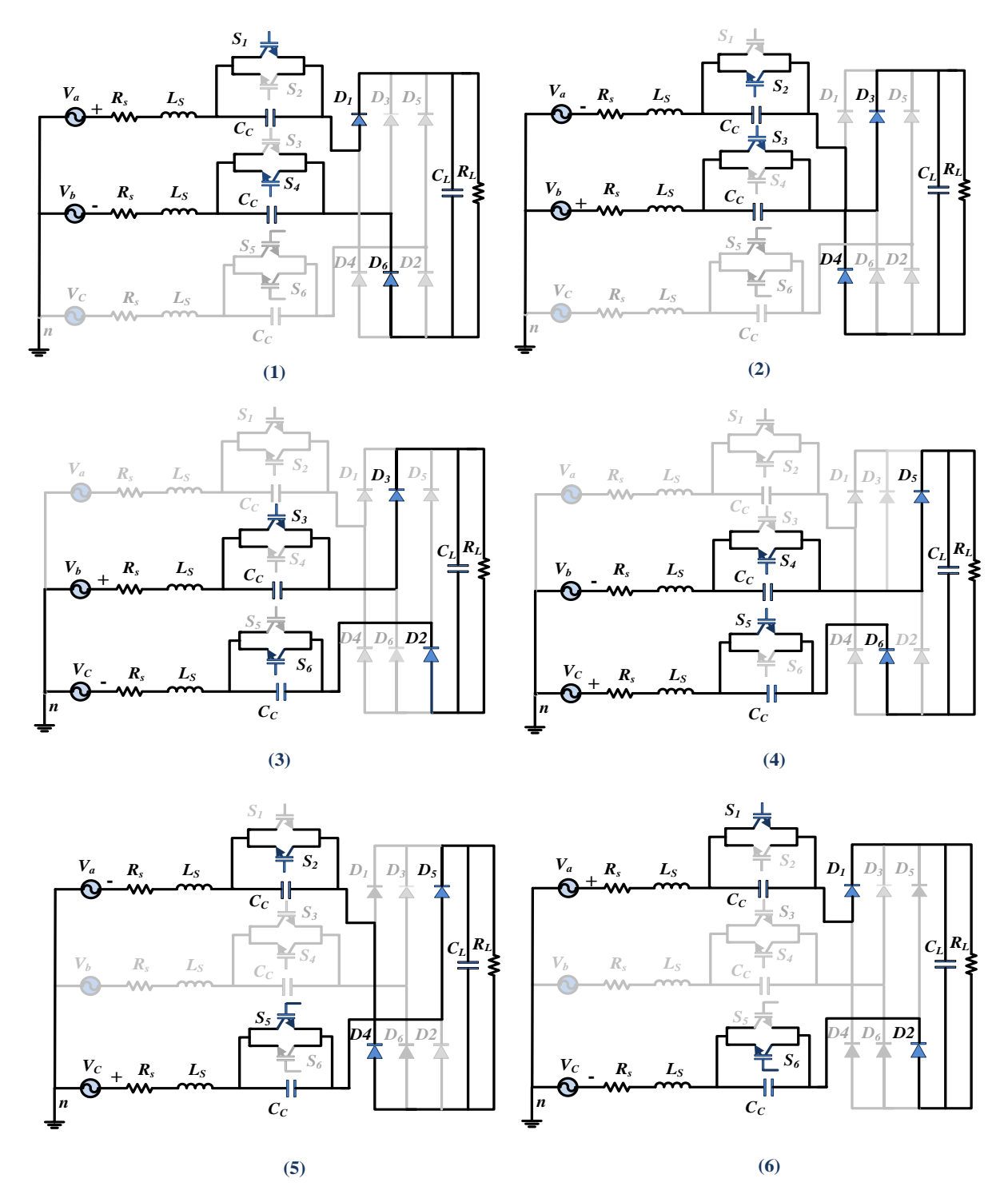


Figure 4.6 Circuit configurations as a function of line-line voltage polarity

4.3 Performance Consideration

In a similar manner to that with the single-phase FCSC converter, this analysis is performed in terms of the power factor, efficiency, and total harmonic distortion in the three-phase FCSC-rectifier. A brief description of these performance measurements in a three-phase system is introduced next.

I. Power factor (PF)

In a three-phase sinusoidal balanced system, the relationship between the active P and reactive Q and apparent power S is similar to that in the single-phase circuit [134]. Recalling the information previously explained in Chapter 3, the three-phase voltage source is sinusoidal in the simulation and the power factor can be expressed as:

$$PF = \frac{I_{L1}}{I_L} \cos \varphi \tag{4-2}$$

It is worth mentioning that, in the experimental test results presented in Chapter 7, the power factor is calculated according to equations (3-34) and (3-35), since the AC source voltage contains harmonics, as will be explained later.

II. Efficiency (η)

The efficiency of the three-phase FCSC converter in variable-voltage variable-frequency three-phase systems can be calculated based on the power flow in such systems. Therefore, the efficiency of the converter can be determined as in the following equations:

$$\% Efficiency \left(\eta_{FCSC} \right) = \frac{P_{dc}}{P_{3ph}}$$
 (4-3)

$$P_{dc} = V_{dc(ave)} \times I_{dc(ave)} \tag{4-4}$$

The three-phase power is calculated from the average of the instantaneous power in each phase, or it can be determined in terms of phase values as given in the formula:

$$P_{in} - 3ph = 3 \times V_{ph} I_{ph} \cos \varphi \tag{4-5}$$

where V_{ph} is the voltage between each phase and a neutral point, while I_{ph} represents the phase current.

III. Total harmonic distortion (THD)

In a three-phase balanced system, the total current harmonic distortion is measured for one phase considering that identical currents are flowing through the other phases.

Equation (4-6) shows the total current harmonic distortion for one phase named a.

$$\% THD_i = \frac{\sqrt{I_a^2 - I_{a1}^2}}{I_{a1}} \times 100 \tag{4-6}$$

where I_{al} represents the fundamental harmonic of the distorted current in phase a.

4.4 Numerical Analysis and Simulation Results

This section presents the numerical analysis for the three-phase FCSC-rectifier employed in a stand-alone system with a higher frequency range of voltage and frequency variations such as in airborne applications. All the analysis is carried out under the assumption of a balanced system.

In the next sections, a performance analysis is carried out to assess the behaviour of the threephase FCSC converter in such a system; this is followed by the simulation results.

4.4.1 SABER model of three-phase FCSC rectifier

The three-phase FCSC-rectifier is modelled and simulated as being controlled by the DSP controller, in conformity with the practical implementation of the system, as described below in Chapter 6. In addition, most of the circuit parameters are chosen in accordance with the practical implementation parameters.

Figure 4.7 shows the SABER model of a three-phase stand-alone system with variable-voltage variable-frequency generator output. In this thesis, the permanent magnet alternator (PMA) is emulated by its back EMF V, its internal resistance R_s , and its inductance L_s . The three phases are named as phase a, b and c. Each phase of the generator is represented by a pure AC voltage source with a phase delay of 120° between them. In this model, the three-phase FCSC is represented by three series capacitors C_c connected in series with the generator inductance and distributed one for each phase. Six IGBT switches labelled from S_1 to S_6 are connected in parallel across the series capacitor and distributed in pairs per phase. These switches are driven by classic drivers to control the effective capacitance for each phase by controlling the IGBT ON times. Six diodes, D_I to D_6 , are used to perform AC to DC conversion. The diodes conduct in accordance with the line-line voltages. The smoothing capacitor C_L is used to reduce the ripple content in the DC output voltage and hence the output current. The load is represented by load resistance R_L . As this converter is proposed for

use in MEA applications, as one type of stand-alone variable-voltage variable-frequency applications, therefore an aero engine generator with a rated speed of 14000 rpm is adopted to supply the three-phase system with a three-phase FCSC circuit.

In the simulation and practical implementation, the permanent magnet generator parameters are based on an aero engine generator presently under development at Newcastle University [140]. In the aerospace application, the PMA provides a redundant power supply to the full authority digital engine (or electronics) control (FADEC) which is used to control all the performance of aircraft engine by a digital computer. The PMA is powered from the engine gearbox via a dedicated low speed output and it must provide constant power across a wide speed range. The power is generated using a passive rectifier on the machine output which is connected across a fixed DC voltage, and when power is not required (when the DC link is fully charged and the DC link voltage is rising) the rectifier is shorted and the machine runs in short-circuit until the DC link voltage falls below the set point. Thus, the machine has a very high per unit inductance to limit the short circuit current to acceptable values. The machine is rated and sized for the low-speed (6% of rated speed) performance requirements, causing it to be heavily over-rated at the high speed performance specifications. This means that this machine suffers from a poor power factor. The full rated speed of this machine is 14,000 rpm. The performance requirement of the machine is shown in Table 4-1.

Table 4-1 Performance requirement of PMA which feeds the FADEC engine control

Speed (RPM)	970	1200	1500	4500	6000	8250
Power (W)	40	48	57	90	100	120

Therefore, the three-phase FCSC circuit is proposed to interface the PMA and the three-phase rectifier to overcome the power factor degradation problem caused by the very high inductance of this machine. This simulation model is verified by the practical implementations of the system in the subsequent chapters. The adopted PMA generator has a linear relationship between back EMF and frequency with speed. The generator parameters are tested as shown in Table 4-2.

In this chapter, the simulation results are based on the assumption that the controller is set to adjust the effective FCSC reactance to fully compensate for the PMA inductive reactance.

Table 4-2 PMA parameters at a frequency of 300 Hz

Speed(RPM)	Frequency(Hz)	EMF _{RMS} (V)	$Rs(\Omega)$	Ls (mH)
2000	300	33.23	2.45	13

In addition, all the measurements will be for one phase, as the system is assumed to be a Y-connected balanced system which means that all three phases have the same electrical parameters. The simulation circuit parameters are listed in Table 4-3. The diodes and IGBT switches used in this simulation are similar to the devices used in the single-phase circuit as described earlier in Chapter 3, and their parameters are shown in Table 3.2.

Table 4-3 Simulation circuit parameters for three-phase system

Circuit parameter	Value	
V _{an} max	78	
F_s	500	
R_S	2.45	
L_S	13 mH	
Сс	7.8 u	
$R_{gI}=R_{g2}$	50 Ω	
$V_{gI} = V_{g2}$	15 V	
C_L	500 μF	
R_L	20 Ω	

4.4.2 Simulation results

The simulation results are divided into two parts. In the first part, the circuit behaviour is tested without using the three-phase FCSC circuit. Then the system performance is assessed when the FCSC circuit is employed in such a three-phase system.

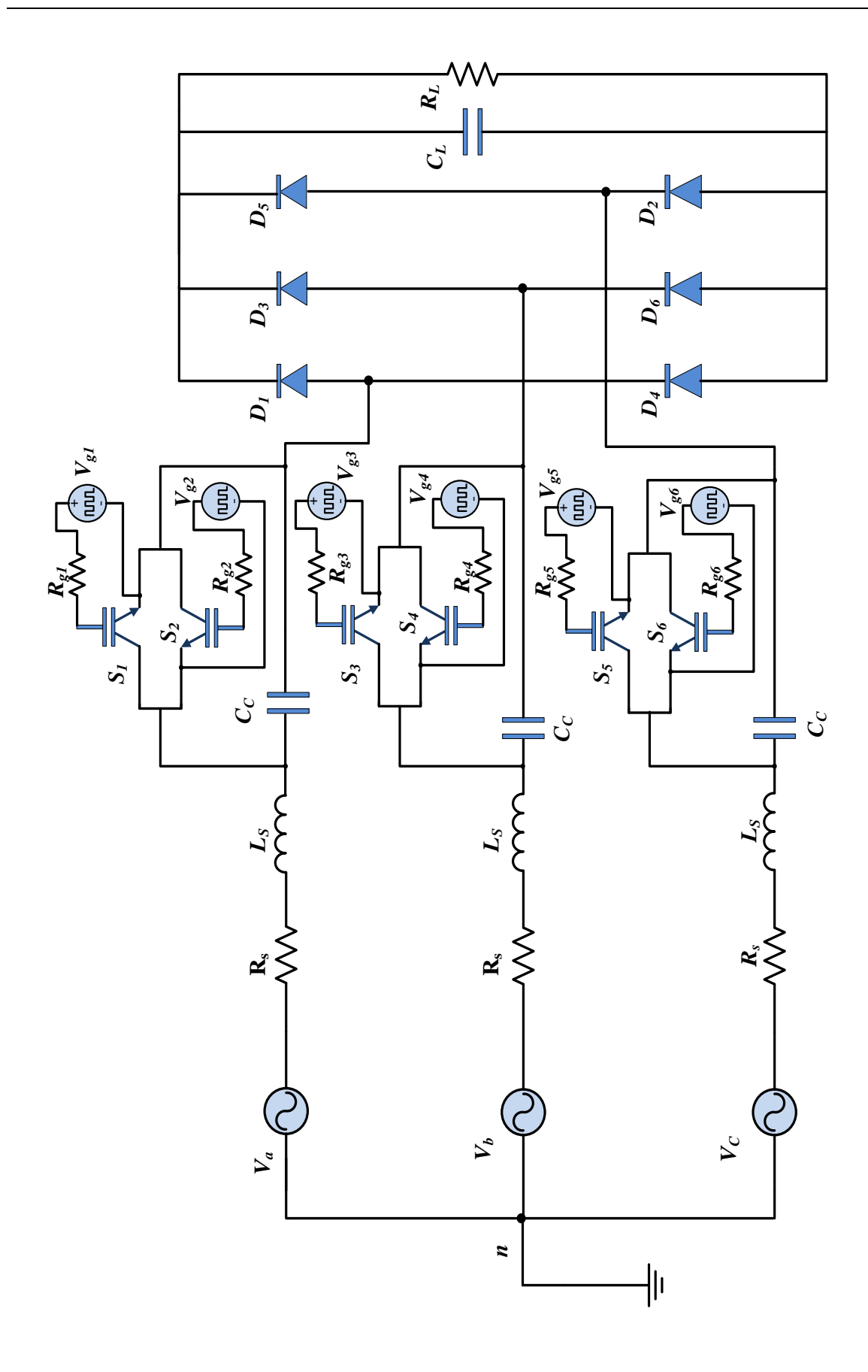


Figure 4.7 SABER model for the three-phase FCSC converter

4.4.2.1 Part A: Simulation results without three-phase FCSC circuit

In this part, the system is operating without the three-phase FCSC circuit as shown in Figure 4.8. As the PMA generator back EMF varies linearly with its frequency, and therefore the peak phase voltage at 500 Hz is 78V.

By using simulator measurement tools, the RMS value of the phase-neutral voltage V_{an_RMS} equals 55.15 V, which satisfies $V_{ph_RMS} = V_{ph_max}/\sqrt{2}$, and the RMS for line-line voltage is equal to 95.5 V, which also satisfies $V_{LL_RMS} = V_{ph_RMS} * \sqrt{3}$. The load capacitor is assumed to be charged with a 50 V.

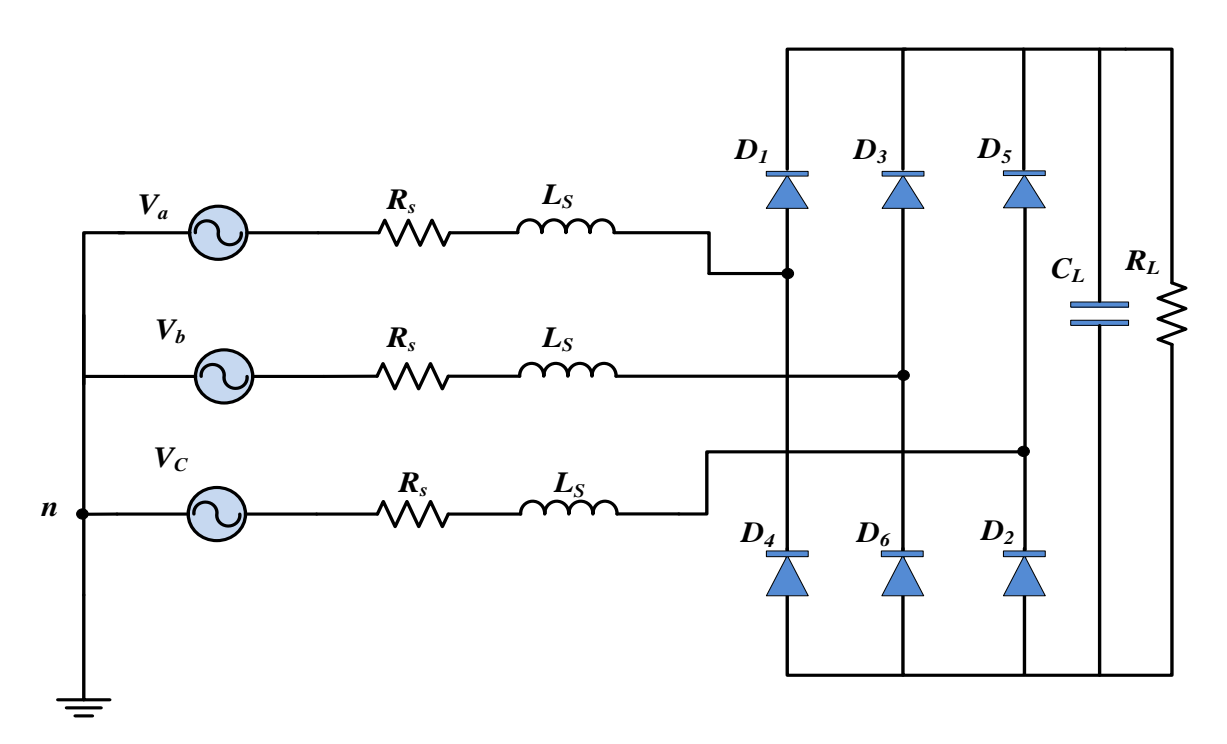


Figure 4.8 SABER model for the system without FCSC

Figure 4.9 presents the voltages and currents waveforms for phase a when the circuit is running without employing the FCSC circuit when the PMA frequency is 500 Hz.

From the simulation measurements, the phase difference between the phase voltage and the phase current is 69.54°. This means that the system has a poor input power factor of 0.35. The RMS value of the phase a current (i_a) is 1.25 A. In addition, with V_{an_max} equal to 78 V the DC load voltage (V_L) equals 33.8 V, which is lower than the system input voltage. The rectifier input voltage (Vin_ab) is a quasi-square wave and it is clamped by the voltage which appears across C_L in the DC side to have a maximum value of 35.2 V. The difference between Vin_ab and V_L is 1.4 V, which represents the diodes voltage drop.

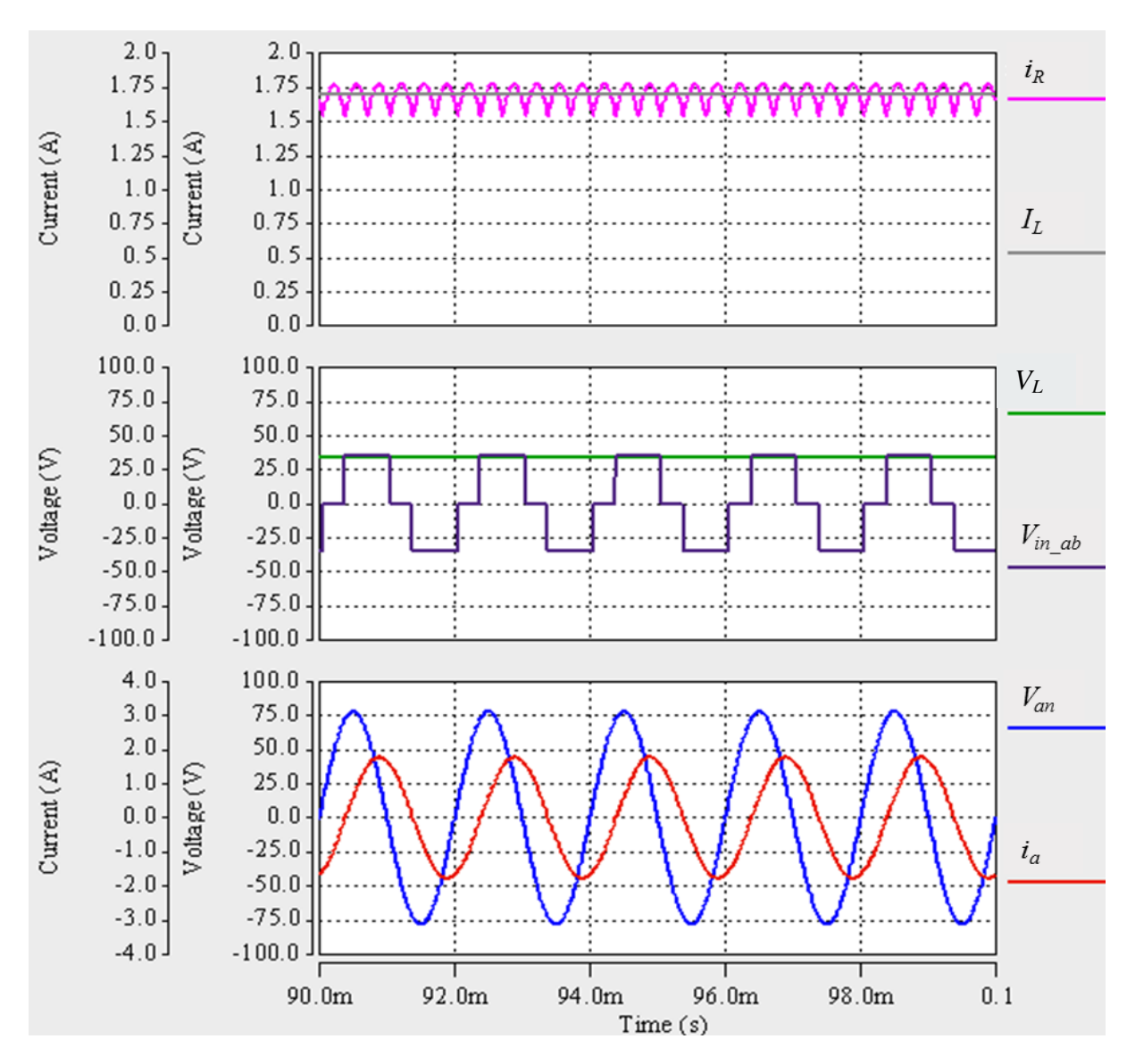


Figure 4.9 Voltage and current waveforms for phase a when the system is working without the FCSC circuit

In other words, the system input voltage has dropped to approximately half of its value. The main reason for this is the occurrence of the overlapping current commutation process due to the high inductance of the PMA. The commutation overlap prevents the instantaneous current transition between the present conducting diodes to the next conducting diodes; it is not instantaneous due to the effect of inductance.

During the overlap period, three diodes conduct, either one from the top group and two from the bottom group or one from the bottom group and two from the top group [114, 127]. For example, when the diodes D_1 , D_3 and D_5 are conducting, the current transition waveforms flowing through diodes are as shown in Figure 4.10. In the three-phase bridge rectifier, the commutation occurs six times in one cycle.

The overlapping period is dependent on the value of machine inductance which can be expressed in terms of the commutation angle u. Assuming Rs is neglected, u can be expressed as:

$$\cos u = 1 - \frac{\sqrt{2} \omega L_S I_d}{V_{IJ}} \tag{4-7}$$

where ω is the angular frequency, L_S is the machine inductance, I_d is the average load current and V_{LL} is the RMS line-line voltage. And the average output voltage V_L when R_S is ignored can be calculated in the equation below as:

$$V_L = 1.35 V_{LL} - \left(\frac{3}{\pi} \omega L_S I_d\right)$$
 (4-8)

It is important to mention that equations (4-7) and (4-8) are derived for a rectifier circuit supplied from a stiff high inductance sinusoidal voltage source, and the output of the rectifier is connected to a constant DC current source [114] which is not the same as the load in this work. However, it is used here for discussion purposes only.

Equation (4-8) shows clearly that a high value of generator inductance reduces the average output voltage, because the voltage drop caused by the machine reactance is subtracted from $1.35\ V_{LL}$. This voltage reduction is increased when the machine inductance increases [136]. Figure 4.10 shows the overlap interval between the diodes. In addition, this figure illustrates how one diode conducts while the other diode is carries the current during the overlap period.

Indeed, in this circuit, the diode conducts for a period of approximately 1 ms, which is equal to 180° as the period is T=2 ms. The phase shift between each diode is equal to $333.1 \, \mu s$, which is equivalent to 60° , as shown in Figure 4.11. This is because the polarity of the line voltage varies every 60° . Therefore, the circuit is operating at CCM.

The results show that when the PMA is connected directly to a three-phase rectifier, the system suffers from both a significant reduction in the average DC load voltage due to current commutation overlap and poor input power factor.

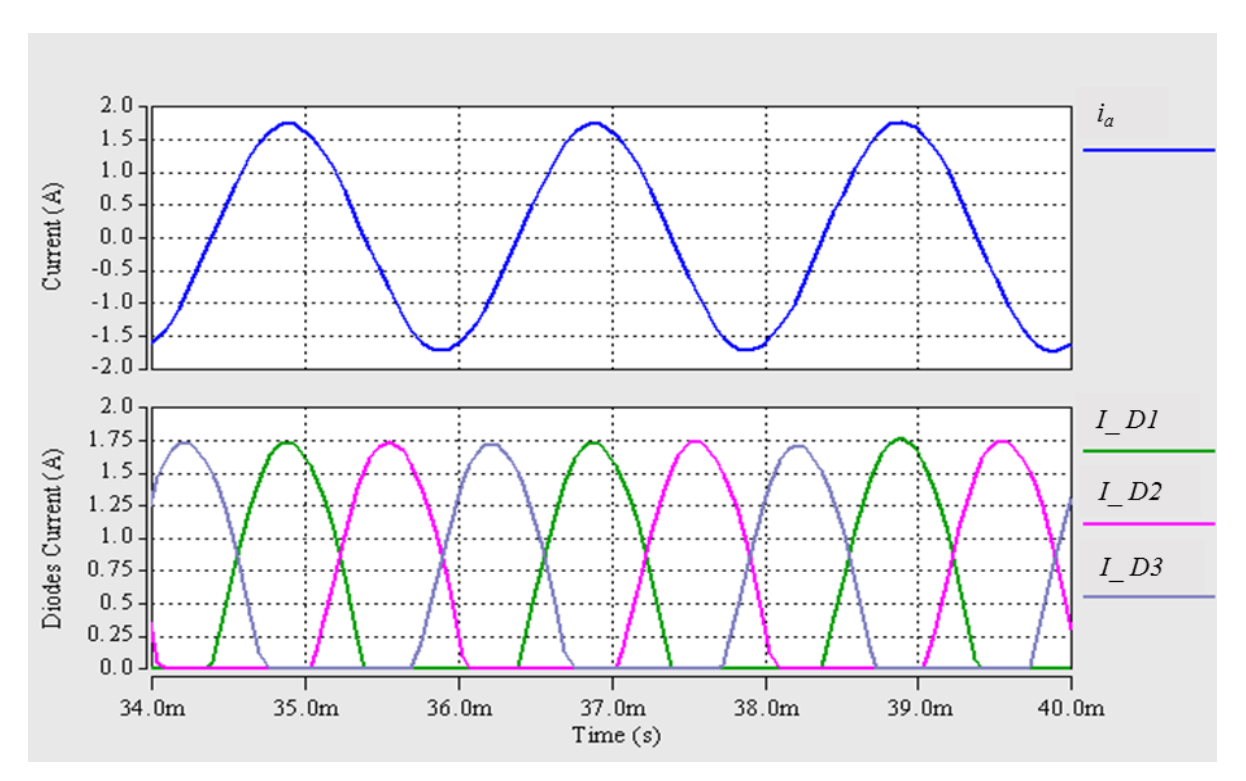


Figure 4.10 Phase a current and diodes D_1,D_3 and D_5 currents during commutation interval

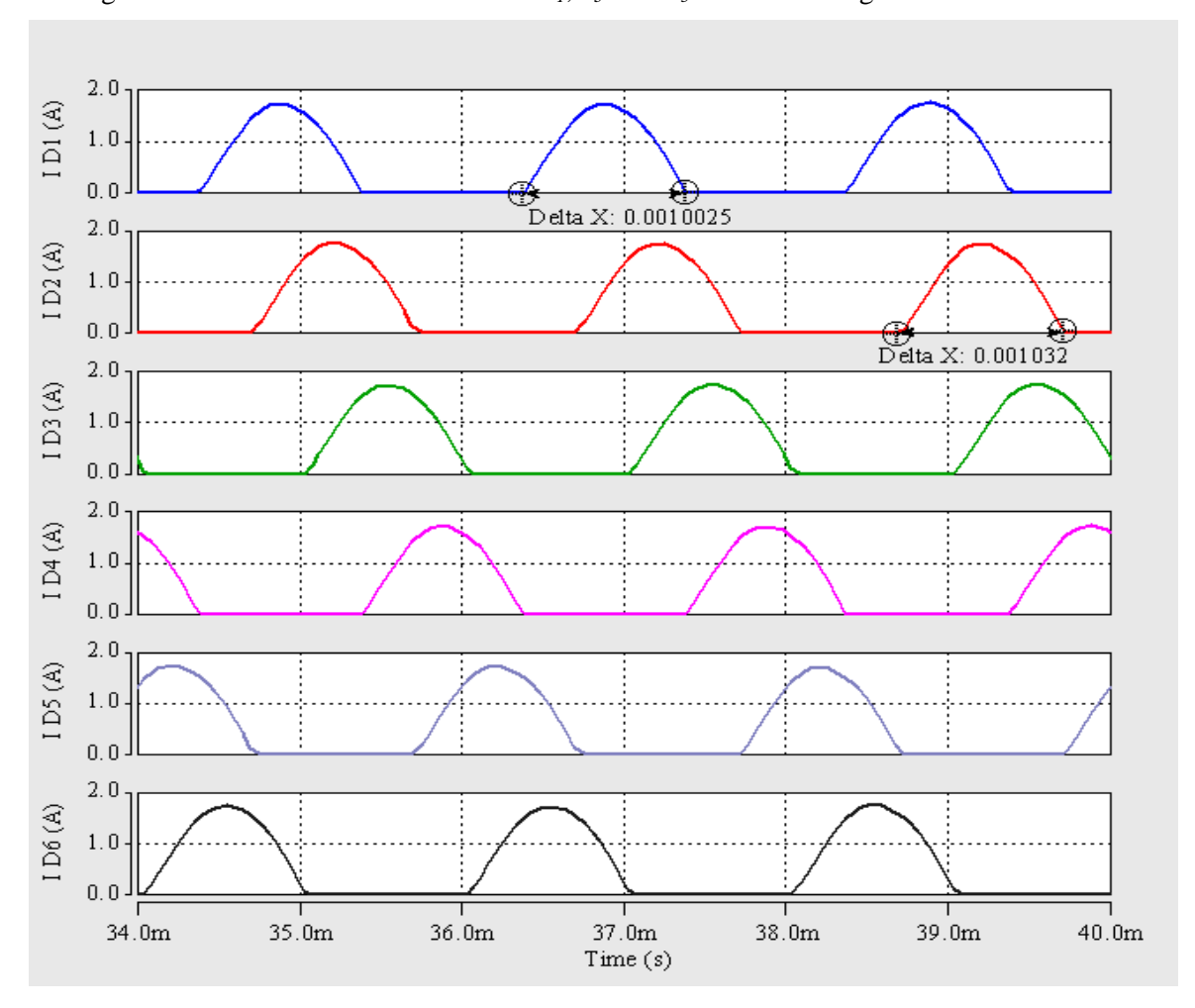


Figure 4.11 Diode current waveforms

4.4.2.2 Part B: Simulation results with the three-phase FCSC circuit

The circuit is simulated with a series capacitor of 7.8 μ F to fully compensate for the effect of PMA inductance. The value of line capacitor is calculated based on equation (4-9), assuming that the resonant frequency (f_r) is similar to the operating frequency (F_s) with a value of 500 Hz and that L represents the PMA inductance in this case.

$$f_r = \frac{1}{2\pi\sqrt{LC}}\tag{4-9}$$

This means that the turn OFF angle γ is zero for all switches and, thereby, the IGBT's ON time is zero. In other words, all the switches are permanently open during the generator frequency cycle. The ESR value of C_C is 65.7 m Ω . Figure 4.12 shows the voltage and current waveforms in all phases. The currents are in phase with the voltage waveforms in all phases in addition to the sinusoidal current shape due to the high inductor value of the PMA generator.

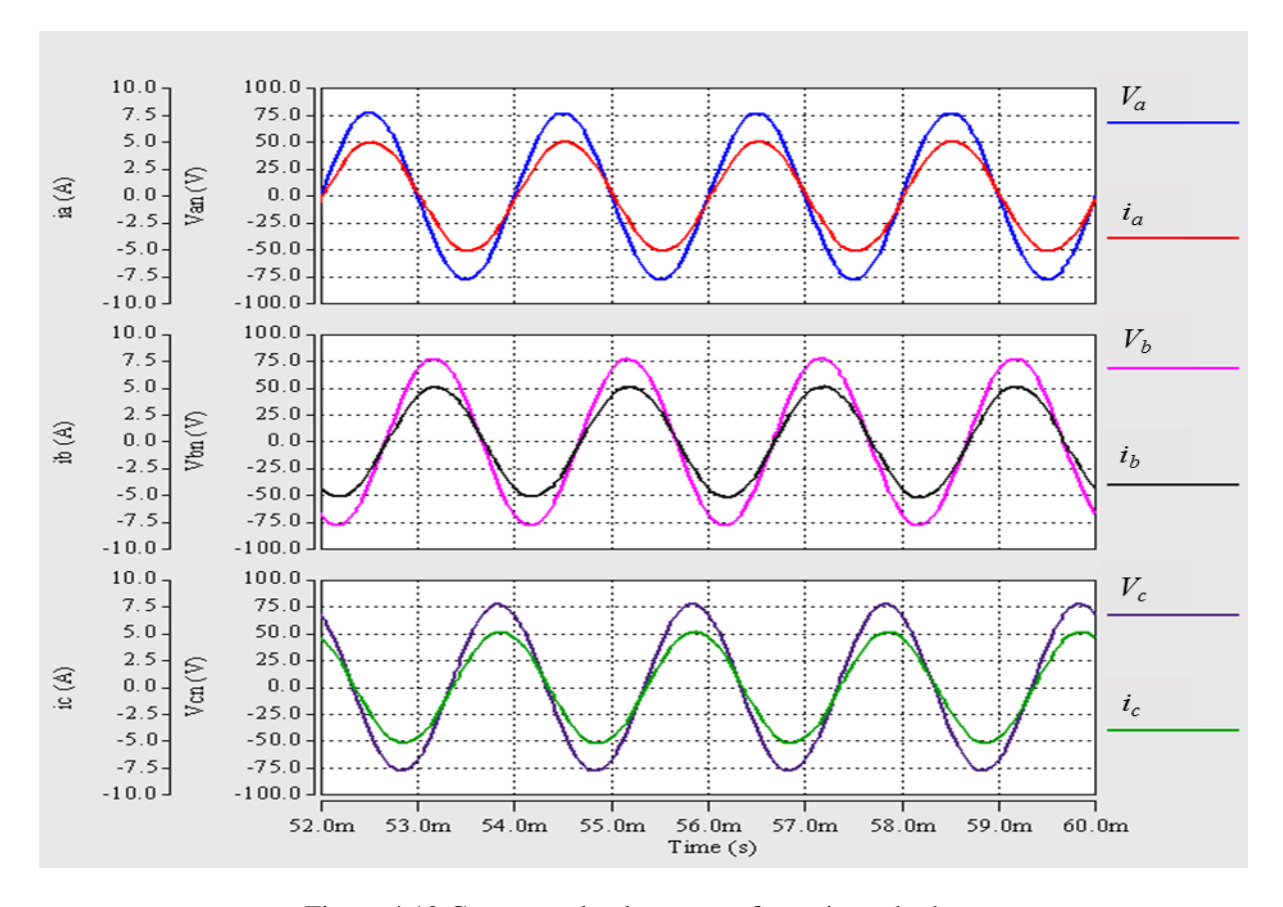


Figure 4.12 Current and voltage waveforms in each phase

The relationship between voltage and current in phase-a is shown in Figure 4.13 in addition to the output voltage in the DC side of the rectifier V_L .

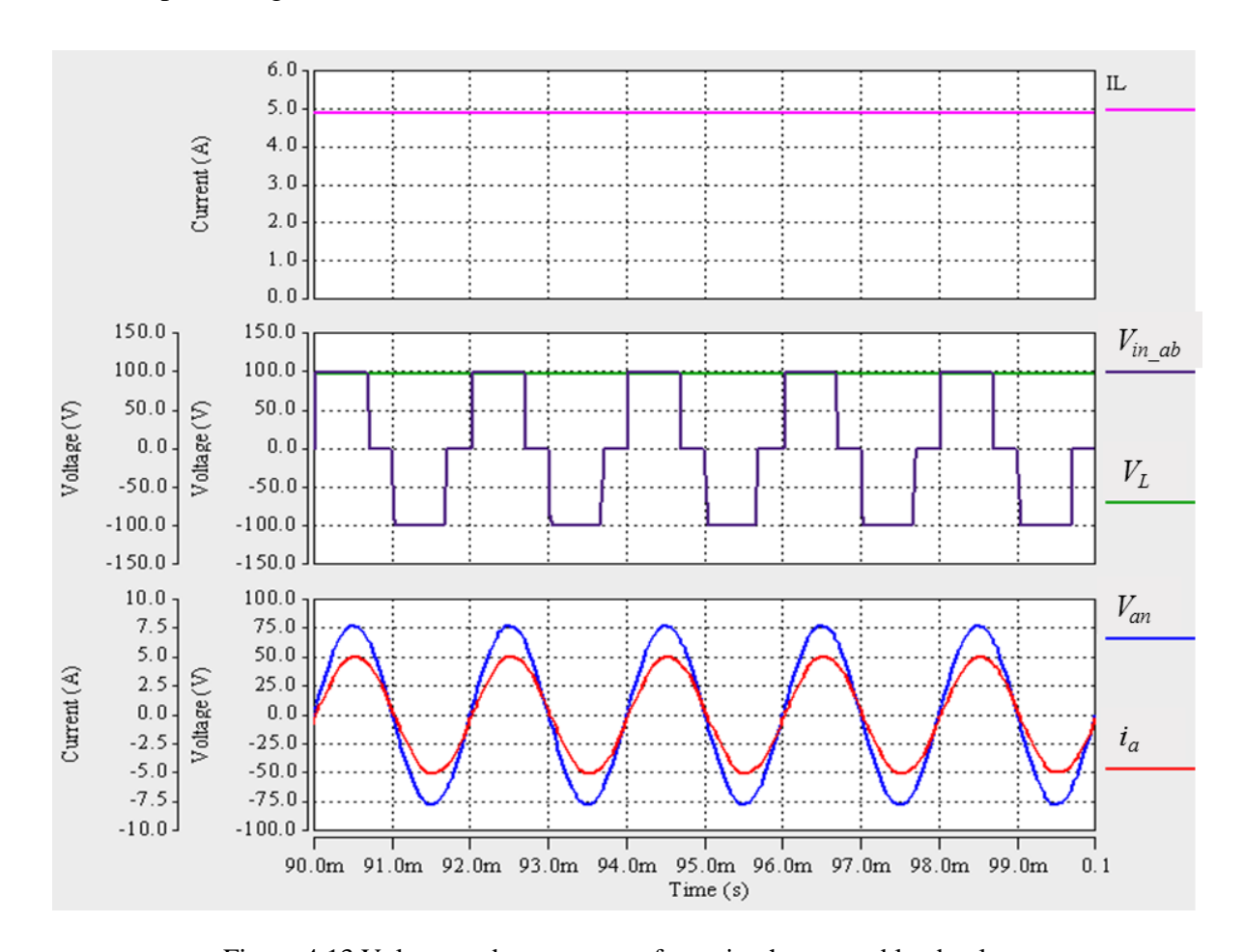


Figure 4.13 Voltage and current waveforms in phase a and load voltage

By comparing Figure 4.9 and Figure 4.13, it is clear that by using the FCSC circuit in series with the PMA generator, the phase difference between the voltage and current waveforms becomes approximately zero. This means that the FCSC is able to improve the power factor to be approximately unity in such system. Furthermore, there is a dramatic increase in the value of the average output voltage when employing the FCSC circuit to interface the PMA generator, as the output voltage increases from 35.2 V to 99 V. This results in increasing the DC load current dramatically, since the load current follows the load voltage in RC circuit as explained in Section 4.2.3. Figure 4.13 also shows that the rectifier input voltage (*Vin_ab*) is also a quasi-square wave and is clamped by the DC load voltage minus the diodes voltage drop.

Figure 4.14 shows that the rectifier output current consists of from six pulses, and each current pulse is produced according to the line-line voltage, as explained earlier in this chapter.

The value of the rectifier peak current is equal to the peak of the input current in each phase. This is similar to the case of the rectifier output voltage in a rectifier circuit connected to the RL load and supplied from a sinusoidal voltage source.

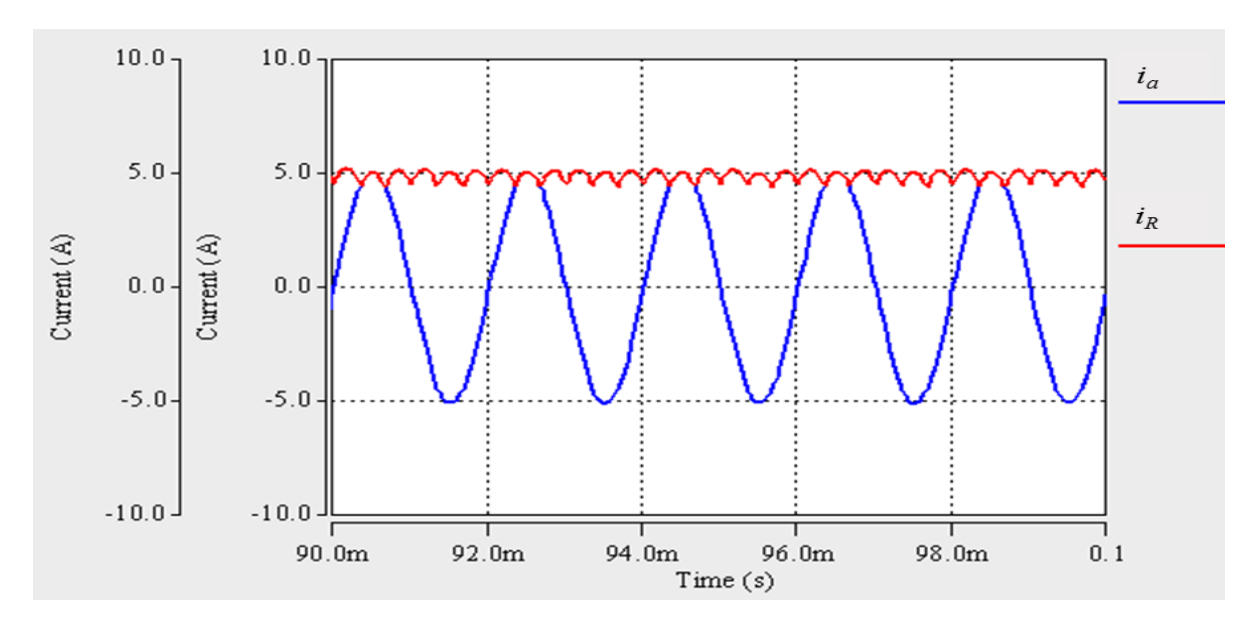


Figure 4.14 Average voltage and current in the DC output

Therefore, it is important to mention that the circuit operation is in accordance with the duality principle in electrical systems. Duality can be described as the relationship between two separate circuits, where voltage behaviour of one resembles the current behaviour of the other and vice versa [141, 142]. For example, the series RL circuit supplied by voltage source is a dual to parallel RC circuit with current source injection. By invoking the duality principle, many expressions can be derived.

Based on this concept, the average rectifier current can be calculated as follows:

$$I_{dc} = \frac{1}{\pi/3} \int_{-\pi/6}^{\pi/6} I_m \cos \omega t \ d\omega t$$
 (4-10)

$$I_{dc} = \frac{3}{\pi} I_m = 1.35 I_{RMS} \tag{4-11}$$

where I_m and I_{RMS} represent the maximum and RMS values of the input AC current, respectively.

This illustrates how the combination of the electrical PMA generator with the FCSC circuit connected in series constitutes a sinusoidal current source which is able to inject a sinusoidal

current into the three-phase rectifier, and, therefore, with the help of the duality concept, many relationships can be derived on this basis when needed. Furthermore, all diode currents are shown in Figure 4.15. Each diode conducts for an interval of 1 ms, which is equivalent to 180° as the frequency is 500 Hz.

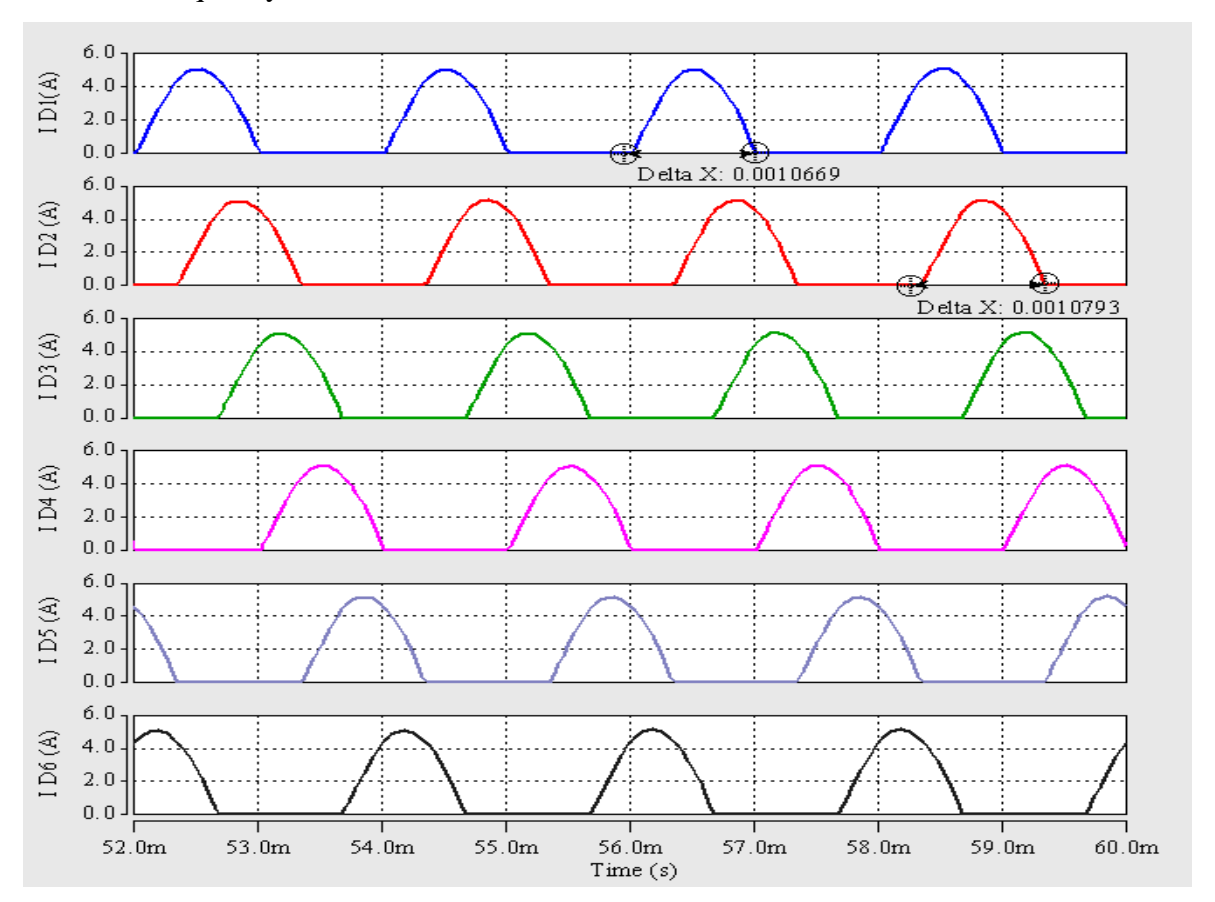


Figure 4.15 Diode currents in all phases

Figure 4.16 shows that the commutation overlap still exists through the current transition between the phases. This figure shows the currents passing through the three diodes in the top group (D_1 , D_3 and D_5). Comparing Figure 4.16 and Figure 4.10, it can be seen that both figures show that the current cannot commutate instantaneously between the diodes, which means that commutation overlapping exists in both cases. However, the use of the FCSC minimizes the reduction in output voltage caused by the commutation overlap, as the commutation interval is reduced.

To employ the FCSC-rectifier in aircraft applications, the current distortion needs to be investigated in more detail. The input current in each phase is approximately sinusoidal, and therefore the fundamental harmonic is the dominant harmonic in the frequency spectrum of the current in phase-a, as shown in Figure 4.17. However, for aircraft applications, because of the strict distortion limits, all harmonics below the 40th need to be considered to compare

them with current harmonics limits set by RTCA DO-160. Monroy *et al.* [143] presented the current harmonic distortion limits for balanced three-phase equipment set by RTCA DO-160 as shown in Table 4-4.

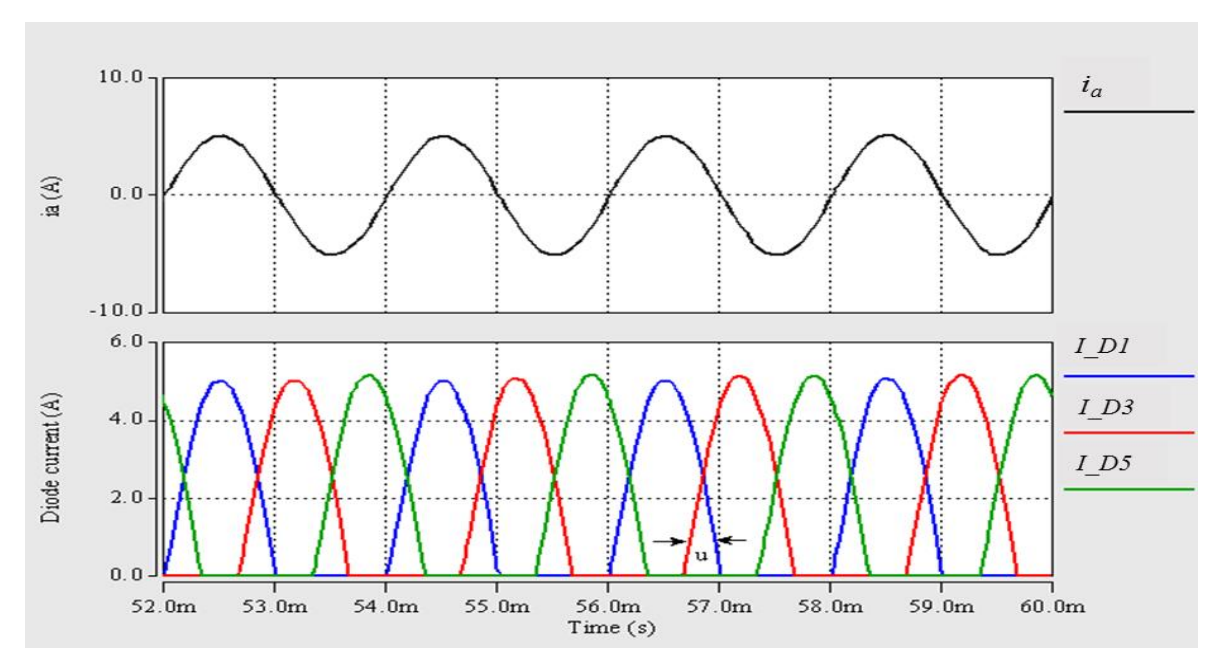


Figure 4.16 Overlap commutation interval between diodes

This table shows the limits for each current harmonic component in terms of the maximum fundamental current.

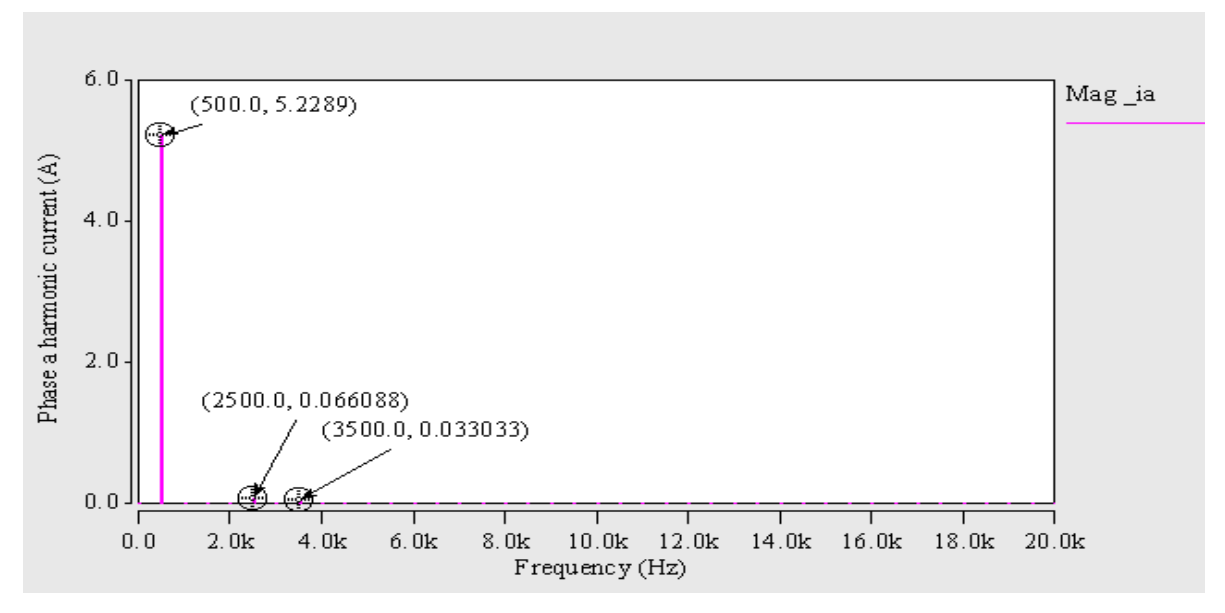


Figure 4.17 Frequency spectrum of the current in phase a when employing three-phase FCSC-rectifier with PMA

In this simulation, the FFT (Fast Fourier transform) analysis is carried out in SABER to calculate the total current harmonic distortion and the harmonic contents of the input current.

The FFT is performed for one frequency cycle of the current waveform with 1024 points and applying a simple rectangular windowing function with truncation error of 0.000001. This table shows the limits for each current harmonic component in terms of the maximum fundamental current.

Table 4-4 Current harmonic limits for balanced three-phase electrical equipment as imposed by RTCA DO-160 [143]

Harmonic order	Limits		
3 rd ,5 th ,7 th	I_3 , I_5 , I_7 = 0.02 I_1		
Odd Triplen Harmonics(h= 9, 15, 21,, 39)	I _h =0.1 I ₁ /h		
11 th	$I_{11}=0.1\ I_1$		
13 th	I ₁₃ =0.08 I ₁		
Odd Non Triplen Harmonics 17,19	$I_{17} = I_{19} = 0.04 I_1$		
Odd Non Triplen Harmonics 23,25	$I_{23} = I_{25} = 0.03 I_1$		
Odd Non Triplen Harmonics 29, 31, 35, 37	$I_h = 0.3 I_1/h$		
Even harmonics 2 and 4	$I_h = 0.01 I_1/h$		
Even harmonics > 4(h= 6, 8, 10,, 40)	I _h =0.0025 I ₁		

where h is the harmonic order and I_h is the maximum harmonic current of order h.

Figure 4.18 provides an example of an FFT analysis and the harmonic spectrum for the system by using SABER. The figure shows that higher order harmonics exist, which need to be compared with the harmonic limits. The 5th and 7th order harmonics exist with values of 1.262% and 0.631% of I₁ respectively; both are lower than the 2 value in Table 4-4. The 11th and 13th order harmonics have values of 0.248% and 0.179%, respectively, which is less than 10% and 8%, the values which are listed in the same table. By comparing all the current harmonics orders with the RTCA DO-160 limits defined in the above table, it can be concluded that all the current harmonics are within the limits for aircraft equipment.

This means that the three-phase FCSC converter can be proposed for aircraft applications without suffering from zero-crossing distortion problems and without the risk of exceeding the allowable current distortion limits at fixed load. The next sub-section investigates the effect of load resistance variations on the three-phase FCSC converter performance.

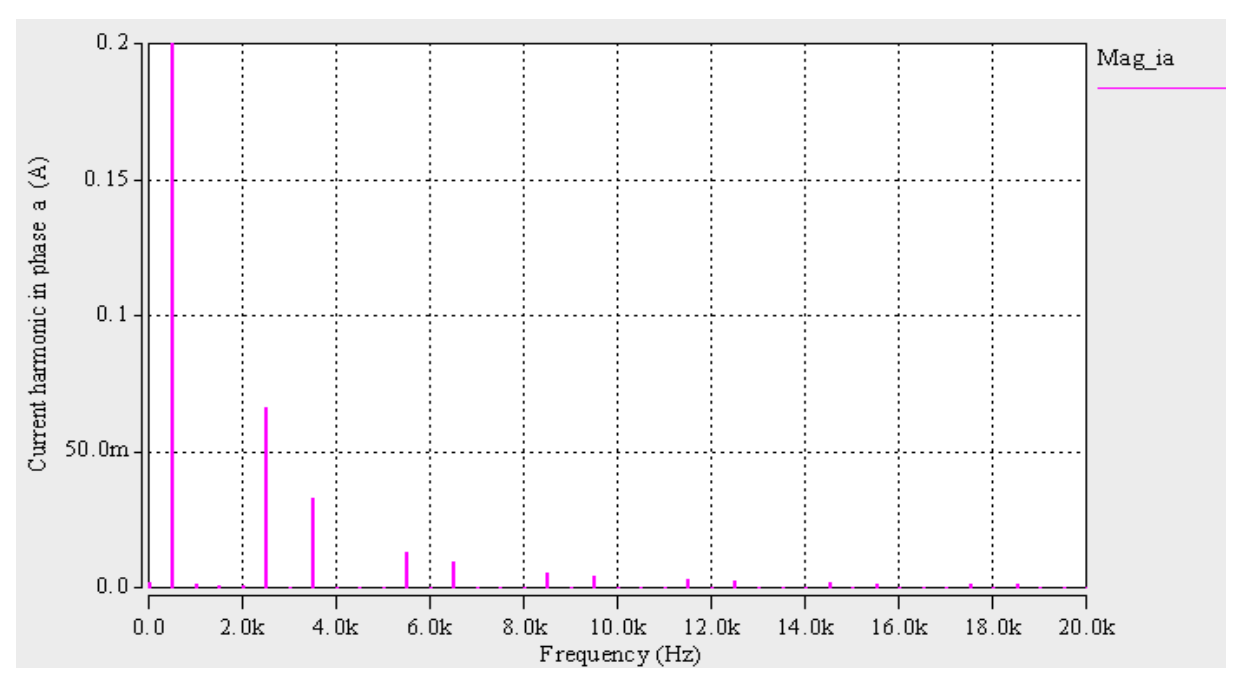


Figure 4.18 Input current harmonics

4.4.3 Operation at various load conditions

The behaviour of the FCSC converter is also investigated under different load conditions. The investigation in this chapter concerns only varying load resistance from $10~\Omega$ to $30~\Omega$ to be compatible with the load variation in the practical test presented in Chapter 7. The load capacitance is kept constant at a value of $500~\mu F$ as explained previously. All simulation results are presented for a maximum frequency of 500~Hz and measurements are taken from phase a, as the other phases are identical.

By varying the load current, the results show that the three-phase FCSC converter is able to correct the power factor to approximately unity (0.999) even when the load is varied. The higher power factor is driven by a high displacement factor DPF and high distortion factor DF, both of which are slightly affected by changing the load condition from a heavy load to light load. Power factor is unity at the lower load resistance value of 10Ω as shown in Figure 4.19.

As the system uses a three-phase rectifier, the THD_i % is low. There is a slight change in THD_i % values when the load condition is varied, especially at higher load currents, as shown in Figure 4.20. This figure shows the percentage efficiency of the FCSC converter η _FCSC at different load conditions. The efficiency is calculated based on equation (4-3) after subtracting the power losses in the PMA resistance for the three-phases.

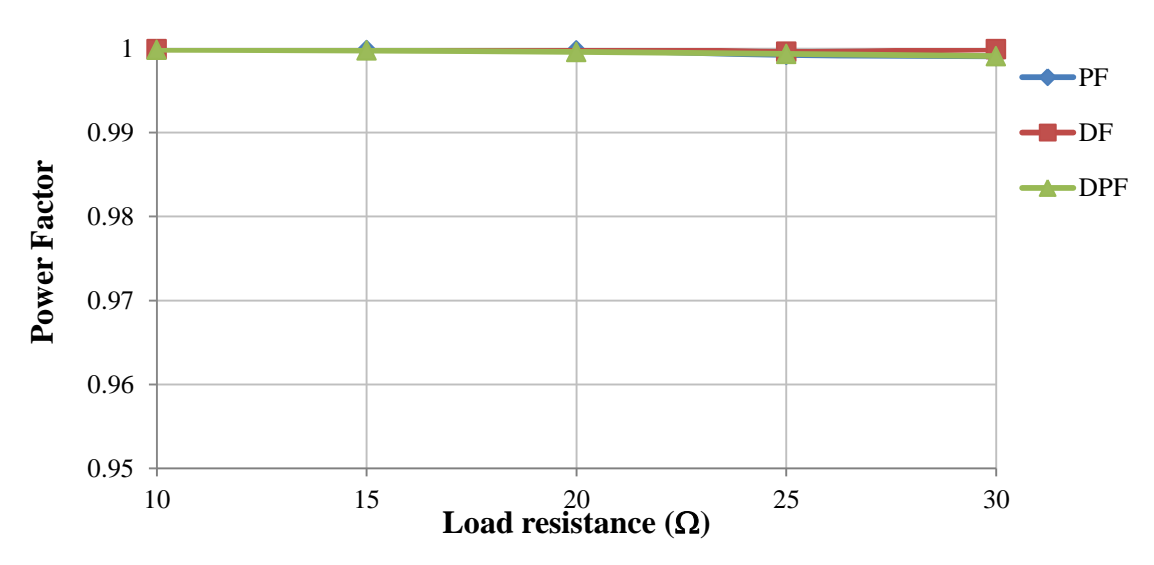


Figure 4.19 Displacement, distortion and power factor as a function of R_L

Based on the power flow in the circuit, the relationship between the three-phase input power $Pin_{_3ph}$ and the DC output power P_{out} can be formulated as:

$$P_{out} = P_{in-3ph} - P_{loss-3ph} \tag{4-12}$$

where P_{loss_3ph} represents the total losses in the three-phase system, and these losses include the total losses caused by PMA resistance P_{Rs_3ph} and the small amount of total losses in the C_C in addition to the diode losses in this case. In this simulation, all IGBT switches are permanently open; therefore, the conduction losses and the switching losses are zero. Therefore, the total power loss P_{loss_3ph} in this case is given as:

$$P_{loss-3ph} = P_{R_S-3Ph} + PC_{C-3ph} + P_{diodes}$$

$$(4-13)$$

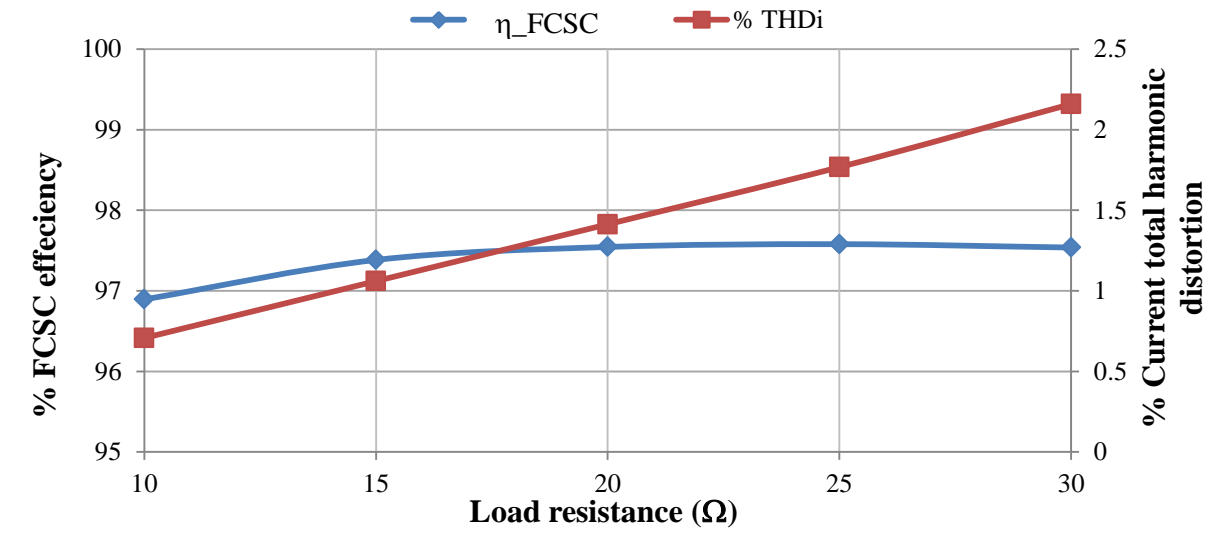


Figure 4.20 FCSC converter efficiency and current total harmonic distortion

Figure 4.21 addresses the relationship between the three-phase input power and the DC output power in terms of power losses in the system at different load conditions.

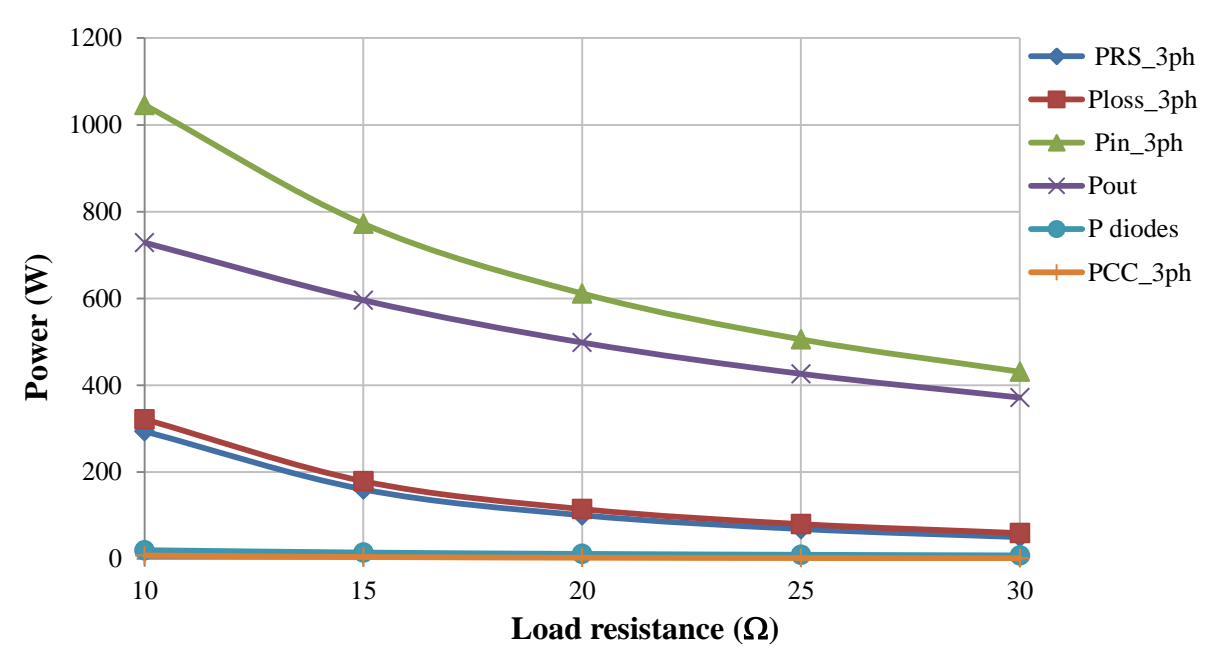


Figure 4.21 Input and output power and power losses in the three-phase system

With the help of SABER, the average instantaneous power is calculated for each component. This figure shows that a large amount of power is dissipated at high PMA resistance R_s . However, the power dissipated in the ESR resistance of C_C is very small. Similarly, a small amount of power is dissipated in the power diodes. When the load current is increased, the output power is increased and, thereby, the input power is also increased. Also, the total losses are higher at lower load resistance. As explained earlier, since the value of each input current harmonic is very important, the magnitude of the percentage maximum input current harmonic distortion is calculated to evaluate the effect of load variation on the current harmonics.

By performing FFT analysis, Figure 4.22 illustrates the relationship between load variation and each harmonic order. In this figure, all the harmonics between the fundamental component until the 40^{th} component are included to cover all the RTCA DO-160 requirements. The figure shows that by increasing R_L ; the magnitude of the 5^{th} harmonic is dramatically increased with increasing R_L , however, it does not exceed the limits presented in Table 4-4, because the maximum value of the 5^{th} harmonics is less than 2 %. Also, despite the increase in non-triplen harmonics values (7^{th} , 11^{th} and 13^{th}) when the load resistance is increased, they all remain well within limits.

According to the table limits, the 17^{th} and 19^{th} harmonics should not exceed 4% and when using three-phase FCSC their values are 0.15% and 0.12%, respectively as shown in the figure. The figure also shows that all the harmonic orders increase with increasing R_L , although the higher harmonic orders have very small values.

The simulation results clearly show that the performance of the three-phase FCSC-rectifier is affected by load resistance variations. The results also show that power factor and efficiency are slightly affected by load resistance variations.

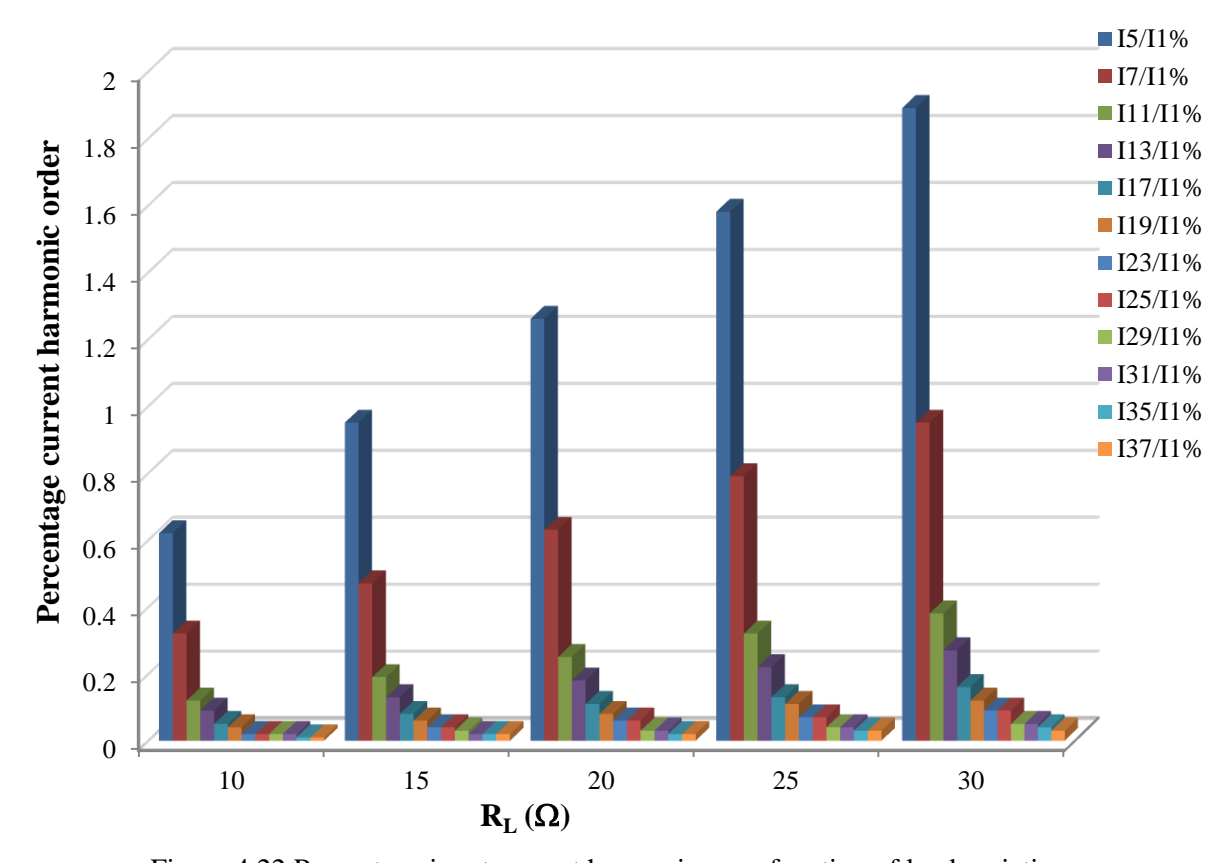


Figure 4.22 Percentage input current harmonics as a function of load variations

4.5 Summary

This chapter investigates the employment of the three-phase FCSC-rectifier to interface the electrical generator with an electrical frequency of 500 Hz, which is one of the operating frequencies used in airborne applications.

In aerospace applications such as a commercial aircraft, the allowable distortion in the current is strictly limited. Most conventional PFC converters suffer from high zero crossing distortion and large distortion levels, which excludes them from serving in aircraft applications according to power quality requirements.

This zero crossing distortion is caused mainly by cusp distortion and DCM distortion. Therefore, it is very important to propose a new PFC topology which has no zero crossing distortion.

The same procedure as presented in Chapter 3 was followed in this chapter to assess the performance of the three-phase FCSC when employed in a medium frequency range application. A description of the principles of operation of the circuit is presented in this chapter. Furthermore, the impact of type load (R, series RL and parallel RC loads) is also highlighted. In addition, simulation results for the PMA generator with the three-phase rectifier only and with the three-phase FCSC converter at a maximum frequency of 500 Hz are presented. A performance analysis is presented for the three-phase FCSC-rectifier operating at 500 Hz. The results show that using the three-phase FCSC-rectifier corrects the input power factor significantly from 0.35 lagging, when the PMA generator is connected directly to the diode bridge rectifier, to approximately unity power factor when the PMA is connected to the FCSC converter. In addition, there is a dramatic increase in the output voltage level from 36 V to 99 V even with the existence of commutation overlap. The efficiency of the FCSC-rectifier is high, at approximately 97%.

It is important to mention that the simulation results show that the system behaves in accordance with the duality principle in electrical systems. The system operates in a duality with the three-phase rectifier supplied by a stiff voltage source. When the FCSC circuit is interfaced with a high inductance electrical generator and three-phase diode bridge rectifier, the FCSC converter injects a sinusoidal current to the three-phase rectifier.

Furthermore, the simulation results demonstrate that the current waveforms in all phases are approximately sinusoidal and in-phase with the voltage waveforms at a frequency of 500 Hz. Therefore, the input current distortion is low and the dominant harmonic is the fundamental component with a small RMS value of the fifth harmonic order which is lower than the limits for aerospace systems. All of the required current harmonics are investigated by performing FFT analysis, and they are found to be lower than the limits set by RTCA DO-160G. This means that employing the FCSC in a medium frequency application as a PFC converter will not cause current distortion problems.

This chapter shows clearly that the FCSC-rectifier can be proposed for employment in medium frequency applications such as aircraft applications without leading to the problem of

zero crossing distortion which occurs in conventional PFC converters. In fact, the simulation results show that the FCSC-rectifier is able to enhance the performance of the PMA generator without exceeding the power quality limits by improving the power factor. Furthermore, it minimizes the overlap current commutation intervals and, thereby, a minimal reduction in the DC output voltage can be achieved.

The performance of the three-phase FCSC-rectifier under different load conditions is presented. The efficiency of the three-phase FCSC converter is maintained at a high level during load variations, and the converter is capable of maintaining a high power factor at different load conditions while a slight increase in the current THD occurs when load current is reduced. However, the simulation results show that, when the load is varied from heavy to light load, harmonics do not exceed the allowable limits which need to be considered for aircraft application. The performance of the FCSC-rectifier is experimentally tested and verified in a practical implementation in Chapter 7. To adopt the FCSC-rectifier in airborne applications when the frequency is varied, a proper control scheme needs to be proposed. The next chapter proposes a new symmetrical duty cycle control in order to help the three-phase FCSC-rectifier to cope effectively with a wide range of frequency variations such as wild frequency variations.

Chapter 5. Control of the FCSC Converter for Variable-Voltage Variable-Frequency Applications

Based on the simulation results in Chapter 4, the three-phase FCSC-rectifier is proposed for employment as a PFC converter at a maximum frequency of 500 Hz in applications such as aircraft. The simulation results show that the three-phase FCSC-rectifier is able to improve the power factor to approximately unity, and can maintain the sinusoidal current waveform without zero crossing distortion problems. However, in aerospace applications, electrical voltage and frequency usually vary. The frequency range is called the 'wild frequency', with a range of 350-800 Hz. Therefore, the FCSC converter needs to be controlled to cope effectively with both frequency and voltage variations.

This chapter proposes symmetrical duty cycle control (SDCC) as the control method for the three-phase FCSC converter, in order to maintain high power quality performance over the complete range of frequencies and voltages. However, because this control technique represents a novel approach to the control of an FCSC circuit in stand-alone variable-voltage variable-frequency systems, the technique is initially presented and simulated on the single-phase topology for simplicity. This is followed by the application and simulation of this approach for the three-phase topology. The same technique is implemented practically using a DSP controller for the three-phase FCSC converter. A full assessment of this approach is presented in the final section of this chapter. The conclusion marks the key research contribution of this work.

5.1 Symmetrical Duty Cycle Control (SDCC) for the FCSC Converter

In general, the operating power factor of a generator can be improved by matching the effective capacitive reactance of the FCSC circuit to the generator's inductive reactance to mitigate the effects of the generator inductance. Symmetrical duty cycle control (SDCC) is a simple control method which does not require sophisticated calculations, and therefore it can be implemented with a low cost microcontroller. The principle of this method is based on the relationship between the effective reactance of the compensator as a function of the IGBT turn-off angle γ , as previously presented in equation (2-8). However, the new FCSC control

strategy can be applied by varying the switch ON time symmetrically around the maximum current point for an interval of δ degrees in line with the frequency variations this allows the FCSC circuit to maintain a high power factor over a wide frequency range [144, 145]. The control technique presented in this thesis is able to extend the range of frequencies over which the FCSC converter can operate effectively to maintain a higher power factor, in contrast with the previously proposed technique [30], which can be used with only a very small range of frequency variations, as explained earlier in section 2.5. Figure 5.1 illustrates how the SDCC technique offers a wider margin to control and vary the IGBT ON time and consequently the effective capacitive reactance when the frequency is varied. However, the previous approach presented in [30] allows only a limited margin for varying the ON times of the switches, since half of the active cycle is uncontrollable as the switch will always be ON. Therefore, by employing the SDCC in the FCSC circuit, the converter can be used in a system with a much wider frequency range of 50-500 Hz.

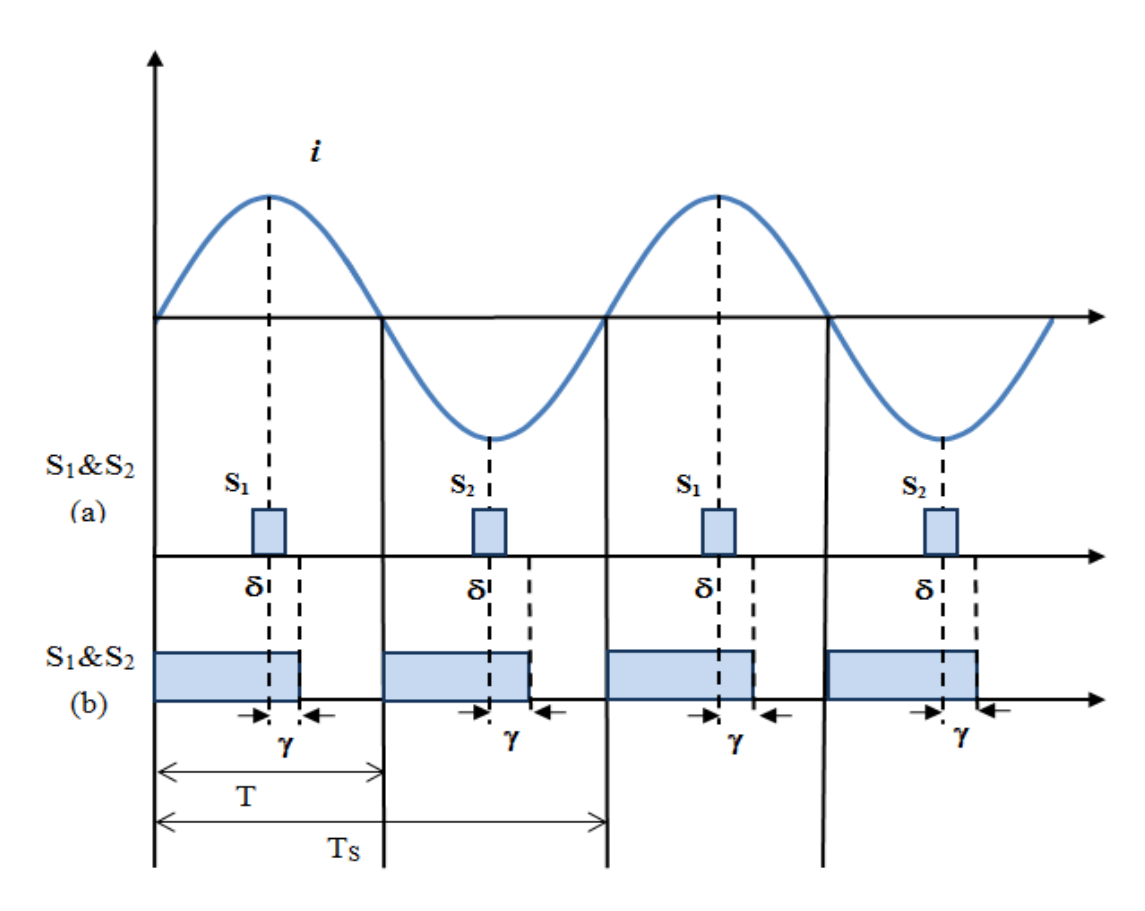


Figure 5.1 Turn-ON periods of FCSC switching devices: (a) SDCC technique (b) Previous technique In addition, this approach enables a simple calculation of the IGBT ON time using a new formula detailed in the following section, with no need to perform a pre-calculation of the value of γ as in the previous method.

In this section, the technique is first adopted for the single-phase FCSC-rectifier, and then it is applied to the three-phase circuit topology. In both cases, the converter is simulated under different frequency ranges, including a low frequency variations range of 1-5 Hz, and a medium frequency range with wider frequency variations 50-500 Hz.

5.1.1 Symmetrical duty cycle control for the single-phase FCSC converter

By turning each IGBT ON for a certain interval δ , which is symmetrically centred around the maximum current instant with a value of γ , the effective FCSC reactance can be controlled. The switching pattern of the IGBTs in the single-phase FCSC converter using symmetrical duty cycle control is also illustrated in Figure 5.1. In this pattern, each switch will be ON for a period T_{ON} , which is equal to 2γ , and both are symmetrical around the maximum current waveform.

The duty cycle (D), can be calculated as:

$$D = \frac{T_{ON}}{T} \tag{5-1}$$

$$T = \frac{1}{2} T_{\mathcal{S}} \tag{5-2}$$

where T_s represents the period of the generator output voltage. Equation (5-1) addresses the relationship between the duty cycle and the system's electrical frequency. Simply, this technique can be described as follows:

When the frequency varies, the inductive reactance changes in proportion to the frequency variation as expressed in the following equation:

$$X_L = 2 \pi F_S L_S \tag{5-3}$$

In order to achieve a high power factor, the effective compensating reactance needs to be varied in accordance with the frequency variations. This can be achieved by controlling the duty ratio of the IGBT switches in conformity with the new frequency value.

In this technique, the value of the series capacitance is chosen to match the generator inductive reactance at the maximum frequency of the operating spectrum, which is considered to be the resonance frequency f_r , and then the value of C_c can be determined from the following formula:

$$f_r = \frac{1}{2\pi\sqrt{L_S C_C}} \tag{5-4}$$

In order to maintain a high power factor when the operating frequency is reduced, the controller will increase the ON time of the switches to reduce the effective capacitive reactance X_{CC} . This is achieved by increasing δ , and therefore X_c is reduced in line with the reduction of X_L at the lower frequency. When the frequency is varied, the duty cycle (D) can be calculated from the following criteria:

$$D = \frac{(f_{max} - f)}{S} \tag{5-5}$$

where f_{max} represents the maximum frequency in the frequency spectrum, f is the new operating frequency, and S is the scaling factor. The scaling factor is a function of the frequency spectrum and its value can be determined according to Table 5-1.

Frequency variation range	Small frequency range 1-10 Hz	Medium frequency range 10-100 Hz	Large frequency range 50-1000 Hz	
Scale factor (S)	Scale factor (S)		1000	

Table 5-1 Scale factor as a function of frequency variations

5.1.1.1 Simulation results for the single-phase topology at various frequency ranges

In order to assess the symmetrical duty cycle control technique in both topologies with voltage and frequency variations, different frequency spectra are used. In this simulation, for comparison purposes, the relationship between the time constant τ and the generator operating frequency is maintained at a constant level when the frequency spectra are changed, in order to provide a reference for the assessment of circuit behaviour. At the minimum frequency this is in the range, τ = 3 T; however, for the maximum frequency it is τ = 15 T. In addition, since the input current of the single-phase rectifier is very sensitive to load variations, it is recommended that τ should be greater than T [7, 114]. This is accomplished by selecting appropriate values of R_L and C_L when the frequency spectrum is modified, since $\tau = R_L * C_L$. However, in actual aircraft systems the load value represented by R_L is dictated by passengers, and is predominantly based on the DC-loads fed by the FCSC converter, as previously discussed in Chapter 4.

1) Frequency range of 1-5 Hz

For low frequency spectrum applications such as in a wave energy converter, the simulation is carried out with the circuit parameters shown in Table 5-2. The parameters of the classical driver circuit used in all the simulations are similar to that of Table 4-3. In this simulation, the maximum voltage and frequency values are varied simultaneously, maintaining the ratio of V_s / F_s constant with a value of 100.

Circuit parameter	V _{S_max}	fs	Rs	L_s	C_C	C_L	R_L
Value	500-100 V	5 Hz-1 Hz	6.4 Ω	384 mH	2.63 mF	300 mF	10 Ω

Table 5-2 Circuit parameters at maximum frequency of 5 Hz

In the single-phase topology, the discharging capacitor time τ is maintained at a level larger than the frequency cycle in all frequency variations. Based on the above, the switches are permanently OFF at the maximum frequency of 5 Hz, which means that δ is zero as shown in Figure 5.2. This figure shows how the current is in-phase with the voltage waveforms when the IGBTs are permanently OFF at a maximum frequency of 5 Hz.

However, when the frequency is reduced, the controller should be adjusted to increase the switch ON time as δ is increased. By applying symmetrical duty cycle control, the single-phase FCSC converter is able to maintain a high power factor at various frequencies.

The generator current (i_s) , generator voltage (V_s) , series capacitor voltage (V_{cc}) , rectifier input voltage (V_{in}) , rectifier output current (i_R) , IGBT currents $(IGBT_1 \text{ and } IGBT_2)$, load current (I_L) and the switch timing signals $(S_1 \text{ and } S_2)$ waveforms (referred to in Figure 3.9) at different frequencies are given in the following figures.

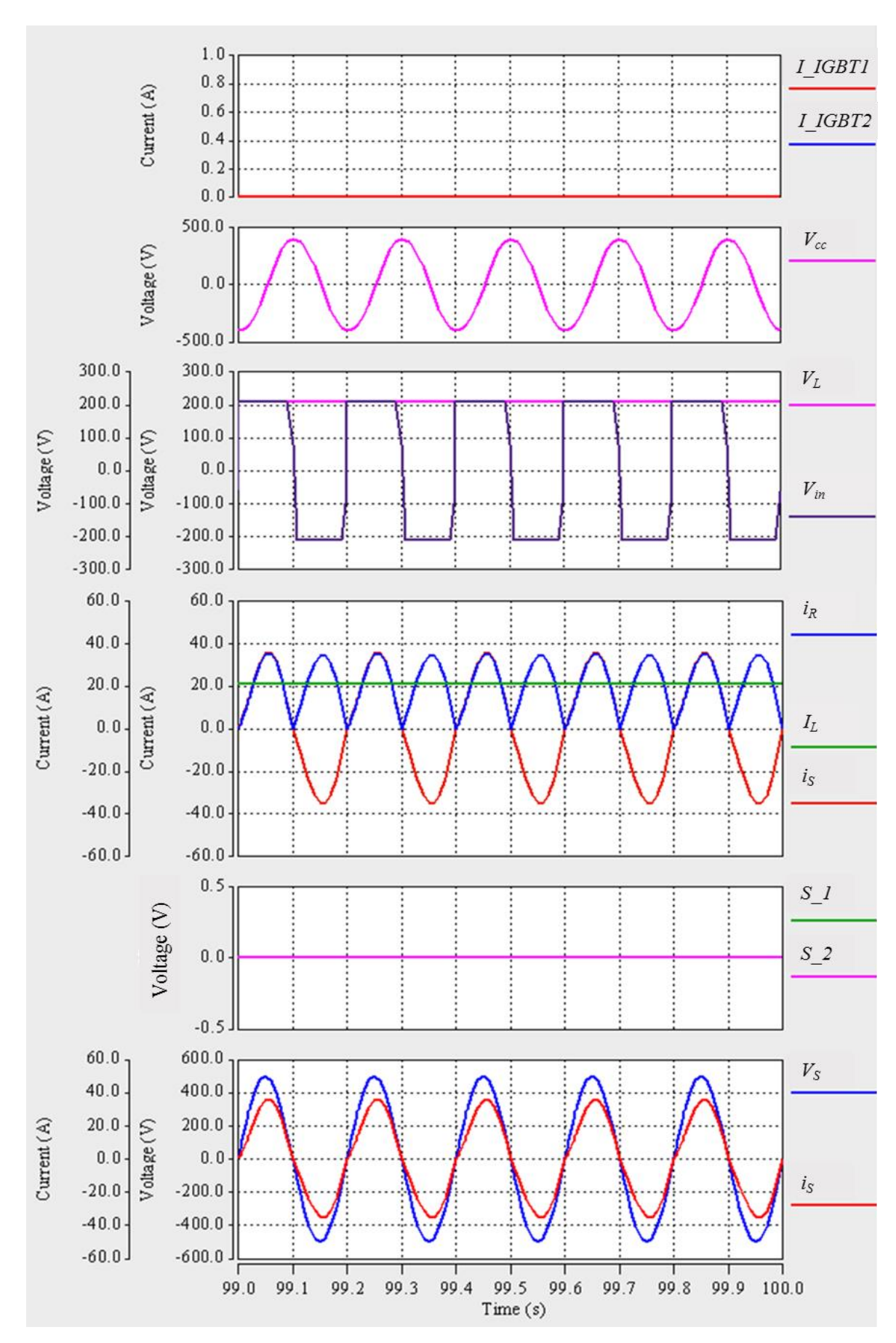


Figure 5.2 Single-phase FCSC converter waveforms at a frequency of 5 Hz

When the frequency is reduced to 4 Hz, the turn-off angle is increased to γ =18°, and each switch is ON for an interval of 25 ms. The input power factor is high and is equal to 0.993 lagging, as shown in Figure 5.3. In this figure, the results show that the voltage across the series capacitor Vcc is zero when the switches are ON. In addition, the peak rectifier output current is 27 A, which is similar to the peak of the input current i_s , and the average load current is 17 A which is equal to 0.9 Is (where Is represents the RMS value of the input current) according to the duality principle, which applies to a single-phase conventional rectifier circuit. The figure also shows that the rectifier input voltage is clamped by the value of the load capacitor voltage at 173 V. This means that the rectifier output voltage is reduced to 173 V even though the electric generator is supplying 400 V as a peak voltage. In addition, the transition of the rectifier input voltage from $-V_L$ to $+V_L$ is instantaneous without any overlap interval. This is because the current transition from diode D_I to D_3 and D_2 to D_4 is instantaneous and there are no conducting diodes at the same leg. This means that there is no commutation overlap interval when applying SDCC for the single-phase FCSC-rectifier, as shown in Figure 5.4.

As the frequency of the generated voltage waveform continues to be reduced to half of its maximum value, which is 2.5 Hz, the generator output voltage is reduced to 250 V. In this case, γ is increased to 45°, which increases T_{ON} to 100 ms, resulting in a power factor of 0.980 lagging, as shown in Figure 5.5. Figure 5.5 shows that by increasing the ON time of the switches, the converter is able to maintain a high power factor even at half the operating frequency, since the current is in-phase with the generator voltage waveforms. All other waveforms have the same behaviour, as explained above.

Figure 5.6 shows that the maximum ON time occurs when the frequency is reduced to the minimum value of 1 Hz with a γ value of 72°. In this case, the switch ON time is equal to 400ms. The figure demonstrates that the current waveform is slightly distorted, producing an operating power factor of 0.947 lagging.

By comparing all simulation results with the frequency reduction, the ripple in the output voltage is increased by reducing the frequency, which satisfies equation [113]:

$$f_r = \frac{V_{Smax}}{2 F_S R_L C_L} \tag{5-6}$$

where f_r is the ripple frequency of the output DC voltage, V_{Smax} represents the maximum input voltage and F_S is the generator output frequency.

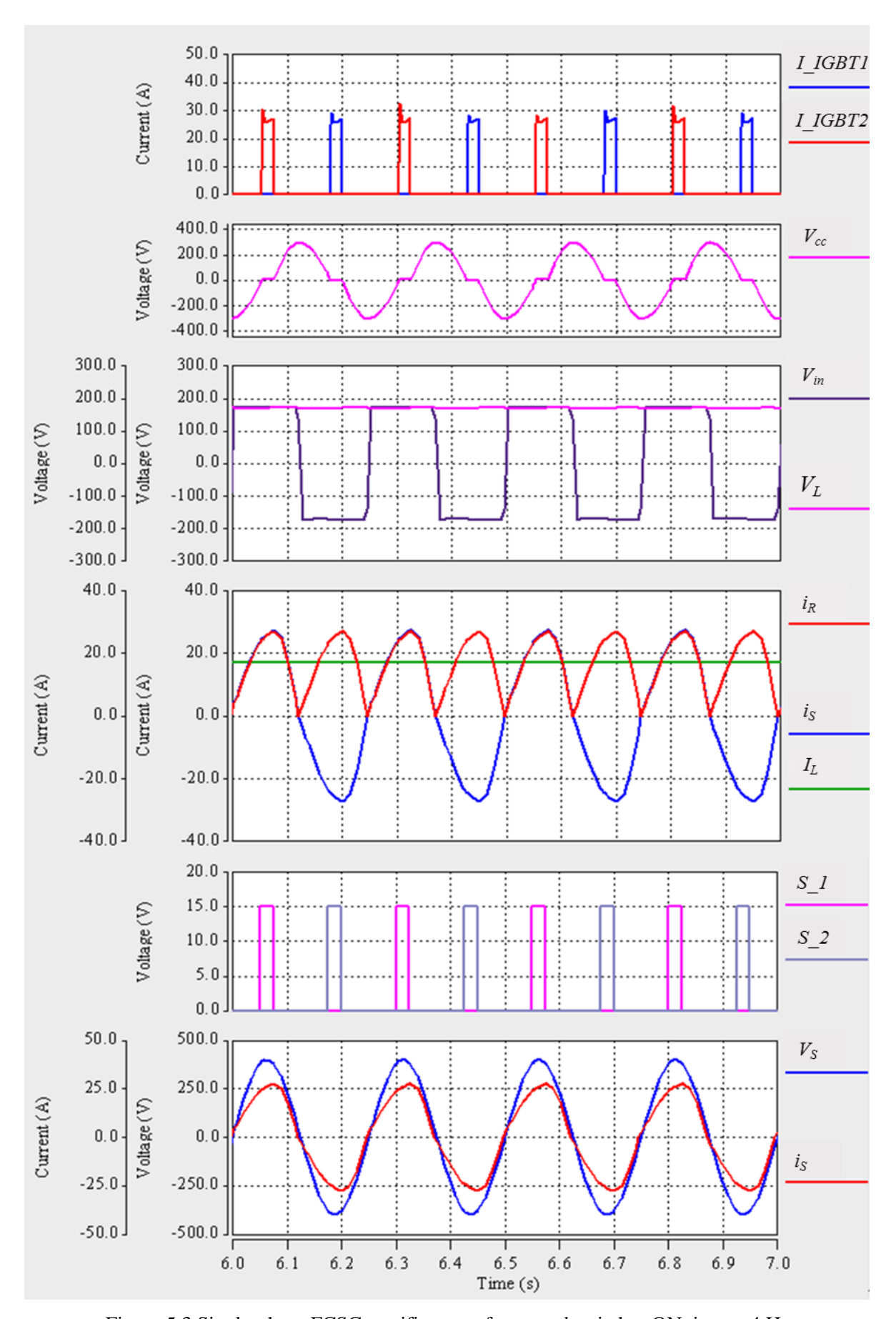


Figure 5.3 Single-phase FCSC-rectifier waveforms and switches ON time at 4 Hz

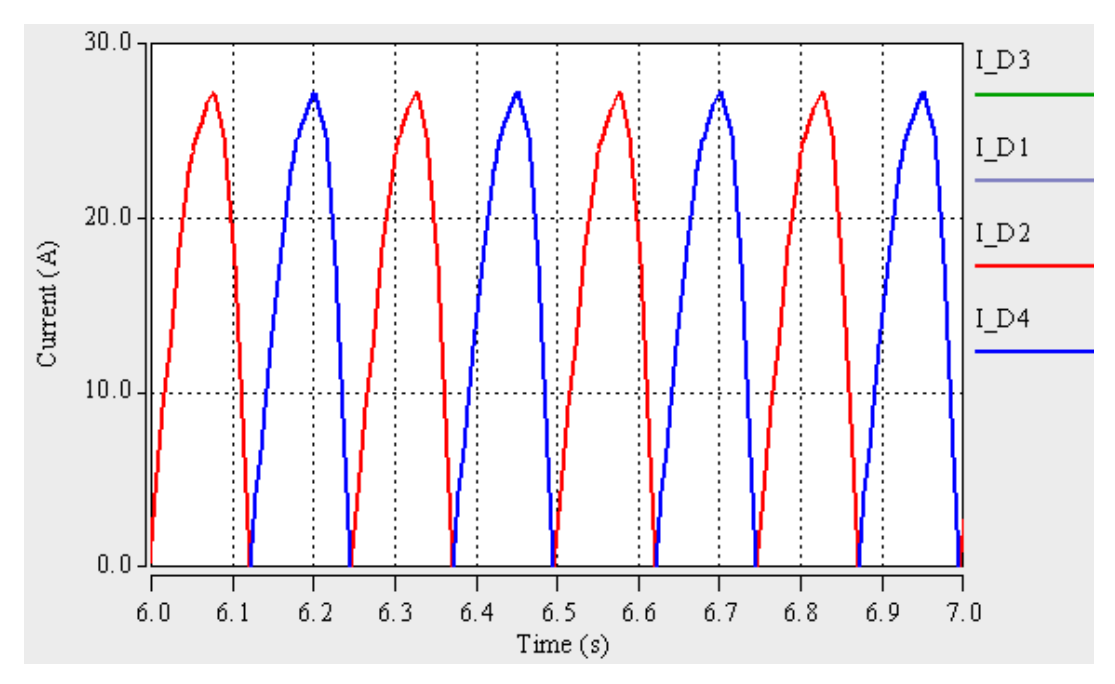


Figure 5.4 Diodes current transitions in single-phase FCSC-rectifier

To assess the impact of symmetrical duty cycle control on the performance of the single-phase FCSC, the power factor in terms of the distortion and displacement factor over the entire operating frequency range (1-5 Hz) is shown in Figure 5.7. The simulation results show that the controller can ensure a very high power factor over the entire range of frequency variations. This is achieved by maintaining the displacement factor at approximately unity, with little distortion over the range of operating frequencies.

In SABER, by using FFT analysis for one current waveform cycle with 1024 sample points and a rectangular widowing function, the corresponding percentage current total harmonic distortion (THDi) is calculated as shown in Figure 5.8. The figure shows that better values of THD are obtained at higher frequencies.

2) Frequency range of 50-500 Hz

To propose the FCSC-rectifier for employment in aircraft applications either in a single-phase or three-phase topology, symmetrical duty cycle control is used to control the FCSC-rectifier when interfacing with a generator with a variable frequency range of between 50-500 Hz in both topologies.

In this section, the maximum voltage and frequency are varied simultaneously, maintaining the ratio of V_m/F_s constant with a value of 1. The load circuitry is modified to maintain the relationship between T and τ as explained in the previous section.

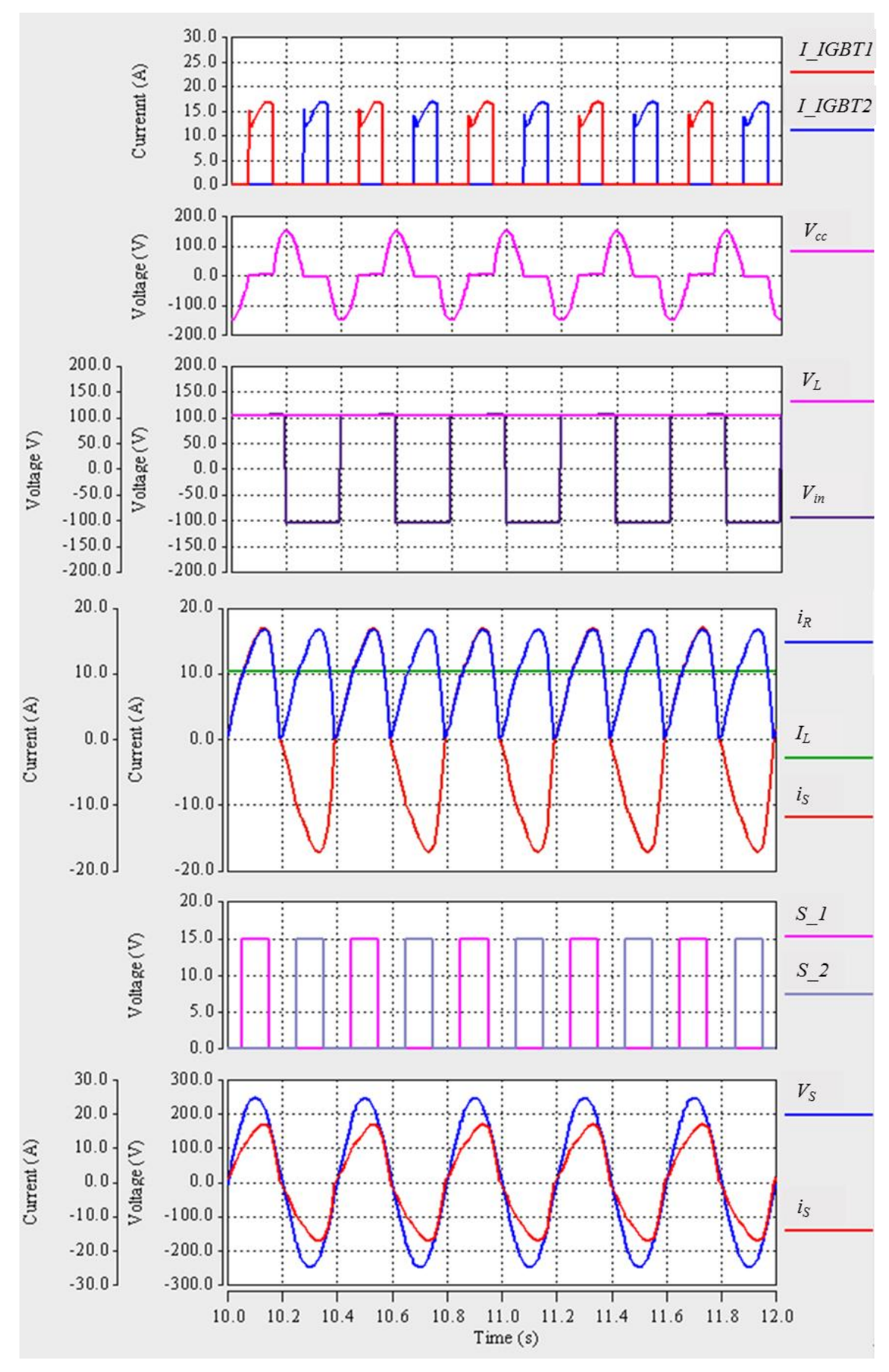


Figure 5.5 Single-phase FCSC-rectifier waveforms and switches ON time at $2.5~\mathrm{Hz}$ frequency

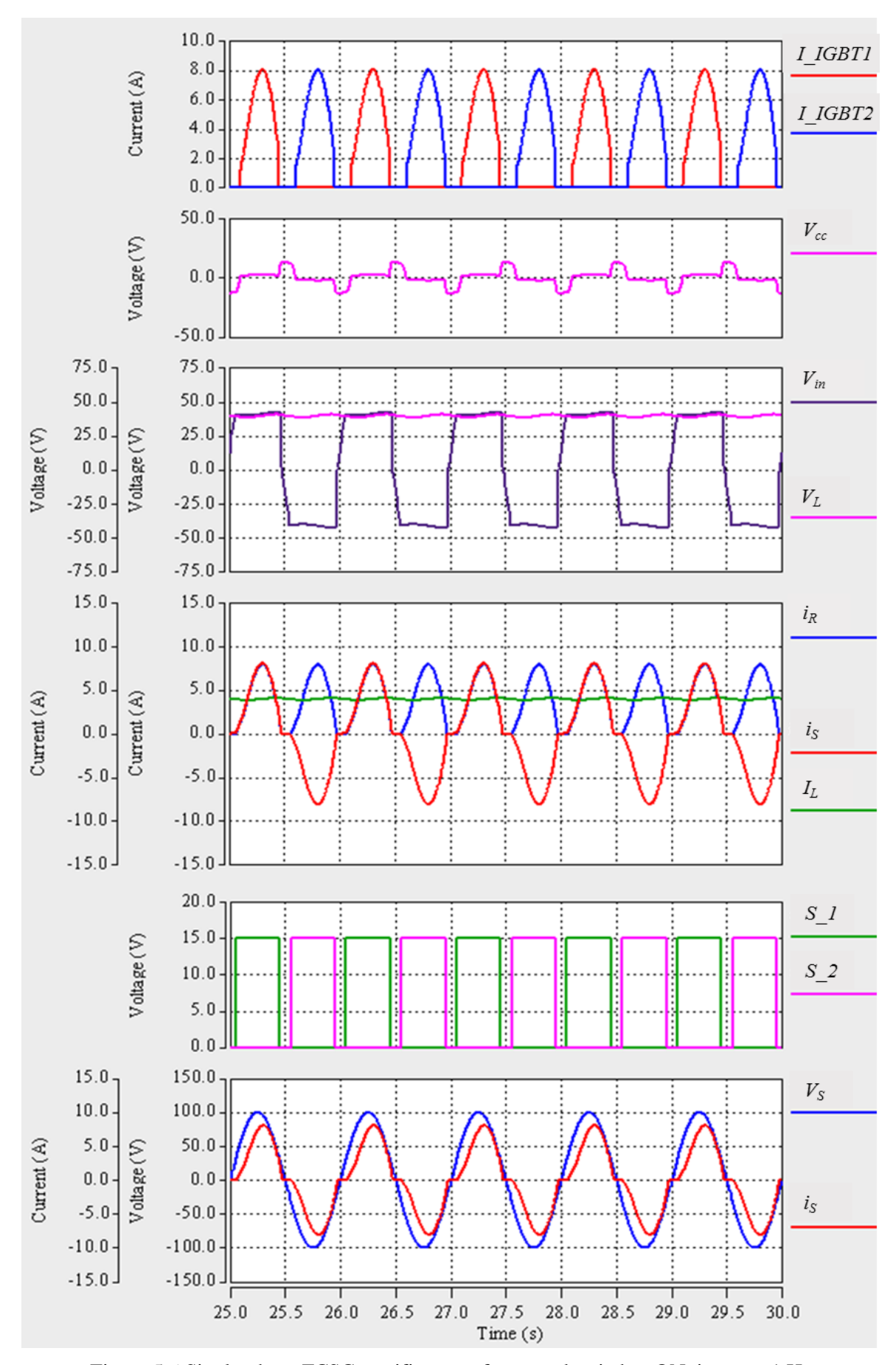


Figure 5.6 Single-phase FCSC-rectifier waveforms and switches ON time at a 1 Hz

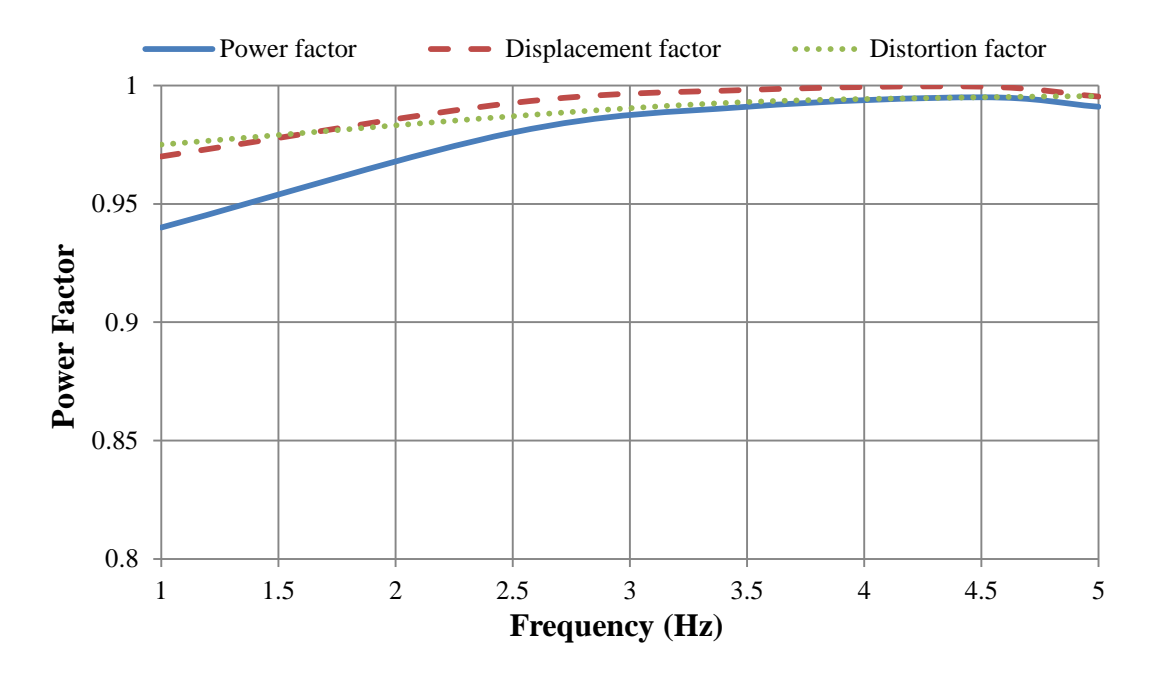


Figure 5.7 Power factor, distortion factor and displacement factor as a function of frequency variation of 1-5 Hz in a single-phase circuit

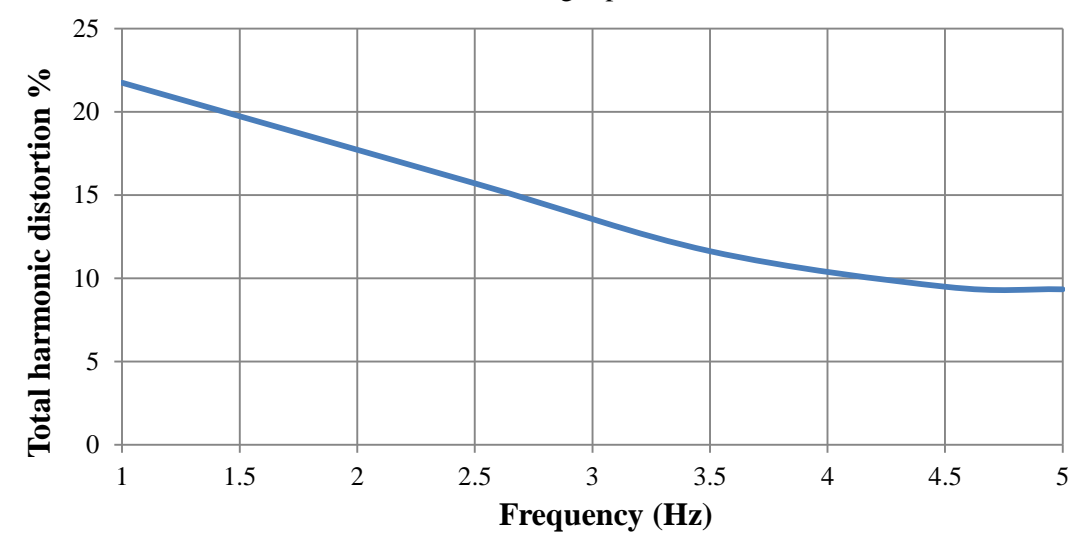


Figure 5.8 Single-phase converter total harmonic distortion as a function of frequency variation of 1-5 Hz in single-phase FCSC circuit

The simulation is carried out with the circuit parameters shown in Table 5-3.

Table 5-3 Simulation circuit parameters for a frequency range 50-500 Hz

Circuit parameter	V_{S_max}	F_S	Rs	L_s	C_C	C_L	R_L
Value	500-50 V	500Hz-50 Hz	2.45 Ω	13 mH	7.8 μF	1 mF	30 Ω

The reduction in load capacitance leads to an increase in the ripple content in the output voltage even at high frequency. However, the generator resistance and reactance are the same per phase PMA generator.

Figure 5.9 shows that the converter reactance is able to cancel out the effect of machine inductance at the maximum frequency of 500 Hz without any control action (γ is zero in this case); therefore, the input current is in-phase with the input voltage. Furthermore, the DC output voltage is reduced from 500 V to 352.24 V, and the same converter behaviour is achieved as previously in the low frequency spectrum. Similarly, the IGBTs ON time needs to be increased when the frequency is reduced to 400 Hz, to adjust the effective capacitive reactance to be equal to the reduced inductive reactance. Therefore, for both IGBT switches, the turn-off angle γ is increased in each half cycle of the generator voltage.

Figure 5.10 shows that the converter is able to maintain a high power factor, since the input current is in-phase with the input voltage and the current is sinusoidal. In addition, the average output DC voltage is 281 V, which is approximately equal to the input RMS value with a ripple component value of 2.844 V. All other voltage and current waveforms have the same behaviour similar to the waveforms presented earlier in the frequency range (1-5 Hz).

For further frequency reduction, the ON time should be increased. Figure 5.11 shows that, in spite of a slight distortion in the input current waveform, the controller is able to maintain the phase shift between the generator output voltage and the input current at equal zero by varying the IGBT turn-off angle at half of the frequency (i.e. 250 Hz). The figure also shows that the ripple component in the output voltage increases, which is to be expected due to the reduction in the supply frequency. In addition, the rectifier output current is also distorted slightly, since it is a function of the input current.

Moreover, the rectifier input voltage changes from $-V_L$ to $+V_L$ without any commutation overlap as in the small frequency spectrum case above. However, at the minimum frequency, which is 50 Hz in this case, the input current is significantly distorted although the controller is still able to adjust the phase shift between the input voltage and current waveforms to zero, as shown in Figure 5.12. A further increase in the ripple component over the DC output voltage is also achieved, with a value of 5.15 V.

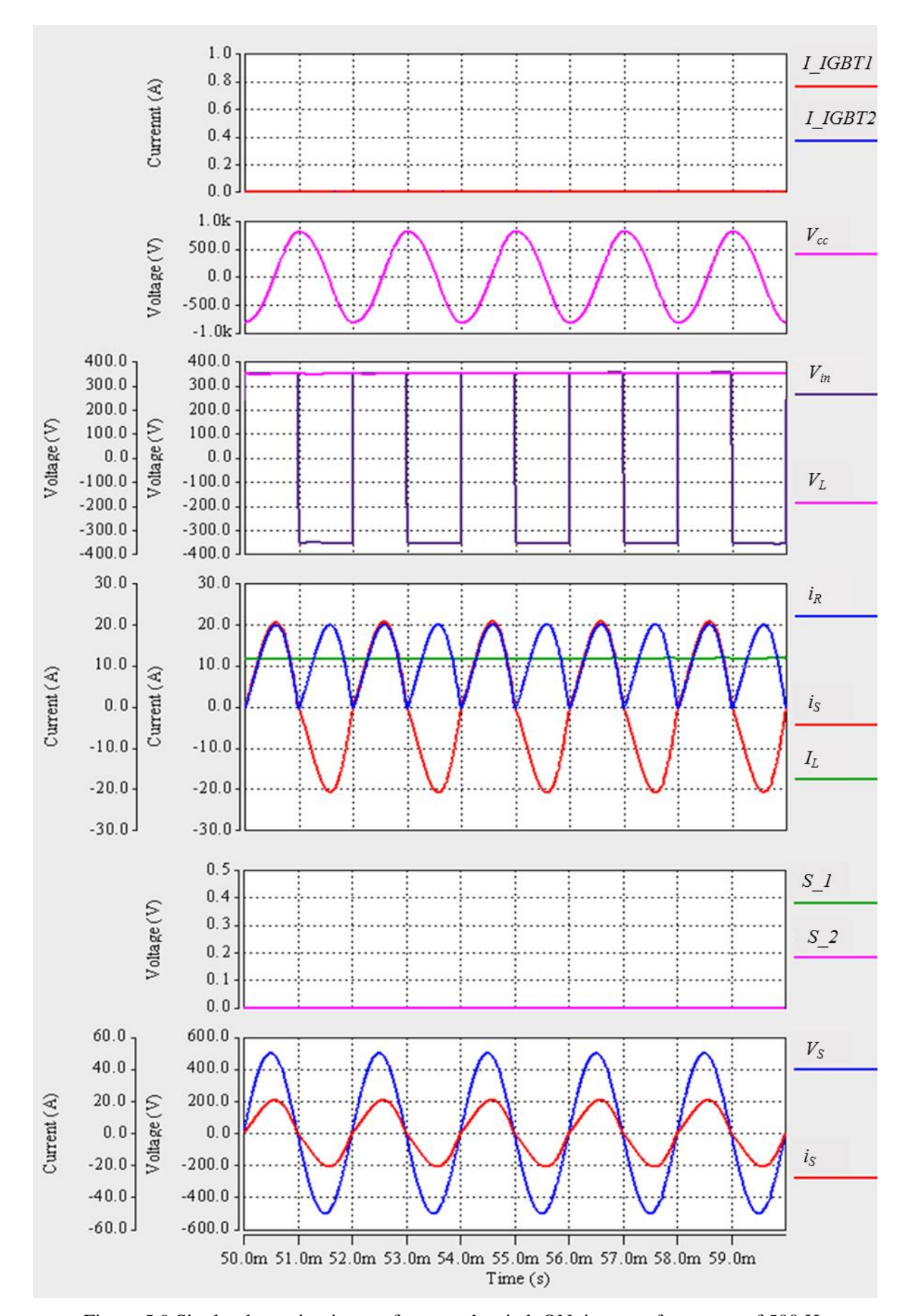


Figure 5.9 Single-phase circuit waveforms and switch ON time at a frequency of 500 Hz

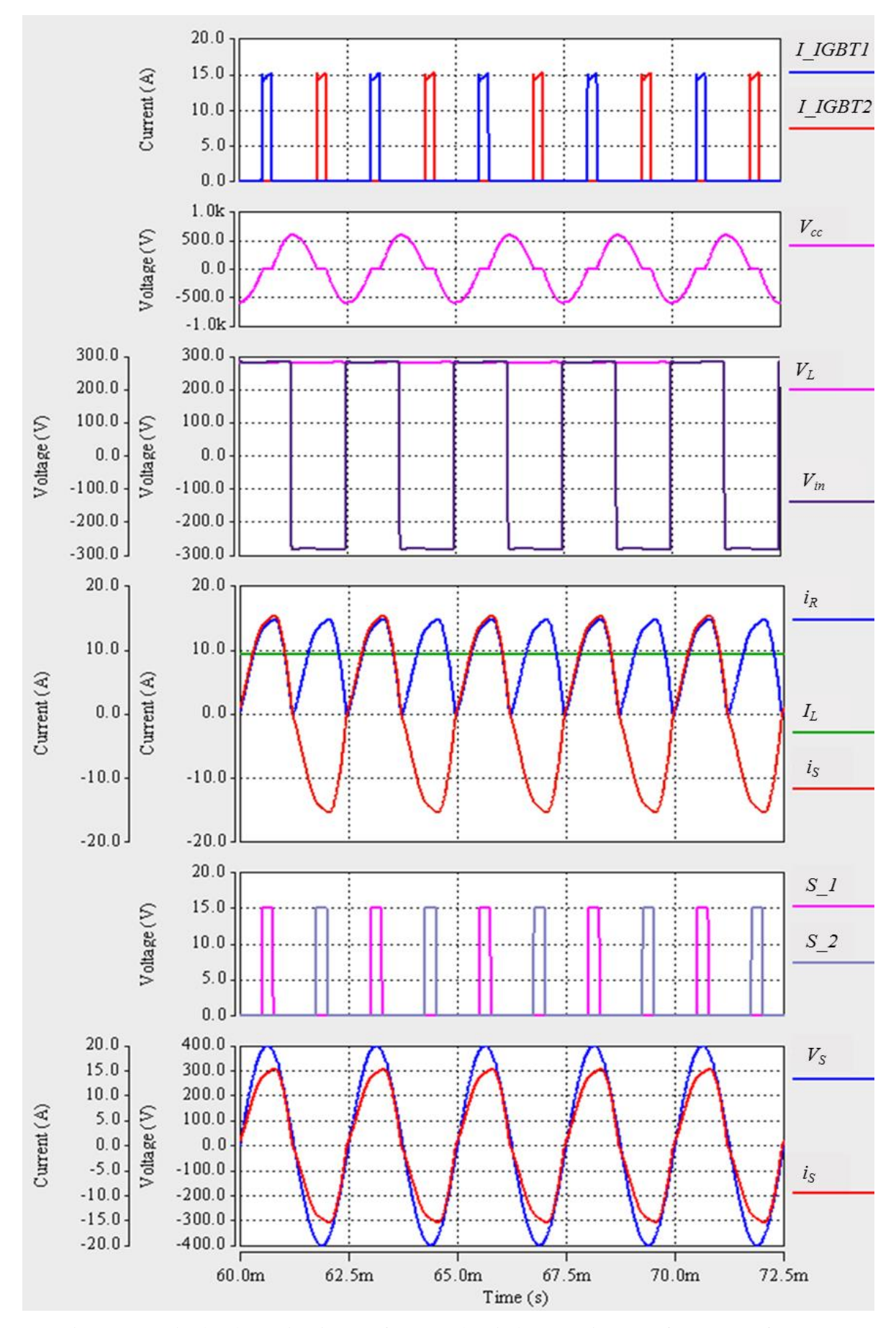


Figure 5.10 Single-phase circuit waveforms and switches ON time at a frequency of 400 Hz

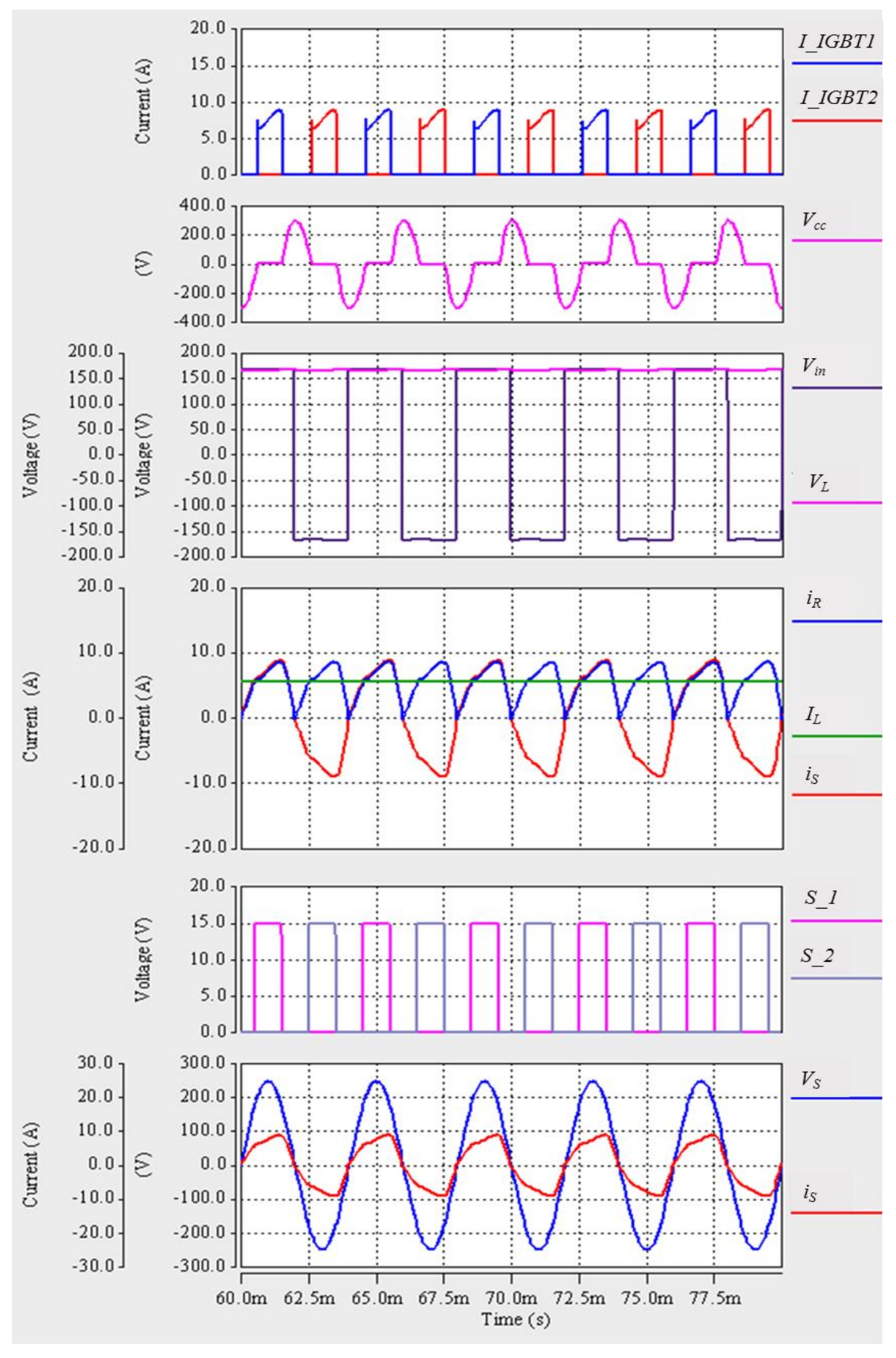


Figure 5.11 Single-phase circuit waveforms and switches ON time at a frequency of $250\ Hz$

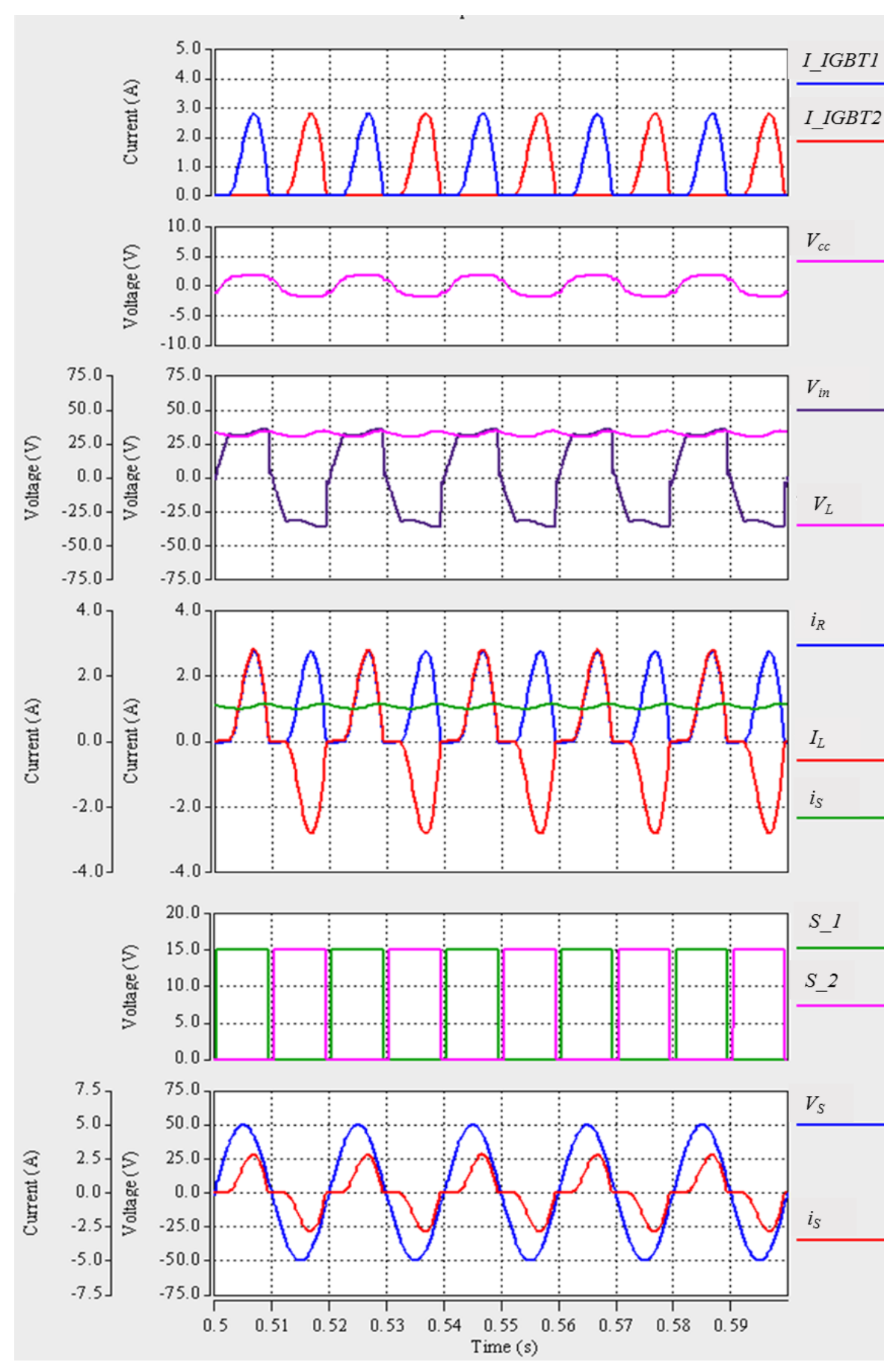


Figure 5.12 Single-phase circuit waveforms and switches ON time at a frequency of 50 Hz \$108\$

Also, to evaluate the overall performance of the single-phase FCSC converter when the frequency is varied between 50-500 Hz and the input voltage is reduced in line with this variation, the power factor in terms of the distortion and displacement factors is presented in Figure 5.13. The figure shows that the power factor is lowest at 50 Hz with a value of 0.835, and it increases to 0.99 at the maximum frequency driven by the increase in displacement factor. It should be mentioned that the displacement factor is reduced further in this frequency range, in comparison to the low frequency range of 1-5 Hz (shown in Figure 5.7). However, the power factor is still high.

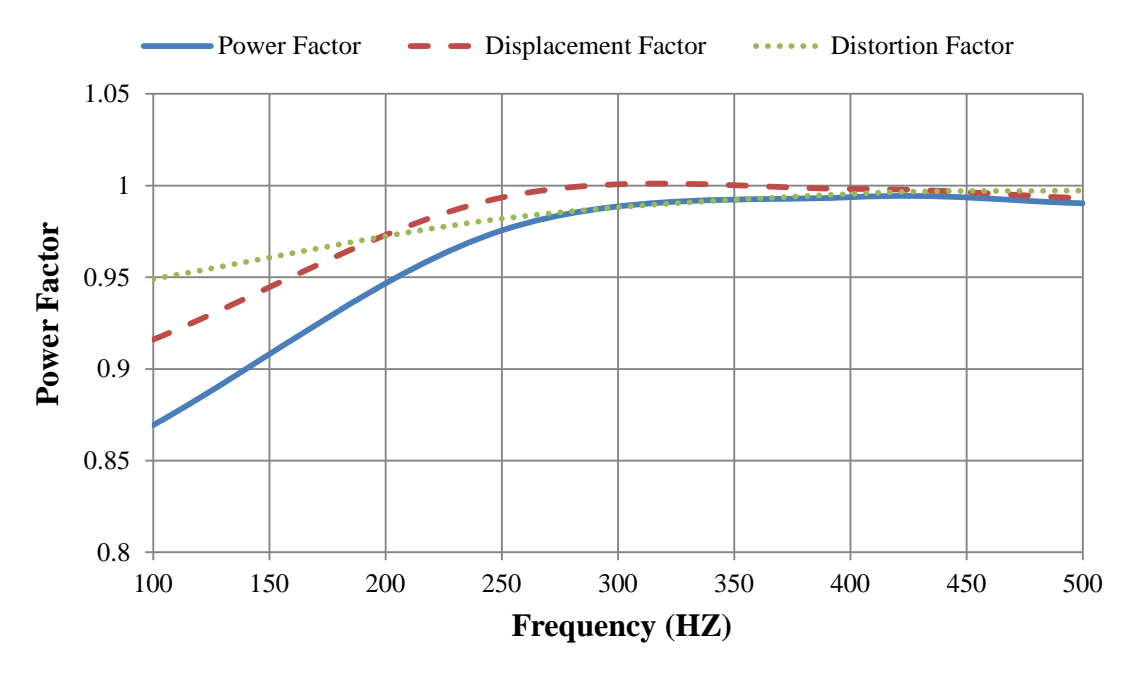


Figure 5.13 Power factor, distortion factor and displacement factor as a function of frequency variation of 50-500 Hz in single-phase circuit in single-phase FCSC circuit

The current total harmonic distortion is higher (by 41%) at lower frequency and reduces dramatically to 7% at the maximum frequency, as shown in Figure 5.14. Furthermore, it is worth noting that in both frequency ranges the current transition between diodes is simultaneous, which means that there is no commutation overlap interval.

5.1.2 Symmetrical duty cycle control for the three-phase FCSC converter

For the three-phase FCSC-rectifier, the aforementioned control technique is applied similarly to each pair of IGBT switches over the three phases while maintaining 120° has shift between the three phases. At the same time as retaining the phase shift, the switch ON time is

controlled in accordance with the variation in frequency for an interval of δ (in degrees), and therefore the value of γ is adjusted as a function of frequency.

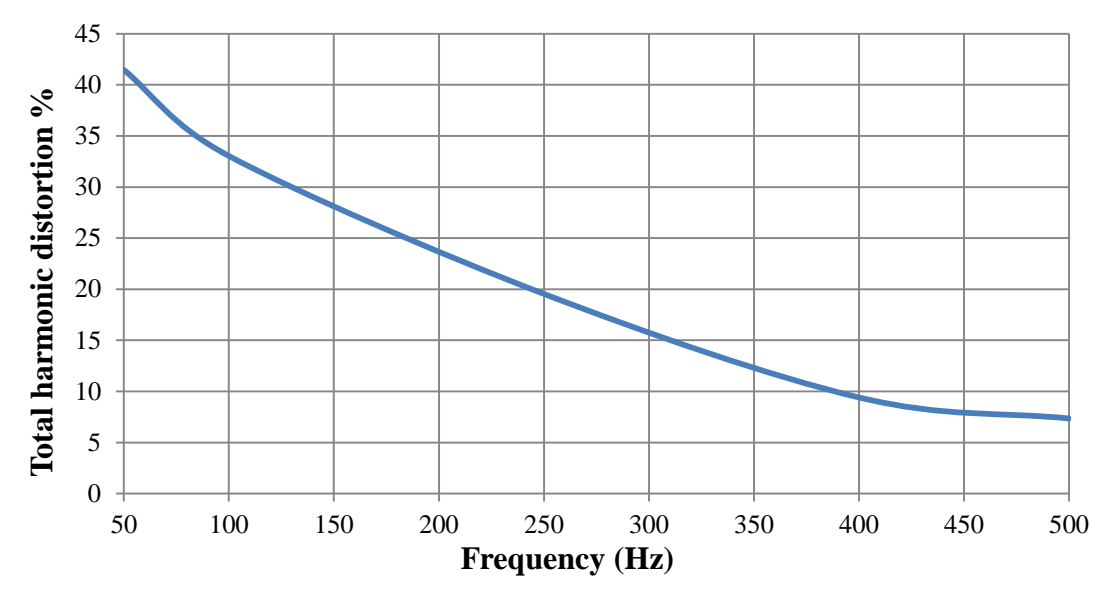


Figure 5.14 Total harmonic distortion as a function of frequency variation of 50-500 Hz in single-phase circuit in single-phase FCSC circuit

During the positive half-cycle of the three-phase generator voltage, the three active switches S_1 , S_3 and S_5 are ON for an interval of 2γ around the maximum current of each phase, with a phase shift of 120° between all three switches. The negative half-cycle of the three-phase voltages S_2 , S_4 and S_6 are ON for 2γ with a phase shift of 120° between them.

The same principle is used to select the value of series capacitance at maximum frequency as explained for the single-phase topology. Equations (5-1) and (5-5) are also used to determine the switch ON time in this topology.

5.1.2.1 Modes of operation of the three-phase FCSC-rectifier

By implementing the SDCC with the three-phase FCSC-rectifier, the circuit configuration changes periodically in accordance with the generator line-to-line voltage (V_{LL}). The reason for this is the change in the switch states and diode conducting times. The diodes conduct for 180° in the three-phase FCSC converter, as illustrated in Chapter 4. Assuming a balanced three-phase system, the three-phase electrical generator has identical values of internal resistance (R_s) and inductance (L_s) in all phases. Figure 5.15 illustrates the diode conducting time and switching pattern of all IGBTs in a three-phase FCSC-rectifier when each switch is held ON for 30° around the maximum instant of the generator voltages.

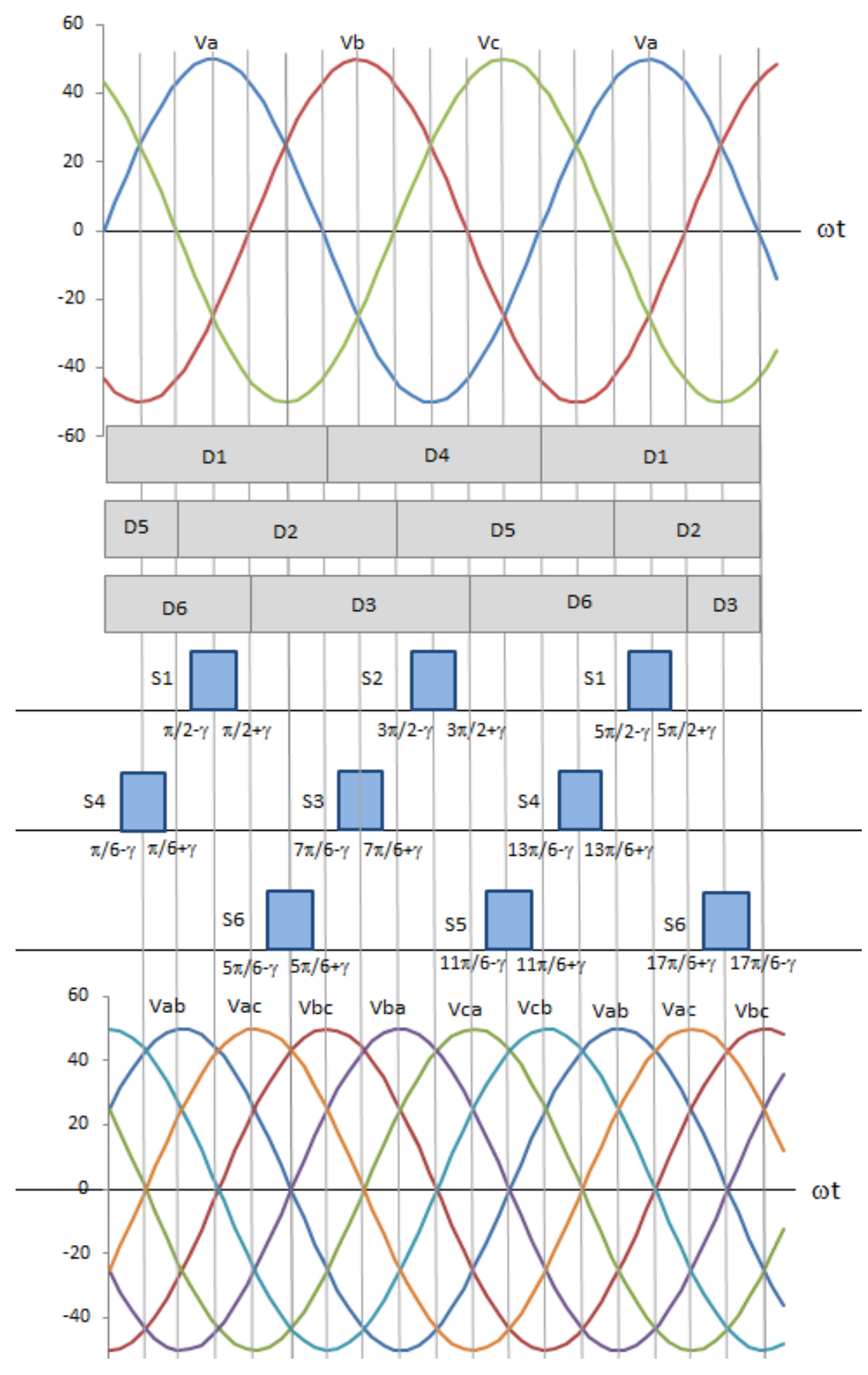


Figure 5.15 Diodes and switching states for three-phase FCSC-rectifier assuming γ equal $\pi/12$

The line-to-line voltages are changed every $\pi/3$. For one generator electrical cycle, there are 24 modes of operation as a function of the line-to-line voltage. However, for each $\pi/6$ of V_{LL} , there are two different circuit configurations. In the first circuit arrangement, the inductors of two phases are compensated by two series capacitors. However, the third phase inductor is uncompensated, as the series capacitor of this phase is shorted by closing the corresponding IGBT switch, as shown in Figure 5.16 (a). In the second circuit arrangement, all the phases are resonating, since the IGBT switches are OFF, and all FCSC capacitors are connected in series to the corresponding phase, shown in Figure 5.16 (b). In the next 30° (π /6) of the lineto-line voltage the two circuit configurations are repeated, with some differences. These include the change in the conducting diode and the uncompensated phase, illustrated in Figure 5.16 (c and d). For the next $\pi/3$ interval, the circuit configurations are repeated with a different order corresponding to V_{LL} . The figure illustrates that the circuit is operating in continuous current mode (CCM). In all modes of operation, the RC load is represented as a single unit for simplicity, which is driven by the load capacitor voltage (V_L) . This voltage represents the voltage across the smoothing capacitor in the rectifier DC side. Based on Figure 5.15, the modes of operation from $\pi/6$ to $\pi/2$ of the phase voltage, such as phase-a, are described as follows:

1) Mode 1: S_4 is ON, D_1 , D_5 and D_6 are conducting

This mode occurs when $\omega t = \pi/6$ to $\pi/6+\gamma$, the switch S_4 is ON and therefore the series capacitor in phase b is shorted. Three diodes conduct at the same time, as shown in Figure 5.17. This figure shows the simplified system model, where the two phases a and c are connected through the conducting diodes D_I and D_5 . Since the series capacitors in both phases a and c are connected, they are able to compensate both inductors in phases a and c. This is because X_c is adjusted by the controller to be equal to X_L through the application of SDCC. In such a case, the voltage drop will be across R_s only and therefore the system model can be simplified by omitting both C_c and L_s .

According to the duality concept, the system is similar in principle to the rectifier connected to a stiff sinusoidal current with a peak value of I_{max} and angular frequency of $\omega=2\pi f_s$. The three-phase currents can be expressed as:

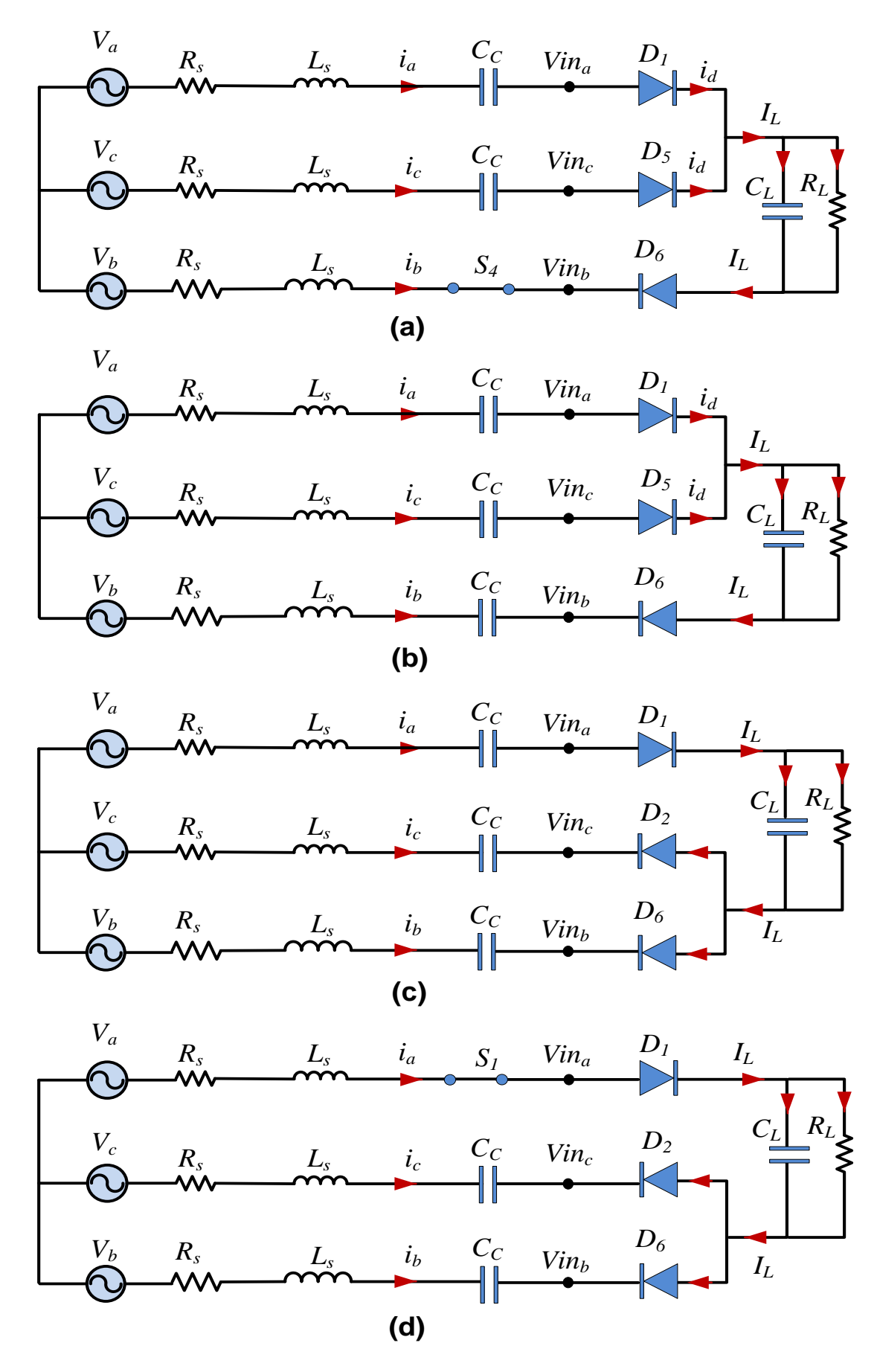


Figure 5.16 Equivalent circuit of three-phase FCSC converter as a function of V_{ab}

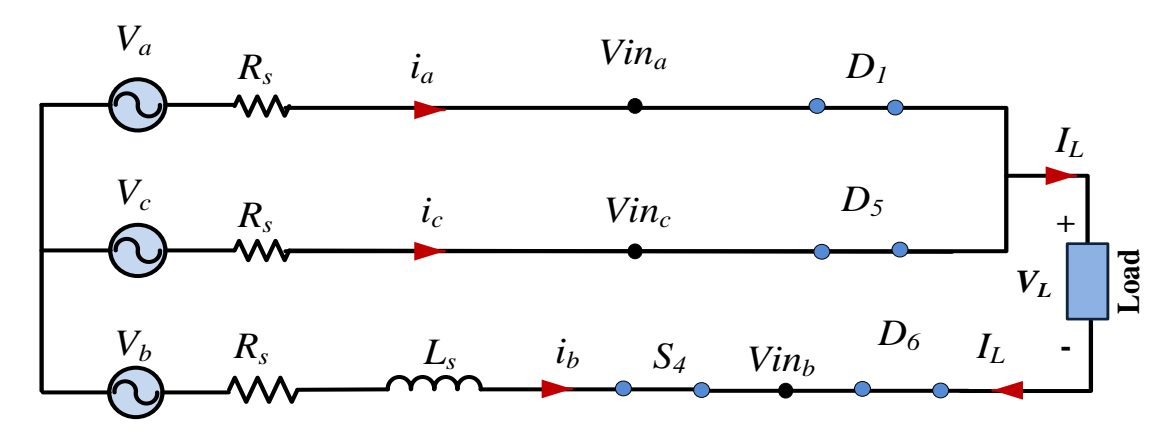


Figure 5.17 A simplified system model with the three-phase FCSC converter during mode 1

$$i_a = I_{max} \sin(\omega t) \tag{5-7}$$

$$i_h = I_{max} \sin(\omega t - 2\pi/3) \tag{5-8}$$

$$i_c = I_{max} \sin(\omega t - 4\pi/3) \tag{5-9}$$

In this interval, the system can be described as:

$$Vin_{ac} = Vin_a - Vin_c = 0 (5-10)$$

$$V_{dc} = V_L = I_L \times R_L \tag{5-11}$$

Using KVL and KCL

$$Vin_{cb} = Vin_c - Vin_b = V_{dc} (5-12)$$

$$I_L = i_a + i_c \tag{5-13}$$

$$I_L = -i_b \tag{5-14}$$

2) Mode 2: all IGBTs are OFF, and D_1 , D_5 and D_6 are conducting

This subinterval starts from $\omega t = \pi/6 + \gamma$ to $\pi/3$. Since all the IGBT switches are OFF, the voltage across the inductor in all three phases is compensated by the series capacitor and therefore the circuit model can be described as in Figure 5.18. The same diodes remain conducting in this subinterval. Therefore, the rectifier input voltage (Vin_{LL}) and the relationship between load current and the rectifier input current in all phases is similar to those in mode one and equations (5-11)-(5-14) can be used in this mode as well.

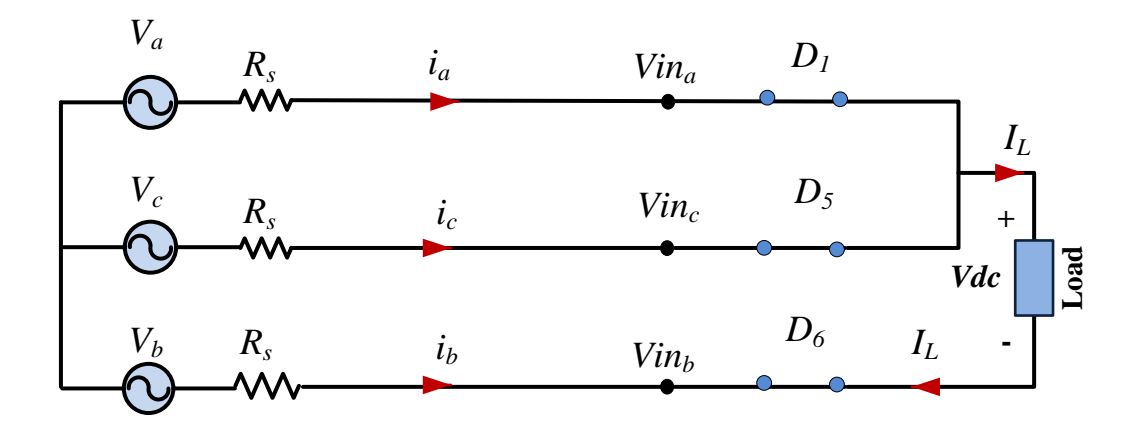


Figure 5.18 A simplified system model with the three-phase FCSC converter during mode 2

3) Mode 3: all IGBTs are OFF, and D₁, D₂ and D₆ are conducting

This mode occurs between $\omega t = \pi/3$ to $\pi/2$ - γ . When the line-to-line voltage (V_{ab}) reaches its peak value, all the IGBT switches remain OFF. However, the current commutates between two diodes which are located in the same leg of the rectifier. In other words, the current commutates from D_5 to D_2 , and D_6 continues in its conducting state in this subinterval. Figure 5.19 shows the system model for this interval with the three compensated phases. In this mode, the fundamental voltage relationships are:

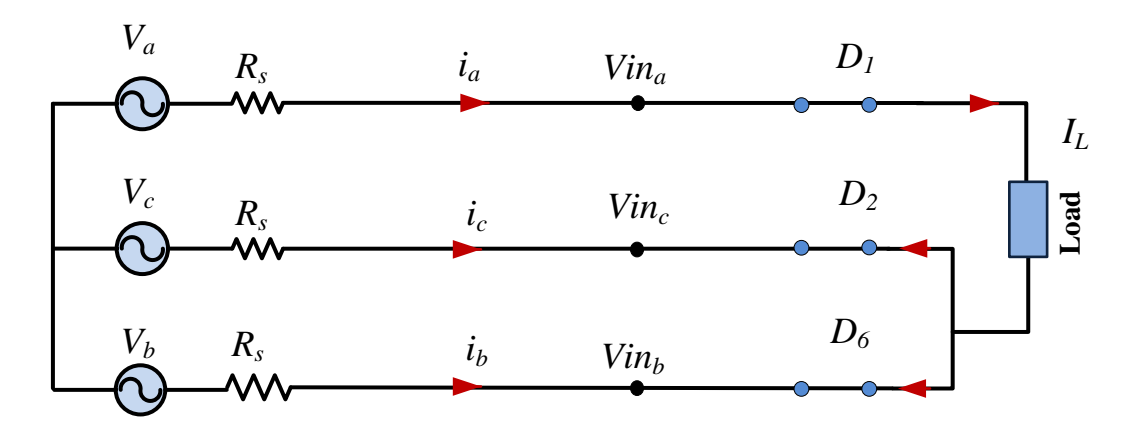


Figure 5.19 A simplified system model with the three-phase FCSC converter during mode 3

$$Vin_{cb} = Vin_c - Vin_b = 0 (5-15)$$

$$Vin_{ac} = Vin_a - Vin_c = V_{dc} (5-16)$$

$$I_L = -(i_c + i_b) (5-17)$$

$$I_L = i_a \tag{5-18}$$

4) Mode 4: S_1 is ON, and D_1 , D_2 and D_6 are conducting

From $\omega t = \pi/2 - \gamma$ to $\pi/2$, phase-*a* is uncompensated since S_1 is ON, while phase b and c are fully compensated and the same diodes are conducting. Again equations (5-15)-(5-18) can be used to express the relationships in this subinterval.

These modes are repeated six times in different orders in accordance with the line-to-line voltage and the active IGBT switch. The above modes clearly show that the rectifier input voltages (Vin_{LL}) vary according to the line-to-line generator voltages. The values of Vin_{LL} change between + V_L , zero and - V_L and vice versa. This complies with the duality concept, since the input current is varying from $-I_d$ to $+I_d$ and vice versa in the conventional diode bridge rectifier with series RL load supplied from a sinusoidal voltage source.

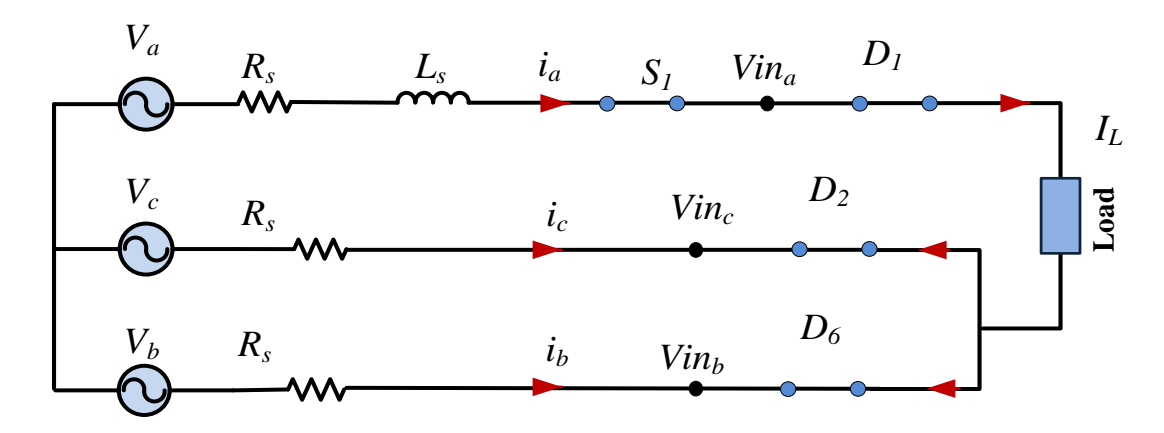


Figure 5.20 A simplified system model with the three-phase FCSC converter during mode 4

5.1.2.2 Simulation results for three-phase FCSC-rectifier

Following the same procedure as that used for the single-phase FCSC-rectifier, the three-phase FCSC converter performance and behaviour are simulated for two frequency spectra in order to determine if the three-phase FCSC converter is suitable to employ in wave energy converter and aircraft applications. Therefore, a small frequency range with narrow frequency variations, which is between 1-5 Hz, and a medium frequency range with a wider frequency variation of 50-480 Hz are investigated in this section. Again, as the system is assumed to be balanced, most of the results are presented for phase-*a* only since current and voltage waveforms for other phases will be identical with a phase shift of 120°.

1) Frequency range of 1-5 Hz

In this simulation, the same electric linear generator parameters as presented previously in Table 5-2 for the direct drive wave energy converter are used to simulate the three-phase FCSC in such an application.

Figure 5.21 shows the circuit waveforms at the maximum frequency of 5 Hz when all IGBT switches are permanently OFF. The power factor is as high as 0.999 with an output voltage of 379 V and an RMS voltage in phase-a of 353.55V. The rectifier input voltages (V_{in}) are clamped by the output load voltage (V_L) to a maximum value of 379V, and the rectifier output current (i_R) consists of six pulses for one cycle of generator voltage. Again, based on the duality concept, the average load current I_L is equal to 37.9 A, and this complies with (4-11) as derived in Chapter 4, as the RMS current in phase-a is equal to 28 A. The series capacitor voltage (V_{cc}) is sinusoidal due to the OFF state of the IGBT switches.

Since the frequency and voltage are reduced together, as explained earlier, the IGBT switches need to be ON for 2γ . The turn off angle γ is increased with the frequency reduction to reduce the effective converter capacitor reactance in line with the reduction in the generator inductive reactance. By applying symmetrical duty cycle control for the three-phase FCSC converter connected to a linear transverse flux linear generator, the converter is able to maintain a high power factor of around 0.9 at all frequencies in addition to achieving a smooth output voltage, as shown in Figure 5.22- Figure 5.24. However, this electrical generator suffers from a very poor power factor of approximately 0.35 lagging when operating with the three-phase rectifier only. The voltage across the series capacitor is zero as long as the IGBT switches are in the ON state. Identical rectifier input voltage and rectifier output current behaviour is achieved at all frequencies. Furthermore, the current distortion is increased at the lower frequency of 1 Hz. In this low frequency spectrum, where the frequency varies between 1-5 Hz, the power factor in terms of distortion and displacement factors at different frequencies is shown in Figure 5.25.

The figure shows that the power factor is kept high as both distortion and displacement factors are high. A slight reduction in power factor occurs at the minimum frequency of 1 Hz, driven by slight reductions in both the distortion and displacement factors.

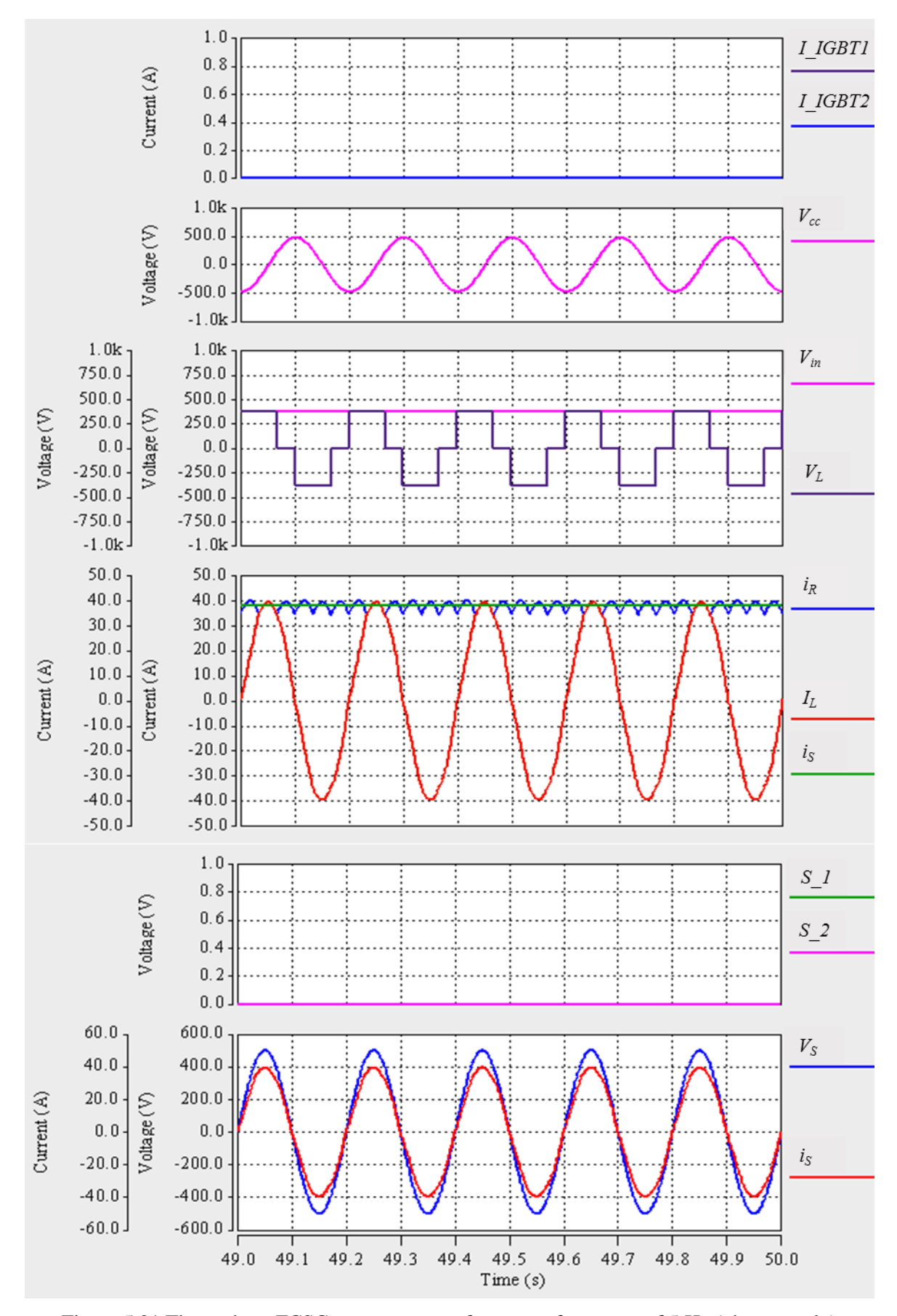


Figure 5.21 Three-phase FCSC converter waveforms at a frequency of 5 Hz (phase-a only)

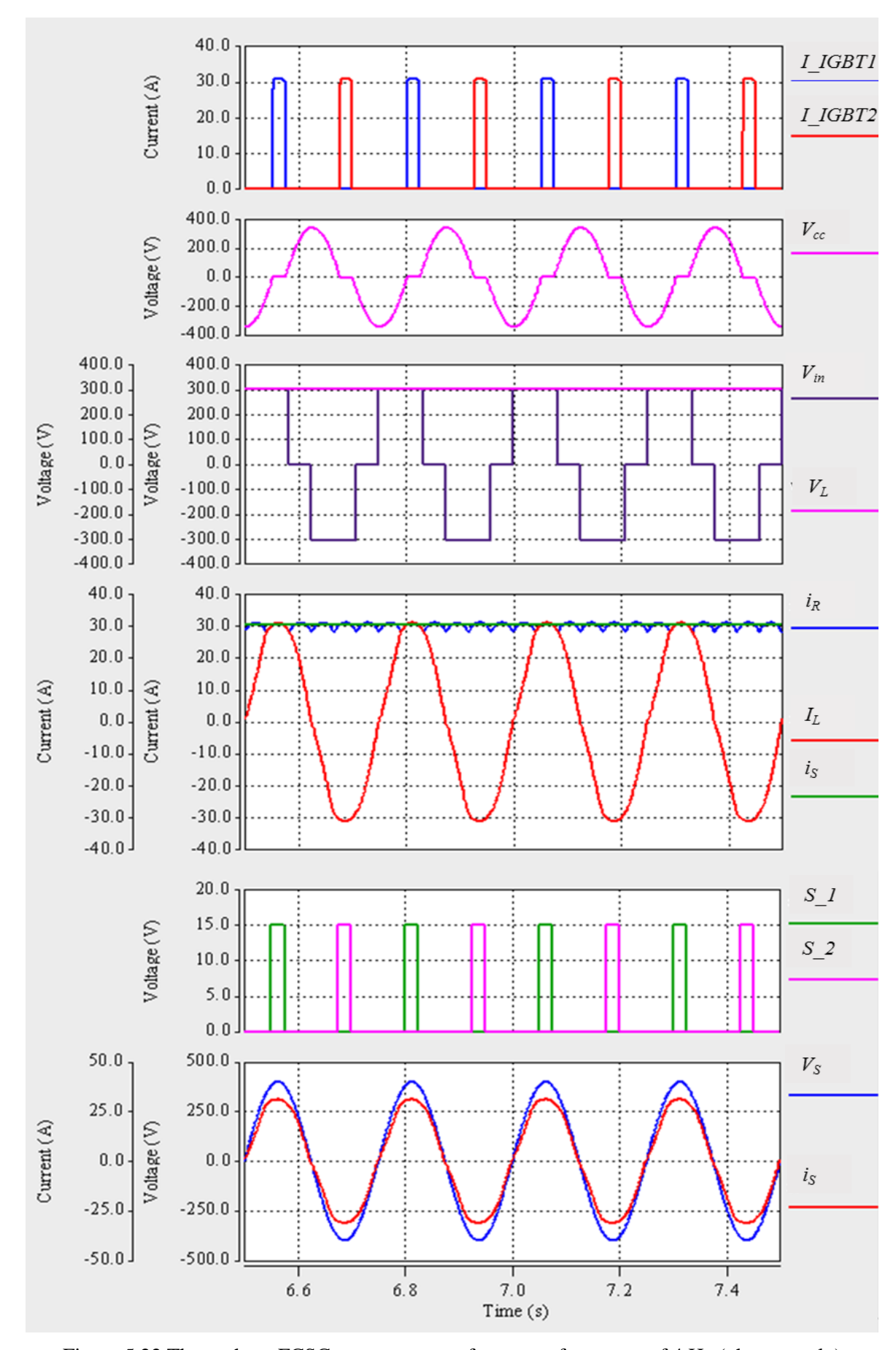


Figure 5.22 Three-phase FCSC converter waveforms at a frequency of 4 Hz (phase-a only)

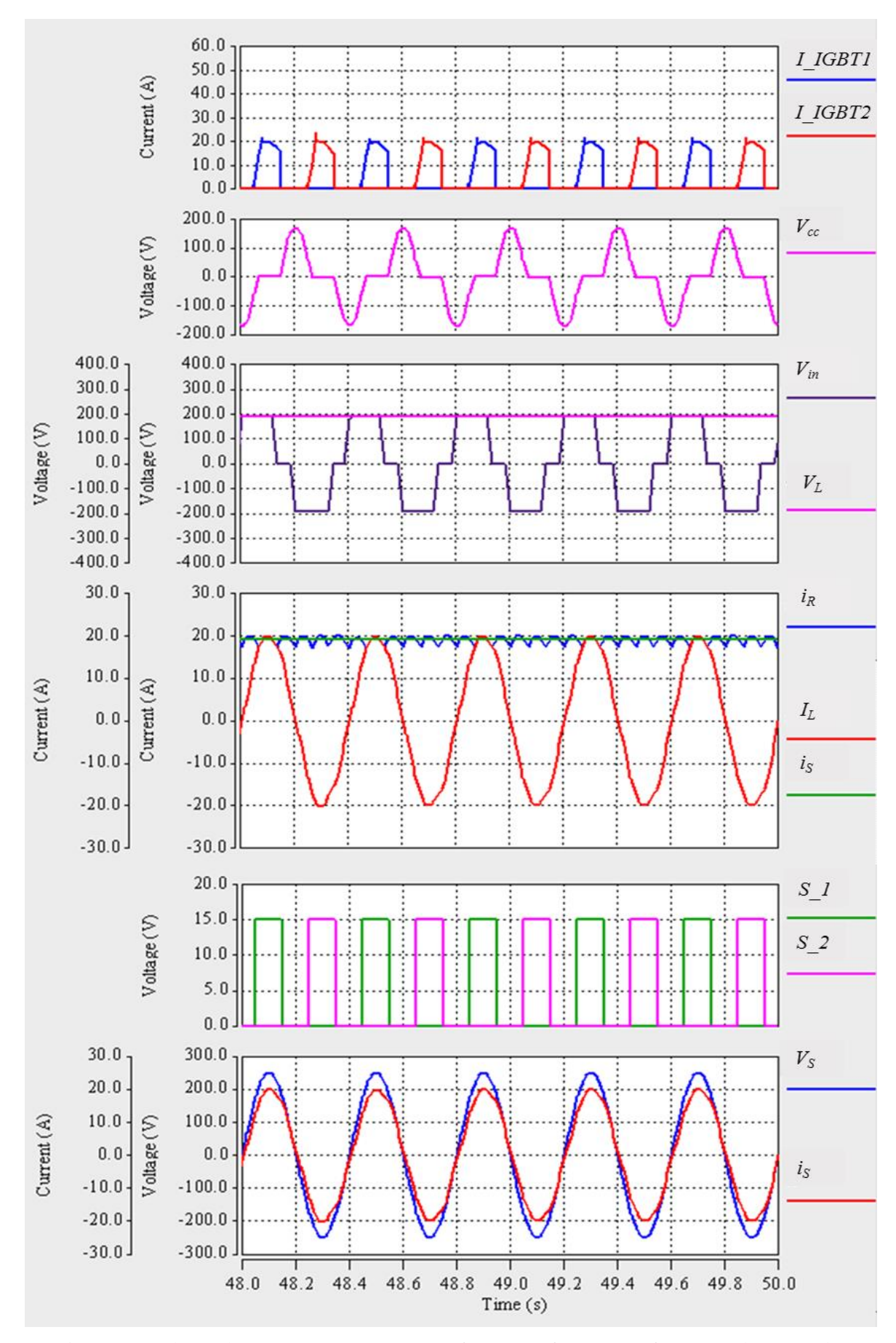


Figure 5.23 Three-phase FCSC converter waveforms at a frequency of 2.5 Hz (phase-a only)

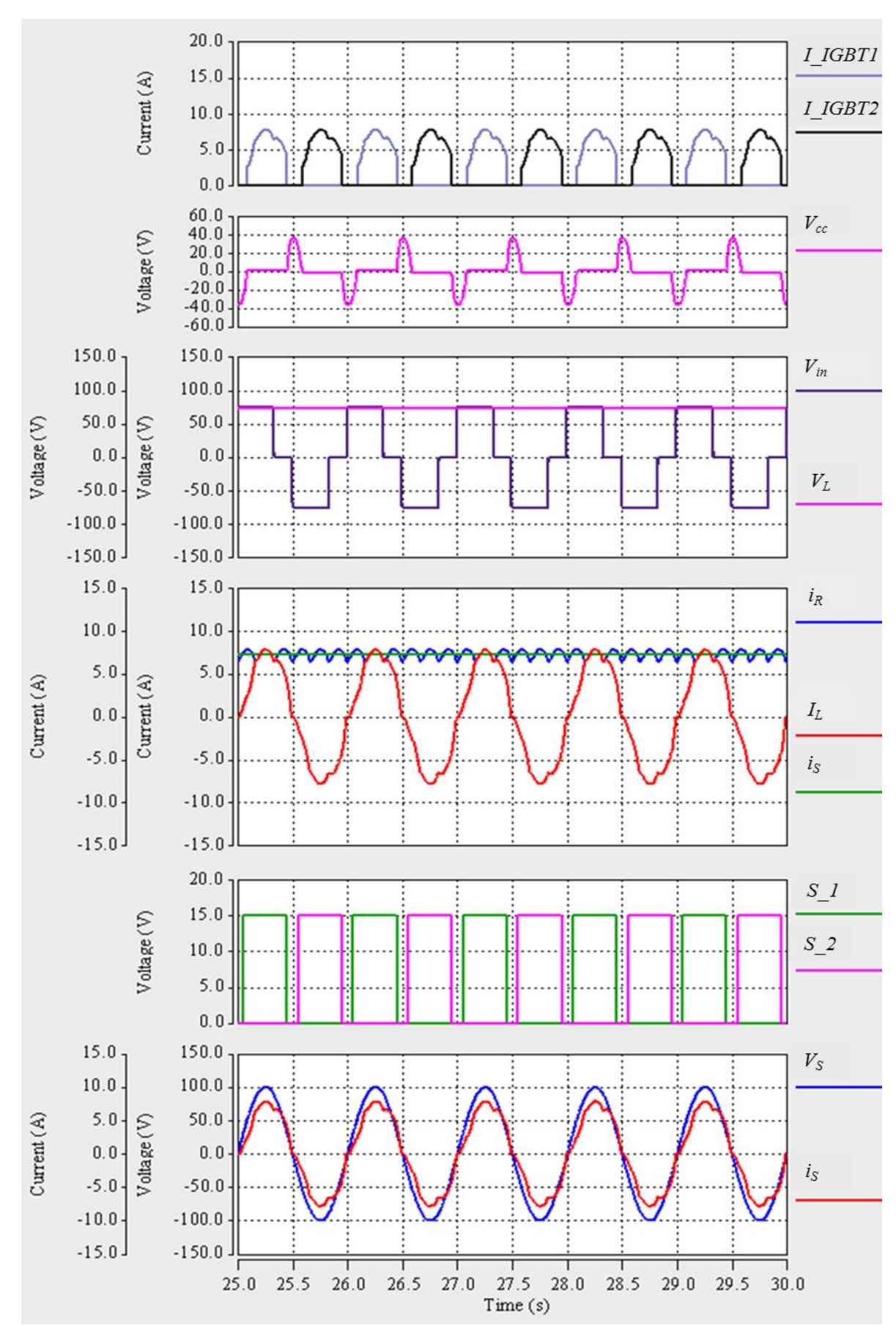


Figure 5.24 Three-phase FCSC converter waveforms at a frequency of 1 Hz (phase-a only)

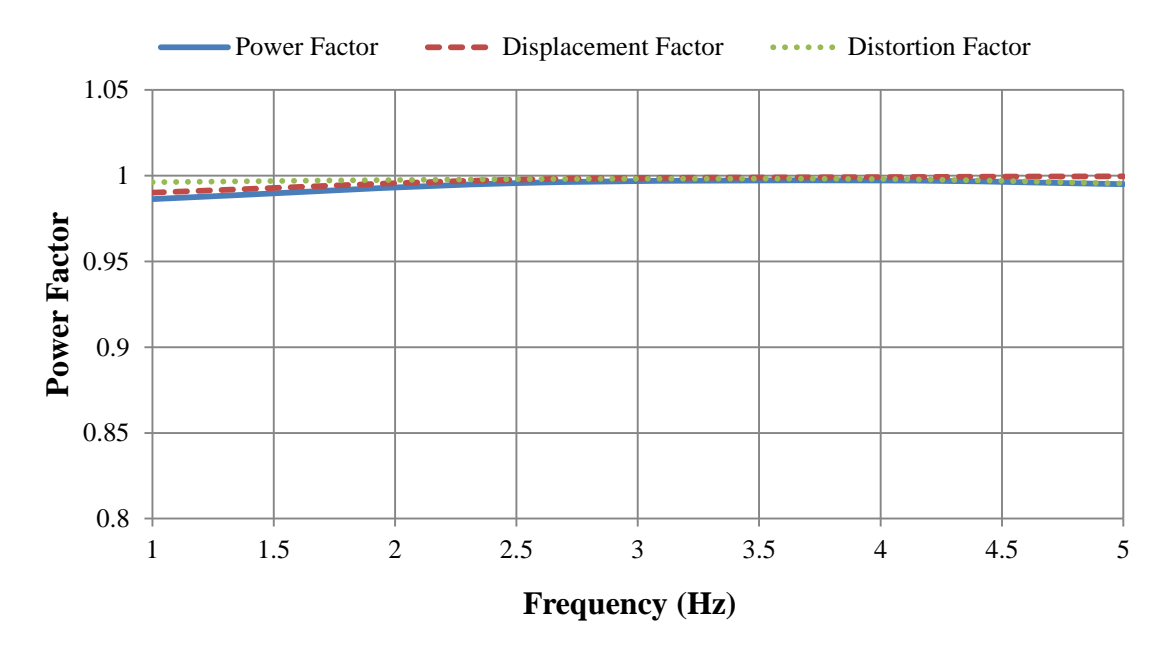


Figure 5.25 Power factor, distortion factor and displacement factor as a function of frequency variation of 1-5 Hz in the three-phase FCSC circuit

The percentage total current harmonic distortion is calculated by performing FFT with a rectangular window function. A lower current harmonic distortion is achieved at the maximum spectrum frequency of 5 Hz with a maximum harmonic distortion of 8.35% at the minimum frequency, as shown in Figure 5.26.

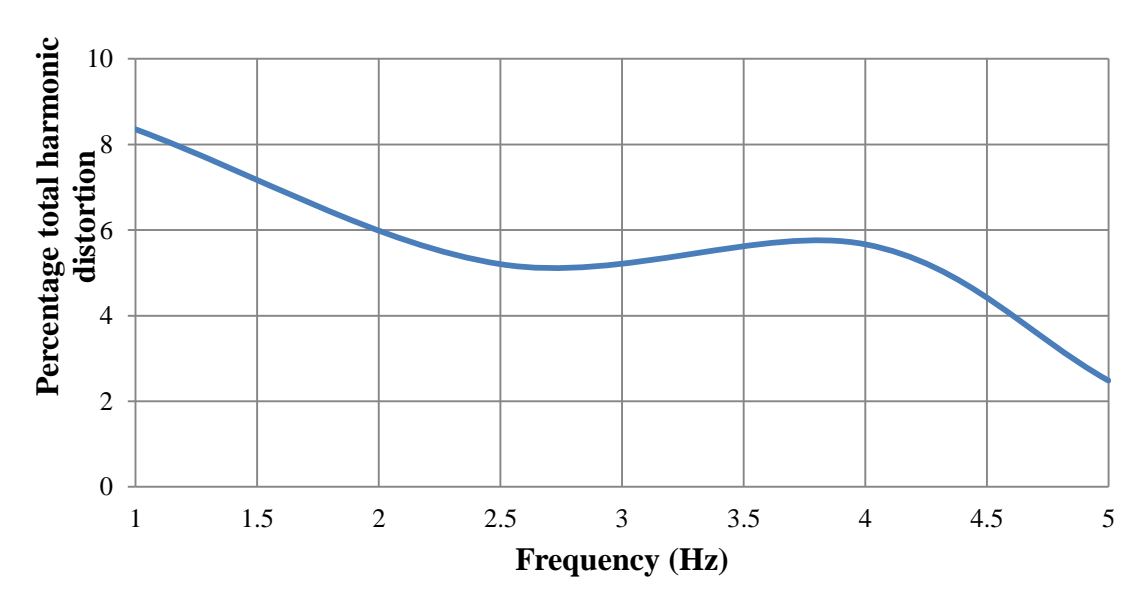


Figure 5.26 Percentage total harmonic distortion of three-phase FCSC-rectifier operating in a frequency range of 1-5 Hz

2) Frequency range of 50-480 Hz

For this frequency spectrum, to verify the simulation results by experimental testing, the circuit is modelled and simulated in accordance with the practical implementation (see Chapter 6), and therefore the maximum frequency in this spectrum is reduced to 480 Hz instead of 500 Hz to comply with the maximum frequency in the practical test. The generator phase voltage is assumed to vary between 50-100 V to be compatible with the experimental test voltage variations. In this simulation, most of the circuit parameters are modified in accordance with the practical benchmark.

These modifications are made to use the simulation results as a reference for comparison with practical test results. The circuit parameters are listed in Table 5-4. The generator parameters are based on the PMA generator parameters presented in Chapter 4.

1) Three-phase FCSC converter operating with constant load

At a maximum frequency of 480 Hz with a voltage of 100 V, all of the IGBT switches are permanently OFF, and the series capacitor is able to maintain the input current in-phase with the voltage waveform in addition to a sinusoidal current waveform, as shown in Figure 5.27. With the advantage of using the three-phase rectifier, the output DC voltage is smooth, and the magnitude of the average DC load voltage is 191.6 V.

Circuit $F_{\mathcal{S}}$ C_C C_L R_L $V_{S\ max}$ Rs L_{s} parameter 100 V-60 V Value 480 Hz-50 Hz 2.5Ω 13.75 mH $8 \mu F$ 500 μF 30Ω

Table 5-4 Circuit parameters for frequency spectrum of 50-480 Hz

This is higher than the maximum input voltage (127.2 V) at this frequency. Again the rectifier input voltage V_{in} is clamped by the load voltage and the rectifier output current (i_R) consists of six pulses with a maximum value of 6.8 A, which is similar to the maximum phase current. The average load current also complies with the relationship I_L = 1.35 I_{RMS} . The voltage across the series capacitor is sinusoidal since all IGBT switches are permanently OFF.

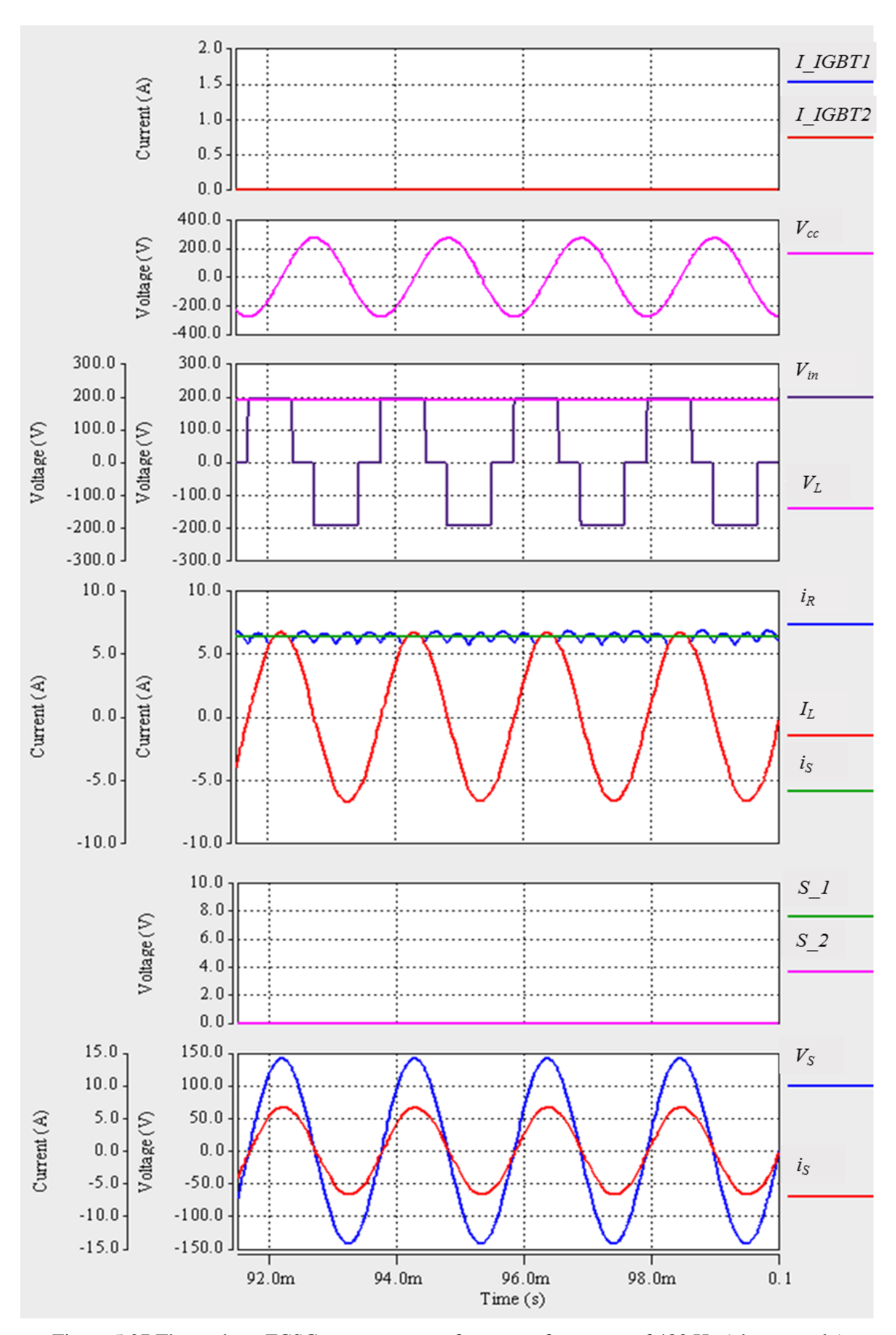


Figure 5.27 Three-phase FCSC converter waveforms at a frequency of 480 Hz (phase-a only)

When the frequency is reduced to 400 Hz and the voltage is 90 V, the IGBT switches are ON for a certain period 2γ . This period is a function of the duty cycle and can be determined using equation (5-5) with a scaling factor of 1000.

The circuit waveforms and the switch pulse sequences are illustrated in Figure 5.28. Obviously, the current is sinusoidal and there is no phase difference between the voltage and current waveforms, so that the power factor is maintained as high as 0.999. The average DC voltage is very smooth with an average value of 172.6V. The rectifier input current and output voltage follow the same behaviour addressed above. The voltage across the series capacitor is zero as long as the IGBTs are in the ON state.

In the half of the frequency range with a phase voltage of 75 V, the power factor is maintained at a high level by applying this control approach and increasing the duty cycle in line with frequency variations. The output voltage in this case is 143.66 V and identical behaviour is also achieved as illustrated in Figure 5.29.

At the minimum frequency and voltage values of 50 Hz and 50 V, respectively, the controller adjusts the IGBTs to be ON for a maximum duty cycle of 0.43. At this frequency, the output voltage is 90.9 V with a very small ripple small of about 0.8 V, as shown in Figure 5.30. The figure shows also that, in spite of the fact that the controller is capable of retaining a zero phase difference between the voltage and current waveforms, the current is distorted and this has a slight effect on the power factor.

Since δ is large at this frequency, the voltage across the series capacitor is maintained at zero for a long interval. The rectifier output current is also distorted since it is a function of the input current. However, its maximum value remains equal to the peak value of the input current.

In order to evaluate the overall performance of the three-phase FCSC converter in this frequency spectrum. Figure 5.31 demonstrates the output voltage and the input current are increasing in proportion to frequency. In addition, Figure 5.32 shows the power factor at different frequencies. The power factor remains high with a minimum value of 0.95, driven by high distortion and displacement factors.

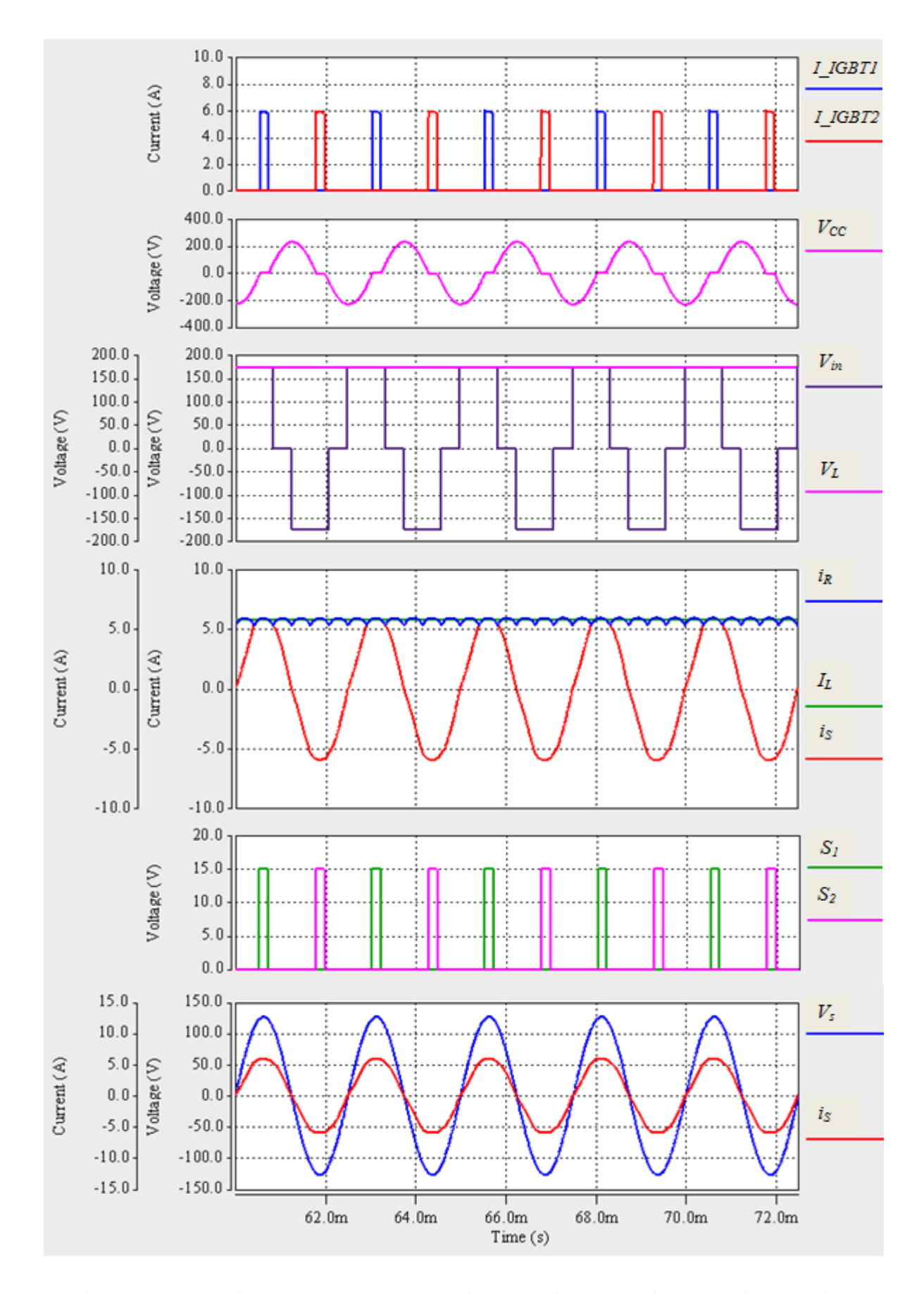


Figure 5.28 Three-phase FCSC converter waveforms at a frequency of 400 Hz (phase a only)

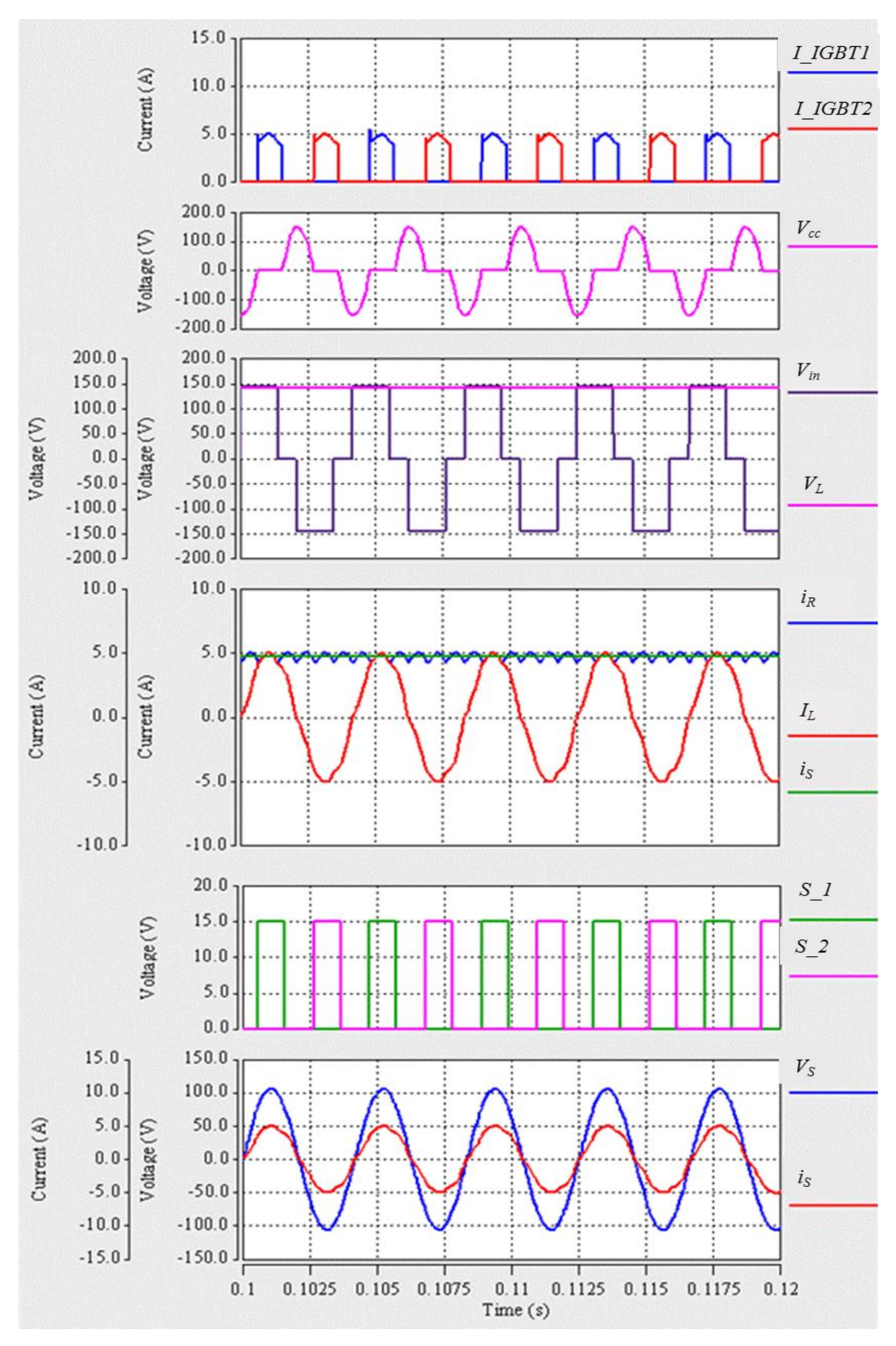


Figure 5.29 Three-phase FCSC converter waveforms at a frequency of 240 Hz (phase-a only)

Figure 5.30 Three-phase FCSC converter waveforms at a frequency of 50 Hz (phase-a only

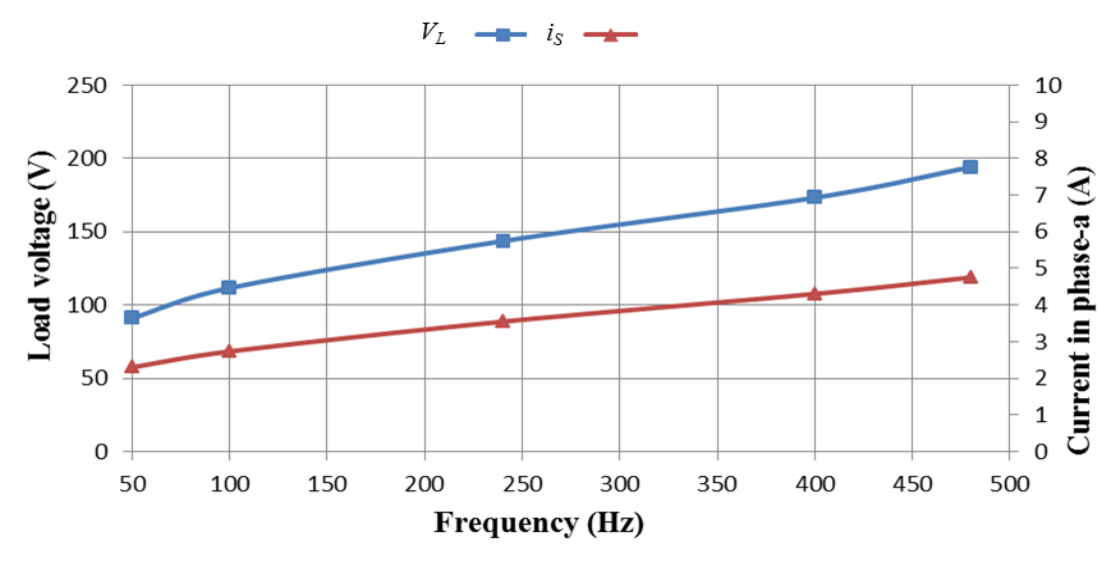


Figure 5.31 DC output voltage and input current under as a function of frequency in FCSC-rectifier

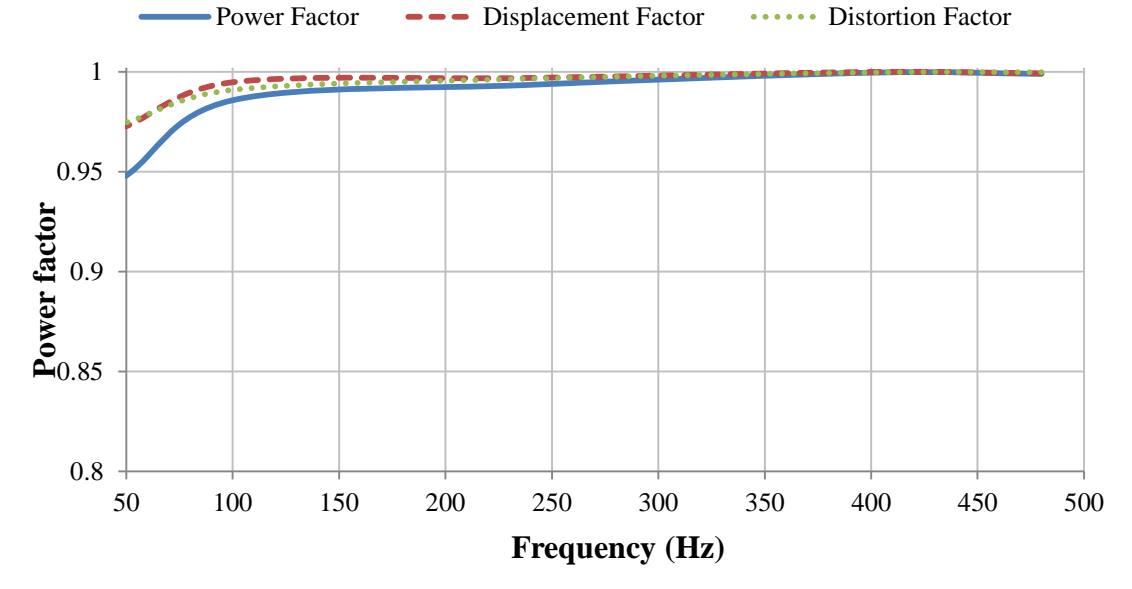


Figure 5.32 Power factor, distortion factor and displacement factor as a function of frequency in FCSC-rectifier

The results also show that the three-phase FCSC converter is capable of maintaining high efficiency over a wide range of frequency and voltage variations, with a minimum efficiency of almost 95% at the minimum frequency of $50~H_Z$. In addition, the percentage total harmonic distortion is higher than in the low frequency scenario (Figure 5.26) and its value is lowest at a maximum frequency of $500~H_Z$, as shown in Figure 5.33.

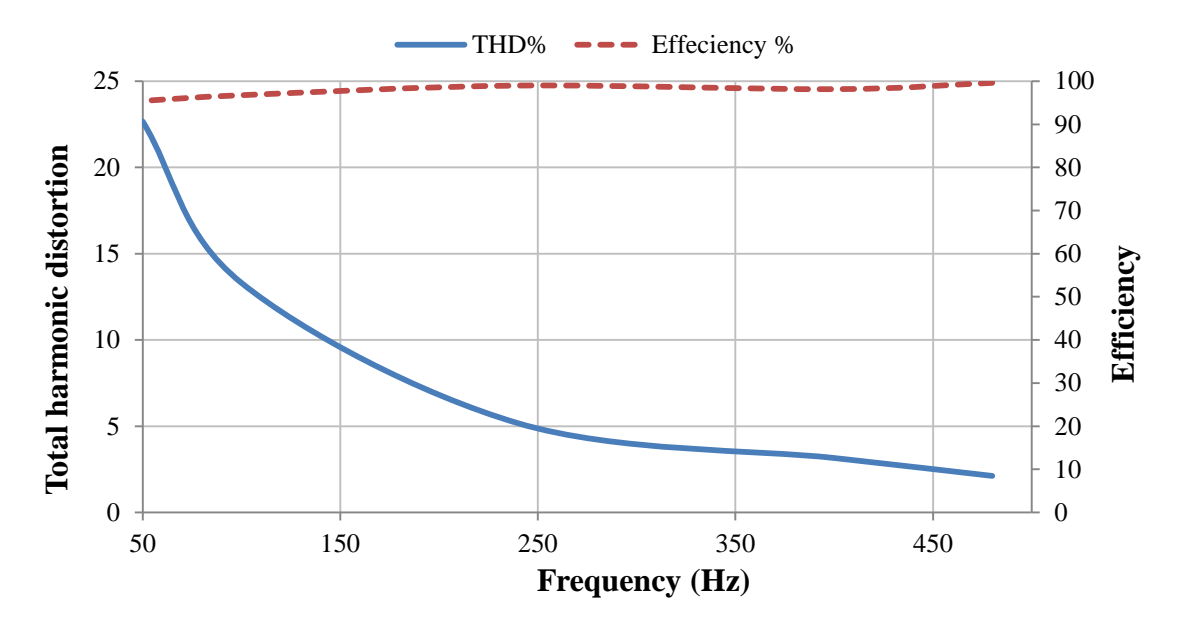


Figure 5.33 Efficiency and percentage total harmonic distortion of the three-phase FCSC-rectifier operating in a frequency range of 50-480 Hz

2) Three-phase FCSC-rectifier under various load conditions

Here, the performance of the FCSC converter is analysed numerically under various load conditions by varying the load resistance between 10 Ω and 30 Ω in line with the voltage and frequency variations. The operating voltage is varied from 100-50 V and the operating frequency is simultaneously changed from 480-50 Hz. The output DC load voltage is reduced in proportion to the reduction in the input phase voltage, as shown in Figure 5.34.

Figure 5.34 shows that the load voltage is higher at light load (R_L =30 Ω). Since the load is an RC load, the output voltage increases proportionally to the load resistance (R_L), according to Ohm's law. As expected, the output current is reduced by increasing the load resistance as illustrated in Figure 5.35.

As explained in Section 5.1.2.1, the input current is a function of the load current, and therefore it is also reduced by increasing the load resistance as shown in Figure 5.36.

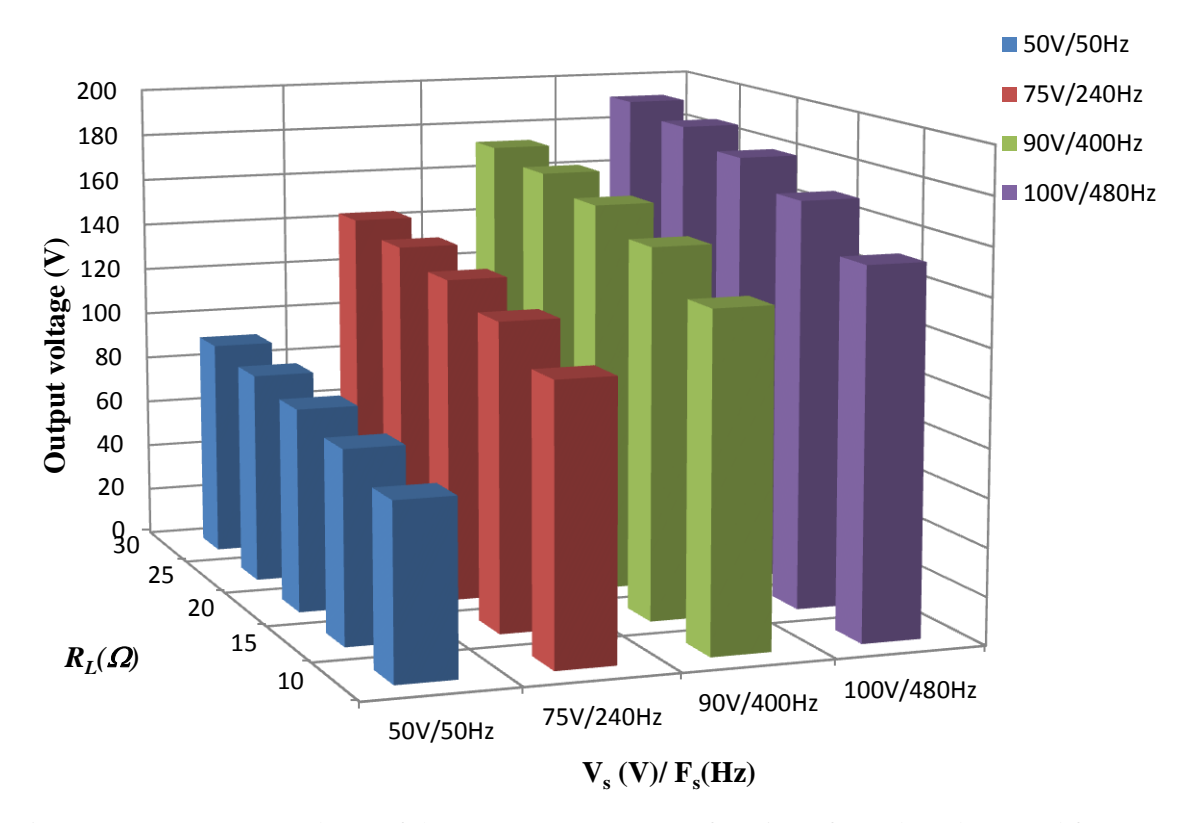


Figure 5.34 DC output voltage of the FCSC converter as a function of supply voltage and frequency variations under various loads

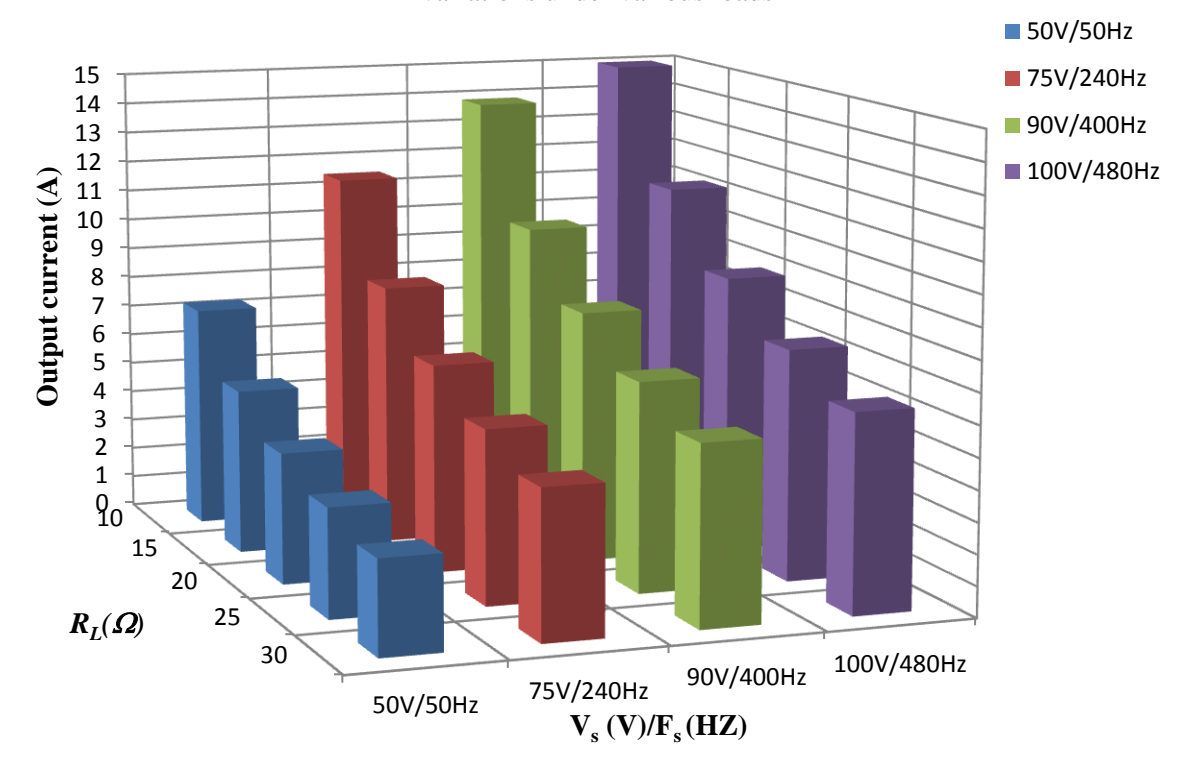


Figure 5.35 Load current of the FCSC converter as a function of supply voltage and frequency variations under various loads

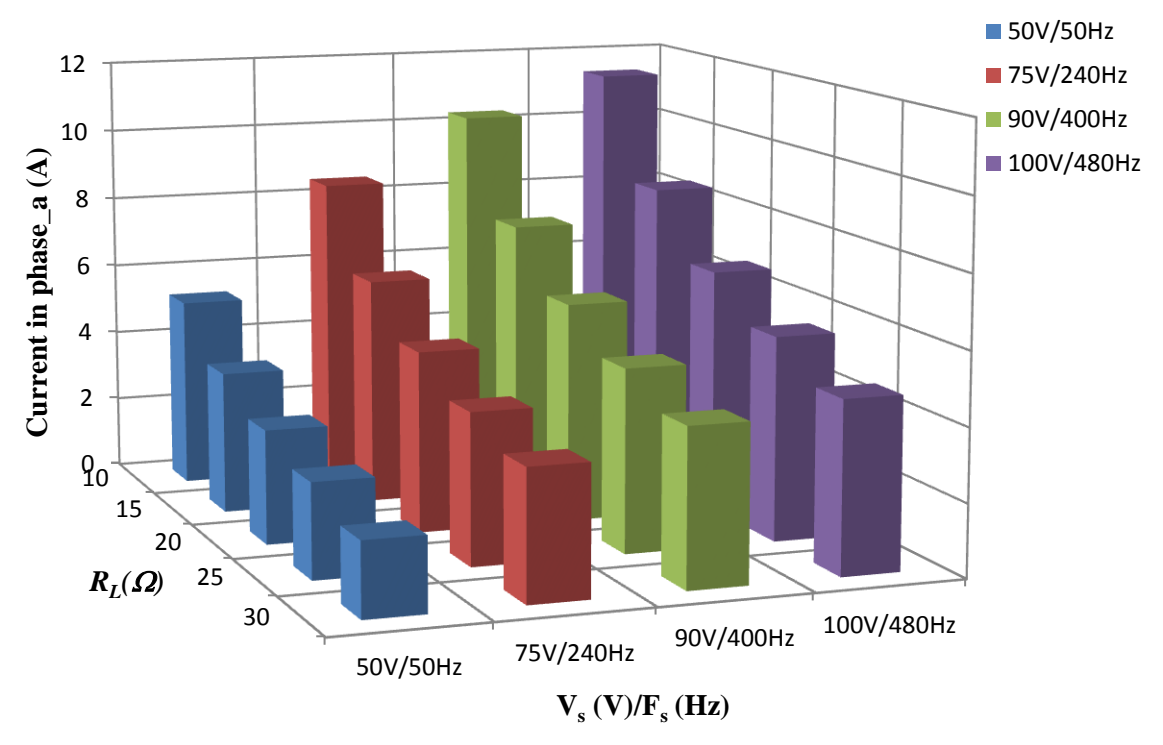


Figure 5.36 Input current of the FCSC converter as a function of supply voltage and frequency variations under various loads

Figure 5.37 clearly shows that the FCSC converter with SDCC in a VVVF system is able to maintain a high power factor under heavy load with a minimum value of 0.96 at various voltage and frequency values. However, the lower power factor value of 0.94 is achieved at the minimum value of V_s/F_s (i.e 50 V/50 Hz) under light load.

Since this research sets out to investigate the impact of the three-phase FCSC converter in the proposed WECs and MEA applications, the assessment of the FCSC converter on the system performance in terms of load voltage, input current and input power factor is based on the three-phase conventional diode bridge rectifier as a reference. Appendix C presents the simulation results for the conventional three-phase diode bridge rectifier under different load conditions, including fixed and variable resistive load, along with variable-voltage variable-frequency operating conditions. The simulation results of both rectifier circuits are validated experimentally in Chapter 7.

5.2 Harmonic Analysis of Three-Phase FCSC Rectifier

As explained in Chapter 4, to propose the three-phase FCSC-rectifier for aircraft applications, the contamination of current harmonics as a function of load variations in a variable-voltage and variable-frequency system needs to be investigated.

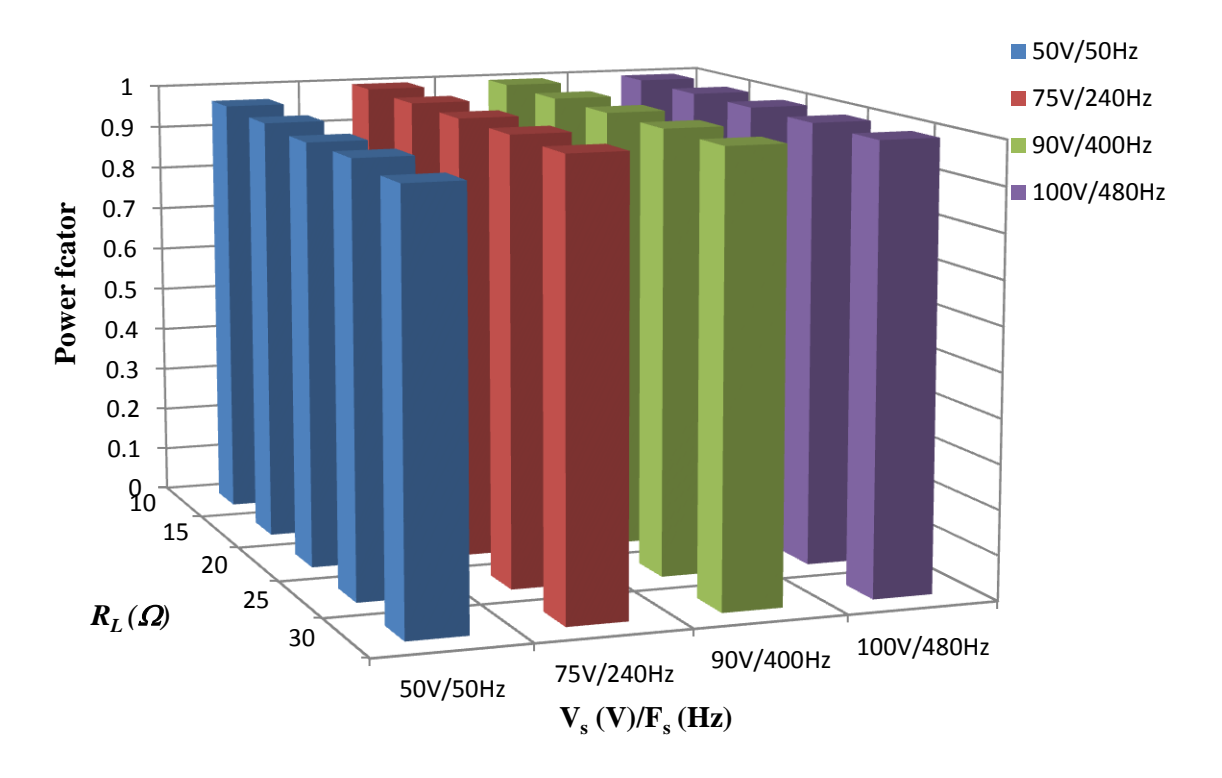


Figure 5.37 Input power factor of the FCSC converter as a function of supply voltage and frequency variations under various loads

This is important due to the strict limits placed on individual harmonics in such applications. Different harmonics exist at different voltage/frequency values with variable load points. Therefore, an analysis of the harmonic input current is carried out using FFT analysis. In the analysis, the harmonic components are calculated up to the 40th harmonic as required in the relevant applications standards. Harmonic values less than 0.002 are ignored. Figure 5.38 to Figure 5.40 compare the simulation results of the input current spectrum with the demands imposed by RTCA DO-160. In other words, the limits of the individual current harmonics listed in Table 4-4 are compared with the system's current harmonics to examine the suitability of employing the FCSC converter in aircraft application. In these figures, h represents the harmonic order.

Figure 5.38 shows that, at a lower value of R_L of 10 Ω , the 4th harmonic appears only at a maximum frequency of 480 Hz, but its value is less than the allowable limit. All the harmonics at frequencies of both 480 Hz and 240 Hz are also lower than the limits. However, at the minimum voltage and frequency, the 5th and 7th harmonics are 18.05 I₁% and 12.0 I₁%, respectively. This means that they exceed the RTCA limits (purple colour bars).

When the load resistance is increased to 20 Ω , the 5th and 7th harmonics at the minimum frequency of 50 Hz are 19.3 I₁ % and 11.7 I₁ %, respectively, which are also above the defined

limits. In addition, at the same voltage and frequency range, although the 11^{th} order harmonic is 4.13 $I_1\%$, its value is lower than the limit set in Table 4-4 (i.e 8 $I_1\%$). Once again, at the minimum value of $V_{s'}F_sI_5$ and I_7 exceed allowable values as illustrated in Figure 5.39. Figure 5.40 illustrates that when the load current is reduced (at the maximum R_L of 30 Ω), more harmonics exceed the allowable limits in half of the spectrum (75V/ 240 Hz). For example, the second order harmonic is bigger than the limit, as are I_5 and I_7 . Similarly, at the minimum range values, I_5 and I_7 are higher than the limits. However, all the harmonics above half of the maximum frequency are within allowable limits. In conclusion, better performance of the three-phase FCSC converter can be achieved at heavy loads, and this needs to be taken into consideration when proposing the three-phase FCSC converter for aircraft applications. Furthermore, at the minimum values of the frequency and voltage ranges, although the three-phase FCSC-rectifier is capable of correcting the power factor to a high value and increasing the output power, some current harmonics will exceed allowable limits.

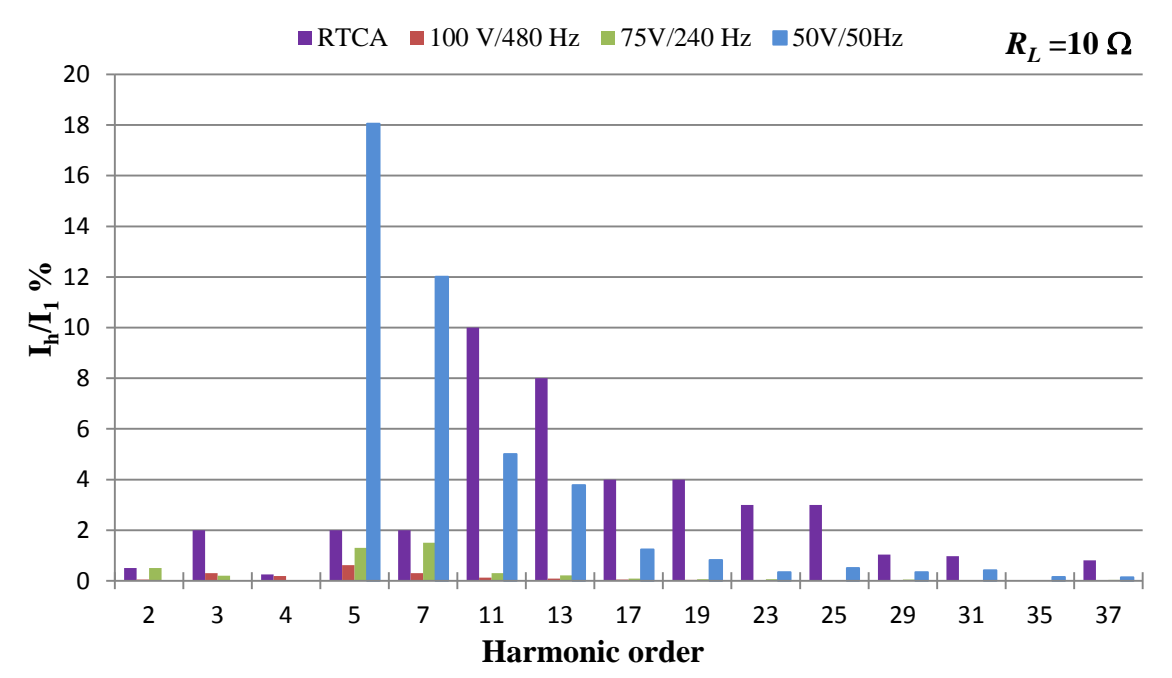


Figure 5.38 Input current harmonic spectrum as a function of V_S/F_S variations when $R_L=10~\Omega$

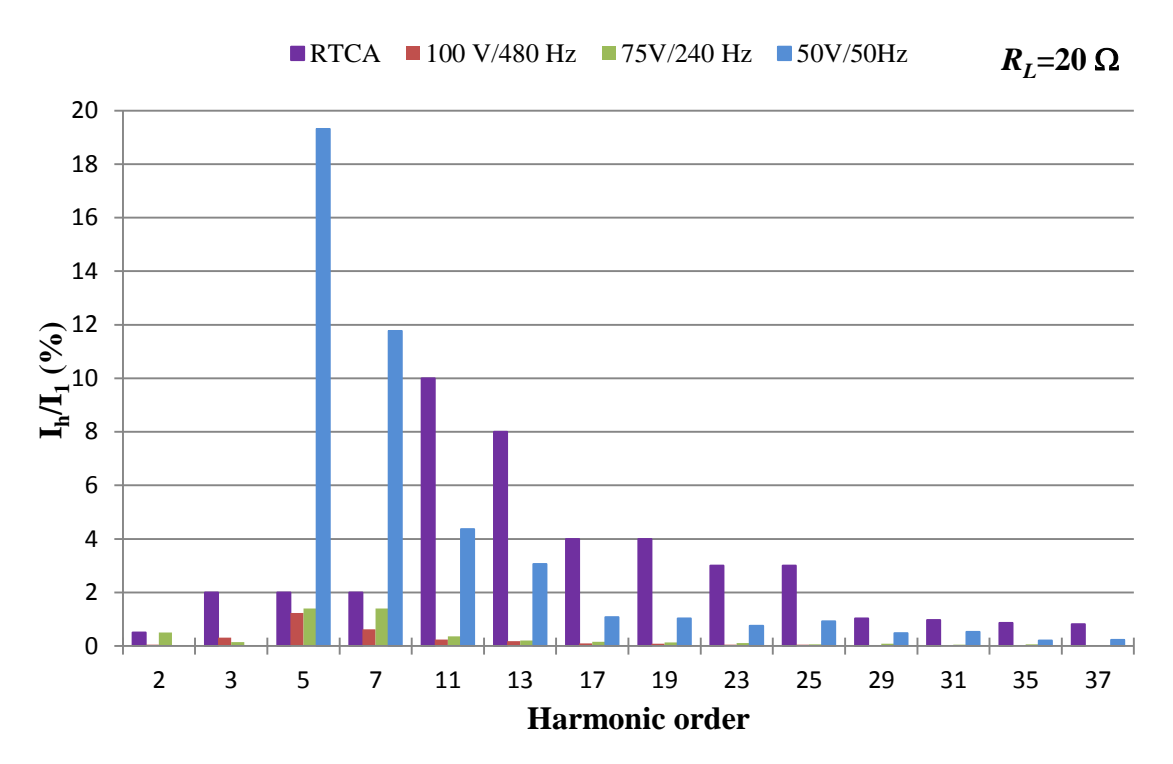


Figure 5.39 Input current harmonic spectrum as a function of V_S/F_S variations when $R_L=20~\Omega$

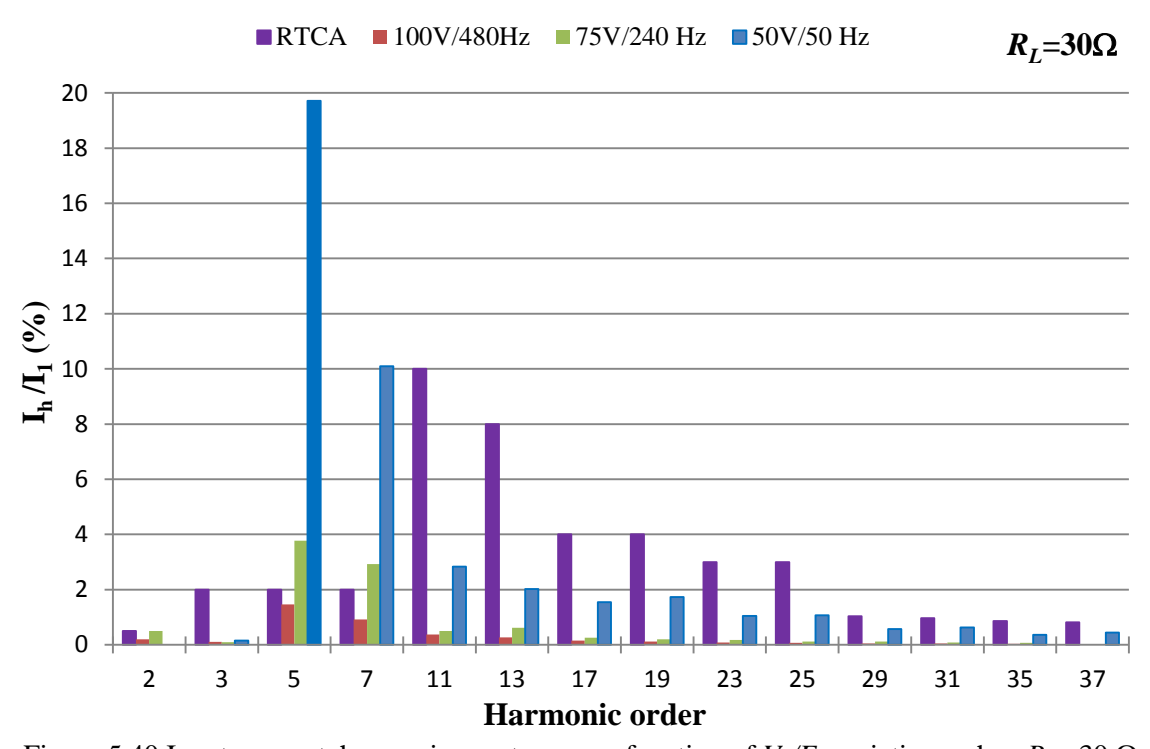


Figure 5.40 Input current harmonic spectrum as a function of V_S/F_S variations when $R_L=30~\Omega$

5.3 Assessment of the Proposed Symmetrical Duty Cycle Control Strategy

In order to assess the proposed control strategy in different applications which have different frequency and voltage spectra in both single and three-phase systems, the comparison presented in this section is based on the investigation of the behaviour of the FCSC in terms

of the overall input power factor and the percentage of total current harmonic distortion over the entire range of operating frequencies.

The comparison includes the behaviour of the single-phase FCSC circuit at both low and medium frequency ranges in addition to the performance of the three-phase FCSC circuit at the same two frequency ranges.

When using symmetrical duty cycle control in the single-phase topology, maintaining similar values of the time constant τ through varying load circuit values allows better values of power factor to be achieved with the frequency range of 1-5 Hz, with a minimum value of 0.94. However with the frequency range of 50-500 Hz, the minimum power factor value is 0.89, and both are achieved at the minimum frequency values in each range. This is because the displacement factor is lower in the frequency range of 50-500 Hz. Nevertheless, excellent results are achieved when using the proposed symmetrical duty cycle control even at very low frequencies. For example, the power factor at 1 Hz is improved from around 0.3 without any control action to a value of 0.947 with the new controller. The current total harmonic distortion is increased as the frequency is reduced, and higher distortion values occur in the frequency range of 50-500 Hz.

The simulation results show that the controller can ensure a very high power factor over the entire range of frequency variations in both single-phase and three-phase systems. This is achieved by maintaining the displacement factor at approximately unity with little distortion over the range of operating frequencies.

Applying this control method in a three-phase circuit at both the low frequency range of 1-5 Hz and the medium frequency range of 50-480 Hz, the power factor in both cases is approximately identical; 0.995 for 1-5 Hz and 0.994 for 50-480 Hz. This means that better generator utilization can be achieved in both applications. Furthermore, by using the three-phase FCSC, the total harmonic distortion is lower than in the single-phase system in both frequency spectra. However, the percentage THD values are lower for the low frequency range in the three-phase circuit.

Surprisingly, the comparison of the SDCC in both topologies shows that circuit behaviour is different. For example, there is no commutation overlap in the single-phase topology while there is an overlap interval in the three-phase FCSC converter. In addition, the three-phase

circuit topology is able to boost the output voltage level; however, the single-phase circuit suffers from a low output voltage.

5.4 Summary

The symmetrical duty cycle control (SDCC) that is presented in this chapter is a novel approach to the control of the FCSC converter in both single and three-phase systems, which the author believes has never been considered in the literature before. This approach proposes a new control strategy for the FCSC converter to cope effectively with both small and wide frequency variations in stand-alone variable-voltage, variable-frequency systems. This new technique can be considered a simple approach to implement without any sophisticated control circuits and pre-calculations. The technique uses a symmetrical switching pattern across the maximum current position point. Compared to previously published work, this offers more flexibility in terms of the range of possible ON times and reduces the required ON time of the converter switches, allowing operation at much higher frequencies which can be applied in both single-phase and three-phase FCSC converter circuits.

The technique is first applied on the single-phase FCSC converter for different ranges of frequency variations, including small frequency variations between 1-5 Hz, such as in wave energy applications where the operational frequency is very low, and medium frequency variations of 50-480 Hz, which is a typical part of an aerospace frequency spectrum.

The simulation results demonstrate how the adoption of the symmetrical duty cycle control SDCC technique allows the FCSC converter to maintain a high input power factor over both ranges of input frequencies and voltage variations in both single-phase and three-phase FCSC circuits. In both cases, the power factor is improved from approximately 0.3 to 0.95.

However, as expected, in the single-phase circuit topology, the input current is very sensitive to changes in load values; in addition, the FCSC converter cannot boost the output voltage to a higher level than the peak input voltage.

On the other hand, besides the ability of the three-phase FCSC circuit topology to improve the power factor to a high level, it is also able to boost the load voltage to be larger than the RMS line-to-line voltage with a smooth DC output voltage within the selected load values. In addition the current distortion level is lower than in the single-phase FCSC circuit.

Chapter 5

In general, better performance is achieved by applying the symmetrical duty cycle control with the three-phase FCSC converter.

To validate the concept of the three-phase FCSC converter as a PFC converter in aerospace applications, this chapter presented a detailed description of the harmonic content of the input current, which is of crucial importance in such applications due to the strict limitations on harmonics. The results show that the three-phase FCSC-rectifier is able to correct the power factor over a wide frequency range and maintain low current distortion even at half of the maximum frequency. However, the minimum frequency spectrum value should be avoided if this converter is selected for applications due to the harmonics limitations.

The impact of load variations has also been investigated in this chapter for the three-phase topology, and the simulation results show that, for employment in aircraft, lower harmonics components can be achieved at heavy load without exceeding the limits when the frequency is reduced even to half of its value. Again, the minimum value in the frequency spectrum should be avoided in such cases. Finally, the difference between the single-phase and three-phase circuit topologies in terms of the commutation overlap is also highlighted.

The simulation results are validated by practical implementations and tests in the next two chapters, the first of which describes the practical set-up, and this is then followed by the practical results.

Chapter 6. Experimental Set up, Hardware and Measurement

The ability of the three-phase FCSC converter to correct the power factor and increase the output voltage level and output power in a stand-alone variable-voltage variable-frequency application is experimentally tested via a laboratory test bench. The system requirements are designed to enable the employment of the three-phase FCSC converter in aircraft applications.

This chapter briefly describes the platform used to test the practical performance of the three-phase FCSC converter operating with a variable-voltage variable-frequency stand-alone system in a laboratory setting. The experimental test is designed to deliver approximately 3 kW to a DC load, and the lab tests are carried out for 1 kW operation. The converter is tested over a frequency range of 50-480 Hz and a line-to-neutral voltage variation of 50-100 V.

The software implementation and programming is performed using a Texas Instruments TMS320F28335 DSP controller and National Instruments LabView TM is used to monitor and control the system in real time.

6.1 General Description of the Laboratory Test Platform

The laboratory test platform is shown in Figure 6.1. The test hardware consists of four major parts. The first part represents the role of the PMA generator, which was emulated to provide the system with a variable-voltage variable-frequency output. The second part is the power stage, which consists of two main blocks. These blocks are a three-phase FCSC circuit and a three-phase six-pulse diode bridge rectifier. Six IGBTs are used to shunt the three capacitors in each phase. Six diodes were employed in the three-phase diode bridge rectifier to perform AC to DC conversion with a smoothing capacitor. Three dual-gate driver circuits are used to provide the six pulses which are required to drive the IGBT switches. The third part is the measurement circuit, and includes the sensor circuits, which are divided into three voltage transducer cards to sense the voltage in each phase, and three current transducer cards to detect the current in the three phases. A zero crossing detection (ZCD) card is also needed to detect the instant at which the voltage crossed the zero value point.

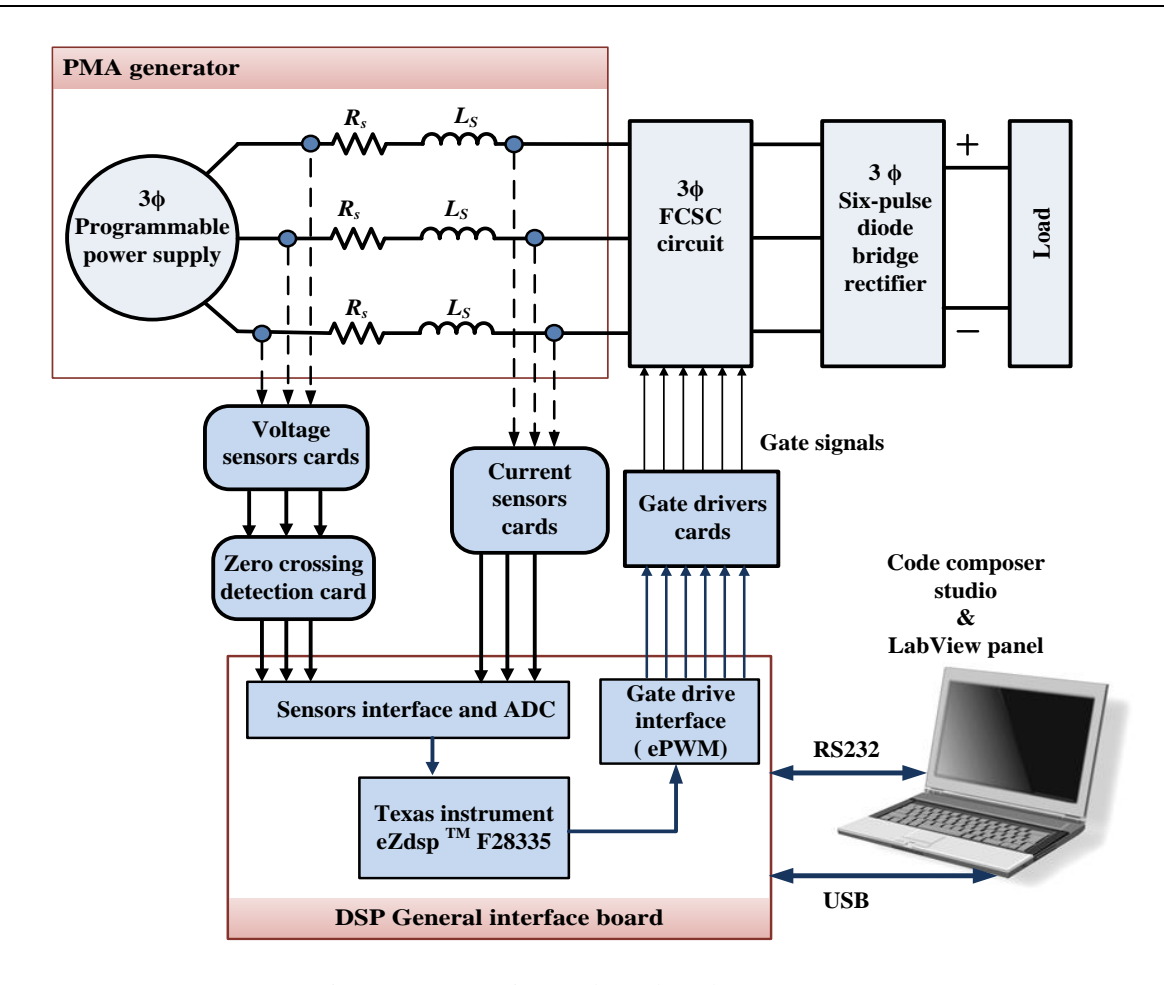


Figure 6.1 Experimental test bench arrangement

The readings of the current sensors and the ZCD card are fed to the microcontroller to be processed. Finally, the controller, which represents the fourth part in this test platform configuration, is based on digital signal processing from the Texas Instruments TMS320F28335 DSP which was mounted on a general interface board. After processing the sensor readings, the DSP generates the required signals to correct the input power factor of the system.

A host computer is required to provide an environment in which to debug the software. A USB connection is used to interface the laptop and the DSP controller. To program and debug the software, Code Composer Studio TM (CCS) software from Texas Instruments TM is installed to provide the required environment. Furthermore, a National Instruments LabView package is used to monitor and control the microcontroller. The communication between LabView and the microcontroller was set via an isolated RS232 serial channel. The resistive load was fed from the output of the three-phase rectifier. As mentioned earlier, the experimental prototype is designed to deliver approximately 3 kW of power to the load, but is tested for 1 kW operation only because of current limitations of the AC capacitors and the

reactors. In addition, several hardware components used in this test are designed to be used with an operating frequency of 50/60 Hz, for which it is recommended not to exceed ten times this frequency for safety reasons, because the losses become excessively high. This will be explained later in this chapter, since it has a material impact on some of the results and must be taken into consideration in the analysis.

It is worth mentioning that, since the power source used in this test is an AC to DC to AC converter, which is based on a pulse width modulation control scheme, the unit suffers from high distortion in its output voltage due to its filter design problem. The output voltage is distorted by a harmonic with a frequency of 20 kHz, which is similar to the switching frequency of the inverter unit. After harmonic analysis is performed with the help of FFT analysis of the output voltage waveform, a 20 kHz harmonic is captured which pollutes the output voltage at different frequencies. This problem is confirmed by the manufacturer. The voltage waveform analyses, with its harmonics components at different frequencies, are presented in Appendix C. However, this problem has no impact on the converter's behaviour in terms of power factor and output power, as described later in Chapter 7. A photograph of the power supply unit is shown also. A detailed description of the hardware used to assemble the whole system is provided in Appendix D. A photograph of the complete laboratory test bench is shown in Figure 6.2.

6.2 Zero Crossing Detection

As explained earlier, each IGBT in the three phases is controlled for one half-cycle of the supply frequency, and therefore it is important to detect the instant when the voltage waveform crosses the zero point. In other words, it is important to synchronise the converter with the power source. Different techniques can be used for this synchronisation such as a zero crossing detection technique and phase-locked-loops (PLL), where each method has its own advantages and disadvantages for different applications, as described elsewhere [146, 147]. In this work, the classic zero crossing technique was used for simplicity in hardware implementation and software programing in addition to its low cost implementation. A photograph of the designed ZCD card is shown in Figure 6.3.

The inputs of the ZCD board are supplied by the three output terminals of the voltage transducers. However, the main power supply suffers from distortion, as mentioned in Section 6. 1, which affects the circuit performance and can cause a false zero crossing.

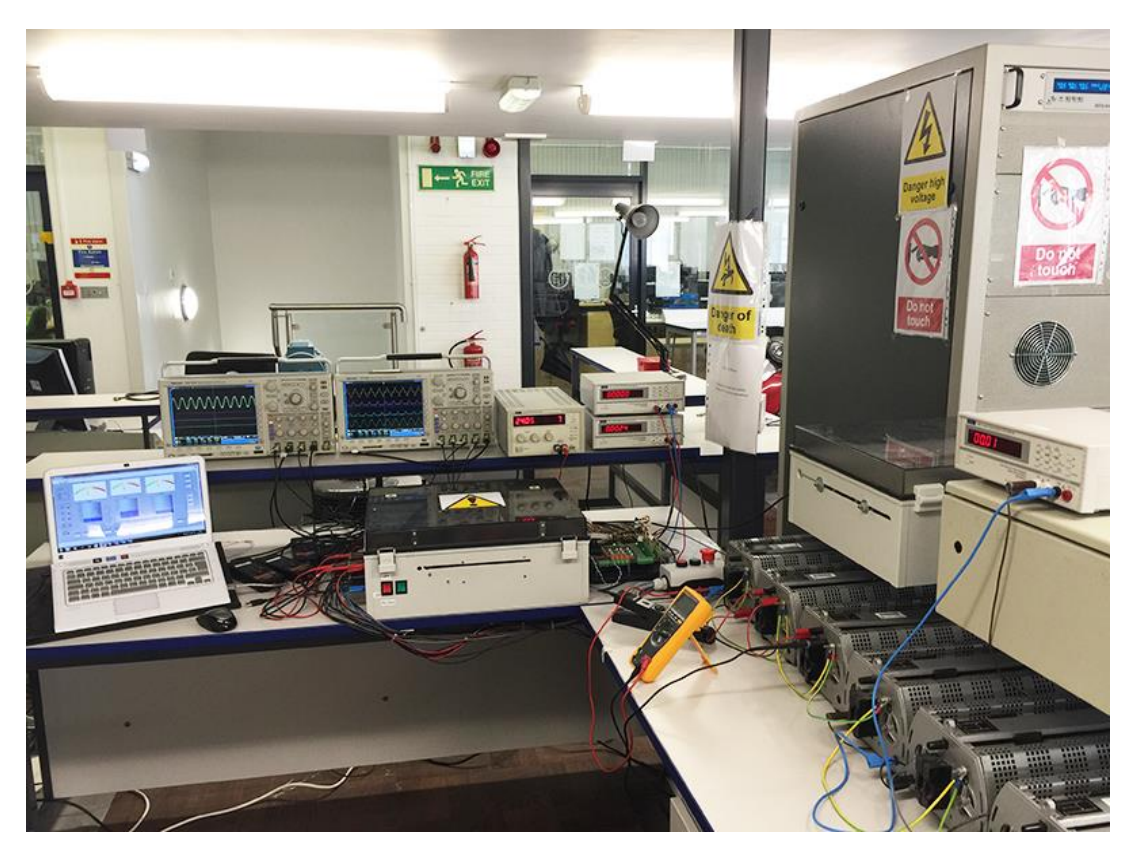


Figure 6.2 Photograph of full workstation for the experimental test

Therefore, a simple low-pass filter is included to prevent spurious zero crossing detections. In this way, the input voltage is filtered using an RC low-pass filter (22 nF capacitor and 390 Ω resistor) with a cut off frequency of 18.5 kHz, as expressed below [148, 149]:

$$f_{cut-off} = \frac{1}{2\pi RC} \tag{6-1}$$

A schematic diagram of the constructed ZCD board is shown in Appendix D, while a photograph for this board is shown in Figure 6.3. The output voltage waveform of the zero crossing detection board is shown in Figure 6.4.

6.3 Hardware Modification of the General Interface Board of eZdsp TM F28335

In order to fulfil the requirements of the experimental test, hardware modifications were carried out as follows:

i. Voltage sensor interface

Since the outputs of the voltage sensors were connected to three ADC channels via the ZCD card for zero crossing voltage measurement, the general interface board was modified to include the additional voltage divider.

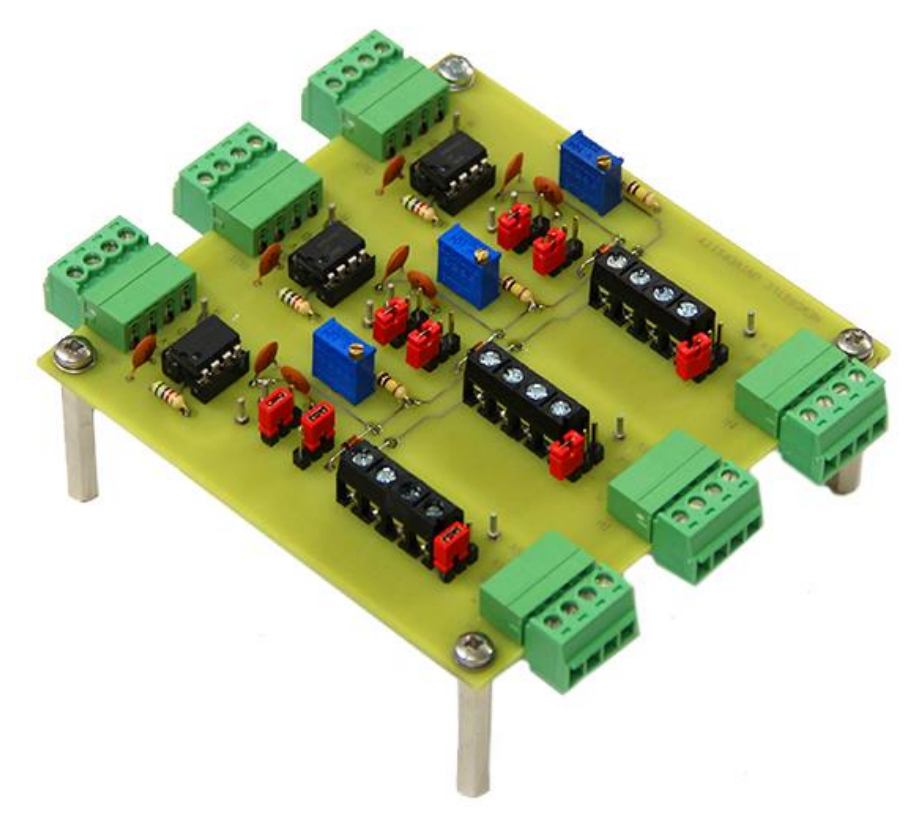


Figure 6.3 Photograph of the designed ZCD board

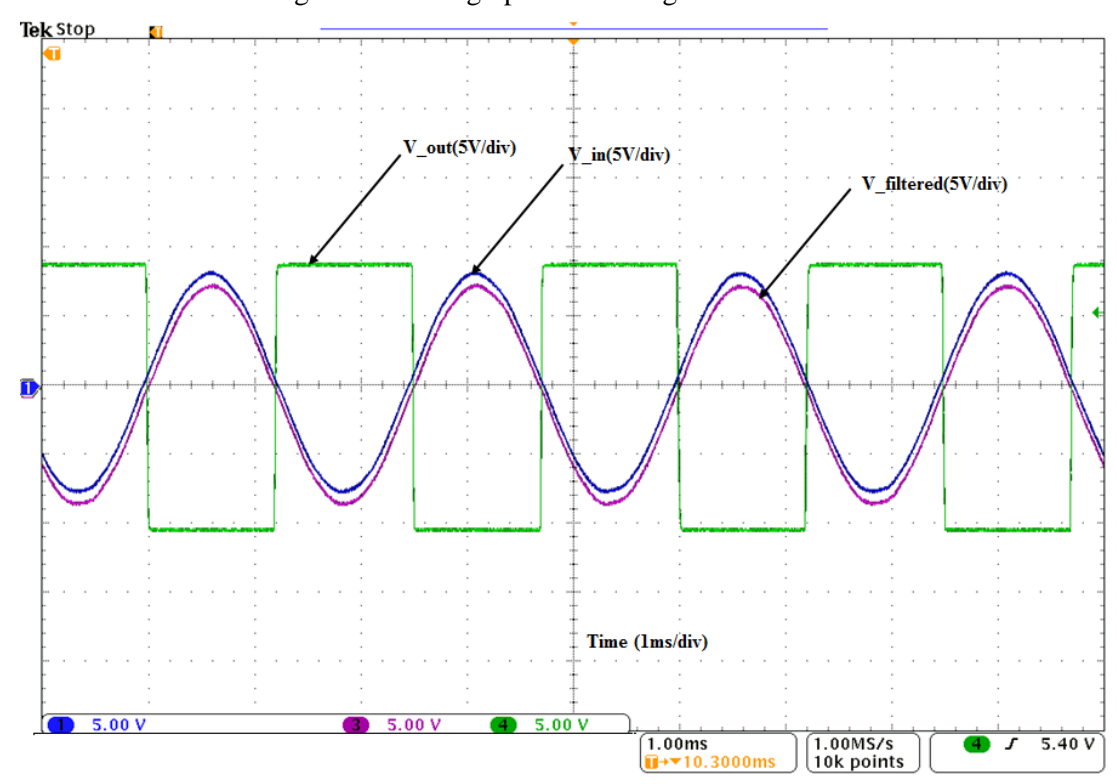


Figure 6.4 Voltage waveforms of the zero crossing detection board

The ZCD output was scaled down via a resistive voltage divider to reduce the voltage to $\leq \pm 5$ V, and then the voltage was scaled down again via a certain configuration on the general interface board to ensure that the input voltage to the ADC channels, was compatible with the

desired range of the ADC channels, which is 0-3 V. A schematic of the circuit configuration is shown in Figure 6.5.

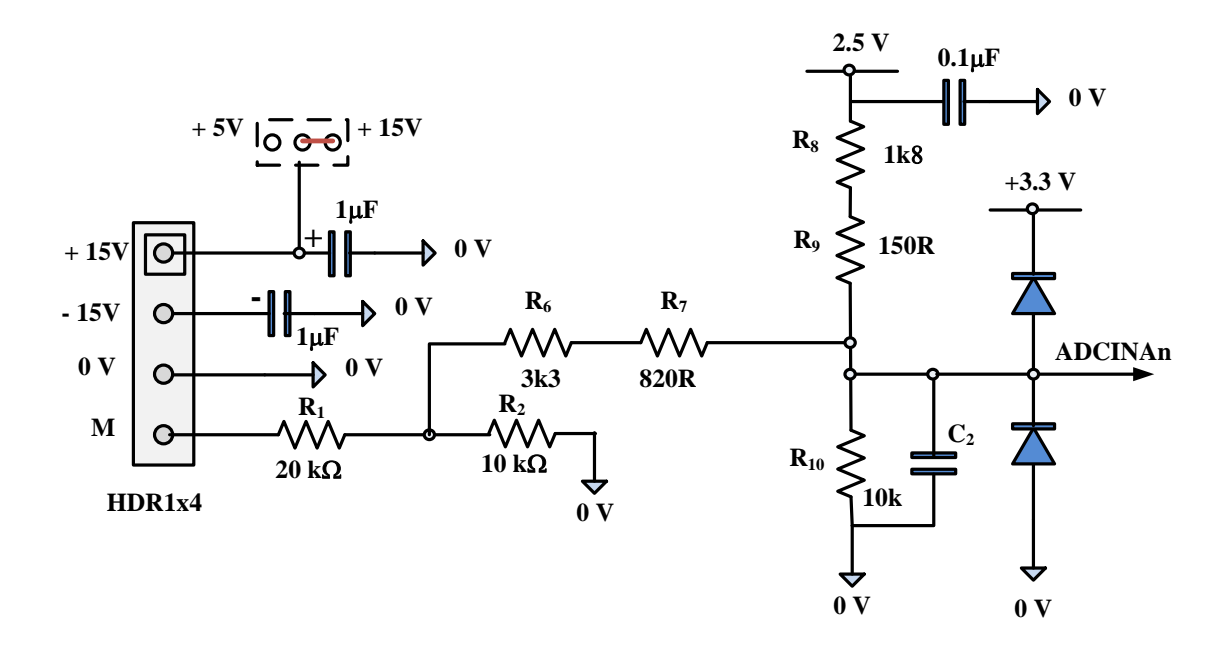


Figure 6.5 The modification in the voltage sensor interface

ii. Gate drive interface

In this experimental test, it was required to generate six pulses as pairs from the gate drive interfaces to feed the dual gate drivers which control the IGBT ON and OFF times. Therefore, three ePWM modules were used. To maintain a phase shift of 120° between the three phases, these modules were configured to synchronise the three phases with a phase shift of 120° by activating the synchronisation scheme via configuring the PHSEN register. The ePWM modules were chained together by clock synchronisation. The synchronisation scheme of the ePWM is used by setting one ePWM module as a master and the two other modules as slaves with a phase difference of 120° between the three phases, as shown in Figure 6.6.

However, the operation of the three-phase FCSC converter requires each anti-parallel IGBT ON/OFF time in each phase to be maintained with a phase difference of 180°, and therefore it was necessary to modify the hardware in the general interface board. In addition, the three dual gate drivers needed to be interfaced with three PWM modules only. Therefore, hardware modifications were implemented in the gate drive interfaces. Since each ePWM module on the general interface board had two PWM outputs (PWMA and PWMB), the modules EPWM4A, EPWM5A and EPWM6A were reconfigured to replace EPWM1B, EPWM2B and

EPWM3B respectively to implement the synchronisation scheme between all modules. The final arrangement of the PWM units is shown in Figure 6.7.

Based on the principle of operation of the three-phase FCSC converter, the phase difference between S_1 S_2 , and S_3 , S_4 and S_5 , S_6 is 180° which is equivalent to 1.25 ms when the supply frequency is 400 Hz, as shown in Figure 6.8.

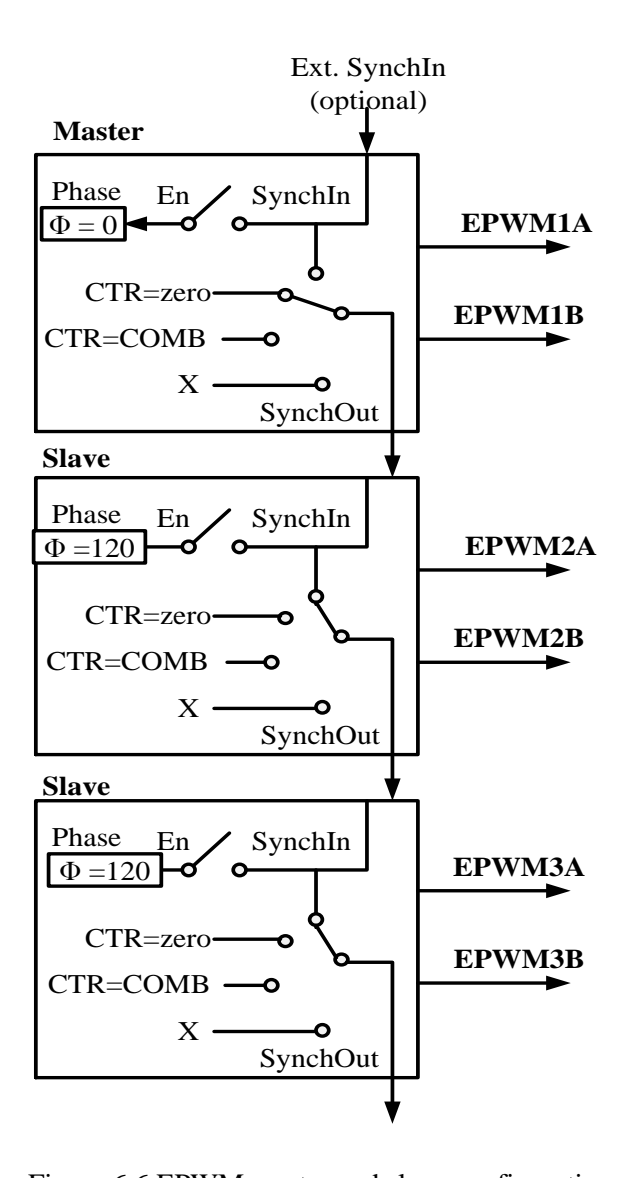


Figure 6.6 EPWM master and slave configurations

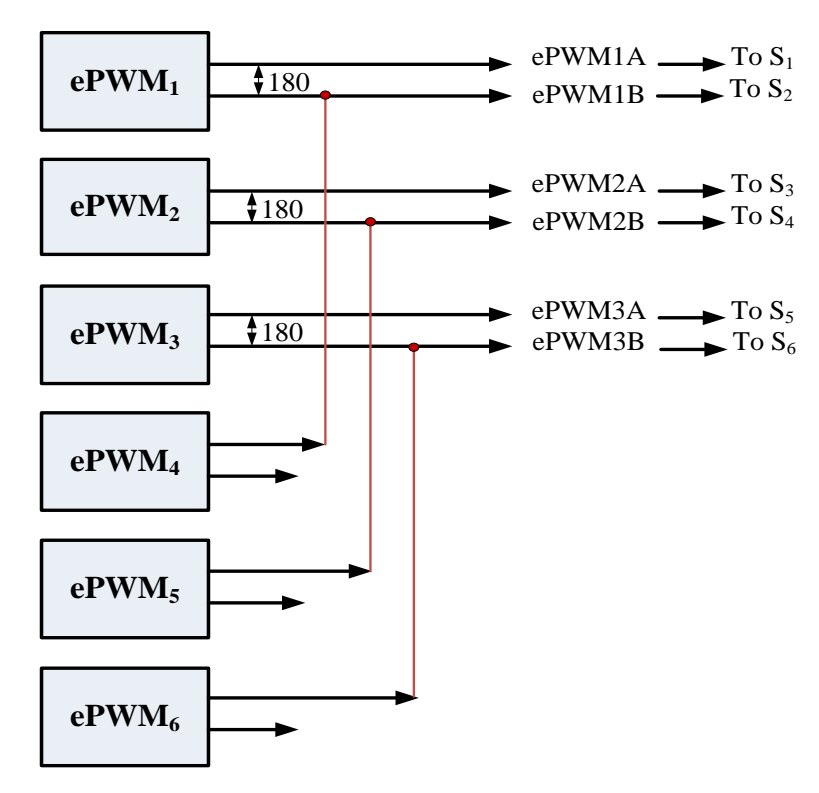


Figure 6.7 The PWM hardware modifications in gate drive interfaces

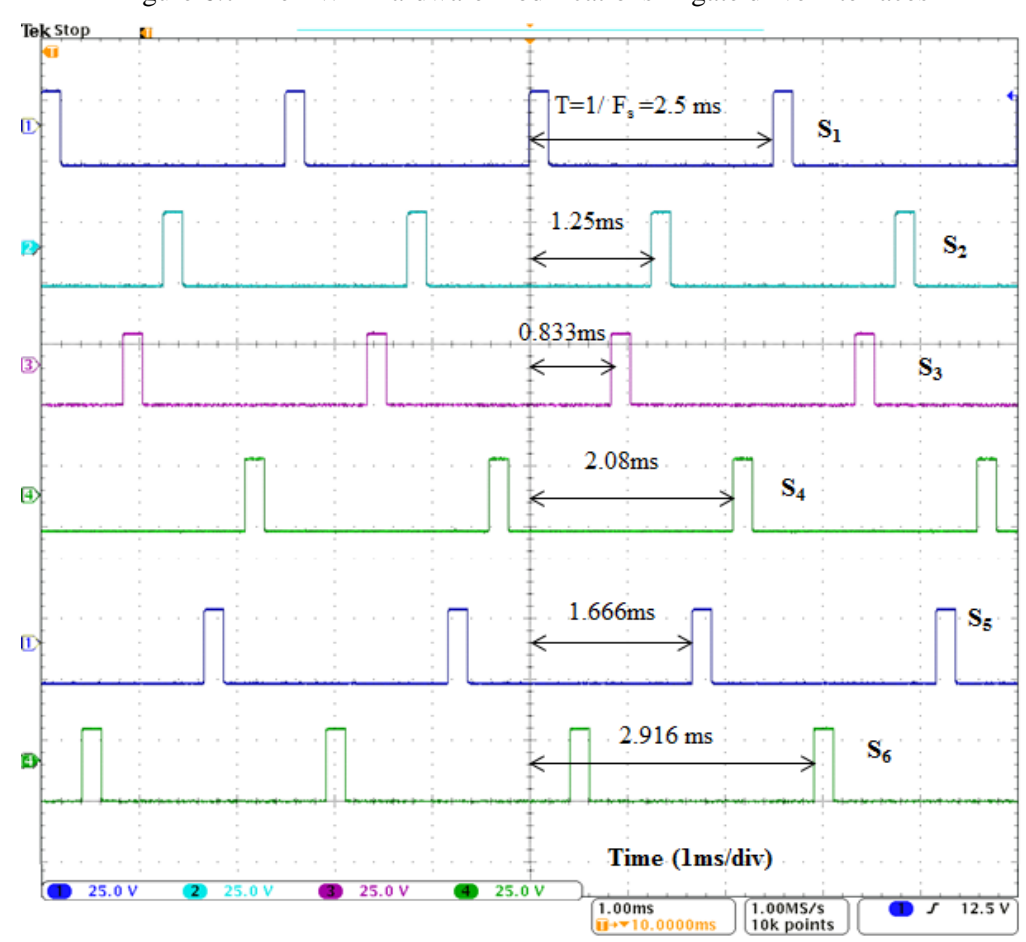


Figure 6.8 Six PWM pulses for IGBT switches at a frequency of 400 Hz

6.4 Laboratory Test Bench Measuring Equipment

When the test was running, several pieces of measurement equipment were used as part of the test rig. These included:

- Tektronix MS 4034 mixed signal oscilloscope, with four channels, 350 MHz and a 2.5
 GS/s sample rate on all channels
- TTI 1604 40000 count digital multimeter
- Tektronix P 5200 high voltage differential probe with a maximum voltage of 1300 V
- Tektronix A622 AC/DC current probe with a maximum RMS current of 70 A.

6.5 Software Development

During real-time system operation, a LabView control panel was designed to control the DSP ON/OFF operation and to upload information to the TMS320F28335 DSP for processing, and downloading several measurements from the DSP to be monitored via the host computer.

The graphical user interface of LabView control panel was programmed to provide the microcontroller with control data, such as to enable, enable/disable the gate drive signals for all IGBT switches via the PWM TRIP push-button on the control panel. This was achieved by sending a trip signal or reset signal to the microprocessor by pressing these buttons. Furthermore, a relay trip signal could be sent from the control panel to energise the relay coil on the DC board via the DSP relay after the smoothing capacitor was fully charged; as a result, the current limiting resistor was shortened by the relay as explained earlier in this chapter. This information was then received by the DSP microcontroller. Conversely, the microcontroller sends a package of data to the LabView control panel for real-time monitoring, including ADC readings of the current sensors, the ZCD board readings, and the interrupt service routine ISR count and execution time in addition to using StorData when needed. The LabView control panel is shown in Figure 6.9.

The software was written to implement the symmetrical duty cycle control digitally on the DSP microcontroller. The programming structure is shown in Figure 6.10. This structure shows that the process is started by the declaration of all variables followed by the definition of all calibrated values of the measurement units. Then, a series of DSP initialisation steps is performed, such as the initialisation of system control and the interrupt vector table, and

initialisation of the CPU timer, configuring the general purpose input output GPIO pins, initialisation of the PWM and ADC sequencer. After executing the initialisation code and functions, the LabView data exchange starts to communicate with the DSP microcontroller.

In this code, the ADC sequencer is configured to convert ADC inputs in the simultaneous pairs with an ADC clock speed of 8.33 MHz (120 ns). This sequencer is triggered by the PWM carrier, which was set to be equal to the supply frequency in this test. The interrupt service routine (ISR) of the DSP was set to trigger at the same frequency which was similar to supply frequency (i.e. the carrier frequency is set to be equal to the supply frequency). In consequence, the switching frequency can be considered to be low, as its value lies between 50-480 Hz. Care was taken with the time base clock TBCLK register division, so that it could deal with these frequencies.

After acquiring all data samples by the ADC, an interrupt is generated which will start the ISR. The ISR contains the commands which are required to implement symmetrical duty cycle control.

During this ISR, several calculations are performed, such as of the new frequency, by sensing the first and second rising edges of the input voltage, the duty cycle, the switch-ON time, the turn-OFF angle (γ), the delay, and the values required to configure all six PWM module registers to generate the desired pulses for all IGBT switches.

6.6 Summary

The experimental laboratory test bench setup is described in general in this chapter. The system is divided into four main parts: the power generating unit i.e. (PMA) generator; the power stage, which includes the three-phase FCSC converter; the measurement sensors and equipment; and the control unit, which is based on a Spectrum Digital eZdsp Texas Instruments TMS320F28335 DSP and National Instruments LabView control panel.

A software development tool using Code Composer Studio CCS is described. Also, the control software is developed to implement the symmetrical duty cycle control for the three-phase FCSC converter, as explained. Furthermore, the development of the graphical user interface via a National Instruments LabView environment for controlling and monitoring purposes on a host computer is also presented.



Figure 6.9 National Instruments LabView panel

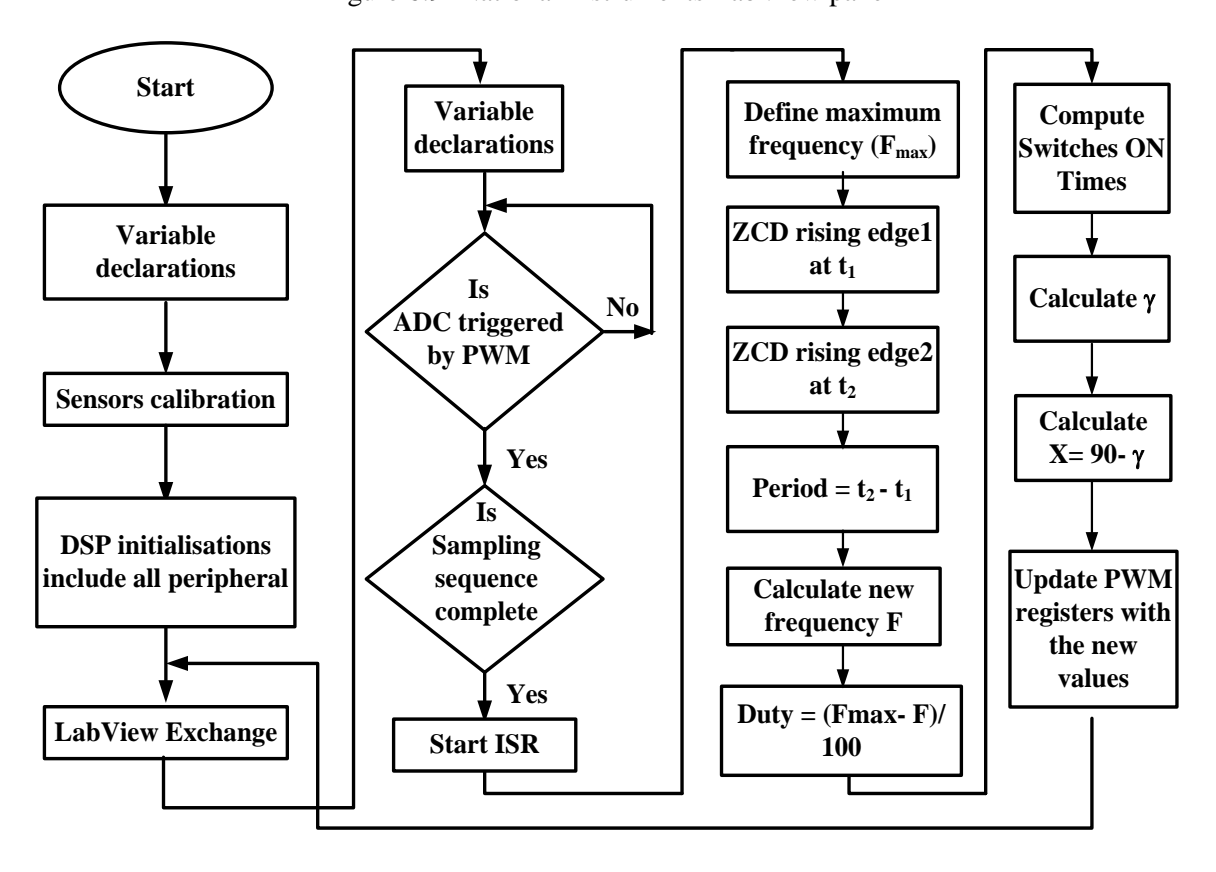


Figure 6.10 The CCS software structure

The experimental results acquired via the hardware and software implementation of the test rig are presented in the next chapter. In addition, an analysis and discussion of these experimental results is presented, to investigate the functionality of the three-phase FCSC converter when employed in a variable-voltage variable-frequency system with frequency range of 50-480 Hz.

Chapter 7. Experimental Results and Analysis

In Chapters 4 and 5, the simulation results showed that the three-phase FCSC with SDCC is capable of correcting the power factor to approximately unity when interfacing the PM generator employed in a VVVF system, which typically suffers from a poor power factor. Furthermore, applying symmetrical duty cycle control to the three-phase FCSC-rectifier enables a better utilisation of the PM generator at different frequencies, and increases output power in addition to output voltage levels. However, it is necessary to verify the simulation results experimentally by building a practical test bench to achieve a robust assessment of the converter's performance under such operating conditions.

This chapter presents the experimental results obtained when the test bench and equipment described in Chapter 6 were implemented. A Texas Instruments TMS320F28335 DSP and a National Instrument LabViewTM platform were used in the experimental test to implement the SDCC control scheme in a real-time environment. All the results have been obtained when the system was supplied with a variable line-to-neutral voltage range of 50-100 V and a variable operating frequency of 50-480 Hz. The impact of the unavoidable AC power source distortion is presented as a first step in the analysis of the practical results in section 7.1. To investigate the impact of employing the three-phase FCSC in the proposed application, the experimental tests are first carried out using only the three-phase conventional diode bridge rectifier, and then tested again when the three-phase FCSC-rectifier is included in the system. The experimental test results are obtained under different load conditions, including fixed and variable resistive load, for both circuit configurations. Finally, an assessment of the FCSC's rectifier performance in terms of load voltage, load current, input current, output power, and input power factor is presented by comparing the experimental results for the conventional three-phase rectifier with those of the three-phase FCSC-rectifier at different operating conditions. A current harmonic distortion analysis was also performed to evaluate the threephase FCSC converter for employment in aerospace applications. It is worth mentioning that, although this converter is proposed for airborne applications operating within a 'wild frequency' of 350-800 Hz (not to be confused with the term wide frequency), the system is tested for a maximum frequency of 480 Hz. This is mainly because the operating frequency range of the power supply unit is 45-500 Hz; in addition, most of the circuit components are designed to be used at a frequency of 50/60 Hz such as the three-phase inductors and the capacitors. This means that they will be used in a test with approximately ten times the nominal operating frequency, which increases the electrical losses. To avoid component failure, the frequency range was therefore limited to a maximum of 480 Hz. The maximum frequency of the test spectrum was selected to be 480 Hz because of the availability of the value of capacitance required to compensate for the inductive reactance.

Furthermore, the limits in the operating frequency range of the AC power supply unit prevent the converter being experimentally tested under low frequency variations, such as the wave energy converter frequency range of (1-5 Hz). Therefore, the converter performance is experimentally tested only under the frequency variation range of 50-480 Hz.

7.1 Realisation of the Programmable AC Power Source Distortion

As referred to in Appendix D, the power supply unit used to emulate the PMA generator suffers from distortion in the output voltage waveforms. An analysis of harmonic distortion can be found in this appendix. This analysis reveals a dominant harmonic component at 20 kHz which interferes with the unit's output voltage at different operating frequencies. In addition, other harmonic components can be seen in the output of the supply, but these are generally much smaller such as 800 Hz 1200 Hz 2 kHz. To investigate the effect of the output voltage distortion on the converter's behaviour, an approach is used which involves the acquisition of the experimental data of the power supply voltage waveforms under certain operating conditions. This is then fed into SABER to enable the circuit simulation to be performed under the same operating conditions. The voltage and current waveforms resulting from the simulation are then compared with the experimental test results. As this thesis is concerned principally with power factor correction, the comparison focuses on the relationship between current and voltage. The experimental waveforms are then compared with the simulation results for the purposes of verification.

The experimental and simulation tests are carried out at an operating frequency of 400 Hz/90 V line-to-neutral voltage with a load resistance of 30 Ω . This operating frequency is selected because it is considered to be a typical aircraft frequency.

Figure 7.1 shows the output of the three-phase voltage waveforms supplied by the power supply unit, and the same waveforms are used to simulate the circuit to ensure that the same input feeds the converter in both the experimental test and the simulation.

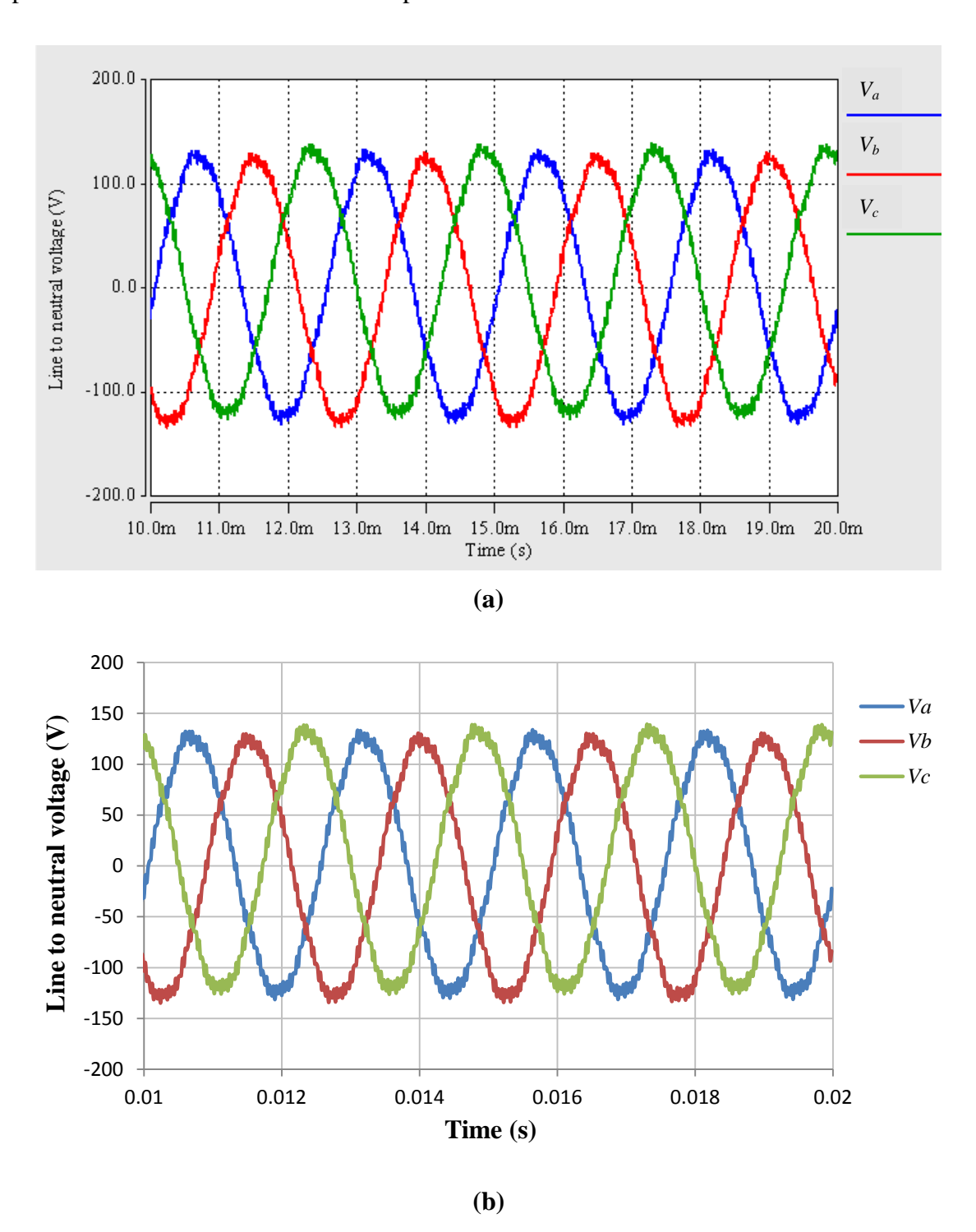


Figure 7.1 Three phase line-to-neutral voltage waveforms: (a) SABER voltage source waveforms; (b) acquired experimental power supply voltage waveforms

In spite of the distortion in the voltage source, the current waveform is approximately sinusoidal in both tests, as shown in Figure 7.2.

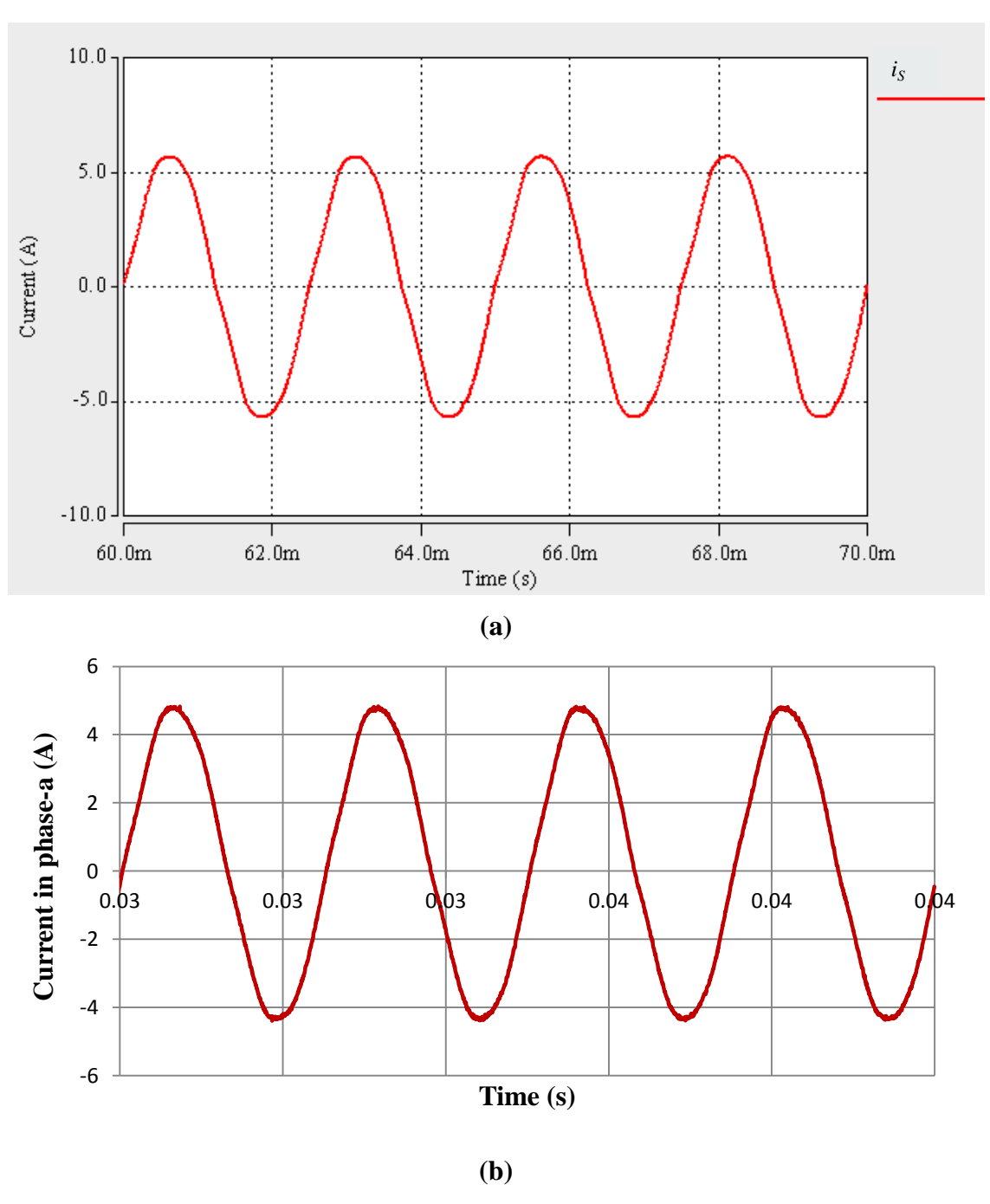


Figure 7.2 Current in phase-a shape in experimental and simulation tests; (a) phase-a current in SABER; (b) acquired experimental phase-a current

By running the simulation of the circuit model with the power supply voltage waveforms, the input current and voltage waveforms relationships in all three-phases are shown in Figure 7.3. This figure shows that the input current waveform is in-phase with the voltage waveform in all phases. Similarly, the input current waveform is in-phase with the voltage waveform during the experimental test, as shown in Figure 7.4. The input current is in-phase with the voltage waveform and the current is approximately sinusiodal.

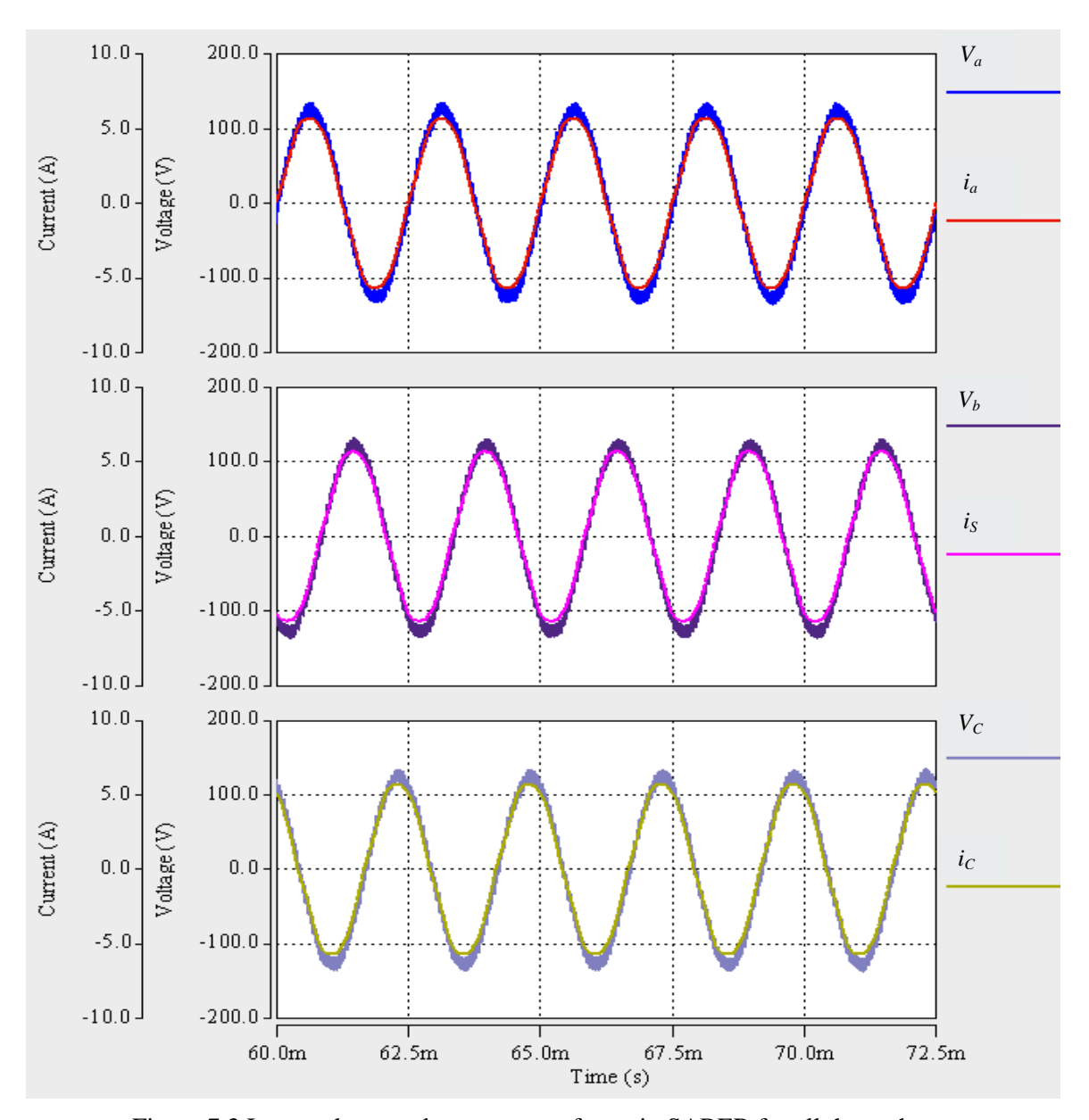


Figure 7.3 Input voltage and current waveforms in SABER for all three phases

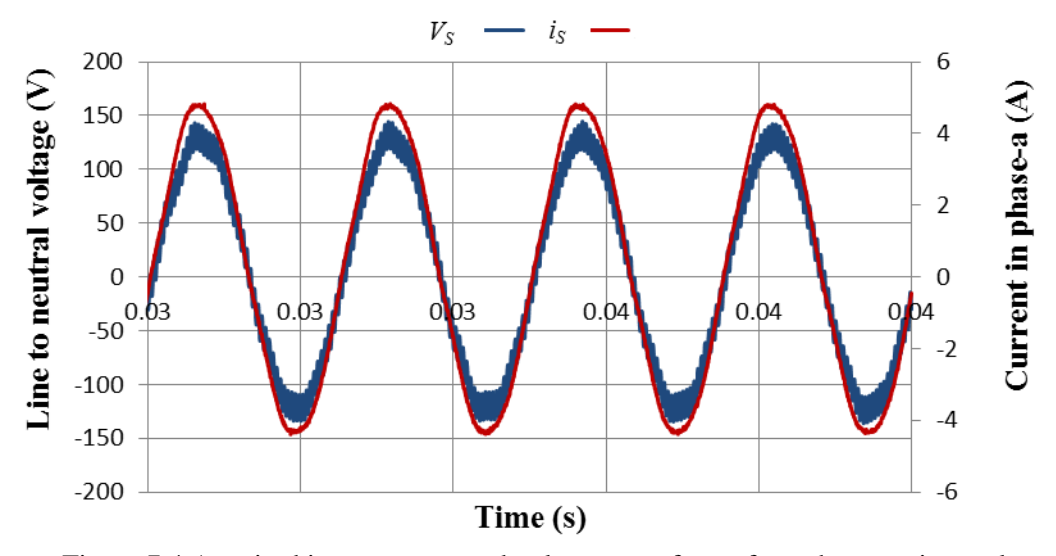


Figure 7.4 Acquired input current and voltage waveforms from the experimental test

After data processing using FFT analysis, the input power factor is calculated to be 0.996 using the simulation results. Likewise, by processing the experimental data with the help of FFT, the input power factor is 0.995, which is very close.

The aforementioned comparison between the simulated distorted voltage waveforms and the experimental results shows that the distortion in the power supply unit has only a very slight impact on the power factor, and therefore this power supply switching frequency distortion will be ignored.

The experimental test was carried out by running the system with a conventional three-phase diode bridge rectifier only in the first instance followed by employing the three-phase FCSC-rectifier at the same operating conditions, to investigate the impact of employing the three-phase FCSC converter. The parameters of the prototyped experimental test bench are similar to those of the circuit parameters presented in Chapter 4. In both cases, the system is investigated as a function of load variations. In addition, all the recorded experimental results have been taken by varying the voltage and frequency simultaneously. The degree of frequency variation differs from that of the voltage variation; however, the same ratios of voltage (V_s) to frequency (F_s) are maintained in the test.

Furthermore, all results are captured for one phase only (phase-a) as it was assumed to be a balanced system. In the next sections, the recorded waveforms are presented mainly for the maximum, half of the maximum and minimum values of the frequency range (50-480 Hz). The experimental results are also acquired at the typical aircraft operating frequency of 400 Hz.

7.2 Experimental Results for a Three-Phase Diode Bridge Rectifier operating at Variable-Voltage and a Variable-Frequency Range of 50-480 Hz

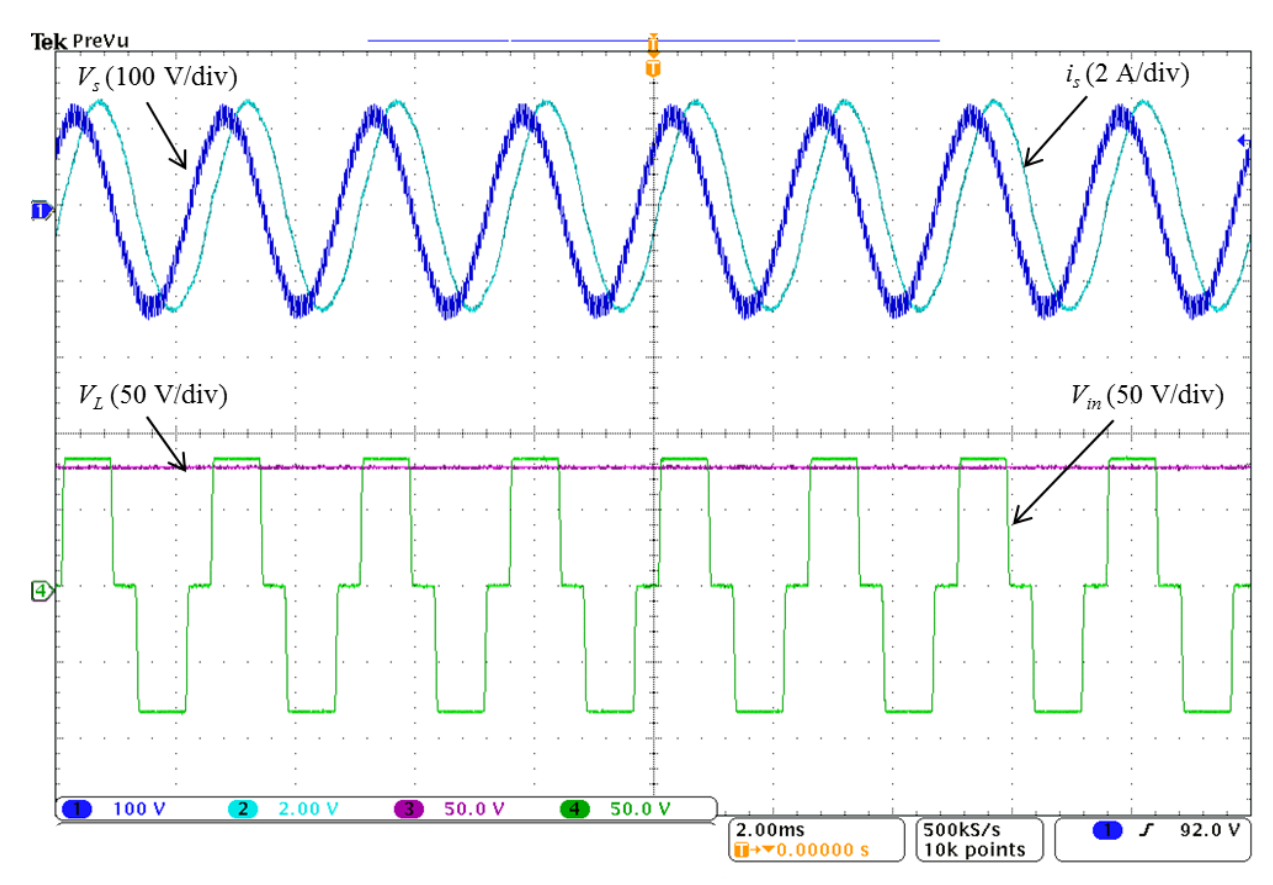
In this section, the results were acquired under different load conditions, including constant load and variable resistive load, as described below.

7.2.1 Operating with constant load

The experimental data is captured by varying the input line-to neutral voltage of the power supply unit from 100 V to 50V and simultaneously varying the frequency correspondingly from 480 Hz to 50 Hz, while maintaining a constant load resistance of 30 Ω .

Figure 7.5 shows the input line-to-neutral supply voltage (V_s) , the input current (i_s) , the average load voltage (V_L) and the rectifier input line-line voltage (V_{in}) . With an RMS value of the supply voltage of 90 V, the input RMS current was measured at 2 A using the oscilloscope. The output voltage is a DC voltage (V_L) which is converted by the three-phase rectifier; the average DC voltage was measured at 81 V, which means that the output voltage was less than the RMS phase-to neutral voltage of 90 V. The recorded results show that there is a voltage drop in the output voltage of the diode bridge rectifier circuit. This is caused by the current commutation during the overlap period due to the input high inductance and the internal circuit resistance in addition to the value of the operating frequency as explained earlier in Chapter 4. The simulation results in Chapter 4 show the same effect of the current commutation occurring during the overlap period, which leads to a reduction in the output voltage of the rectifier. The DC load current (I_L) value was recorded using the TTi digital multimeter and is equal to 2.7; this satisfies $I_L = V_L/R_L = 81/30 = 2.7$ A. Furthermore, the figure shows the input line-to-line voltage to the three-phase rectifier circuit V_{in} which is measured between phase-a and phase-b (V_{ab}) with a maximum value of 85.7 V. As expected, the rectifier input voltage is clamped by the smoothing capacitor voltage, which is about 81 V, and the diodes voltage drops. The lower oscilloscope traces in Figure 7.5 represent the DC load current and the rectifier output current. These traces verify that the rectified current consists of six pulses per one operating frequency cycle (i.e. 2.5 ms). The figure also shows that the average of the rectified current is equal to 2.74 A, which verifies equation (4-11) since the input RMS current is 1.93 A. Since the three-phase rectifier uses a smoothing capacitor, the ripple in the output voltage and current is very small and can be ignored. Figure 7.5 shows also that the input current is sinusoidal and lags behind the input voltage waveforms. The recorded input current and voltage were taken to be processed in SABER to calculate the fundamental components of voltage and current for power factor calculation.

After performing FFT, the phase-angle between the fundamental components of the supply voltage and current was calculated to be 55.15°. This means that the circuit's operating input power factor is 0.571. The experimental voltage and current waveforms for selected frequencies are shown in Appendix G, which includes the test results under the maximum, the minimum and half of the frequency range values.



Time (2 ms/div)

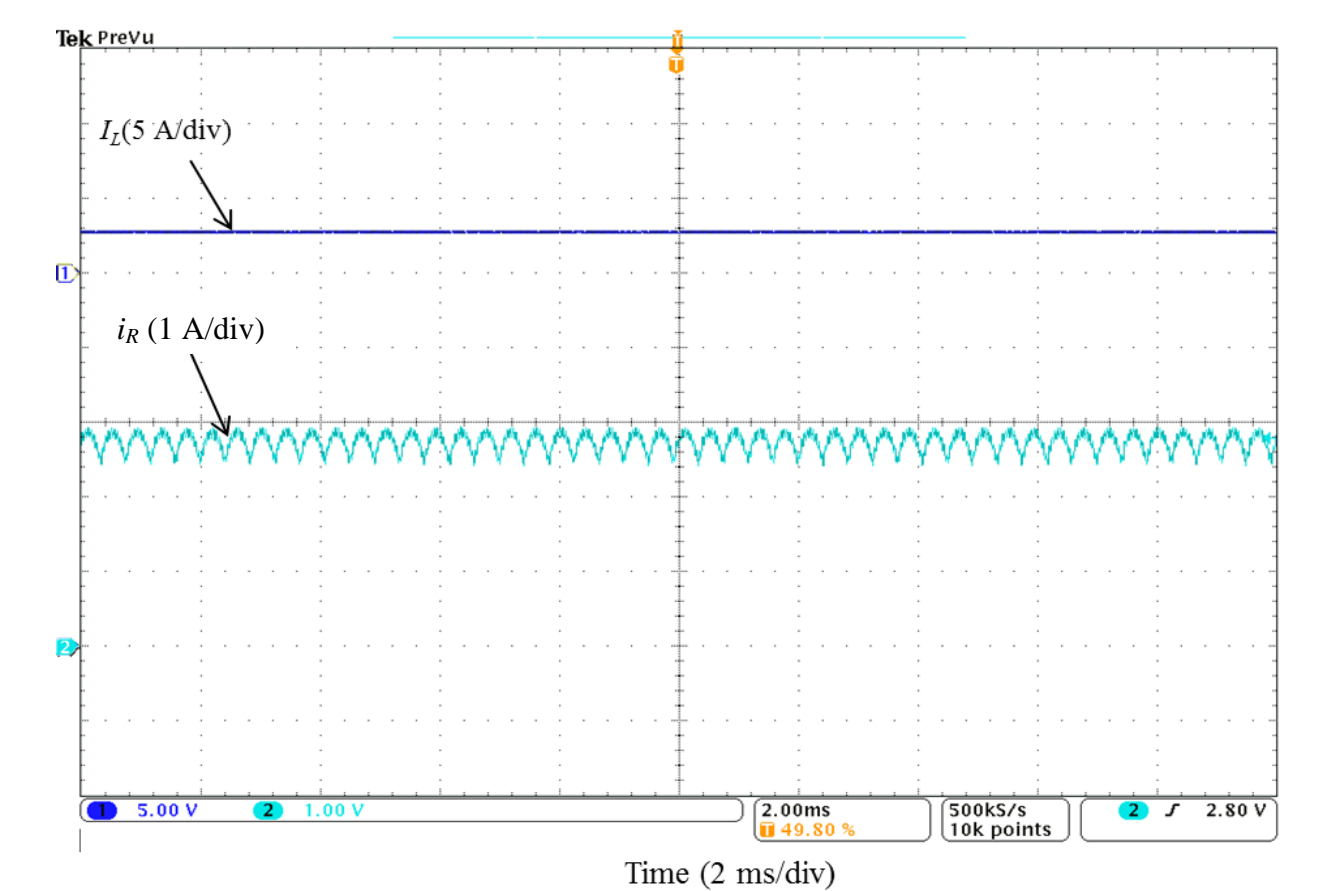


Figure 7.5 Voltage and current waveforms under $F_s = 400$ Hz, $V_s = 90$ V and $R_L = 30$ Ω 158

Furthermore, the rectifier circuit is examined when increasing the operating frequency from 50-480 Hz and the supply voltage from 50-100 V simultaneously in different steps, while maintaining the same load condition of R_L =30 Ω . The measurements acquired show that the load voltage is reduced when both voltage and frequency are increased, as shown in Figure 7.6. The figure illustrates that, although the input voltage increases, the average output load voltage is reduced. Since the inductive reactance (X_L =2 π Fs L_s) is large at higher frequencies, the voltage drop across it will be also large, which leads to a reduction in the average output voltage. This occurs as long as the time constant τ is greater than the frequency cycle (τ > 1/ F_s) which ensures that the load capacitor will not be discharged quickly. However, at the minimum frequency (F_s =50 Hz) τ is smaller than 1/ F_s . Therefore, the voltage is reduced since the capacitor is discharged quickly. The recorded result match closely the simulation results presented in Appendix C (Figure C.5). Figure 7.6 also shows that the input AC current is reduced by increasing the voltage and frequency.

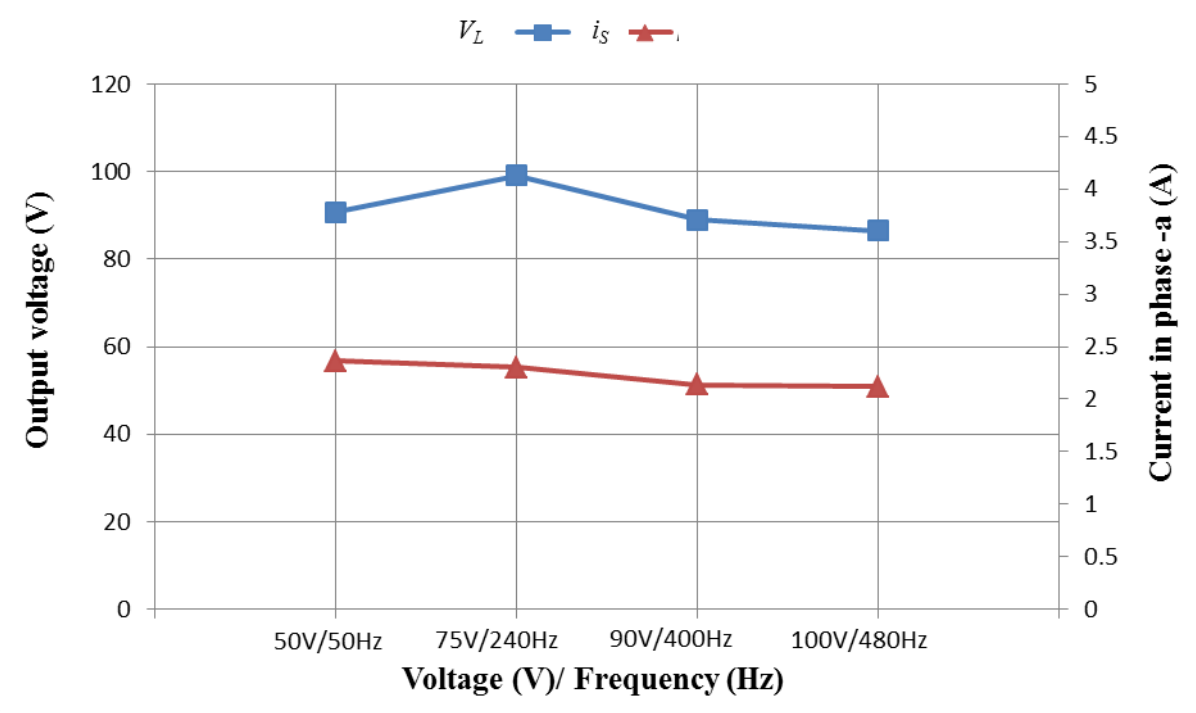


Figure 7.6 Output voltage and current under constant load (R_L =30 Ω) (conventional rectifier)

Figure 7.7 shows that the power factor is poor at the higher frequency of 480 Hz and its value improves when the frequency is reduced to 50 Hz. As explained in Chapter 3, the power factor is a function of the displacement and distortion factors, and at low frequency the distortion factor is low which reduces the power factor in spite of a high displacement factor. This corresponds to the simulation results demonstrated in Appendix C (Figure C.6).

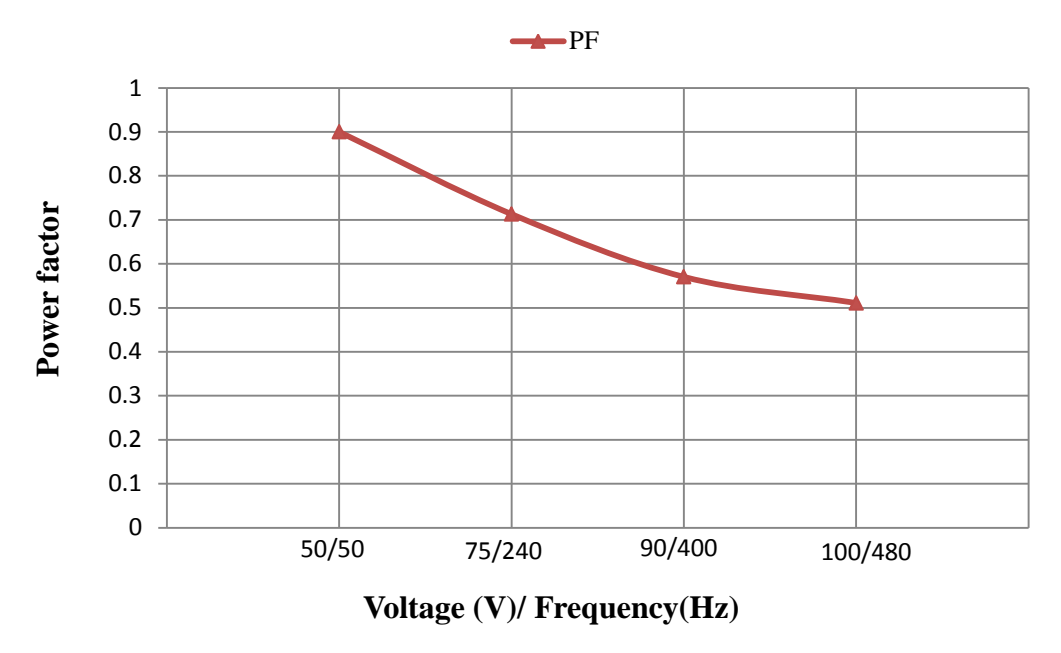


Figure 7.7 Power factor under constant load (R_L =30 Ω)(conventional rectifier)

7.2.2 Operating with variable load resistance

The performance of the conventional rectifier is tested at different supply voltage and frequency values in addition to load variations. The load resistance is varied between 10-30 Ω with steps of 5 Ω .

As explained in the previous section, the average output voltage is reduced when increasing the supply voltage and frequency and, as expected, this voltage is lower at higher load current, as illustrated in Figure 7.8. However, Figure 7.9 reveals that the input current is higher at the lower load resistance of 10 Ω , which is because the load current is at a maximum value at lower resistance. Also, the figure shows that the reduction in currents is significant at low frequency and voltage (50 V/50 Hz), while a slight current variation occurs at maximum frequency.

The results are then processed to calculate the power factor. Figure 7.10 illustrates that the input power factor is very low at high supply voltage and frequency of 100 V/480 Hz, with a value of 0.311. Similarly, at a frequency of 400 Hz (typical aircraft frequency), the power factor is very poor with a value of 0.358, and even with increasing load resistance the power factor continues to be poor with a value of 0.5 at both frequencies. On the other hand, at lower supply voltage and frequency such as 50 V/50 Hz, the power factor is higher with a value of 0.85 with a small improvement with varying load resistance.

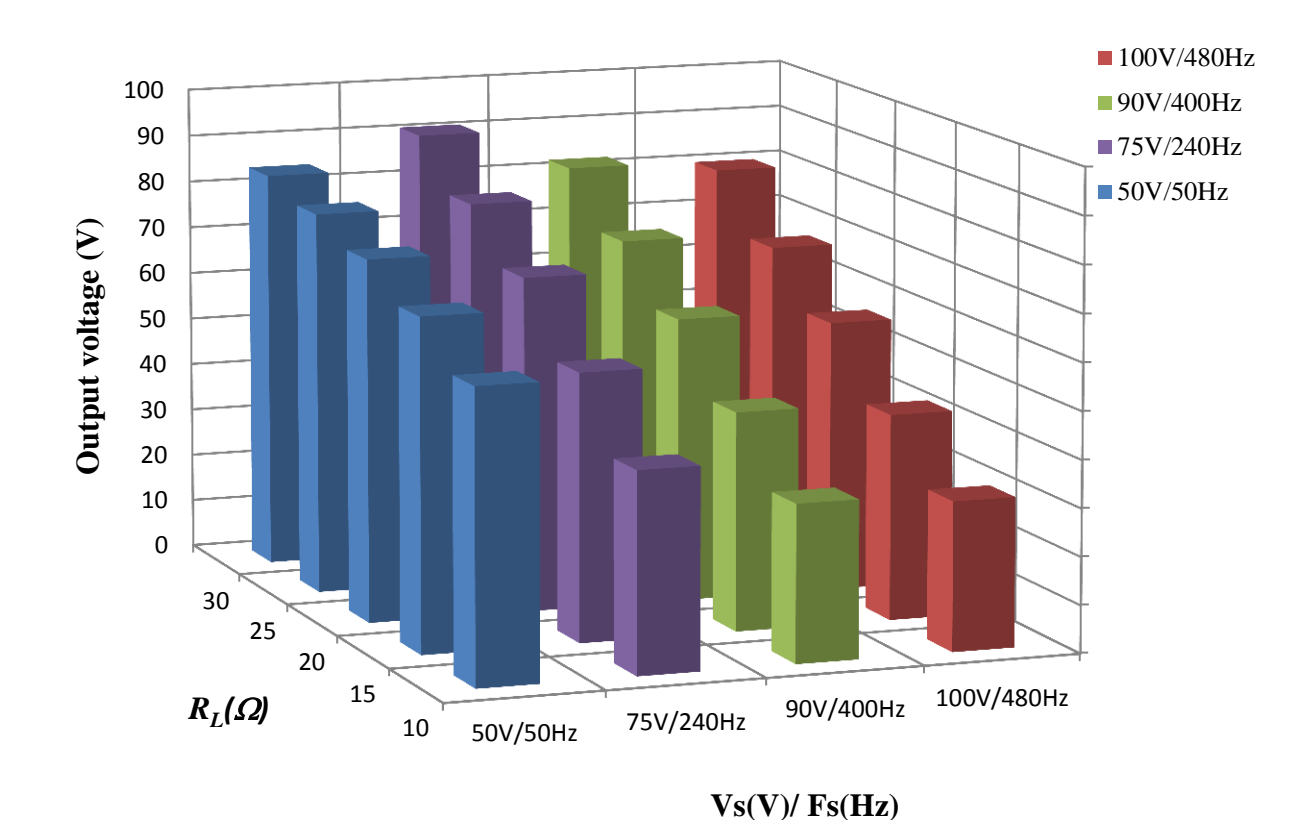


Figure 7.8 DC output voltage as a function of supply voltage and frequency variations (conventional rectifier)

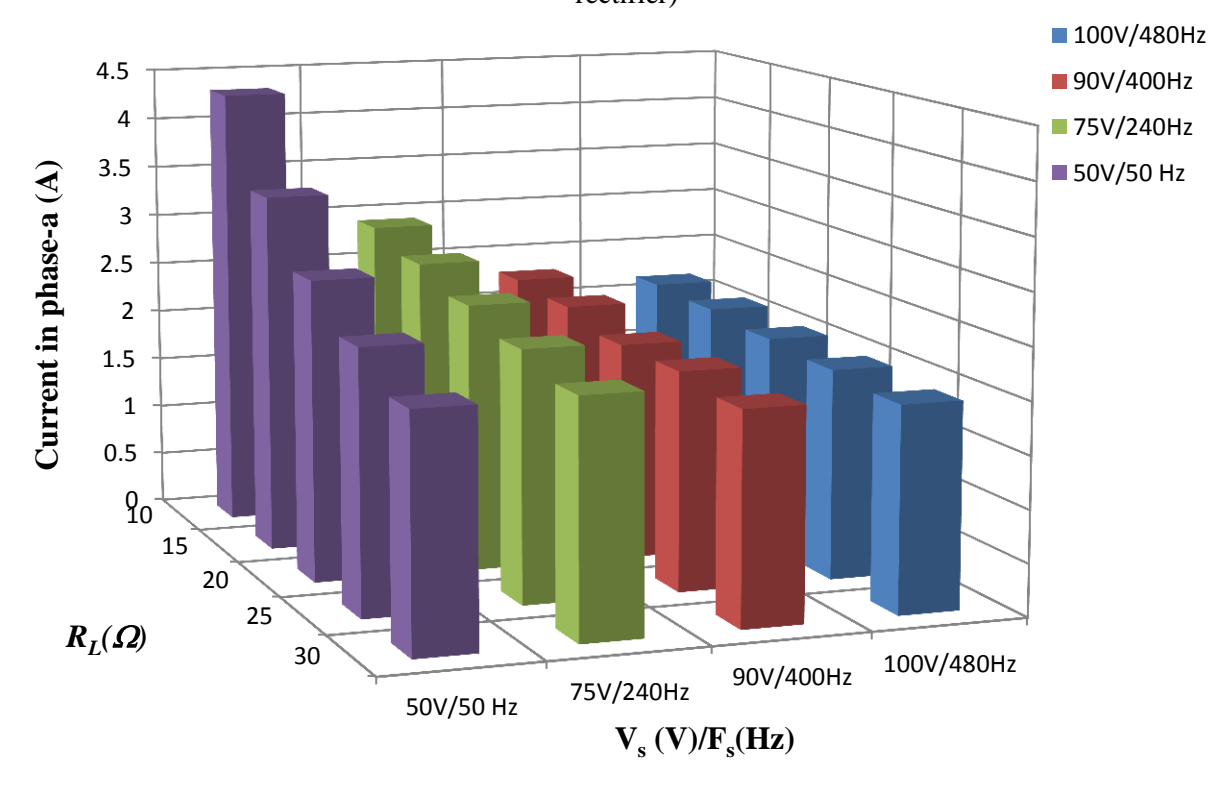


Figure 7.9 Input current as a function of load resistance and supply voltage and frequency variations (conventional rectifier)

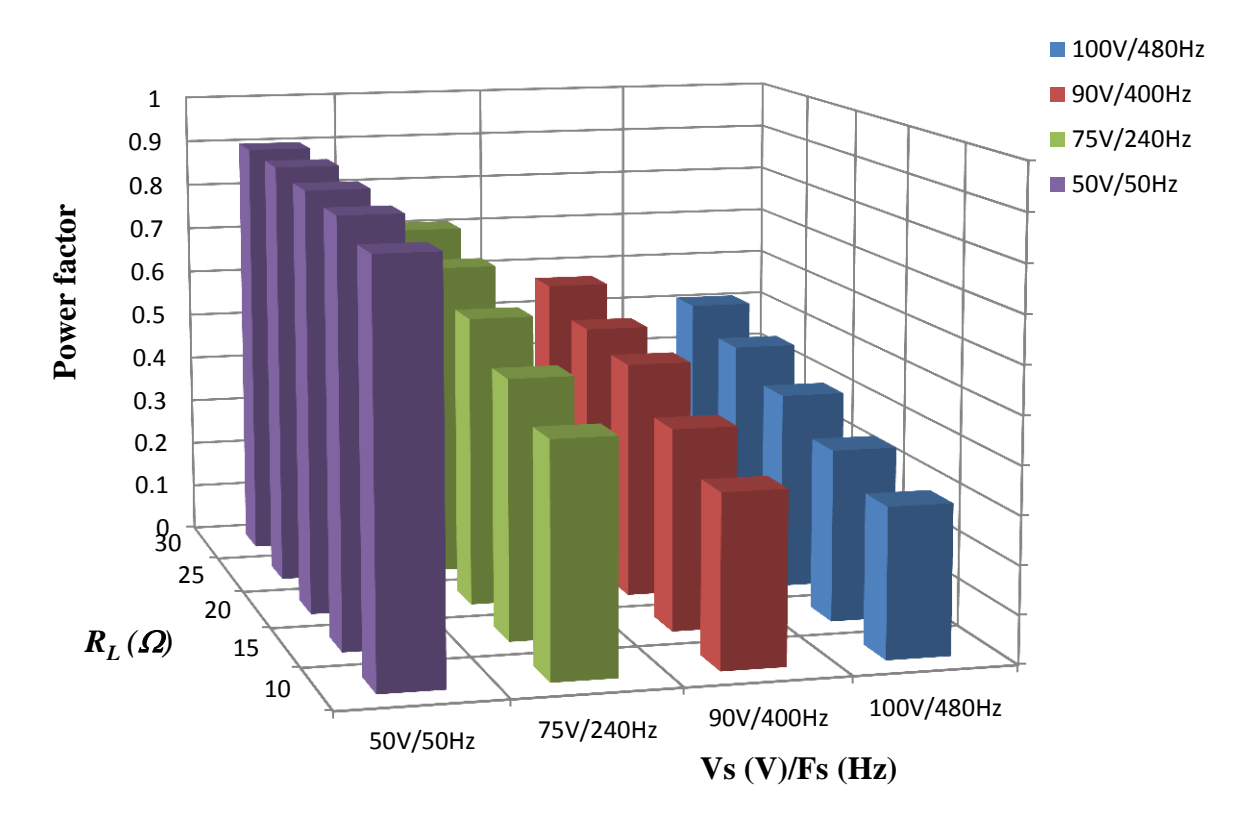


Figure 7.10 Power factor as a function of load resistance and supply voltage and frequency variations (conventional rectifier)

Therefore, employing the conventional three-phase rectifier alone at frequencies as high as 400 Hz is not recommended since the power factor is very poor.

7.3 Experimental Results for a Three-Phase FCSC-rectifier operating at Variable-Voltage and a Variable-Frequency Range of 50-480 Hz

The three-phase FCSC converter is tested to provide a power of 1 kW only to the DC load due to the limitations of several of the circuit components, as explained in Chapter 6. The same procedure described in Section 7.2 is followed to vary the supply voltage and frequency simultaneously.

Similarly, the converter is tested under constant load and variable load resistance. Likewise, to calculate the power factor, the data are acquired and then processed using FFT analysis with similar settings to the FFT analysis presented in the previous chapters.

7.3.1 FCSC operating with constant load

Measurements are taken by varying the supply voltage and frequency while maintaining the load with a value of 30 Ω . All recorded AC measurements are captured for phase-a only.

Figure 7.11 to Figure 7.14 show the circuit waveforms at different supply voltages and frequency values when implementing a symmetrical duty cycle control SDCC with the three-phase FCSC converter. Each figure consists of two sets of results, with the first showing the line-to-neutral supply voltage V_s for phase-a, the input current i_s , DC load voltage V_L , DC load current I_L . The second set presents the voltage across the series capacitor of phase a V_{CC} and the pulses supplied to the switches S_1 and S_2 through one dual driving circuit board.

As explained in Chapter 5, since the maximum frequency value is assumed to be 480 Hz, all IGBTs are permanently OFF at this operating frequency, which means that the duty cycle is zero (i.e. the pulse width is zero), as shown in Figure 7.11. In this case, the input current is inphase with the supply voltage since the value of the series capacitance is selected to match the inductive reactance which leads to a reduction of the circuit impedance to its minimum value at this operating condition (which is the resonant condition). The ripple in the output voltage is very small as the ripple level depends on the chosen smoothing capacitor value.

When the frequency is reduced to 400 Hz, inductive reactance decreases. Therefore, the IGBT switches are switched ON for an interval of 2γ to maintain the resonance between the capacitive and the generator's inductive reactance. For this reason, the duty cycle of the IGBT switches is increased to 0.08 (see equation (5-5)). Subsequently, the FCSC converter is able to maintain the input current in-phase with the supply voltage as shown in Figure 7.12.

Furthermore, it is worth mentioning that the output voltage is 135 V, which is higher than the maximum input voltage V_{s_max} (127.2 V). This means that the FCSC converter is capable of increasing the load voltage to higher than the maximum system input voltage at load resistance of 30 Ω , which shows that the three-phase FCSC circuit is able to reduce the current commutation overlap intervals which cause the reduction in the output voltage. This behaviour closely matches the simulation analysis (Figure 5.28). In contrast, only employing the three-phase rectifier, leads to a significant reduction in the output voltage, as shown in Section 7.2, at different operating voltage and frequencies.

As expected, the load current is a DC current with an approximate value of 5 A, and since a constant load of 30 Ω was used the load current can be calculated as given below:

$$I_L = \frac{135 \text{ V}}{30 \Omega} = 4.5 \text{ A} \tag{7-1}$$

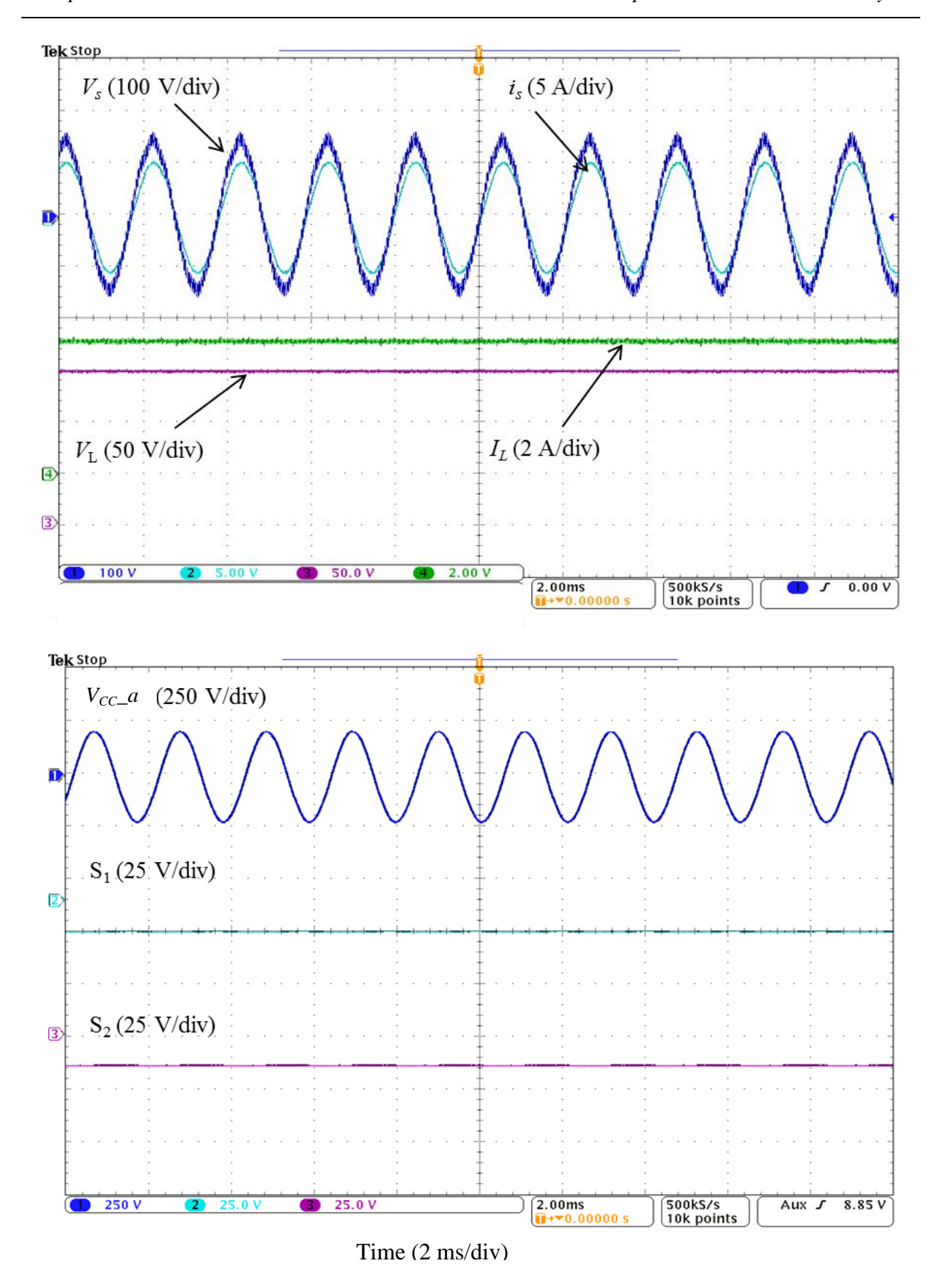


Figure 7.11 Circuit waveforms with $V_s = 100 \text{ V}$ and $F_s = 480 \text{ Hz}$ (FCSC circuit)

The second part of Figure 7.12 shows that the capacitor voltage is zero when S_1 and S_2 are closed consecutively in each half-cycle of the supply voltage; however, the series capacitor is charged to a certain voltage level when the IGBT switches are open because the current is passing through the capacitor in this case.

Based on the symmetrical duty cycle control scheme, a further increase in the duty cycle and hence in the switch ON time 2γ is required to cope with the frequency reduction while maintaining the current in-phase with the supply voltage. This is achieved in accordance with the reduction in supply voltage and frequency and is illustrated in Figure 7.13 and Figure 7.14.

These figures show that the current waveforms are almost sinusoidal at all values of frequency and voltage variation except at the minimum frequency spectrum value of 50 Hz. At this frequency, although the current is approximately in-phase with voltage, which means that the displacement factor is high, the current is clearly distorted and this affects the distortion factor and consequently the power factor value, as revealed in Figure 7.14. A similar distortion in the input current waveform was observed by simulation at the same frequency of 50 Hz (Figure 5.30). An additional trace for the rectifier output current (i_R) is added to Figure 7.14 as an example image of the rectifier output current. This trace clearly shows that the rectified current consists of six pulses per frequency cycle (20 ms) in this case. The distortion of these pulses is driven by the distortion in the input phase current. The average value of the rectified current verifies equation (4-11) with an approximate value of 4.6 A, since the RMS value of the current is 3.46 A in this case.

In conclusion, the recorded test results presented in the above figures illustrate that by applying symmetrical duty cycle control (SDCC), the FCSC converter is able to maintain the current approximately in-phase with the supply voltage at different supply frequency values, and the same finding is achieved in the simulation results presented in Chapter 5 (Figures 5.27-5.30).

The captured results for the FCSC-rectifier's output voltage and current at different voltage and frequency values are shown in Figure 7.15.

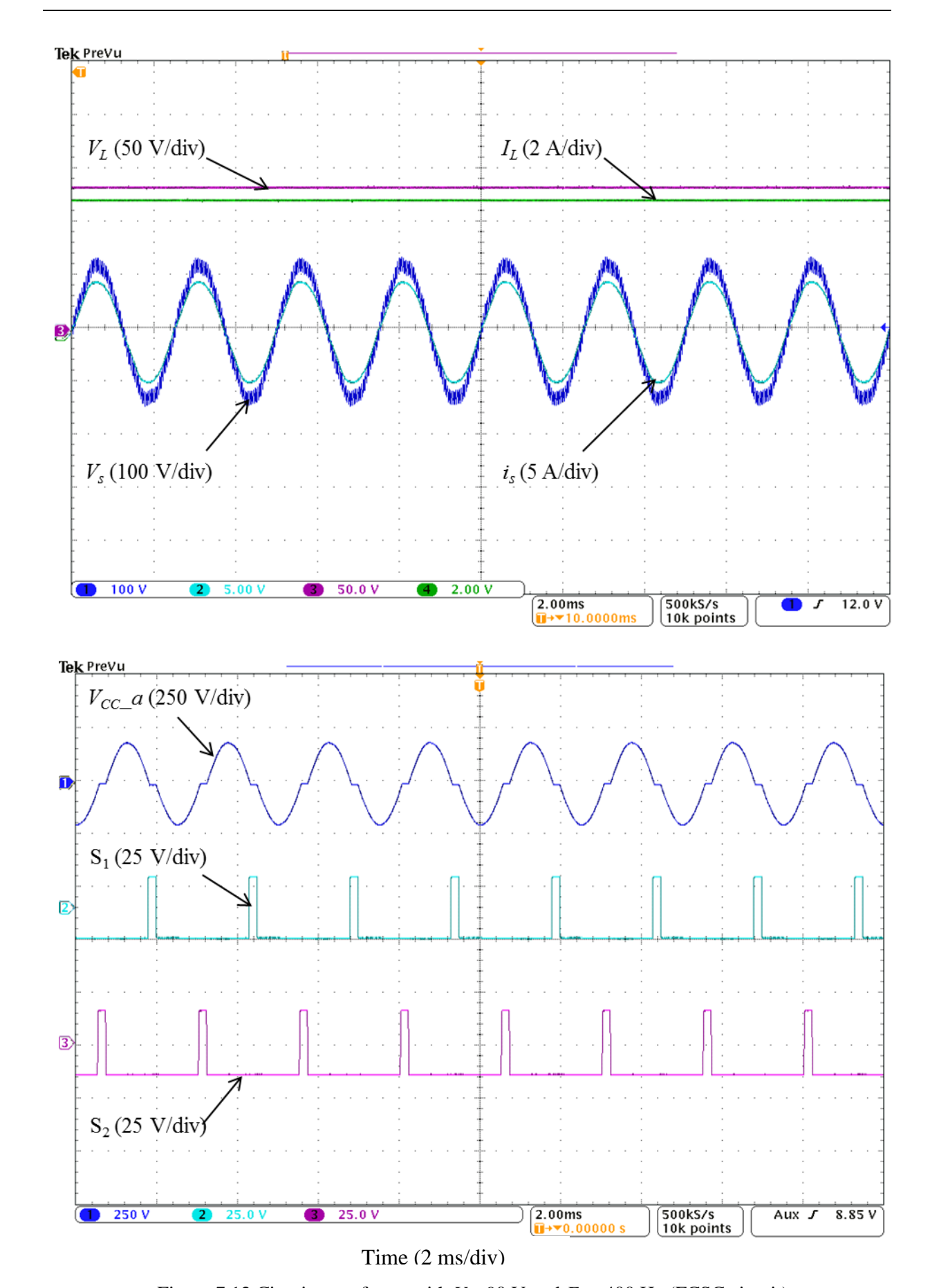


Figure 7.12 Circuit waveforms with V_s =90 V and F_s = 400 Hz (FCSC circuit)

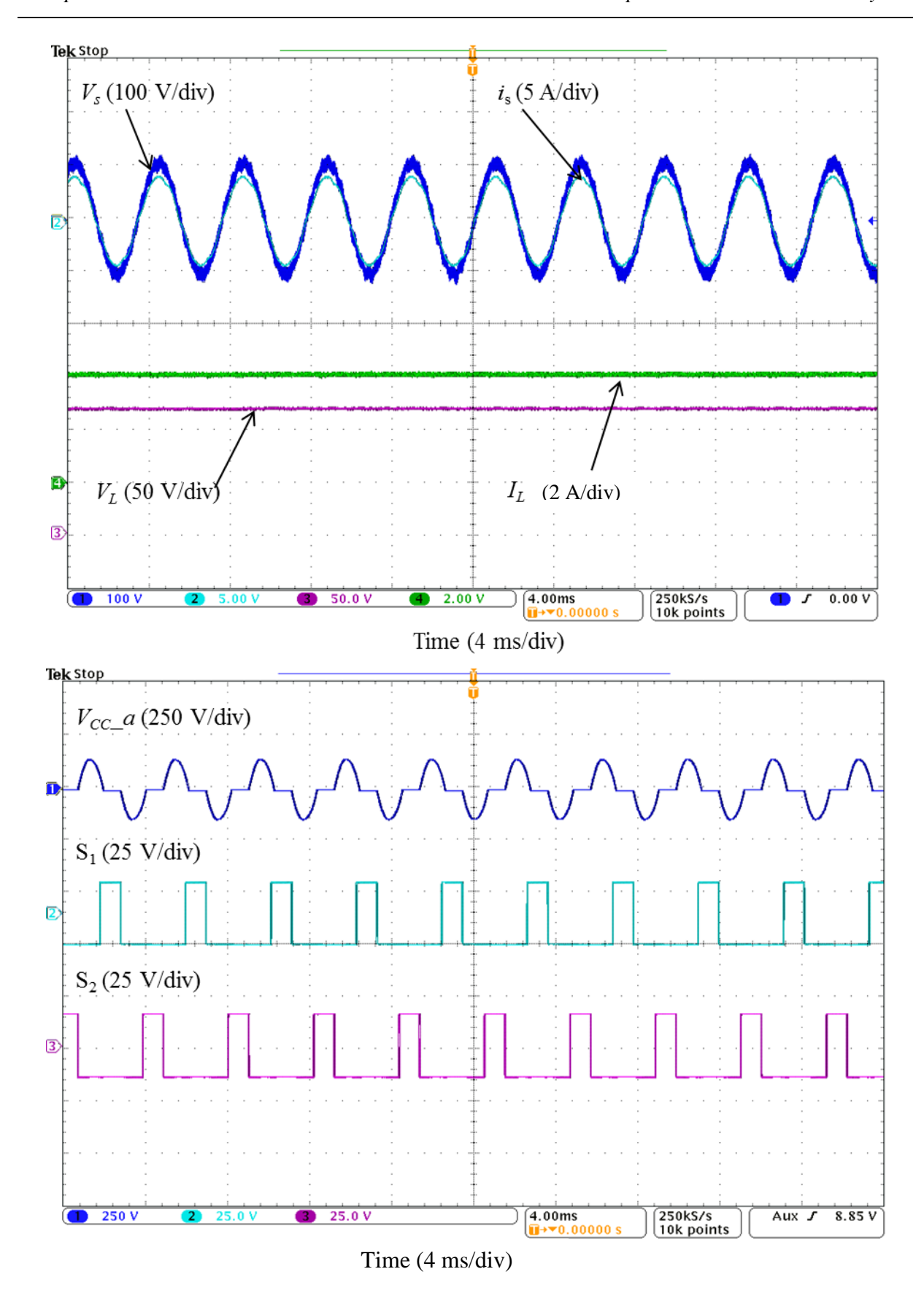


Figure 7.13 Circuit waveforms with V_s =75 V and F_s = 240 Hz (FCSC circuit)

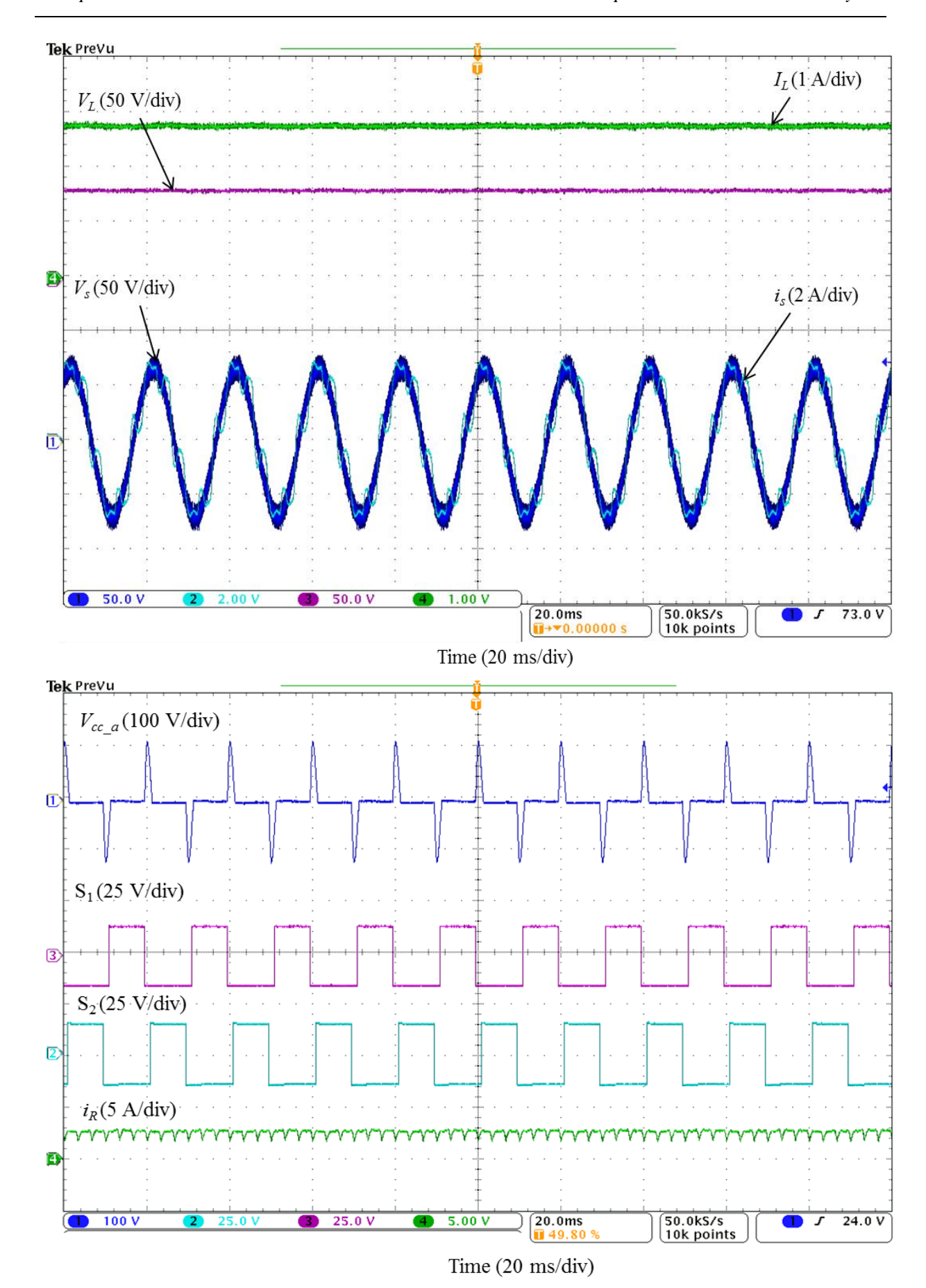


Figure 7.14 Circuit waveforms with $V_s = 50 \text{ V}$ and $F_s = 50 \text{ Hz}$ (FCSC circuit)

In contrast with the results when only employing the conventional rectifier circuit in the system, presented earlier in Figure 7.6, the output voltage increases linearly with input voltage even at higher frequencies; this reveals how the FCSC-rectifier is able to reduce the effect of current commutation in terms of the output voltage drop even at high frequencies.

Moreover, since the load is constant with a value of 30 Ω , the input current also increases when the output voltage is increased, as shown in Figure 7.15.

The acquired results are processed to calculate the power factor. The power factor is high at all frequency and voltage values, as shown in Figure 7.16. The figure illustrates that the input power factor is high even at the lower frequency value of 50 Hz with a value of 0.94, and its value increases to 0.99 at the higher frequency of 480 Hz. The higher values of power factor are driven by high values of the displacement factor and distortion factor.

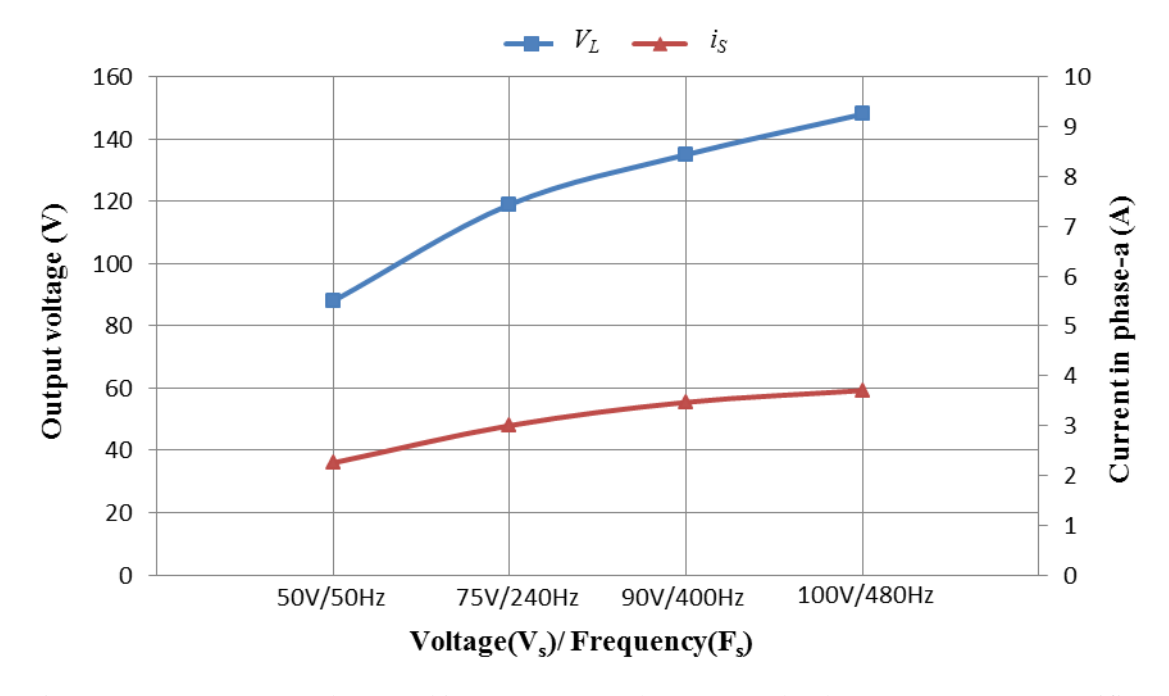


Figure 7.15 DC output voltage and input current under constant load (R_L =30 Ω)(FCSC-rectifier)

The experimental behaviour of the three-phase FCSC-rectifier under symmetrical duty cycle control validates the simulation results presented in Chapter 5. The measured values of load voltage, input current, and power factor match closely the simulation results presented earlier in Chapter 5 (Figure 5.31 and Figure 5.32).

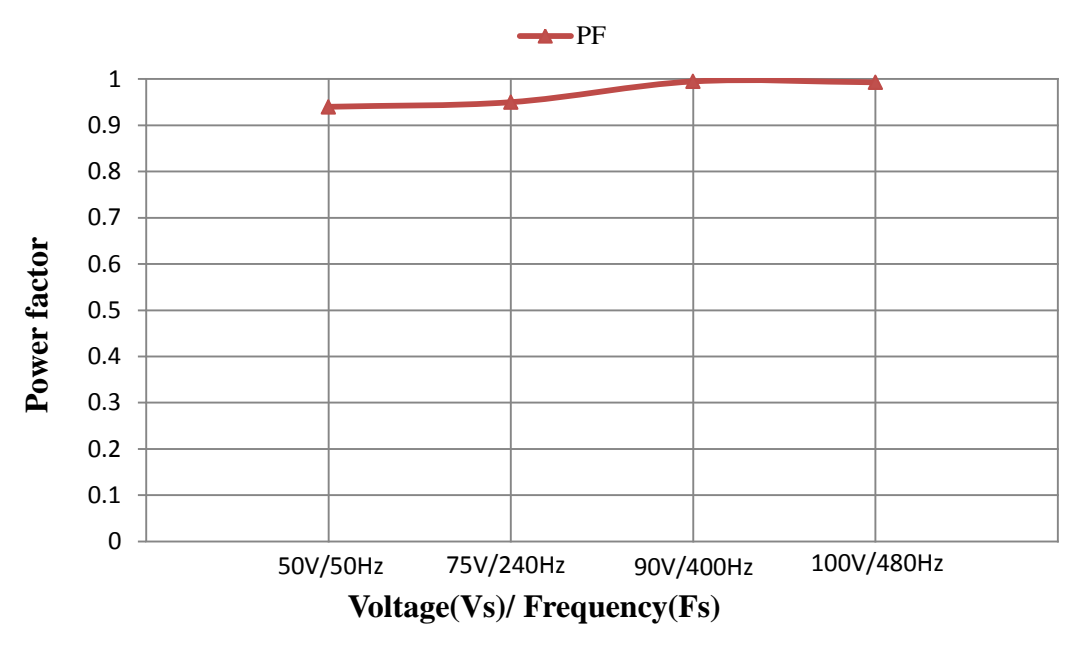


Figure 7.16 Power factor under constant load (R_L =30 Ω)(FCSC-rectifier)

7.3.2 Three-phase FCSC-rectifier under various load conditions

Similar to the analysis of the three-phase rectifier circuit only, the FCSC-rectifier is analysed under different load conditions by varying the load resistance between 10-30 Ω , in addition to varying the supply voltage and frequency simultaneously.

Figure 7.17 shows the output DC voltage across the resistive load at different supply voltage, frequency, and load resistance values. In this figure, it is clear that a higher output voltage is achieved at higher supply voltage and frequency (100 V/480 Hz) and the maximum voltage is captured at the maximum load resistance of 30 Ω . The figure also shows that the load voltage is reduced by reducing R_L at each V_s/F_s variation. As expected, the load current is reduced by increasing R_L based on the type of the load, as shown in Figure 7.18.

In addition, based on the equivalent circuit presented in Chapter 5, the input current is a function of machine resistance and the supply line-to-line voltage such as V_{ab} . By increasing the supply line-to-neutral voltage, the line-to-line voltage is increased ($V_{LL} = V_{ph} * \sqrt{3}$). By increasing the supply voltage and frequency, Figure 7.19 shows that the input current is increased and also a function of load; hence, the input current is also lower at a load resistance of 30 Ω .

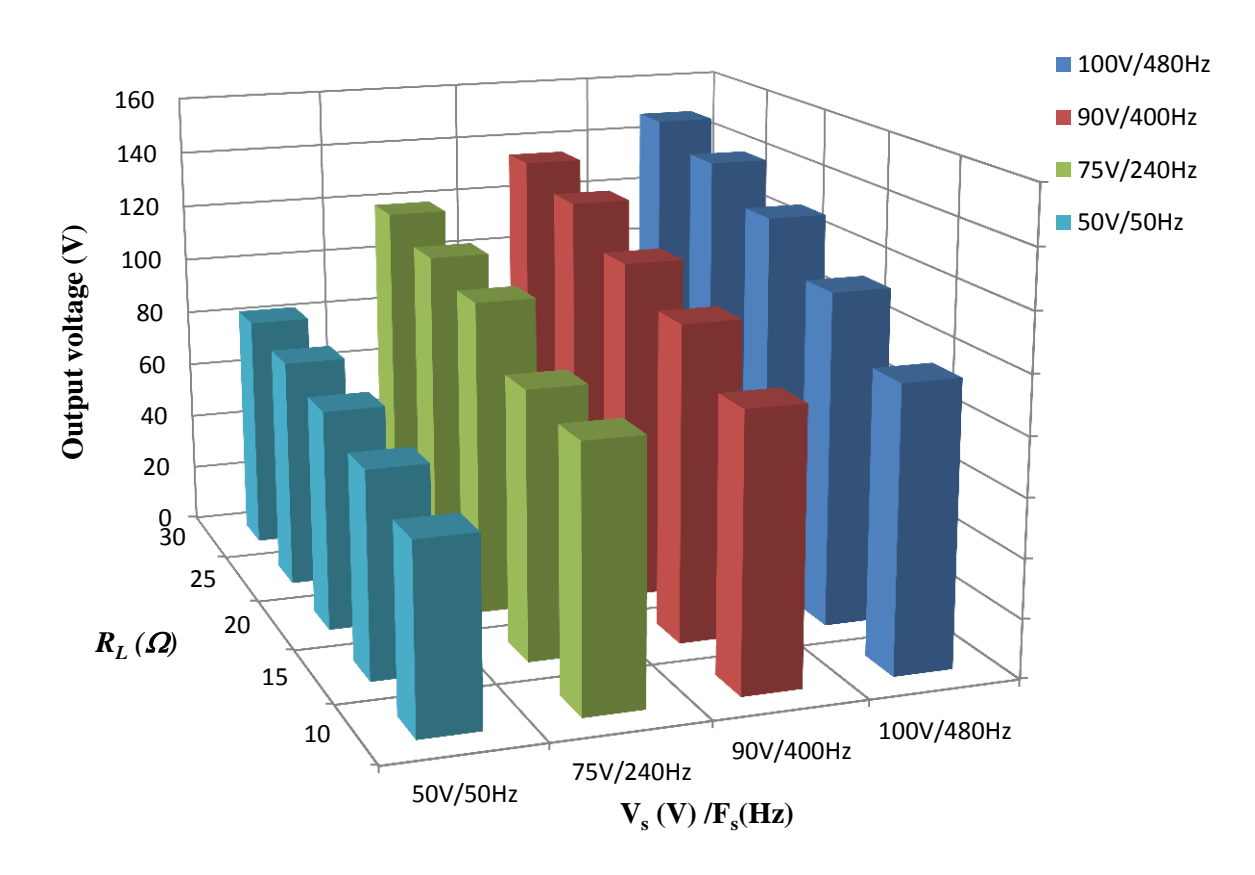


Figure 7.17 DC output voltage as a function of supply voltage and frequency variations (FCSC-rectifier)

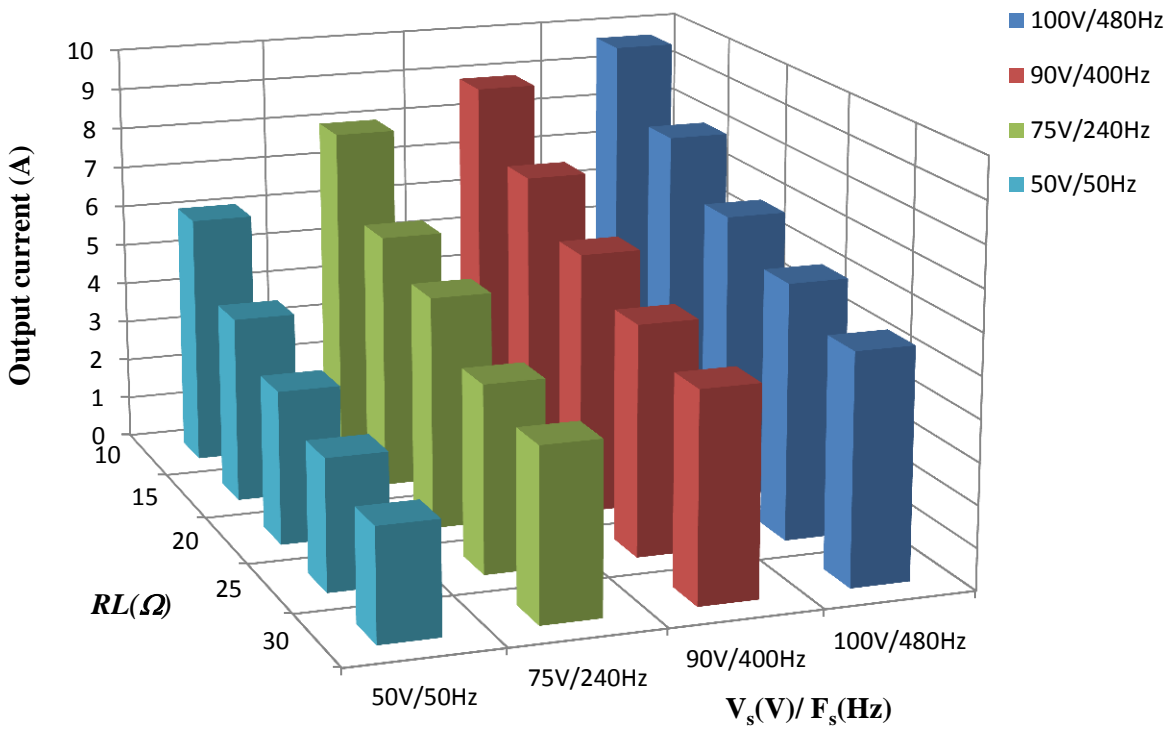


Figure 7.18 The output load current as a function of supply voltage and frequency variations (FCSC-rectifier)

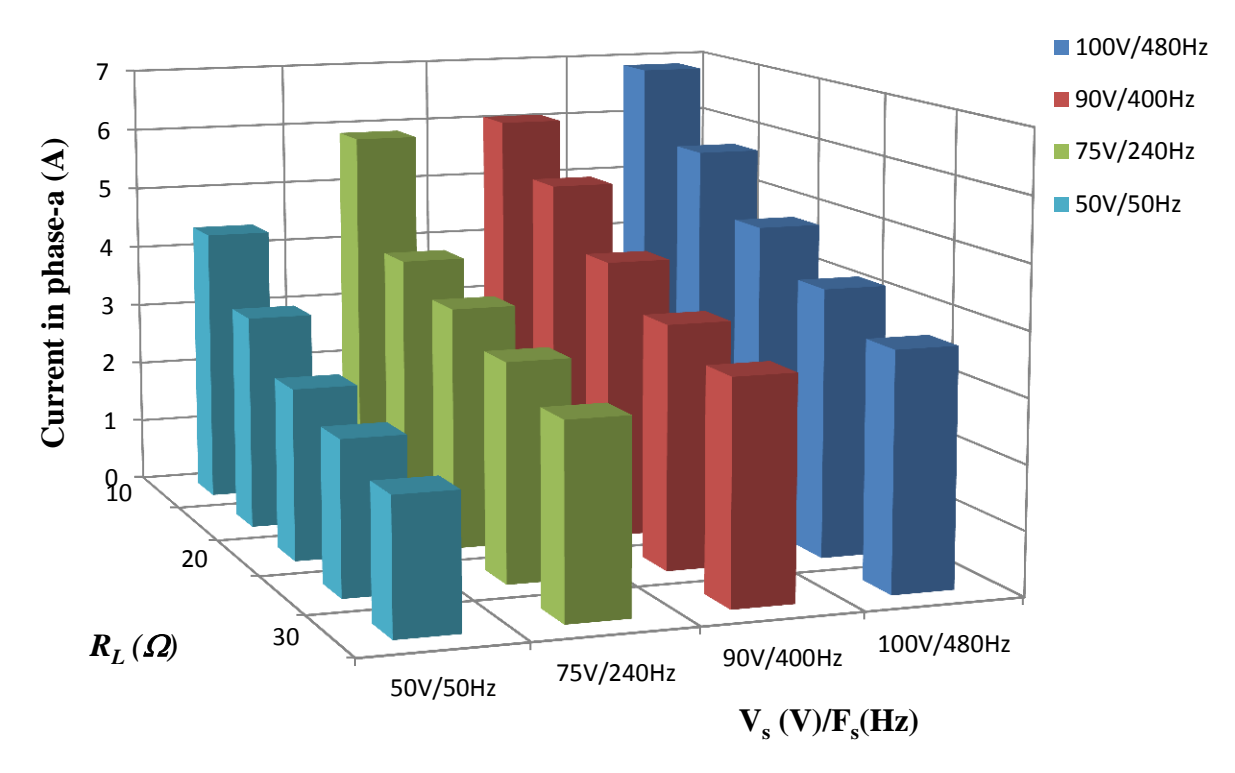


Figure 7.19 Input current as a function of supply voltage and frequency variations (FCSC-rectifier)

Figure 7.20 clearly shows that the input power factor is high at all values of supply voltage and frequency (the minimum value is 0.94). The higher power factor is achieved at the higher voltage and frequency of 100 V/480 Hz with a value of 0.994; however, the minimum value of power factor occurs at the maximum load resistance of 30 Ω with a value of 0.94, which has been recorded at 50 V/50 Hz. The figure also shows that the variation in load resistance has a small impact on the power factor at different voltage and frequency values. Similar FCSC-rectifier's behaviour has been observed under various load conditions in the earlier simulation analysis (Figures 5.34- 5.37).

It is worth mentioning that, although there is reasonable agreement concerning the behaviour of the FCSC-rectifier in both simulation and experimental results, there are differences in the magnitude of the results driven mainly by the design of the inductor on 50/60 Hz frequency and used over variable frequency range of 50-480 Hz, and Behlman power supply distortion (see Section 7.6 for more details).

7.4 Harmonic Analysis of the Three-Phase FCSC-Rectifier

To validate the harmonic analysis presented in Section 5.2. FFT analysis is carried out of the experimental results. The recorded results were processed to have one cycle of each waveform under various operating voltage and frequency and load conditions.

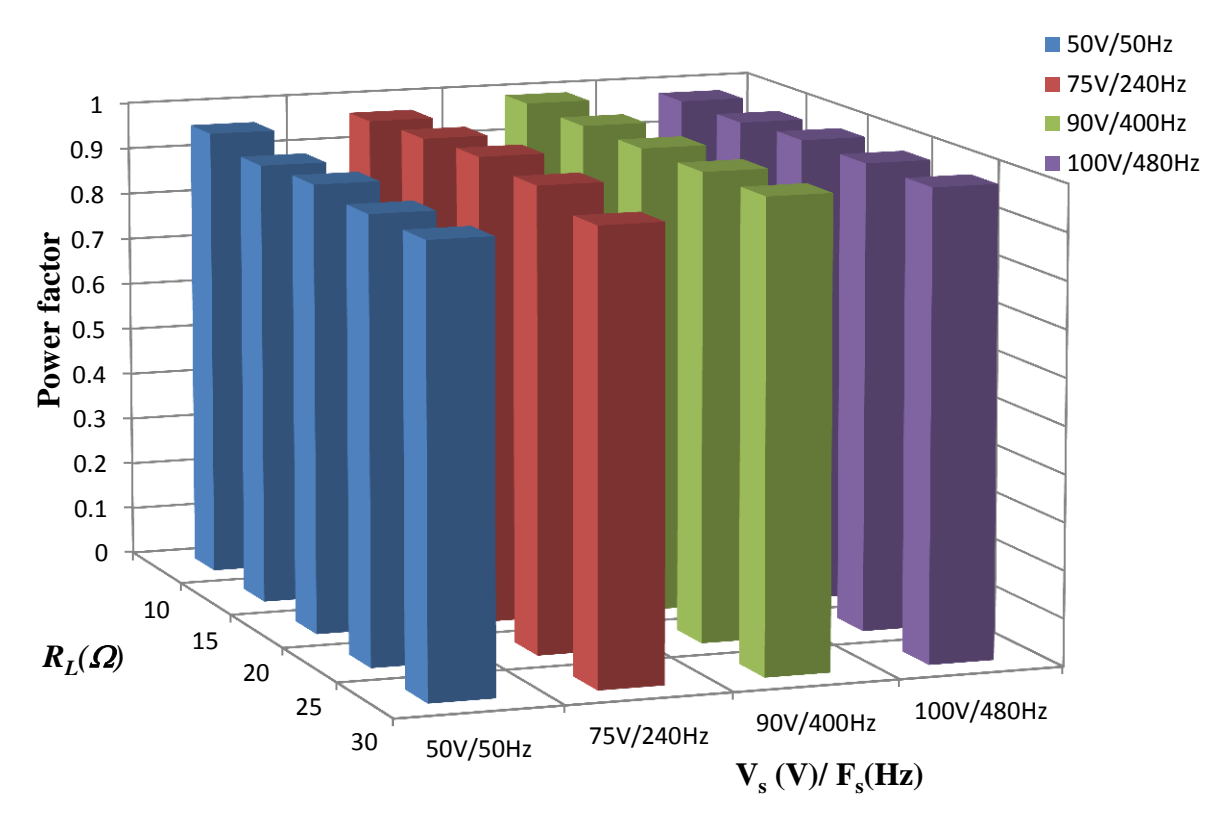


Figure 7.20 Power factor as a function of supply voltage and frequency variations (FCSC-rectifier)

Using the same assumptions seen in Chapter 5, the individual harmonics of the input current are then examined and compared with the limits for each harmonic imposed by RTCA DO-160. Figure 7.21 shows that at maximum voltage and frequency of 100 V/ 480 Hz, none of the individual harmonics exceed RTCA limits at the lower load resistance of 10 Ω . The figure also shows that at half of the maximum frequency of 240 Hz, the individual harmonics also fall within the limits except for the second harmonic order, which is slightly higher than the limits with a value of 0.7 $I_1\%$. However, at the minimum frequency of 50 Hz, the 5th and 7th harmonics considerably exceed RTCA limits with values of 17% and 10%, respectively.

When increasing R_L to 20 Ω , all the individual harmonics are lower than the RTCA limits at maximum and half of the maximum frequency of 480 Hz and 240 Hz respectively. At a frequency of 50 Hz, the 5th and 7th current harmonics also exceed the limits with values of 19%, 12.5%, respectively, as shown in Figure 7.22.

Figure 7.23 illustrates how increasing the load resistance to 30 Ω affects the individual harmonics at a frequency of 240 Hz. At this operating condition, the 5th and 7th harmonics are higher than the limits for frequencies of both 240 Hz and 50 Hz. However, all individual

current harmonics for 480 Hz are within the limits, although some harmonic orders have higher values at this load condition.

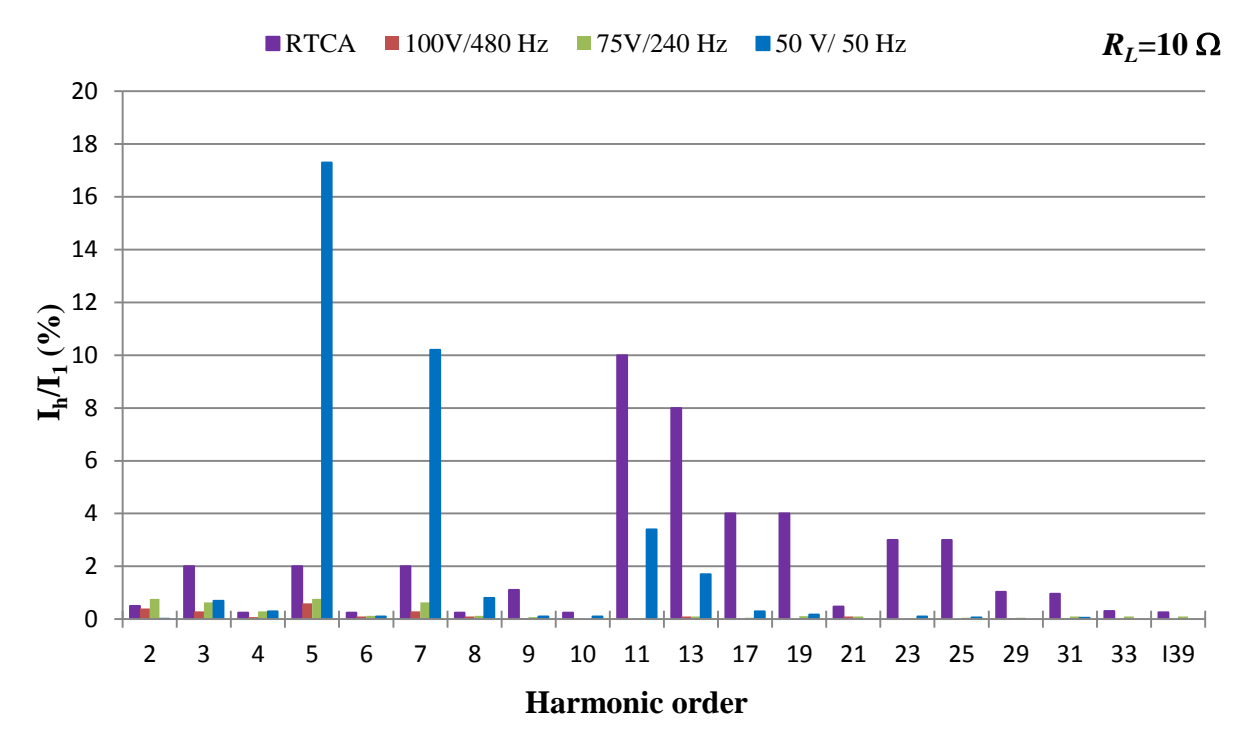


Figure 7.21 Input current harmonic spectrum as a function of V_S/F_S variations when $R_L=10~\Omega$

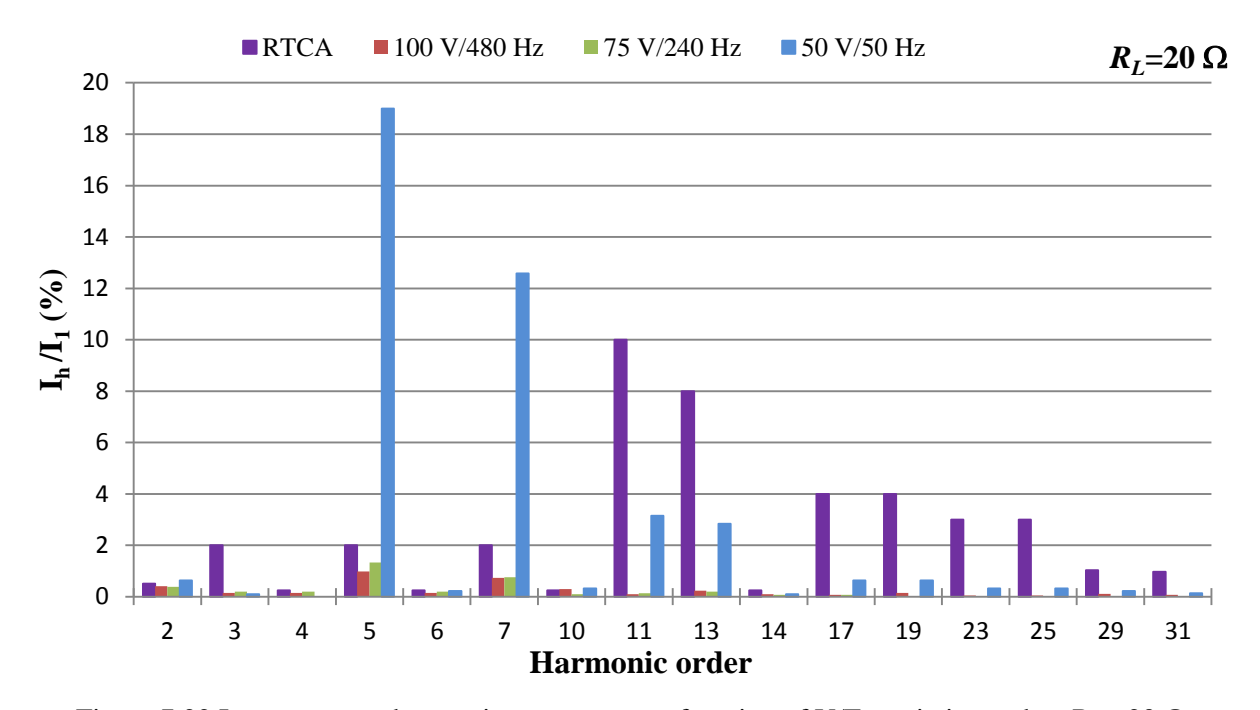


Figure 7.22 Input current harmonic spectrum as a function of V/Fs variations when R_L = 20 Ω

To sum up, improved FCSC converter performance in terms of individual harmonics is achieved with heavy loads.

However, with light loads the number of individual current harmonics which exceed the limits increases.

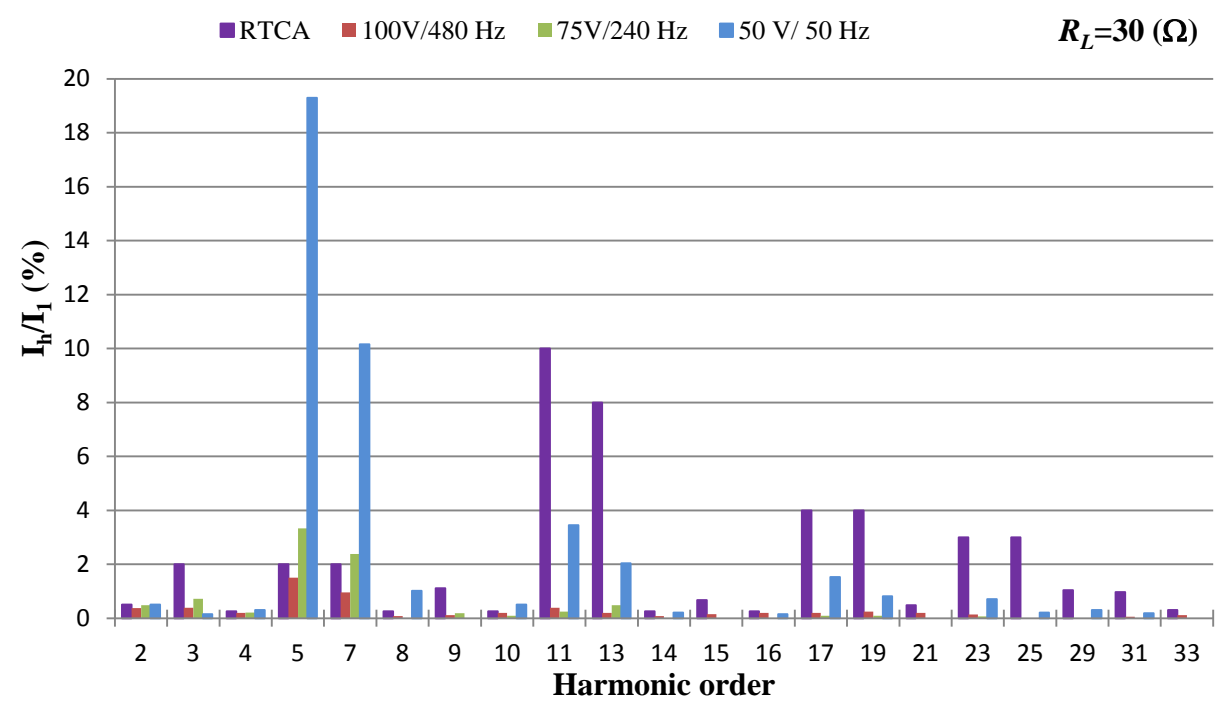


Figure 7.23 Input current harmonic spectrum as a function of V_S/F_S variations when $R_L=30~\Omega$

Reassuringly, the above figures lead to the same conclusion as those achieved previously through simulation analysis (Figures 5.38-5.40). The figures also show that in spite of the additional individual current harmonics appearing in the spectrum from the recorded test results, their values are below the RTCA limits and therefore their effect can be ignored.

7.5 Comparison between the Use of the Three-Phase Diode Rectifier and the Three-Phase FCSC-Rectifier

In order to highlight the impact of employing the three-phase FCSC-rectifier instead of the conventional three-phase rectifier in the VVVF applications, comparisons between both topologies were carried out at different load conditions, including fixed and variable load. The two topologies were compared in terms of the average output voltage, average output current, input current, output power, and the input power factor, as given below.

7.5.1 Operating under constant load

In this section, the two topologies are compared at a constant load resistance of 30 Ω . The measured output voltages V_L of both topologies under different supply voltage and frequency variations with a fixed load current are compared in Figure 7.24. By increasing the supply

voltage and frequency, the diode bridge rectifier output voltage is reduced due to the increased current commutation interval and voltage drop across the internal resistor.

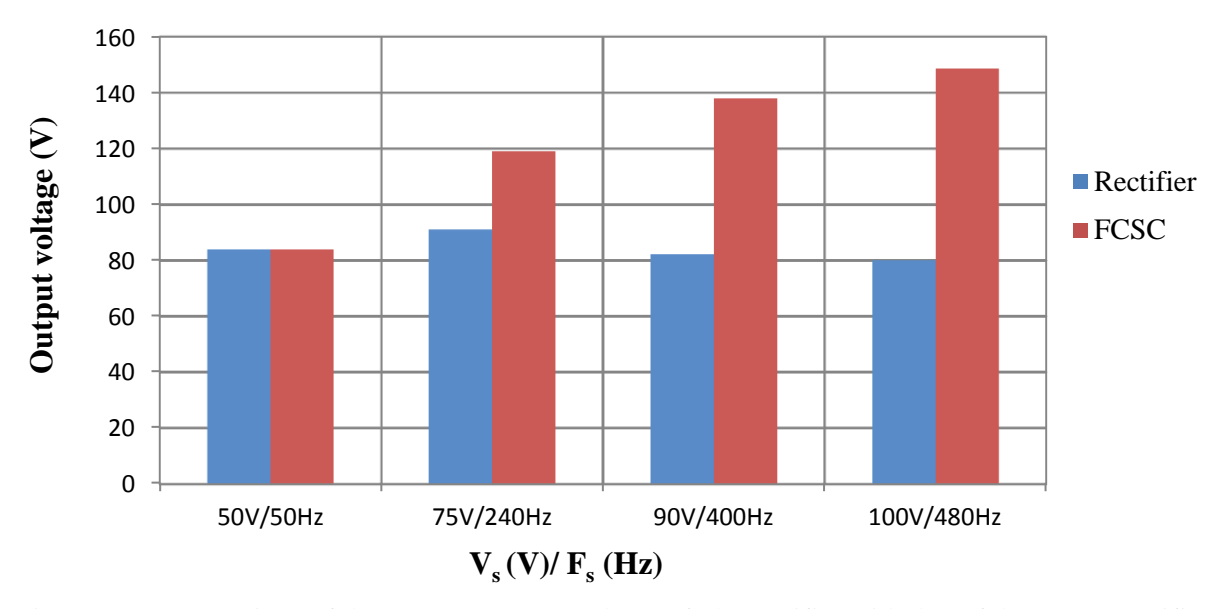


Figure 7.24 Comparison of the average output voltage of the rectifier with that of the FCSC-rectifier under constant load of $R_L = 30 \Omega$

However, the FCSC-rectifier is able to increase the output voltage at higher values of supply voltage and frequency due to its ability to reduce the current commutation. Therefore, the output voltage of the FCSC-rectifier is increased when the supply voltage and frequency are increased. The figure also illustrates that a high output voltage can be achieved by using the FCSC-rectifier, especially at the maximum voltage and frequency range of 100 V/480 Hz with a voltage difference of 85% between them.

Similarly, the output current of the FCSC-rectifier is increased when the supply voltage and frequency are increased, while the diode bridge rectifier output current is reduced accordingly.

A significant increase in the output current is also found in comparison with the DC current converted by the conventional rectifier circuit at the highest voltage and frequency of 100 V/480 Hz, as shown in Figure 7.25. Since there is a dependency between the output current and the input current i_s , the input current behaviour is similar to the DC current in both topologies, as shown in Figure 7.26.

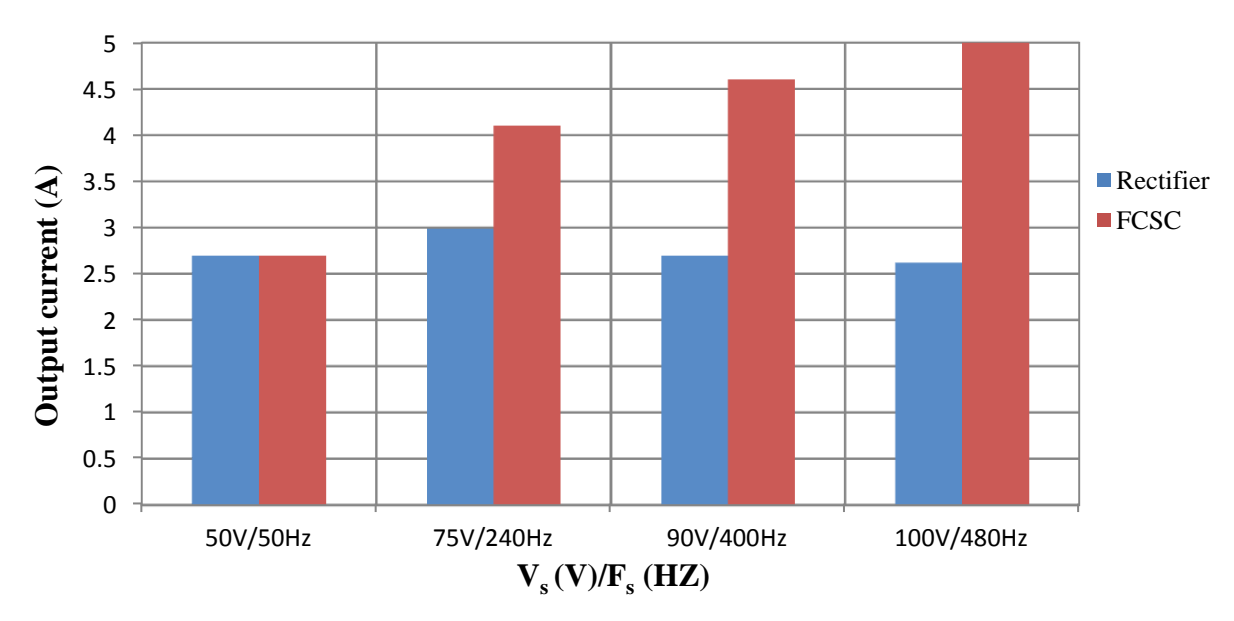


Figure 7.25 Comparison of the average output current of the diode bridge rectifier with that of the FCSC-rectifier under constant load of $R_L = 30 \Omega$

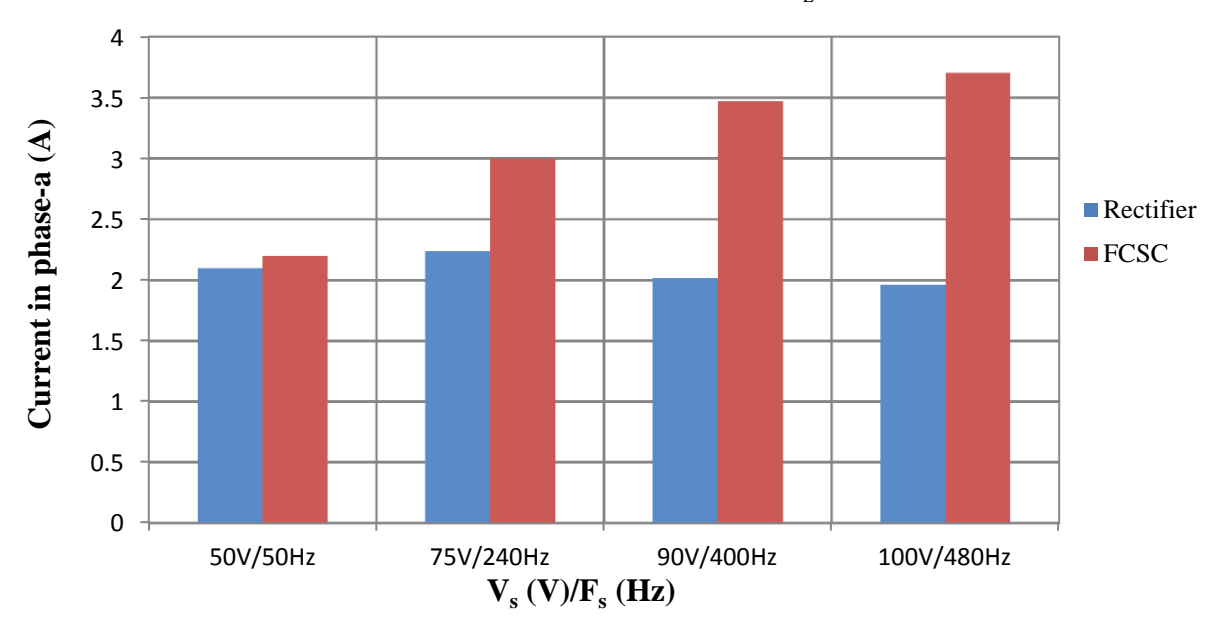


Figure 7.26 Comparison of the input current of the rectifier with that of the FCSC-rectifier under constant load of $R_L = 30 \Omega$

Figure 7.27 demonstrates how employing the FCSC-rectifier enables a high output power to be delivered at constant load in comparison with using the conventional rectifier circuit alone, especially at higher values of supply voltage and frequency. For instance, the output power of the FCSC-rectifier is 817.19 W at 100 V/ 480 Hz while it is 209.6 W for the conventional rectifier circuit. This ability of the FCSC to deliver higher output power to the load is because the power factor is very high when employing the FCSC-rectifier in the circuit, especially at higher supply voltage and frequency values, which enables the generator to be utilised more efficiently to deliver higher output power.

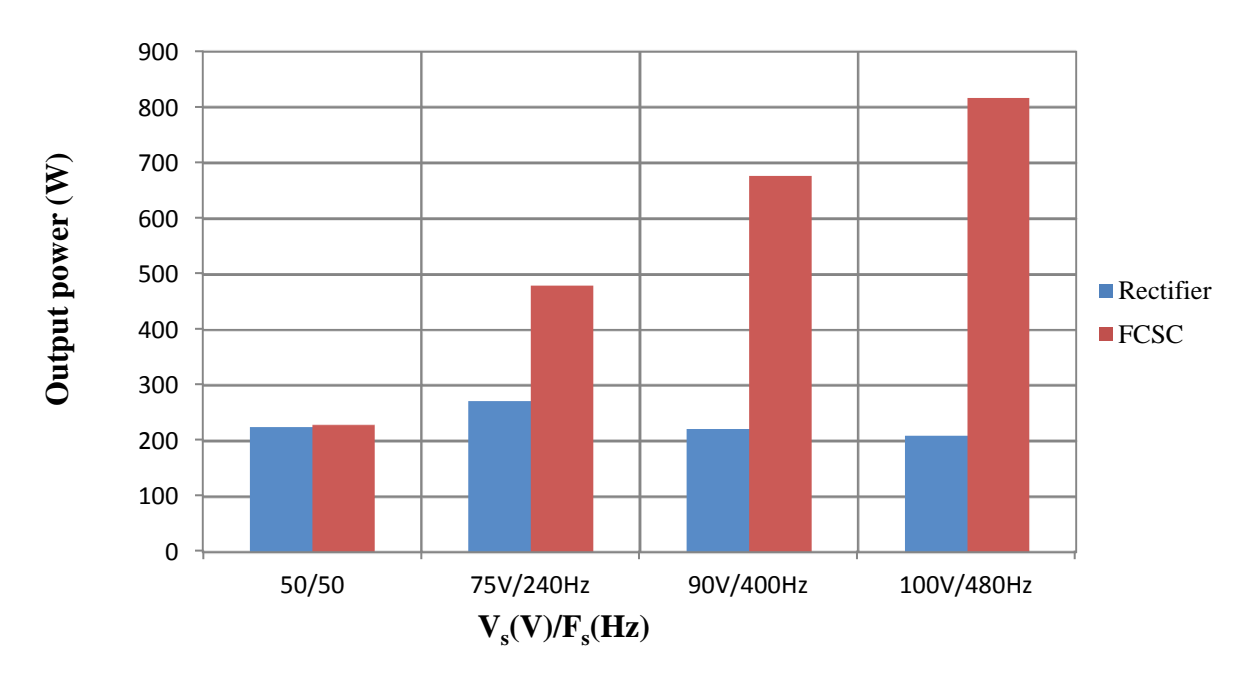


Figure 7.27 Comparison of the output power of the conventional rectifier with that of the FCSC-rectifier under constant load of $R_L = 30 \Omega$

The differences between the input power factor values for the two topologies are shown in Figure 7.28. The improvement in the input power factor values between FCSC-rectifier and conventional rectifier is reduced at low values of voltage and frequency of 50 V/50 Hz. However, significant power factor improvements are achieved at high supply voltage and frequency values.

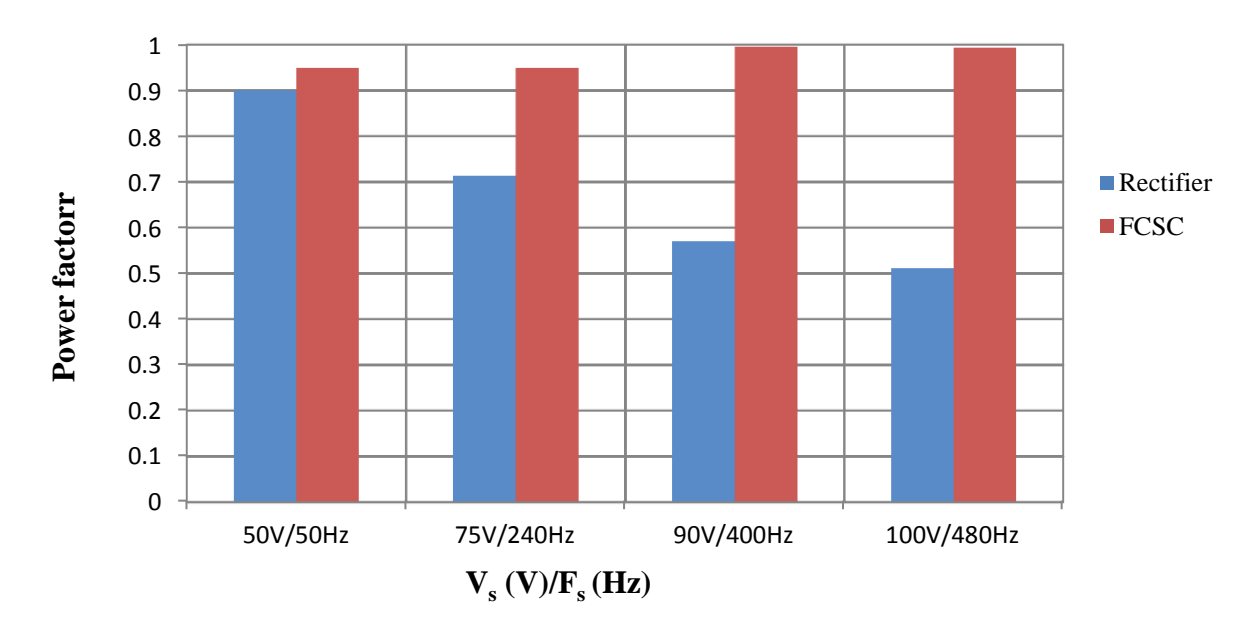


Figure 7.28 Comparison of the input power factor of the conventional rectifier with that of the FCSC-rectifier under constant load of $R_L = 30 \Omega$

7.5.2 Operating under variable load condition

This section compares the results for the FCSC-rectifier and conventional rectifier under various load conditions in terms of load voltage and current and output power. The experimental results were captured at a typical aircraft frequency of 400 Hz with a supply voltage of 90 V. The load resistance was also varied between 10 Ω -30 Ω to investigate the impact of load variations on system behaviour in both topologies.

The results acquired show that the load resistance variations have an impact on the DC output voltage for both the FCSC-rectifier and the conventional rectifier, as shown in Figure 7.29. However, with the same input voltage and frequency, a significantly higher load voltage can be achieved using the FCSC-rectifier. The lowest output voltage is achieved at heavy load $(R_L=10 \Omega)$.

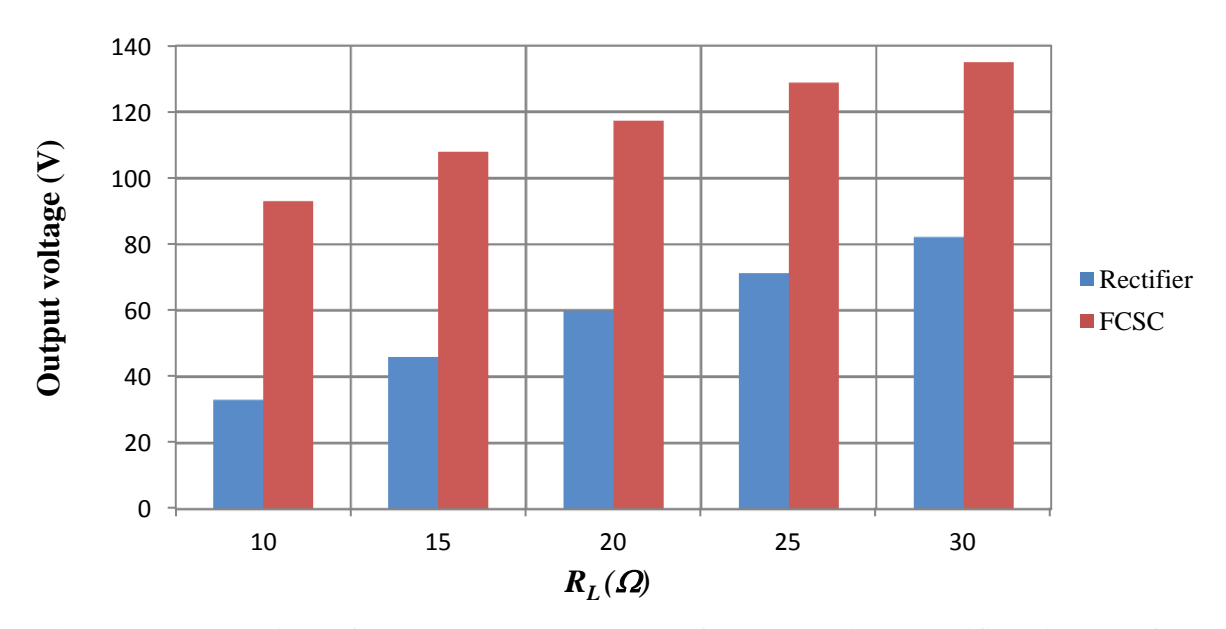


Figure 7.29 Comparison of the average output voltage of the conventional rectifier with that of the FCSC-rectifier under 90 V/400 Hz

Figure 7.30 shows a slight variation in the output current as a function of load resistance, while the FCSC-rectifier is capable of supplying heavy load since the output current is much higher than the DC current when employing the conventional rectifier only. This means that a heavy load can be supplied using the FCSC-rectifier in spite of the impact of load variations on the output current. Furthermore, the input current behaviour is identical to that of DC output current, as shown in Figure 7.31.

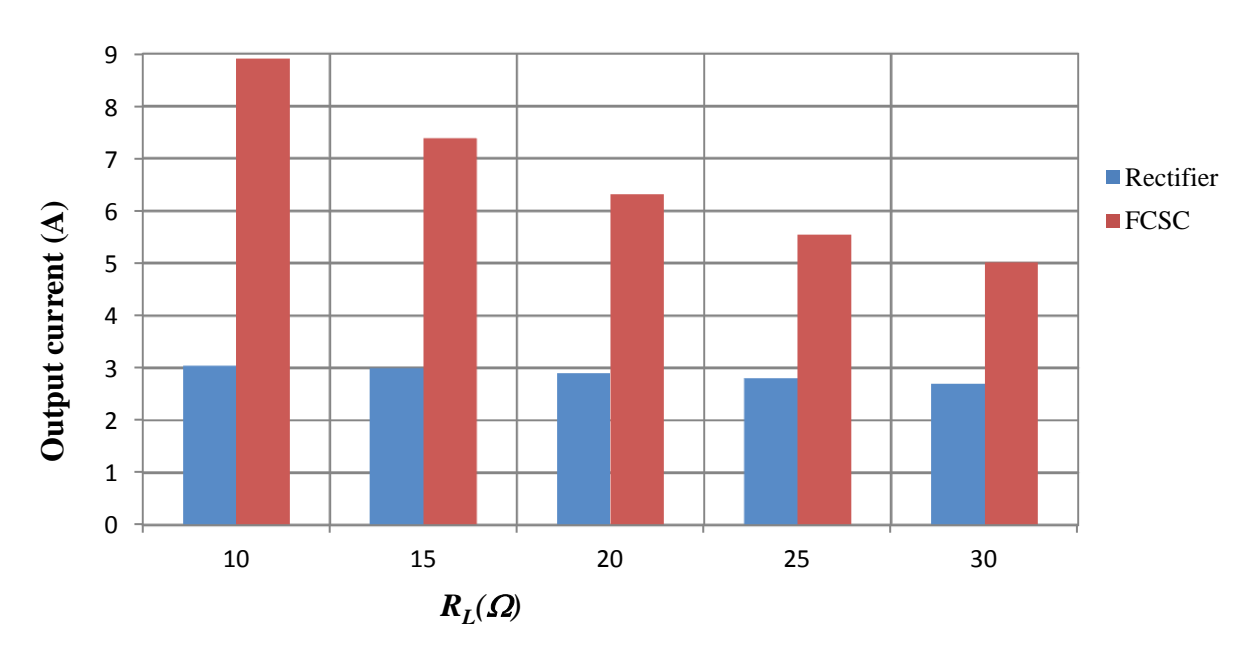


Figure 7.30 Comparison of the average output current of the rectifier and that of the FCSC-rectifier under 90 V/400 Hz

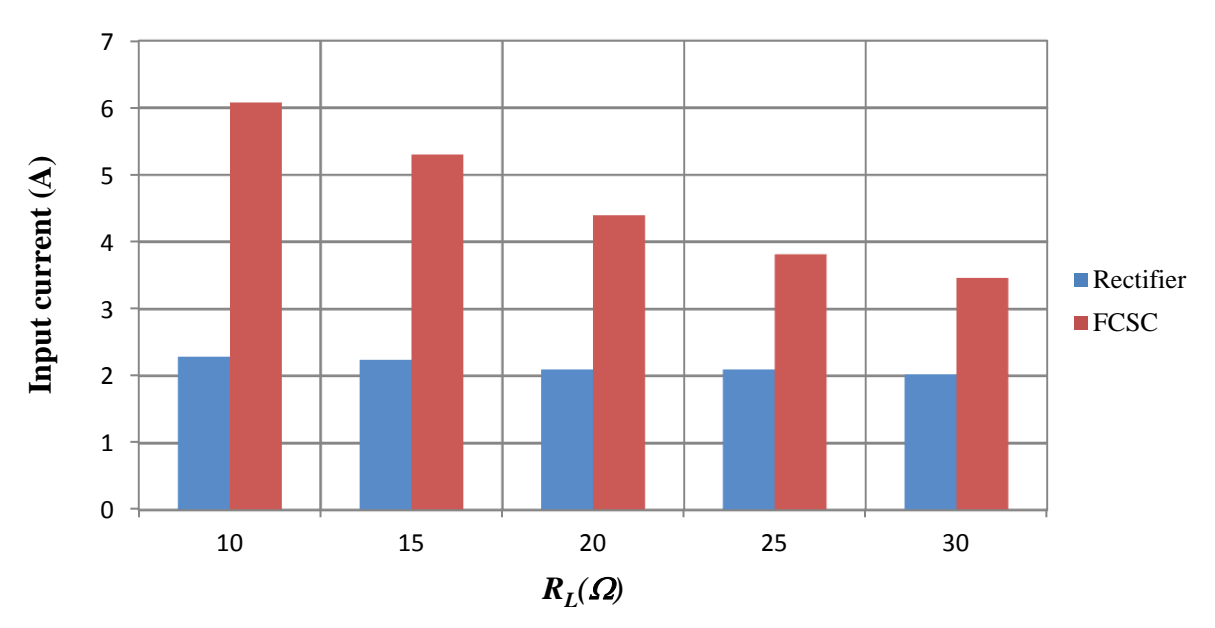


Figure 7.31 Comparison of the input current of the conventional rectifier and that of the FCSC-rectifier under 90 V/400 Hz

Therefore, the FCSC is capable of delivering much higher output power in comparison with the conventional rectifier as shown in Figure 7.32, and in addition there is a considerable impact of load variation on the output power developed when employing the FCSC circuit.

It is worth mentioning that the practical test results for the FCSC-rectifier's output power operating under various values of load resistance validate the simulation results presented in Chapter 4 (Figure 4.21).

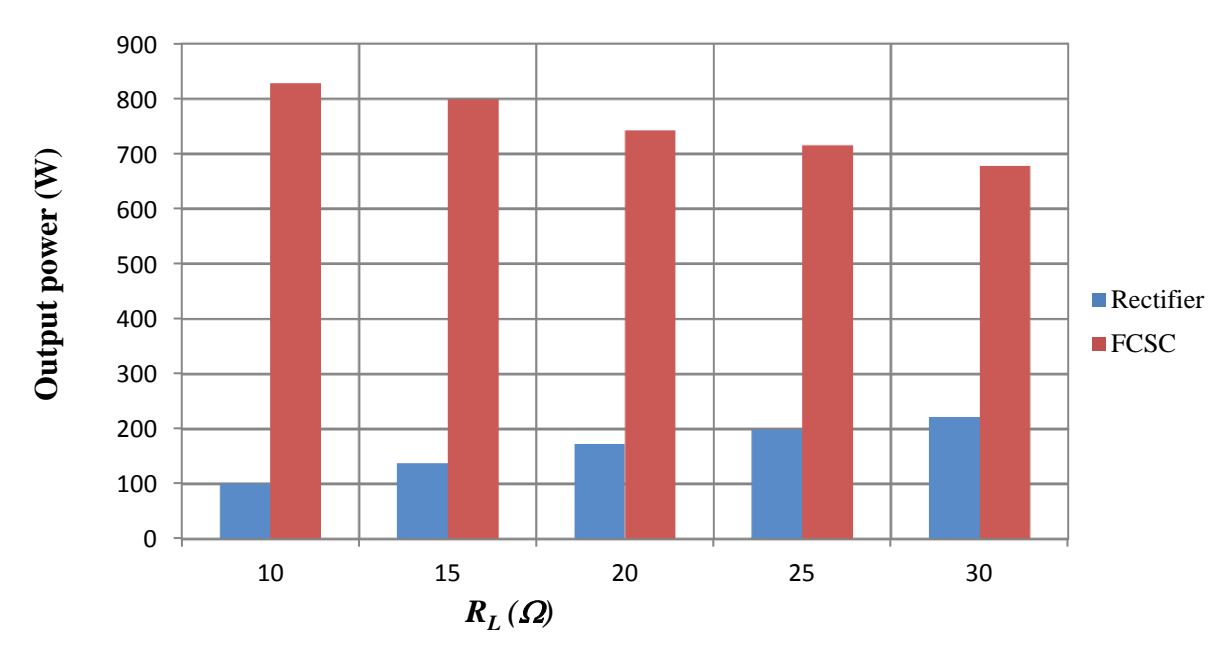


Figure 7.32 Comparison of the output power of the conventional rectifier and that of the FCSC-rectifier under 90 V/400 Hz

The processed experimental data show that, when employing the FCSC-rectifier, the input power factor is maintained at a high level with a minimum value of 0.99 under different load conditions, and its value is improved slightly to 0.992 when the load resistance is reduced to 10Ω , as shown in Figure 7.33. The same impact of load resistance variation was obtained earlier in the simulation analysis presented in Chapter 4 (Figure 4.19).

In addition, Figure 7.33 also shows that the employment of the three-phase FCSC-rectifier offers a significant improvement in the input power factor in comparison with the conventional rectifier. Hence, better utilisation of the electrical generator is achieved using the FCSC circuit.

The aforementioned investigation shows that the FCSC-rectifier is capable of improving the power factor to a high value at different load conditions, including fixed and varying load, and therefore providing a better utilisation of the electrical generator. In addition, the FCSC-rectifier has the ability to improve the output voltage level and output power in comparison with the conventional rectifier. However, employing the FCSC-rectifier at the lower voltage and frequency values of 50 V/50 Hz has less impact on the improvement in power factor, output voltage, and output power, as shown in this chapter.

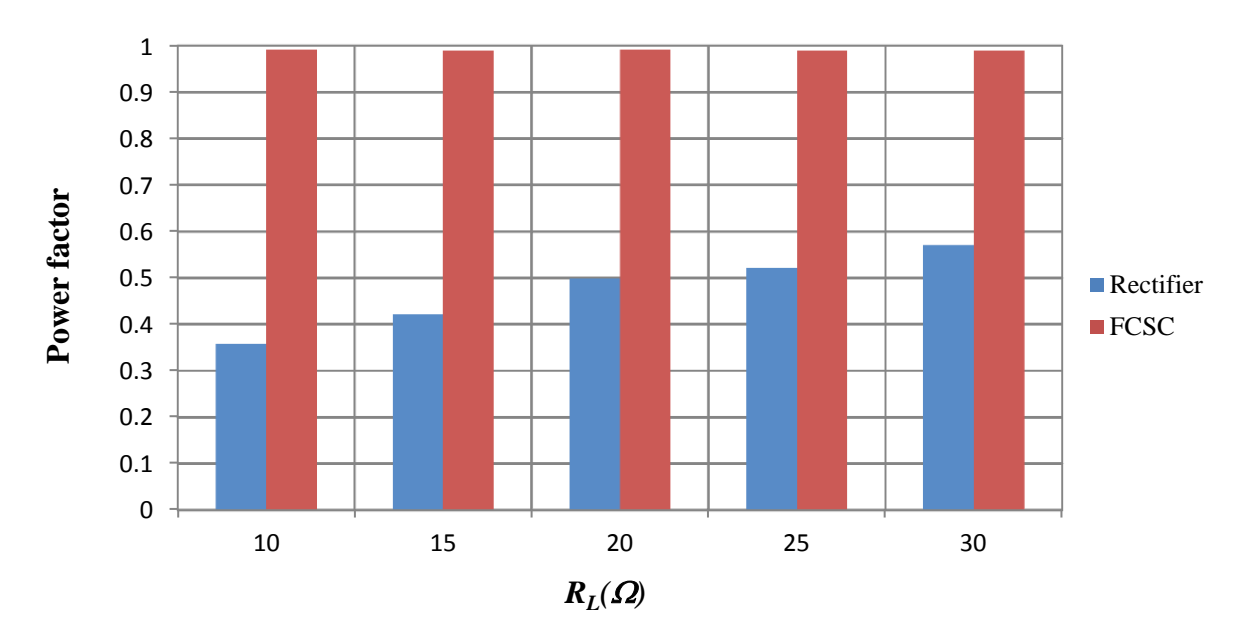


Figure 7.33 Comparison of the input power factor of the conventional rectifier and that of the FCSC-rectifier under 90 V/400 Hz

7.6 Comparison of the Experimental and Simulation Results

The captured experimental waveforms (Figure 7.11 to Figure 7.14) are similar to the simulation waveforms presented in Chapter 5 when implementing symmetrical duty cycle control (Figures 5.27-5.30). Identical system behaviour is achieved when the simulation and experimental results are compared. However, the recorded test results show certain differences in the magnitudes of voltage and current compared with the simulation results, with a very slight effect on the power factor (which is the main concern of the thesis). This difference is a function of voltage and frequency variations. The highest errors between the simulation and experimental values occur at the highest voltage and frequency of 100V/480 Hz with a value of 22.9% in the average load voltage. This error is decreased by reducing the operating voltage and frequency to the minimum value in the spectrum; for example, the lowest DC voltage error is calculated to be 8.6% when at 50 V/50 Hz. Similarly, the error in the input AC current is higher when operating at 100 V/480 Hz with a value of 22.8%, while this error is reduced to 8.6% at 50 V/50 Hz.

This difference is expected to be due to various factors, including: the use of components which were designed to be employed at low frequencies of 50/60 Hz such as the inductors and the capacitors in the AC side; the distorted voltage waveforms supplied by the Behlman power supply unit; the tolerances of components; and the accuracy of the measurement equipment. Indeed, it is expected that the use of inductors designed to be used in applications

operating at 50/60 Hz, would play a significant role in producing this difference, due to the fact that core losses depend on frequency. At the same time, other factors may have been responsible for minor errors in the results.

To ascertain the main reasons for this discrepancy between the sets of results, two approaches were used to determine whether the dependency of the inductor losses on the frequency variations had the highest impact on the results, or if the distortion passing from the power supply unit to the system played a role in converter behaviour and how much this affected the system.

The first approach includes capturing the distorted voltage waveforms produced by the power supply unit with its entire harmonics for various voltages and frequencies, and then inputting this data into SABER by customizing a voltage source based on the recorded data, which consists of three-phase voltage waveforms (fundamental and harmonics). This can provide an understanding of the system behaviour in the presence of distorted operating voltages with variable frequencies, and could clarify how much the power supply unit is involved in the error between the simulation and experimental results. Appendix H shows the differences between the simulation results and the injected voltage results in terms of DC load voltages and the input current. It is explained that this distortion is involved in the differences in the results with an error calculated to be around 4% at various voltages and frequencies with a constant load of 30 Ω . After subtracting the error caused by the distorted voltage waveforms, the highest average voltage net error occurs at the highest voltage and frequency of 100 V/480 Hz with a value of 20% decaying to 4.6% at 50 Hz. This approach shows that the power supply distortion participates in producing this difference in the results; however, varying the frequency hadthe greatest impact on the error.

In order to validate the effect of changing frequency on the circuit's behaviour, a second experimental approach is used to observe system operation with a sinusoidal voltage supply of a fixed frequency of 50 Hz. This was accomplished by replacing the Behlman AC power unit with a three-phase fixed voltage/frequency supply. A three-phase autotransformer (three-phase variac) was connected to the three-phase main supply terminals in order to control the AC output voltage. A soft starter was used to prevent the inrush current at starting instant. Three Cornell-Dubilier polypropylene film capacitors were used with a value of 730 μ F 800 V DC \pm 10% as series capacitors with circuit inductors in the AC side. All other parameters were the same as before. By applying a voltage of 50 V to the system and comparing the

simulation and experimental results, the error in terms of both load voltage and input current is approximately 5% at R_L =30 Ω .

The aforementioned approaches show that the largest part of the difference between the experimental and simulation results is caused by frequency variations. This means that the system losses are increased by increasing the frequency to 480 Hz. Since the inductors used in this test are designed to operate with a 50/60 Hz voltage source, the results show that inductor losses increase in proportion with increasing frequency.

In general, one important factor which affects the inductor losses is frequency [150, 151]. However, in power factor correction applications with switching power converters, an accurate calculation of inductor loss is highly challenging. In such applications, the conventional methods for core loss estimation based on the core manufacturer's data sheet cannot be used when the switching frequency or the duty cycle are varied [152]. In this work, the results also show that inductor losses increase proportionally with frequency.

7.7 Summary

This chapter has presented and analysed the experimental test results when employing the three-phase FCSC-rectifier with symmetrical duty cycle control in a variable-voltage variable-frequency system. The experimental investigation was carried out under different load conditions, including fixed and variable resistive load. The test operating voltage and frequency ranges used in the test were between 50-100 V and 50-480 Hz respectively. Power supply distortion was investigated at the beginning of the chapter, and it was concluded that there is no significant impact of the frequency harmonics of power supply switching on the performance of the FCSC-rectifier in terms of the power factor, which is the main aim of this work.

The experimental investigation was carried out and is separated into two parts. The first investigation is dedicated to examining the system performance when operating with only a conventional three-phase rectifier. The second experimental investigation is devoted to demonstrating the system performance when employing the three-phase FCSC-rectifier. In both parts, the investigation has been carried out in terms of the output voltage, output current, output power, and power factor, for both fixed and variable resistive load. Harmonic analysis was carried out to assess the individual harmonic levels and the suitability of employing the FCSC converter in aerospace applications. Then, a comparison of the two rectifier circuits

was conducted to assess the impact on system performance of implementing symmetrical duty cycle control with the FCSC-rectifier during various operating conditions.

The functionality of the hardware and the three-phase FCSC-rectifier with symmetrical duty cycle control were validated by the measured experimental results. These recorded results show that the FCSC-rectifier is able to improve the power factor to values as high as 0.992, offering a better utilisation of the electrical generator. Hence, the electrical losses in the system were reduced and therefore high output power was achieved.

Furthermore, a similar behaviour for the three-phase FCSC converter under symmetrical duty cycle control is achieved by comparing the recorded experimental and simulation results. Also, the differences in the load voltage, and input current values are also highlighted and verified between both results.

To sum up, the experimental results demonstrate that, by implementing symmetrical duty cycle control, the three-phase FCSC-rectifier is able to cope with voltage and frequency variations typical of some aerospace applications. The test results also show how employing the FCSC-rectifier improves system performance in terms of power factor, output voltage, output current, and output power under different load conditions and with various voltages and frequencies, compared with the three-phase diode bridge rectifier. In addition, the test results also demonstrate that the substantial improvement in system performance was achieved by employing the FCSC-rectifier at higher supply voltages and frequencies, including 90 V/400 Hz which is a typical aircraft frequency. While at the lowest voltage and frequency values in the spectrum, which were 50 V/ 50 Hz in this test, the experimental results showed that the FCSC-rectifier introduces only limited improvement in system performance.

Chapter 8. Conclusion and Future Work

This thesis investigates the impact of applying symmetrical duty cycle control (SDCC) on the performance of the three-phase FCSC-rectifier operating in stand-alone variable-voltage variable-frequency applications. The performance of the circuit has been evaluated in terms of power factor, output voltage, input current, output power, total harmonic distortion and individual harmonics levels. In this work, the circuit has been considered for wave energy converters and aircraft systems. Converter behaviour under various load conditions, including constant and variable load, has been examined. The principal aims of this research are:

- To propose a control scheme which enables a three-phase power electronic converter to cope effectively with a wide range of frequency variation in a stand-alone variable-voltage variable-frequency systems, and to maintain a high power factor
- To investigate the performance of the three-phase converter under various operating conditions, including fixed and variable load, and to examine its suitability for employment in aerospace applications.

This thesis makes an important contribution to research in power factor correction of variable-voltage variable-frequency systems. A new symmetrical duty cycle control scheme is proposed, and experimentally validated for the three-phase circuit topology of the FCSC-rectifier.

Furthermore, this thesis presents a detailed investigation into the three-phase performance of the FCSC-rectifier operating over a wide range of operating frequencies. The research contribution is made by examining the individual harmonics levels of the FCSC-rectifier circuit, and considering the impact on more electric aircraft systems. The author believes that this analysis has not previously been presented in the literature.

This chapter presents a summary of the investigation's key points as reported in this thesis and highlights the main conclusions of this work, in addition to providing suggestions for future work.

Conclusion

In some stand-alone variable-voltage variable-frequency applications such as direct drive wave energy converters (WECs) and more electric aircraft (MEA), a three-phase electrical generator is connected directly to a conventional three-phase diode bridge rectifier, for simplicity and cost reduction, to deliver power to the DC load. The majority of published studies in this area have been concerned with the design of the three-phase generator in terms of reduced size, volume, cost, and weight, at the expense of higher values of generator reactance. The use of a diode bridge rectifier with a high inductance generator causes the overall power factor to deteriorate due to commutation overlap as the current is transferred from one diode to the next. It is therefore very important to correct the power factor in such systems to ensure better utilization of the electric generator.

Different power factor correction techniques have been used over the decades. In this research, a variable switched capacitor has been used to inject a capacitive reactance which can compensate the inductive reactance of the generator. Due to the nature of variable-voltage variable-frequency systems, it is crucially important to inject a variable capacitive reactance, since the generator's inductive reactance varies as a function of frequency variation. The series compensation technique was applied in this project using controlled series capacitor circuits.

The thesis presents a detailed investigation of CSC topologies commonly employed in power systems by critically reviewing the published literature. A theoretical comparison has been presented to summarize the advantages, disadvantages and limitations of each circuit configuration, to determine its suitability for different applications. Various common CSC types are compared, including the magnetic energy recovery switch, static synchronous series compensator, dynamic voltage restorer, thyristor controlled series capacitor, thyristor switched series capacitor, switched variable series capacitor, and forced-commutation controlled series capacitor. Based on this comparison, it is noted that the FCSC circuit is the most promising compensator, which could be employed in three-phase stand-alone variable-voltage variable-frequency systems due to its ability to provide a continuous variable capacitive reactance through the IGBT switch action. Although the TCSC was found to be the most common type of FACTs controller in power systems, the risk of internal resonance between the circuit components leads to its exclusion from consideration for the application considered here.

Here, the research is focused on the three-phase FCSC circuit topology, which is able to cope with high frequency variations between 50 Hz and 500 Hz, and which is within the range of typical frequencies for aircraft systems.

An investigation into the performance of the single-phase FCSC circuit is also presented to provide an understanding of converter behaviour before investigating the more complicated three-phase topology. The use of the single-phase topology is limited to the wave energy converter in this work.

The modes of operation of the single-phase FCSC converter were first described. A performance analysis was then presented numerically by simulation, in terms of the input power factor, output voltage, output power, efficiency, and total harmonic distortion. A significant improvement was achieved in terms of the input power factor. The results show that the power factor was improved from 0.35 lagging to 0.99 lagging under fixed load, which enables the single-phase FCSC-rectifier to provide better power take-off from the electrical generator.

The impact of load variation is also investigated in detail. Results show that any increase in load resistance reduces the value of the power factor, and that this reduction is driven by a drop in the distortion factor rather than the displacement factor. In addition, the simulation results showed a minimal impact of load capacitance variation on converter performance.

Typically, most PM generators employed in VVVF systems are three-phase generators. This work has therefore focused on the investigation of the performance of the three-phase FCSC-rectifier topology. Numerical and experimental investigations were carried out under constant and variable load conditions, and numerical simulations were performed using SABER.

A description of the problem of the high level of distortion arising from the employment of a conventional PFC converter in aerospace applications has been presented in this thesis. This distortion is caused mainly by zero crossing distortions which develop in conventional PFC converters. In such applications, the allowable current and voltage distortions set by the authorities are strictly limited and this effectively excludes several conventional PFCs from being employed in aircraft systems. The three-phase FCSC-rectifier was therefore proposed in this thesis to be employed in aerospace systems as well as in marine renewable systems.

A description of the three-phase FCSC converter is introduced; a brief description of the effect of the load type connected to the output of the rectifier is also presented. The principle of operation of the three-phase FCSC-rectifier with various IGBT switch ON/OFF actions is then presented in detail. The circuit is modelled and simulated for both marine and aerospace frequency ranges.

Numerical analysis is carried out for two circuit configurations to examine the impact of employing the three-phase FCSC converter in aircraft systems. In the first configuration, the permanent magnet alternator is connected directly to the three-phase six-pulse diode bridge rectifier, and in the second the three-phase FCSC-rectifier is interfaced with the PMA generator to supply the DC load. Simulation results indicate that a power factor of approximately unity can be achieved by employing the three-phase FCSC-rectifier compared with a power factor of 0.35 lagging without the FCSC circuit. The use of the three-phase FCSC-rectifier also increases the output voltage level dramatically for the given load value, because the FCSC converter is able to reduce the duration of the commutation period which occurs in a conventional three-phase diode bridge rectifier. In this research, the circuit operation is discussed in accordance with the duality concept. Simulation results show that the circuit behaviour is in duality to the three-phase rectifier supplied by a stiff sinusoidal voltage source and connected to a series RL load. This means that the circuit can be described as a three-phase rectifier fed by a sinusoidal current source and connected to an RC load. Therefore, the rectifier output current was calculated as 1.35 I rms. The results also show that the three-phase FCSC-rectifier has a high efficiency of 97%.

To fulfil the power quality requirements for aerospace systems, an extensive harmonics analysis of current harmonics was carried out using FFT analysis. From the analysis it was concluded that all of the current harmonics were lower than the required limits when the converter is operating at the maximum frequency in the range (50-500 Hz).

The results demonstrate the ability of the three-phase FCSC converter to enhance PMA generator performance by maintaining a high power factor at high efficiency under various load conditions, while maintaining the level of harmonics components within the limits imposed by RTCA DO-160.

A novel symmetrical duty cycle control scheme (SDCC) is proposed in this research to qualify the three-phase FCSC converter to deal with significant frequency variations, such as

those of wave energy converter and aircraft system frequencies. The scheme was tested with both the single-phase and three-phase systems. The approach was very simple to implement, with no need for a sophisticated circuit. The controller was synchronised with the supply frequency, and the ON/OFF time of the switches was determined by applying a symmetrical switching pattern across the maximum current instant. In the proposed scheme, the switch ON time is a function of the supply frequency, which allows the converter to cope with frequency variations. For both topologies, the simulation results showed that the FCSC-rectifier can correct the power factor to a high value over a wide frequency range. Better performance, however, was achieved by employing the three-phase topology. It had less distortion in the input current waveform and was able to boost the output voltage to a higher value than the maximum line-to-neutral input voltage at a given load. The three-phase FCSC circuit was capable of correcting the power factor and meeting the power quality requirements for aircraft systems over a range of frequencies from the maximum value to half of this maximum value. However, the converter exceeded the allowable harmonics level at the minimum operating frequency due to the large duty cycle and the switch ON-time associated with such a frequency.

Interestingly, the simulation results also show that the circuit behaves differently in its singlephase and three-phase topologies in terms of the commutation overlap interval and the output voltage level.

A 1 kW three-phase FCSC-rectifier was then built and experimentally tested in a laboratory environment. A general description of the experimental test bench is provided. The laboratory set-up is comprised of the power generating unit, the power stage, the measurement sensors, and the control unit implemented on a Spectrum Digital eZdsp Texas Instruments TMS320F28335 DSP and National Instruments LabView control panel.

The functionality of the hardware and the three-phase FCSC-rectifier with symmetrical duty cycle control were validated experimentally at voltages and frequencies between 50-100 V and 50-480 Hz respectively for different load conditions. Despite the output voltage distortion that arises from the switching frequency of the available Behlman AC power supply, the experimental results showed good agreement with the simulation results. The experimental results were acquired for both the three-phase conventional diode bride rectifier and the FCSC-rectifier under the same operating conditions.

The recorded experimental results validate the ability of the FCSC-rectifier in practice to improve the power factor to high values up to 0.992 in comparison with the diode bridge rectifier when implementing the symmetrical duty cycle control.

Other aspects of system performance, including output voltage, output current and output power under different load conditions and various voltages and frequencies, were also investigated experimentally and the results compared with those for the three-phase diode bridge rectifier. The recorded results demonstrated that a strong improvement in system performance is achieved by employing the FCSC-rectifier at higher supply voltage and frequencies, including at 90V/400 Hz, which is a typical aircraft frequency. However, only a marginal improvement in system performance was realised at the minimum frequency in the range tested due to the high conduction losses caused by the large duty cycle.

The simulation and experimental results demonstrate the effectiveness of the three-phase FCSC-rectifier in maintaining high input power factor, output voltage, and output power with low harmonic distortion, at a frequency range between the maximum and half of the maximum frequency. The results also show that the three-phase FCSC-rectifier is less effective at the minimum frequency in the range.

8.1 Future Work

Simulation results and experimental tests have shown that the three-phase FCSC circuit is capable of delivering excellent performance characteristics in terms of input power factor, output voltage, output power, efficiency and lower harmonic distortion when employed in a variable-voltage variable-frequency application, in particular at the higher frequencies in the frequency range. However, improvements could possibly be achieved by improving the ON/OFF control scheme time for the IGBT switches. In addition, the number of switches implemented in the three-phase FCSC-rectifier circuit could be reduced by replacing asymmetrical IGBTs with symmetrical devices. In this case, there would be no need to embed a diode in series with each IGBT switch. This would reduce the number of switches by six.

Although a comprehensive investigation of the impact of load variation is presented in this thesis, further investigation to take into account the load resistance in the control scheme is considered to be worthwhile. Moreover, a stability analysis of the three-phase FCSC converter may be useful to introduce the circuit for aircraft HV DC power distribution systems.

Further investigations may also be interesting which employ the three-phase FCSC-rectifier in different variable-voltage variable-frequency applications, such as free-piston engine applications, using different frequency ranges such as 10-100 Hz.

Finally, the investigation of the three-phase FCSC-rectifier has shown its ability to maintain lower harmonics distortion, especially at the higher frequencies in the range, and so a harmonics reduction technique for lower frequencies may also need to be proposed.

Appendix A. Variable-Voltage Variable-Frequency Applications

A brief overview for two variable-voltage variable-frequency applications is described as follows.

A.1 Wave energy converters (WEC)

One type of wave energy converter is the buoy. It is able to extract energy from ocean waves and convert it into electrical power. In addition, buoys can be used as stand-alone devices to warn the system of any seismic events such as tsunamis and may also serve as navigation lights. To power up the electronic equipment and batteries, a solar panel is used, which has the drawback of low levels of sunlight in some countries such as the UK. The other alternative is to use an electrical generator to supply the buoy's electronics with a DC power. A linear permanent magnet generator is proposed to be used due to its high efficiency and power density. This is because it generates electrical power with a variable-voltage variable-frequency. However, it suffers from low power factor due to its high inductance. To supply the electronic loads, the generator is connected directly to a conventional diode bridge rectifier for simplicity and cost reduction. The system suffers from a low power factor due to the commutation overlap.

In 1910, the first wave energy converter used to supply electricity to French home was designed by Praceique-Bochaux using a pneumatic system. This was followed by the Japanese researcher Yoshio Masuda, who developed the idea of the oscillating water column (OWC) in 1940. Recently, due to the energy crisis and environmental awareness, wave energy is attracting more support and interest as a part of a renewable energy strategy.

Many challenges face this conversion technology, such as needing to work with as low a frequency as 0.1 Hz, and the problem of wave oscillatory movement, which has to be converted to 50 Hz to connect to the grid. In addition, there is a need to increase the voltage level generated by the WEC to be transmitted from the sea to the sub-station. Furthermore waves vary in height and period, and therefore the power produced varies accordingly. This creates offshore converter challenge. Moreover, the devices also need to align themselves to wave direction.

Many projects have been supported to develop WEC systems for many years and several types of WECs have been developed to economically extract energy from the water. Wave energy converters can be categorised in different ways. Based on location, they can be classified as on-shore, near-shore, and off-shore. They are also categorised based on the working principles used into six types: attenuator (A), point absorber (PA), oscillating wave surge converter (OWS), oscillating water column (OWC), overtopping device (OT), and differential pressure (DP). Many governments supporting WEC projects have employed well-known types of wave energy converters, as summarized in Figure A. 1. In fact, over several decades hundreds of WEC systems have been proposed.

In order to extract power from waves, different power take-off (PTO) mechanisms are used, including hydraulic, mechanical, pneumatic, and direct drive PTO systems [153-156]. Figure A. 2 illustrates the conversion stages in wave energy systems for converting the wave energy to electricity, including different PTO systems. This figure also shows the role of the power electronic converter in such systems.

Various designs of electrical generator topologies have been proposed to efficiently employ electrical generator in WECs, including rotary and linear generators.

The direct drive PTO conversion system is considered to be a promising technique in wave energy conversion systems in relation to cost reduction, efficiency, and reliability, since there is no need to use mechanical or pneumatic energy equipment in this topology [124, 157]. Several researchers have investigated the most promising generator topologies to be employed in direct drive WEC, comparing the longitudinal flux machine (LFM), the transverse flux machine (TFM), and the Vernier hybrid linear generator. The transverse flux PM machine has been proposed as the most promising topology for a generator to be used in direct drive WEC [123, 124, 153]. However, this type of generator suffers from high inherited inductance, which causes a very poor power factor, and this needs to be corrected.

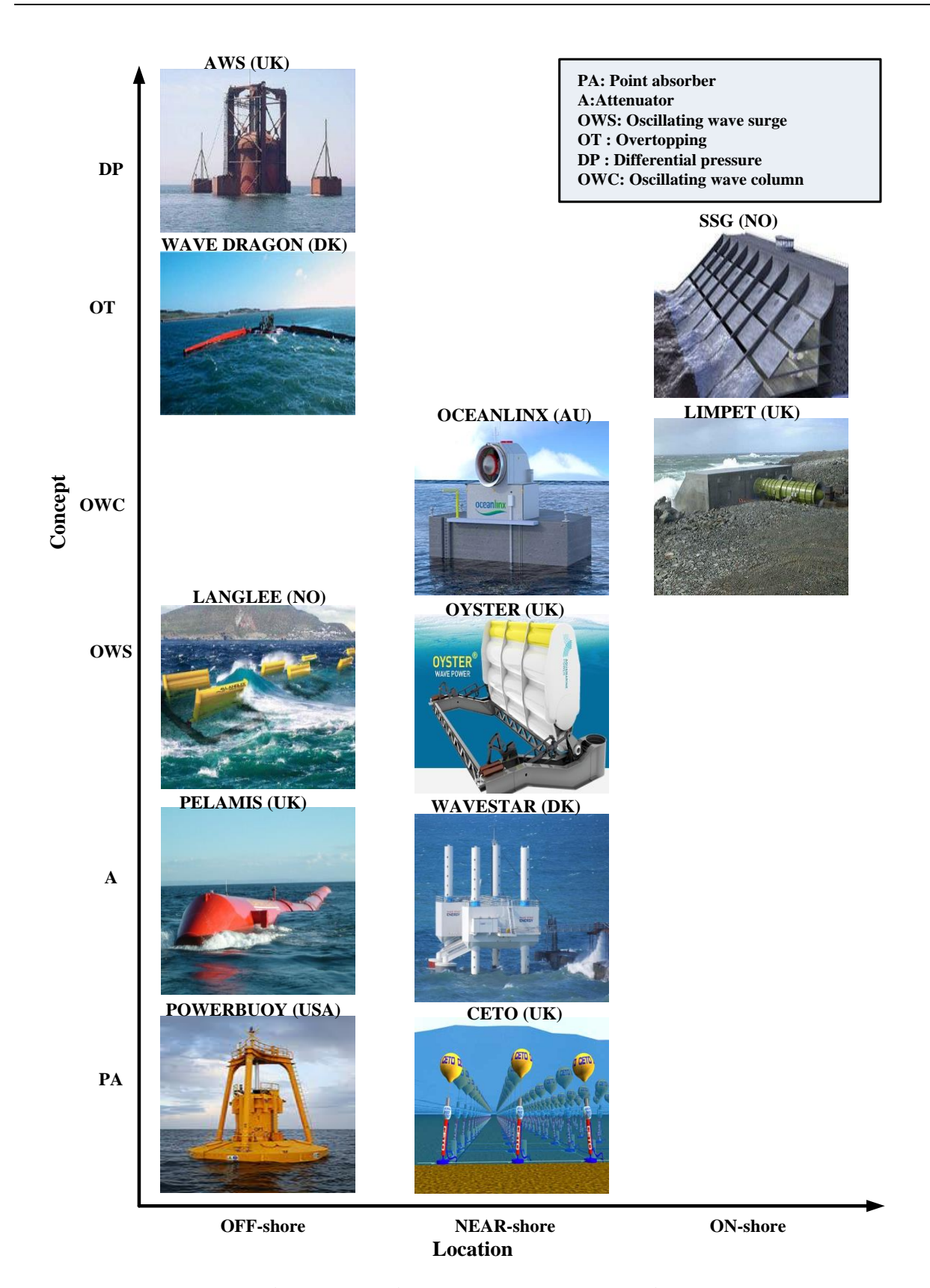


Figure A. 1 Main wave energy converter projects

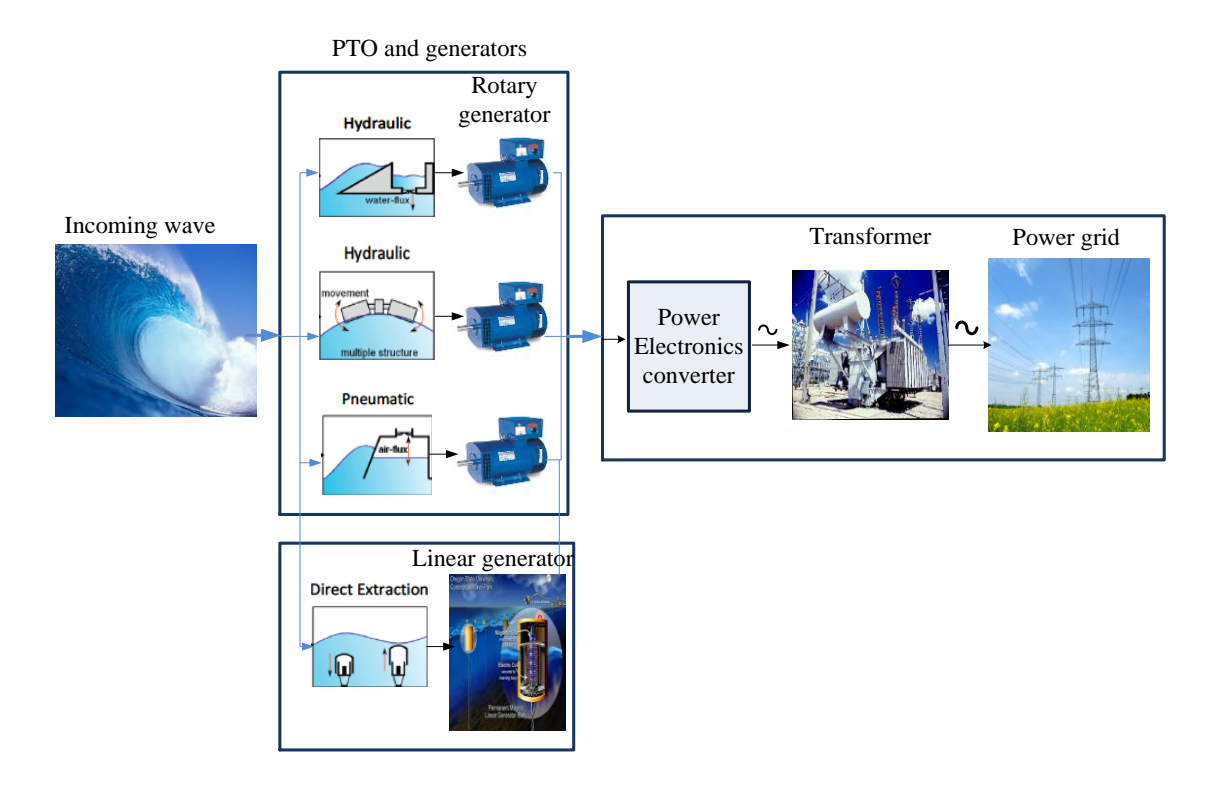


Figure A. 2 Different WEC conversions stages

A.2 More electric aircraft (MEA)

In conventional civil aircraft, the engine converts the fuel to power. Most of the power is used as propulsion power for the moving aircraft, and the rest is transformed into non-propulsive power. There are four main non-propulsive power systems which can be classified as hydraulic, pneumatic, mechanical, and electrical, shown in Figure A.3. The hydraulic and electrical power systems are driven by the gearbox. All of the commercial loads are fed by the generator, including the avionics, galleys, entertainment systems and lightning. The complexity of each system and the interaction between different pieces of equipment decreases the overall efficiency of the system. Hence, a new trend has emerged towards a reduction of the number of non-propulsive power systems used [158].

The trend towards all-electric aircraft (AEA) is considering the use of a single power system to replace multiple systems. This has potential benefits which can be summarised briefly as: maintenance being easier in relation with replacing parts, and the maintenance routine remaining almost the same; power being consumed only during operation (power on demand); reduced weight when the hydraulic system is removed; and reduced operating cost [159-161].

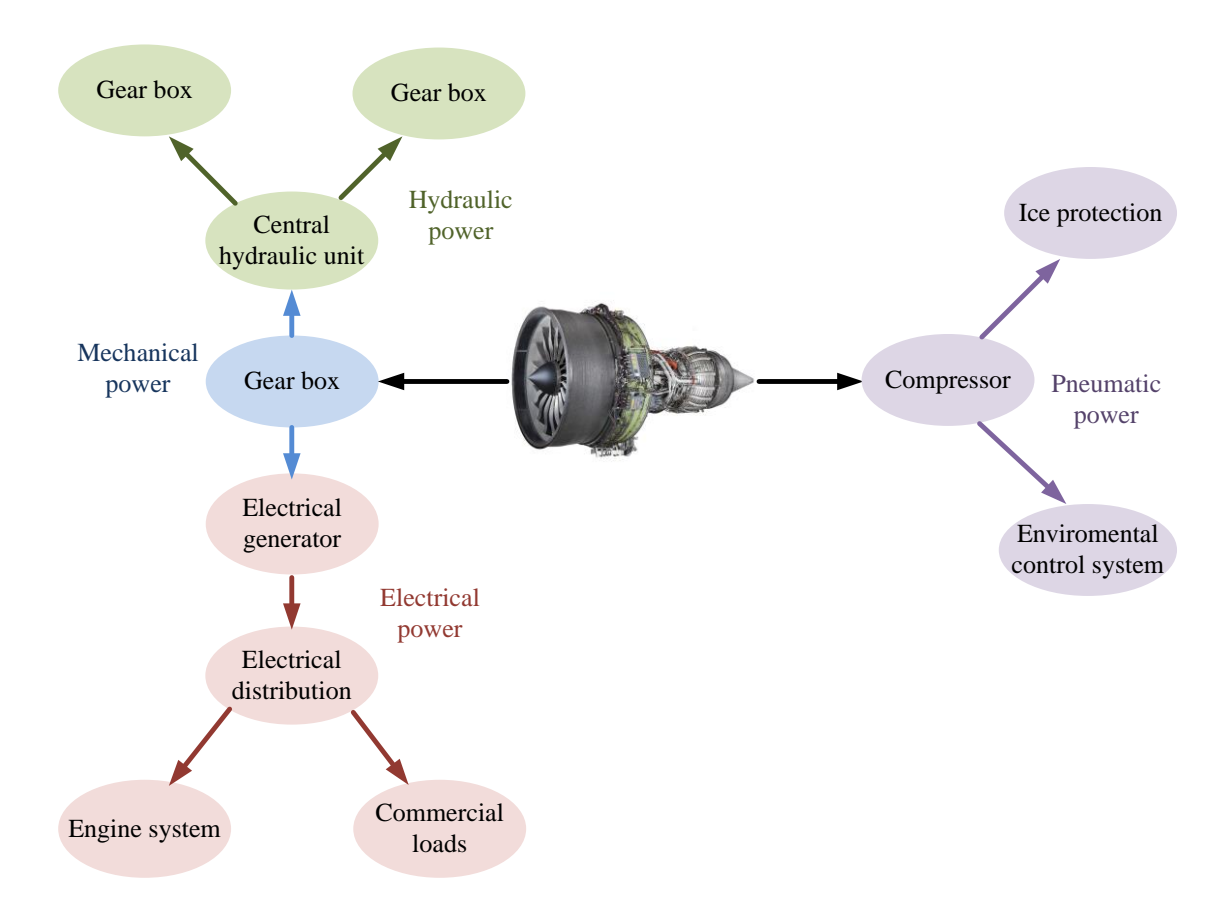


Figure A.3 Conventional civil aircraft system

Nevertheless, in the aircraft industry, reliability has the highest priority, and therefore there is a reluctance to embrace entirely new systems. Hence, the aerospace industry has recently begun moving toward more electric aircraft instead of all-electric aircraft, which entails the introduction of hybrid systems.

The concept of more electric aircraft can involve the replacement of some parts of the hydraulic system with electrical systems, and particularly in increasing the involvement of a power electronics converter in the main engine generation system, as shown in Figure A.4. However, replacing the non-propulsive power systems in the conventional aircraft requires significant developments in power generation, distribution and management, and advances in monitoring and control systems. In fact, the most crucial technologies for MEA are the power electronics and control system. Hence, the development of power electronic technology is playing a key role in moving toward a more electrical system, in addition to the advances in power engine technology and embedded digital controllers [11, 158, 162].

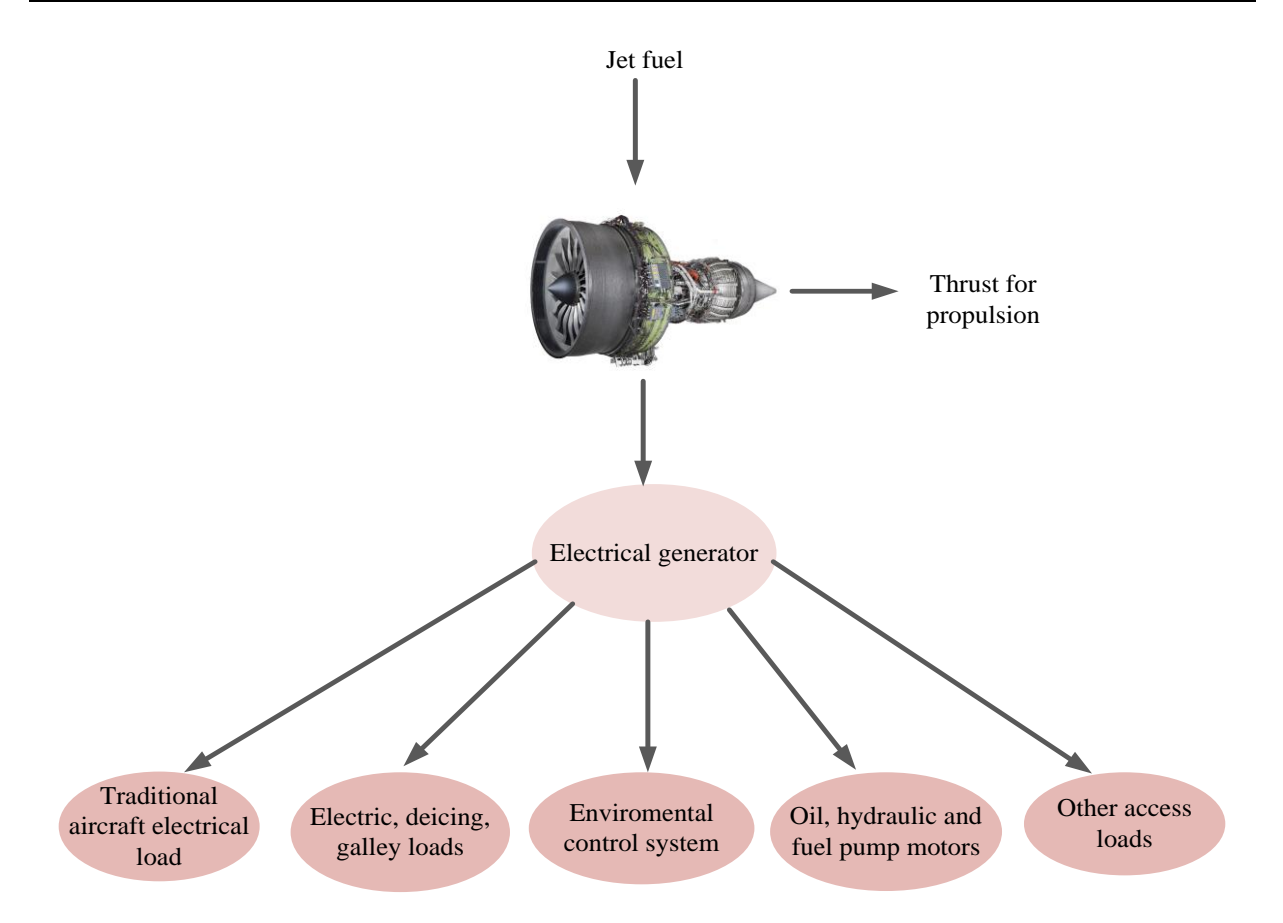


Figure A.4 Typical MEA electric aircraft system

Starting from the 1990s, many projects have investigated advances in aircraft power systems and power management, which are important in moving toward less reliance on hydraulic power systems [158, 163]. For instance, the European Community (EC) 5th framework programme introduced the power optimised project (POA). In this project, the concept is to move to more/full electrical architecture by embedding the starter generator, bleed-less environmental control and the use of electrical flight control and landing actuators.

Figure A.5 shows conventional civil aircraft power generation and distribution and the power optimized counterpart, introduced as part of EC framework [164].

Recently, several new electrical technologies have been employed in passenger aircraft such as the Boeing 787 and Airbus 380. High on-board electrical power is required due to high electrical power loads such as those for the galley equipment, communication systems, weather radar, environmental systems, in-flight entertainment systems, and flight instruments. Therefore, it is important to employ an electrical system with the ability to generate, regulate, distribute, and supply high power loads.

In the Boeing 787, four generators with a capacity of 250 KVA are driven by two engines which produce a total power of 1000 kVA, but higher powers in the future are predicted. In addition, the electrical system in this aircraft is able to provide different voltages, such as variable frequency (VF) AC and DC, in contrast with most other available aircraft systems which provide 115 V AC at 400 Hz and 28 V DC [6].

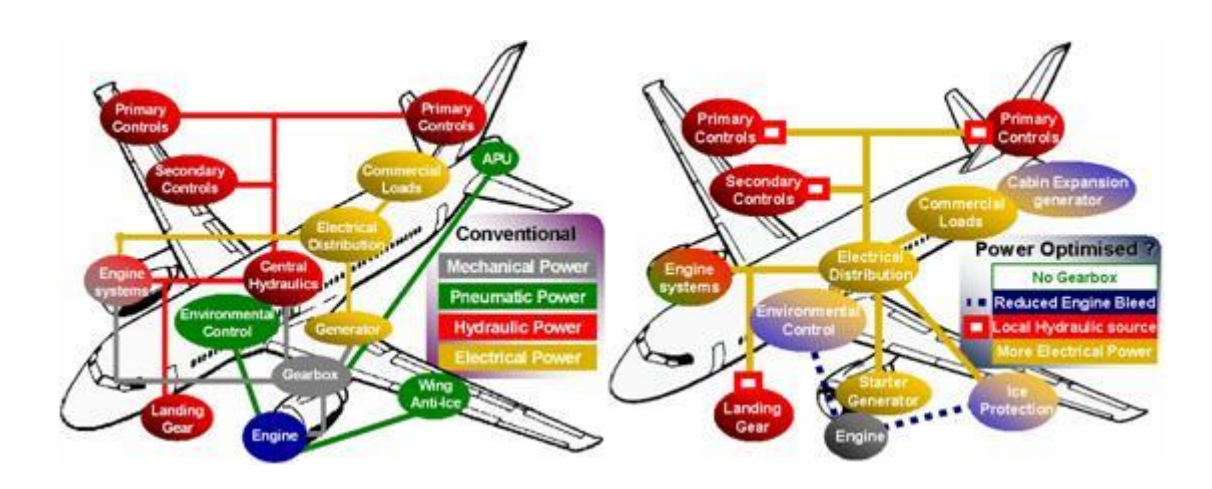


Figure A.5 Conventional and MEA aircraft architectures adapted from [164]

The use of VF power in the MEA architecture has been proposed to improve overall efficiency and reduce the volume and weight compared to the constant frequency CF electrical system. Therefore, it is seen as the future trend for aircraft systems. In addition, many AC loads require specific frequency control to produce the desirable torque, such as in AC motors [12].

Figure A.6 illustrates different architectures of electrical power generation which are currently deployed in aircraft systems. In this figure, the first system is based on three-phase AC generation integrated drive generator (IDG) with 400 Hz CF 115 V. The next system has a variable speed constant frequency (VSCF) cycloconverter. This is followed by VSCF with a DC link system. The variable frequency (VF) architecture is also illustrated in this figure, with a three-phase 115 and 230 V and (380-760 Hz). A 270 V DC bus voltage can be achieved with VF of 115 V AC input given an appropriate conversion stage. Finally, emergency power with 28 V DC is supplied by permanent magnet generators (PMGs) [6]. A significant advantage can be achieved when moving toward high voltage AC and DC power systems in aircraft, including increasing the effective capacity of the aircraft electric power system, which reduces current dramatically and, as a consequence, reduces cable weight while lower losses and higher efficiency can be achieved. However, the commonly used PWM

converter, which already uses a very sophisticated control strategy, could cause the unstable operation of the distribution network [17, 18].

These developments show that more progress is needed in moving toward more electric aircraft. Many challenges require additional investigations including the need for high power semiconductor switches and a high capacity generating unit, along with a high quality power converter, to comply with the harmonic standards; complex filtering systems are also required in addition to advanced control units.

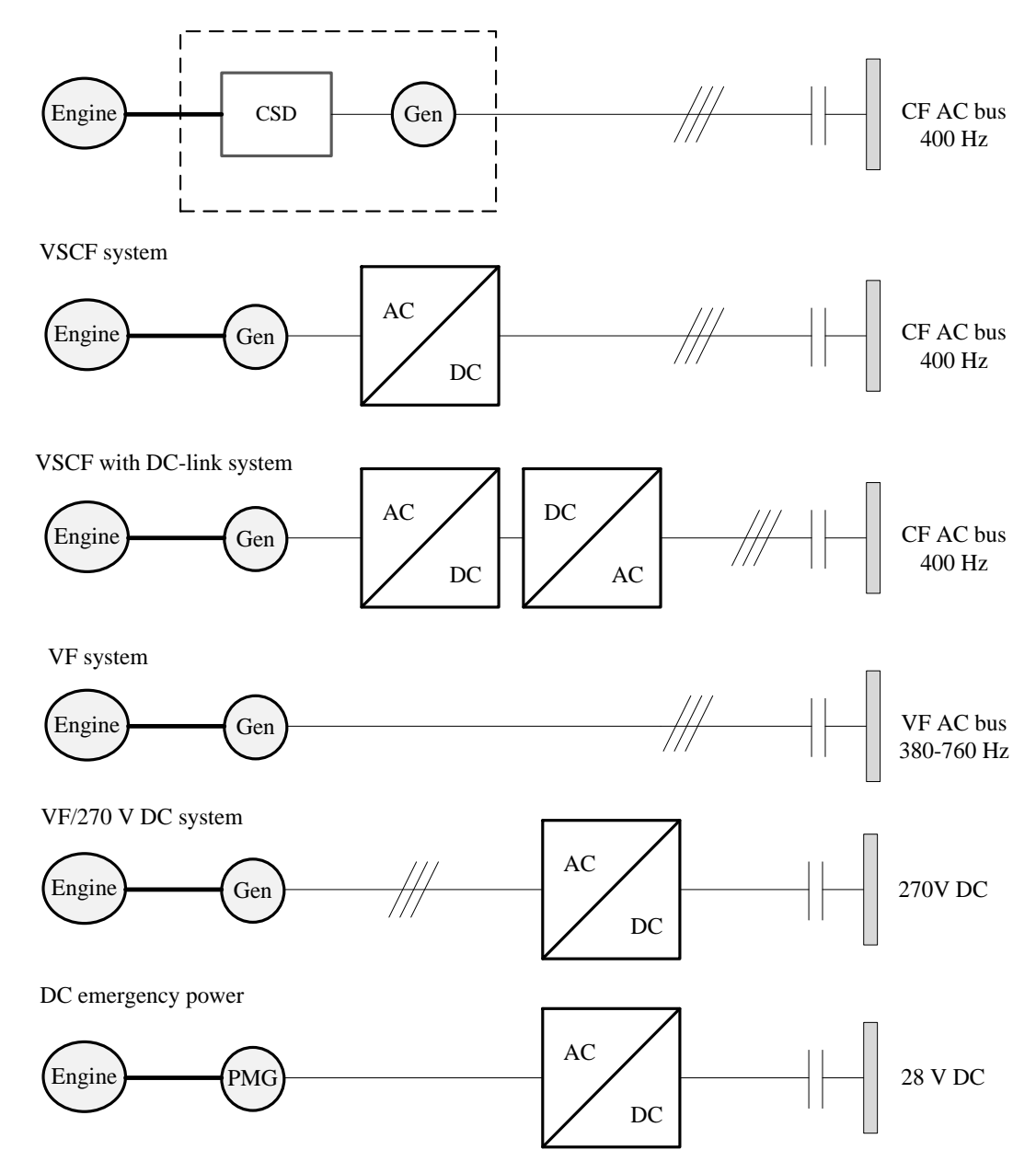


Figure A.6 Different strategies for electrical power generation [6]

Appendix B. Three-phase six-pulse bridge rectifier with pure resistive load

In high power applications, a three-phase diode bridge rectifier is commonly used because of its high efficiency and the lower ripple content in its output waveform in addition to its capability of handling large power levels.

In order to analyse the ideal operation, the rectifier is connected directly to a three phase Y-connected power supply with no inductor and feeds pure resistive load, as shown in Figure B.1. In this circuit, the diodes are ideal and numbered in accordance with the conduction sequence. A three-phase AC voltage source is used in this simulation with a phase shift of 120° between phases a, b and c with an RMS phase voltage of 100V.

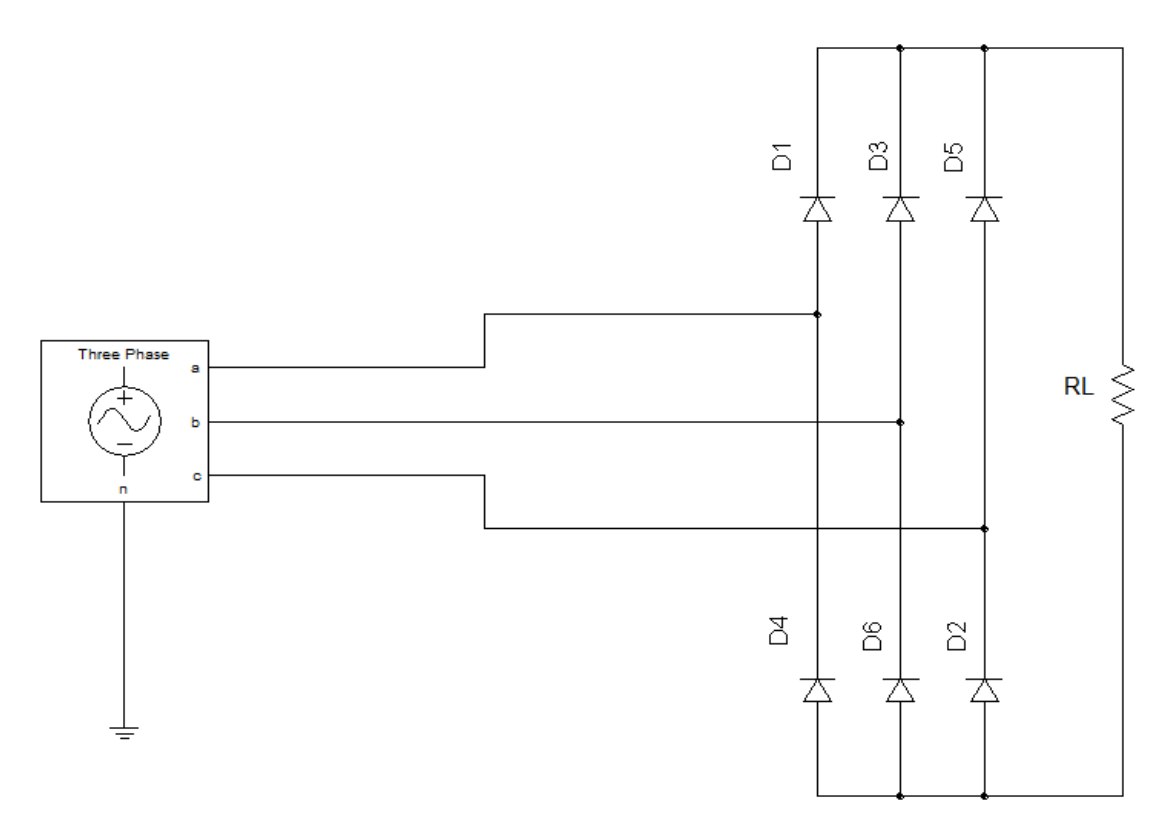


Figure B.1 Three-phase six-pulse diode bridge rectifier

Figure B.2 shows the relationship between the line to line voltages V_{LL} (V_{ab} , V_{bc} , V_{ca}) and line-to-neutral voltages V_{ph} (phase voltages) for the phases a, b and c. There is a phase shift of 120° between all three line-to-line voltages. Furthermore, the line to line voltages V_{ab} , V_{bc} and V_{ca} leading the corresponding phase voltage by 30°. As the maximum phase voltage is 142V, the maximum line-line voltage (V_{LL} max) is approximately 246 V, which satisfies the following basic formula:

$$V_{LL\ max} = \sqrt{3}\ V_{ph\ max} = \sqrt{3} \times 142 = 245.95\ V$$
 (B-1)

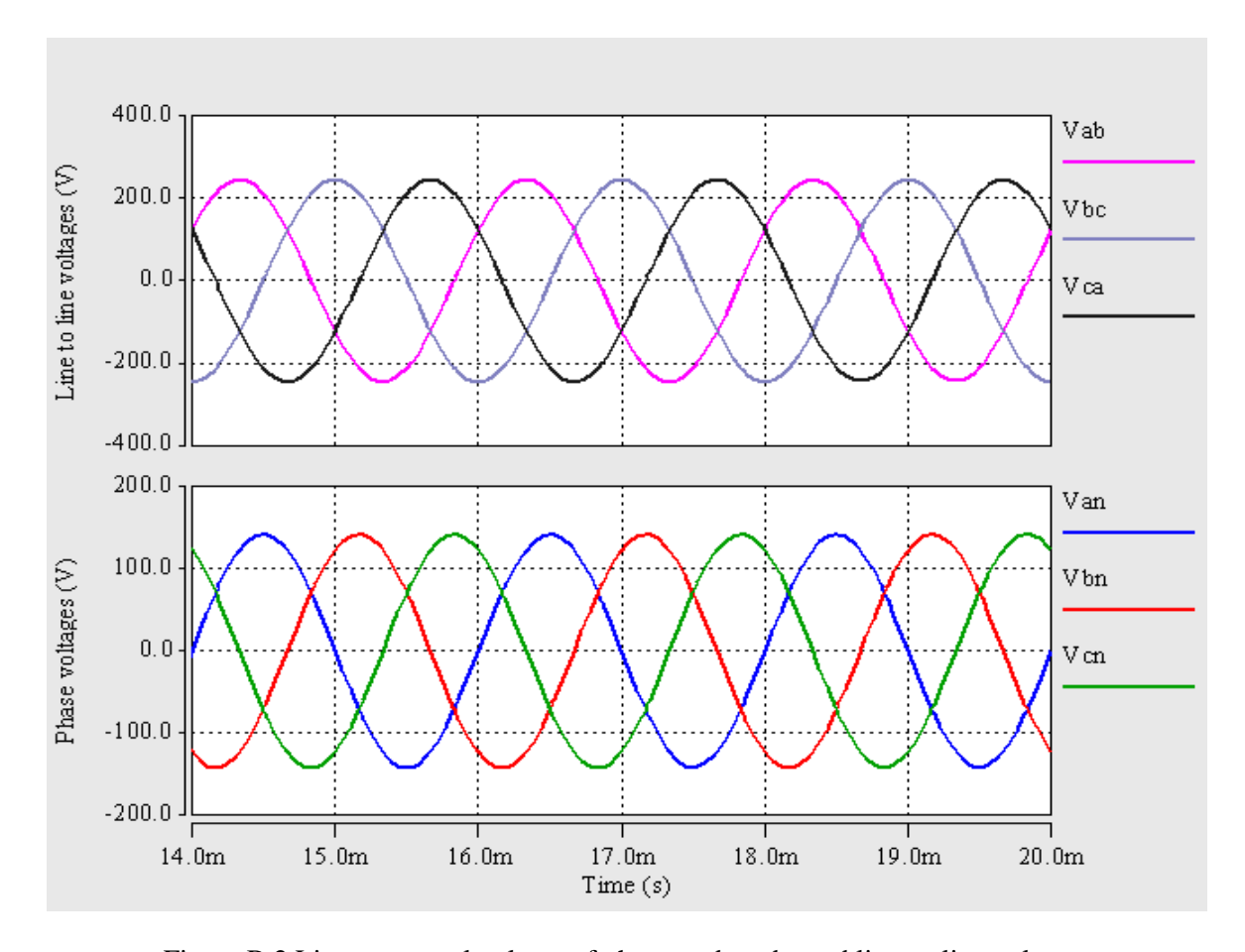


Figure B.2 Line-to-neutral voltage of phases a, b and c and line-to-line voltages

The load voltage is composed of six pulses during one frequency cycle according to six AC sinusoidal voltages V_a - V_b , V_a - V_c , V_b - V_c , V_b - V_a , V_c - V_a , V_c - V_b [165], as shown in Figure B.3. This means that two diodes conduct at each instant (one from the top group and one from the bottom group). The average value of output voltage is calculated from

$$V_{DC} = \frac{1}{\pi/3} \int_{-\pi/6}^{\pi/6} \sqrt{2} \ V_{LL} \cos \omega t \ d\omega t$$
 (B-2)

$$V_{DC} = 1.35 V_{LL}$$
 (B-3)

$$= 1.35 \times \sqrt{3} \times 100 = 233.82 V$$

where V_{LL} represents the RMS value of the line-to-line voltage.

Using the SABER, the average DC voltage is equal to 232.42 V and the DC output current is 7.761 A, as shown in Figure B.3. It is clear that there is a difference approximately equal to 1.4 V (twice 0.7 V) between the calculated and the measured value of V_{DC} . This is because the diode forward voltage is taken into account in simulator. The load current can be calculated analytically using equation (B-4).

$$I_{DC} = \frac{V_{DC}}{R_L} = 7.79 A \tag{B-4}$$

The rectifier DC output contains a ripple component which needs to be absorbed to obtain a pure DC output. The ripple frequency can be calculated as given in the formula [7]:

$$f_r = 6 \times f_s \tag{B-5}$$

where f_r is the ripple frequency and f_s is the supply frequency.

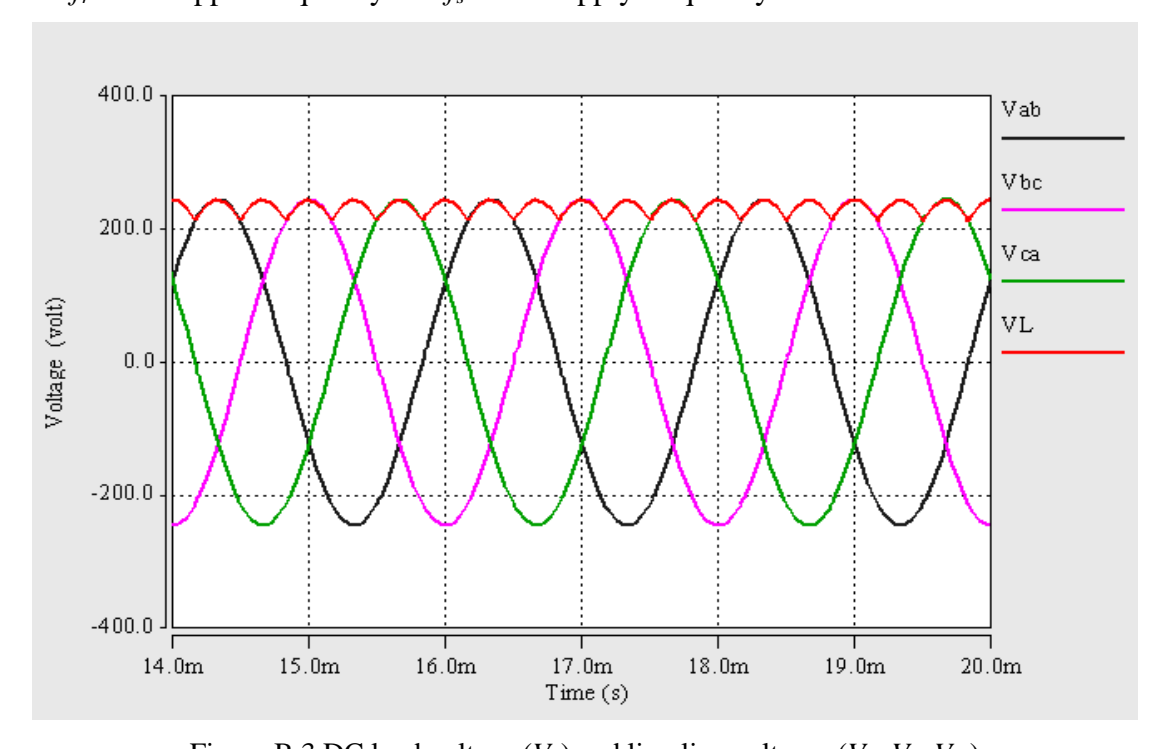


Figure B.3 DC load voltage (V_L) and line-line voltages (V_{ab}, V_{bc}, V_{ca})

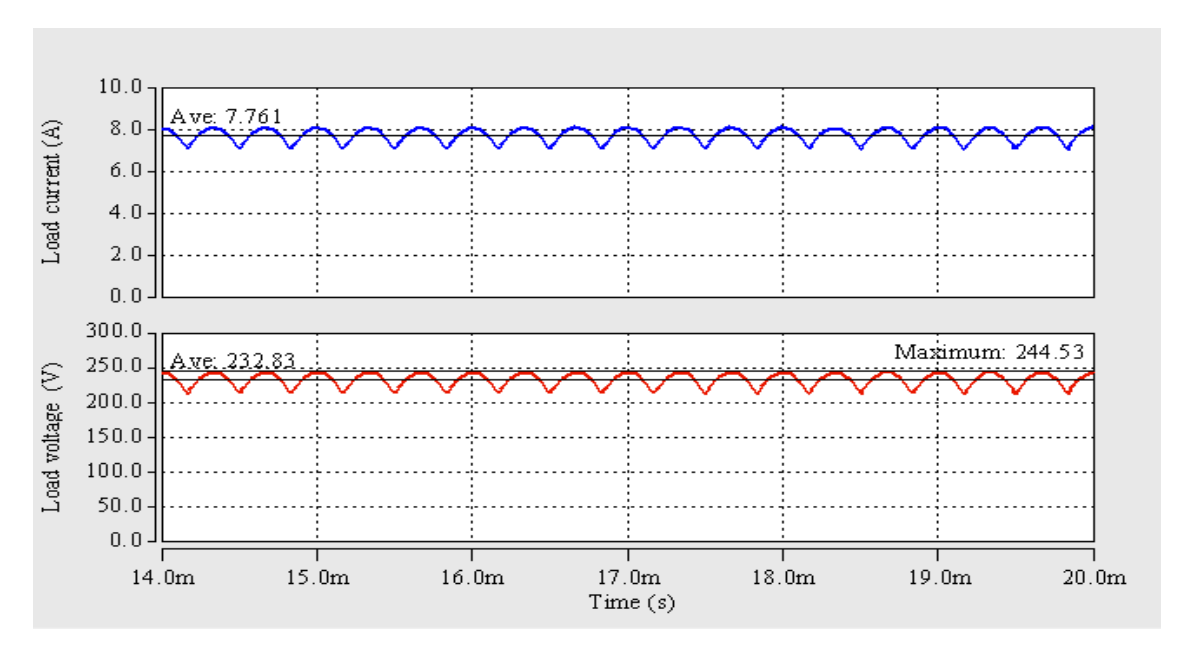


Figure B.4 DC load voltage and current

Figure B.5 shows that there are phase shifts of 120° between the input phase currents.

The rectifier efficiency η can be calculated as given below [166]:

$$\eta = \frac{Output \ average \ DC \ power}{Average \ AC \ power} = \frac{P_{DC}}{P_{AC}} \tag{B-6}$$

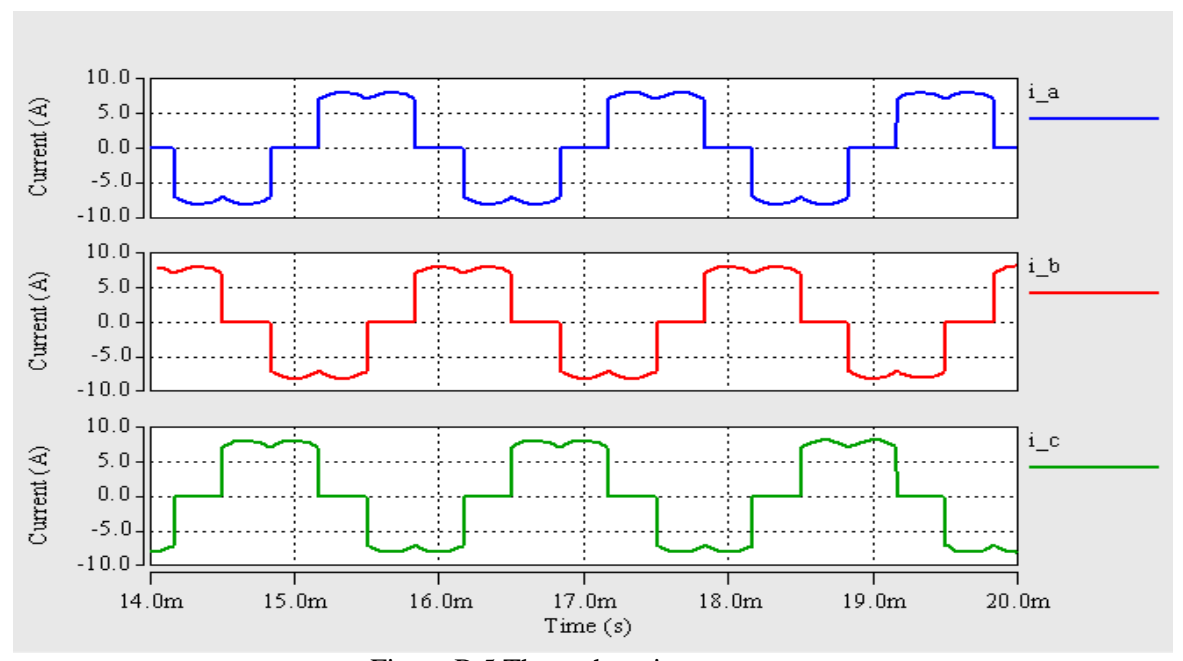


Figure B.5 Three phase input currents

The average output power can be calculated as:

$$P_{DC} = V_{DC} \times I_{DC} \tag{B-7}$$

The average three-phase AC power can be calculated from the formula:

$$P_{AC} = 3 \times V_{RMS_av} \times I_{RMS_av}$$
(B-8)

where V_{RMS_av} and I_{RMS_av} represent the average RMS value of the phase voltage and current respectively. Therefore, the efficiency of the rectifier is:

$$\% \ \eta = \frac{1819.9}{1830} \times 100 = \% \ 99.4 \tag{B-9}$$

The current flowing through the diodes is presented in Figure B.6 as explained above; two diodes conduct according to the effective line-to-line voltages. Therefore, the conduction time of each diode is approximately 667 µs, which means that each diode conduct for 120°. This figure illustrates also that there is no commutation period between the current transfer to another diode, and this means that the current is transferred instantaneously to the second diode. This is because the source inductor is neglected, which cancels any delay in the current transfer between diodes. With the presence of machine inductance, the voltage and current waveforms are different since commutation overlap occurs.

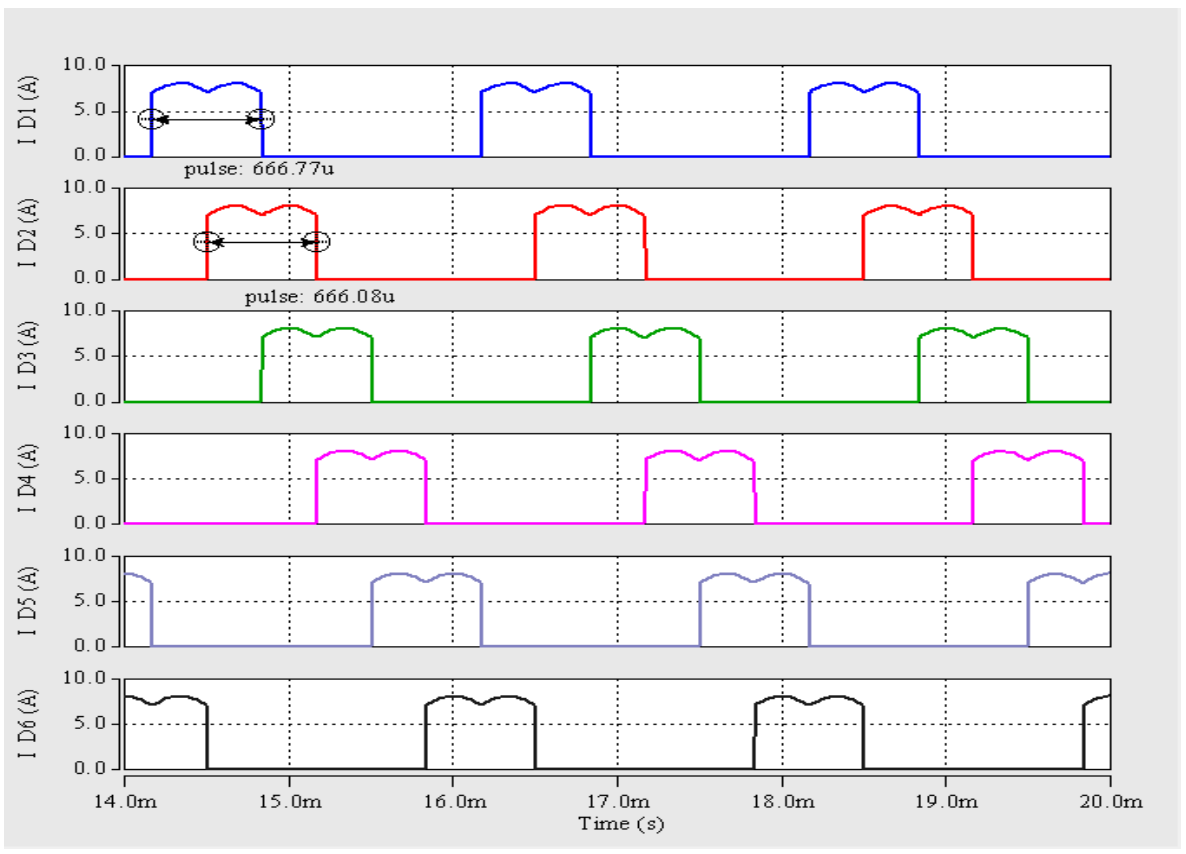


Figure B.6 The diodes current waveforms

Appendix C. Simulation Results of the Three-Phase Diode Bridge Rectifier Feeding RC Load under Constant and Variable Load

In Chapter 4, it was demonstrated that the three-phase uncontrolled rectifier operates differently depending on the load connected to the DC side of the rectifier. This appendix describes the behaviour of the three-phase diode bridge rectifier when it is connected to parallel RC load (see Figure 4.8). This behaviour is described under various operating conditions. The first section describes the performance of the three-phase rectifier at fixed load, and the subsequent section demonstrates its behaviour under varying load conditions.

C.1 Three-Phase Diode Bridge Rectifier Operating with Fixed Load

Figure C.1 to Figure C.4 illustrate the rectifier input and output voltage and current waveforms when operating with a constant load of R_L =30 Ω .

All of the figures show that the rectifier input voltages are clamped by the load capacitor voltage, as explained in Chapter 4. The rectifier output current consists of six pulses per operating frequency cycle. The maximum rectified current is equal to the maximum input current; however, its average value is equal to 1.35 I_s, where I_s represents the RMS value of the input current in one phase.

These figures also illustrate clearly that a large phase-shift occurs between the input voltage and current waveforms at various values of voltage and frequency due to the high inductance of the PMA generator, which leads to a poor power factor. In addition, a high current distortion occurs at the lower frequency, as shown in C.4.

To sum up, the variation in DC load voltage as a function of voltage and frequency variations is shown in C.5. The figure shows how the time constant (τ) governs the behaviour of the three-phase rectifier. The load voltage is reduced by increasing the frequency due to the high voltage drop driven by the high inductive reactance of the PMA generator. However, when $\tau < 1/F_s$ (when the frequency is 50 Hz), the load capacitor is discharged quickly which reduces the output voltage levels. The figure also shows that the input current is reduced by increasing the operating voltages and frequencies.

A poor power factor is achieved at higher voltage and frequency, while a higher power factor is achieved at the lower frequency of 50 Hz, as shown in C.6.

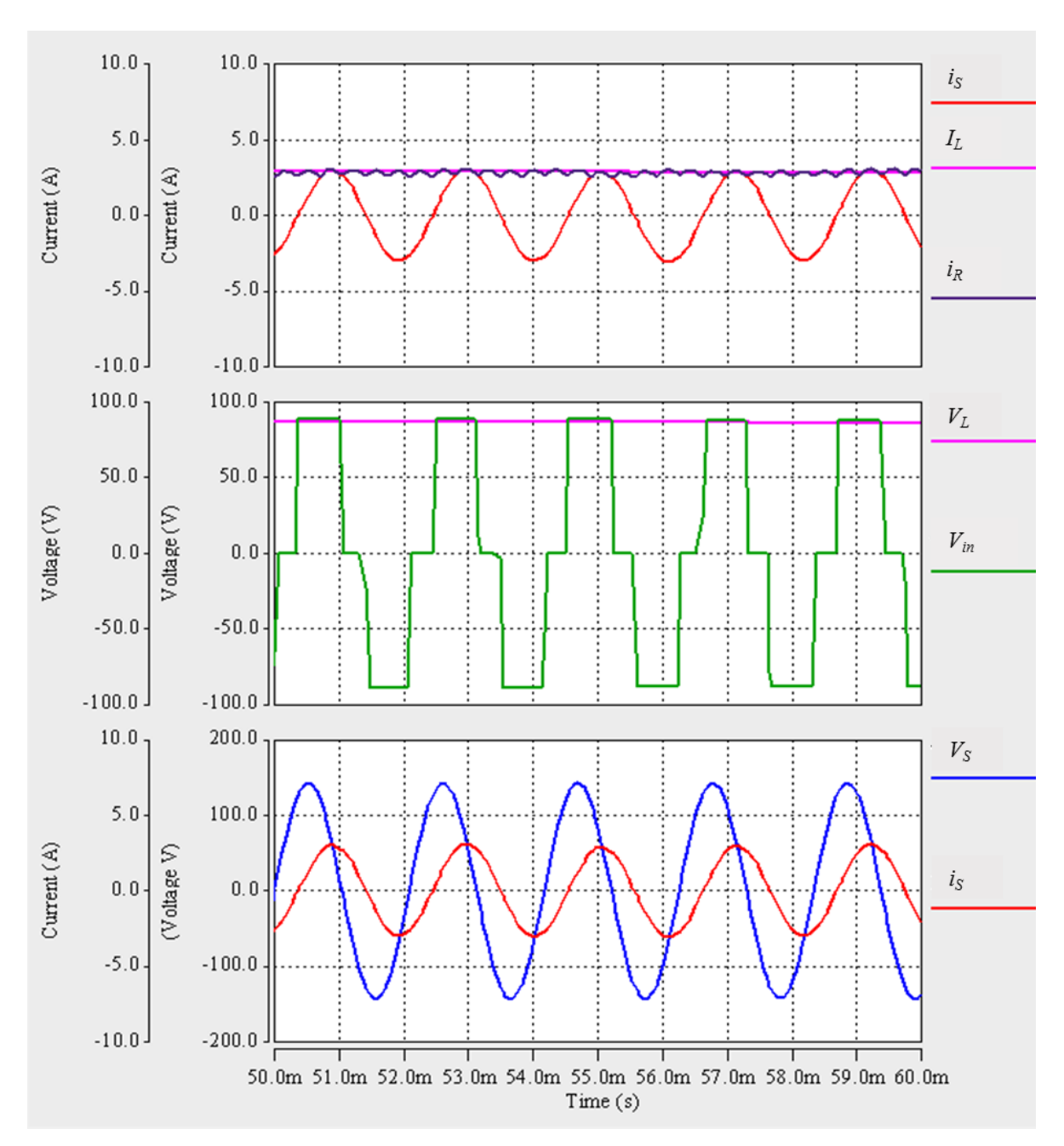


Figure C.1 Voltage and current waveforms under F_s =480 Hz, V_s = 100 V and R_L =30 Ω

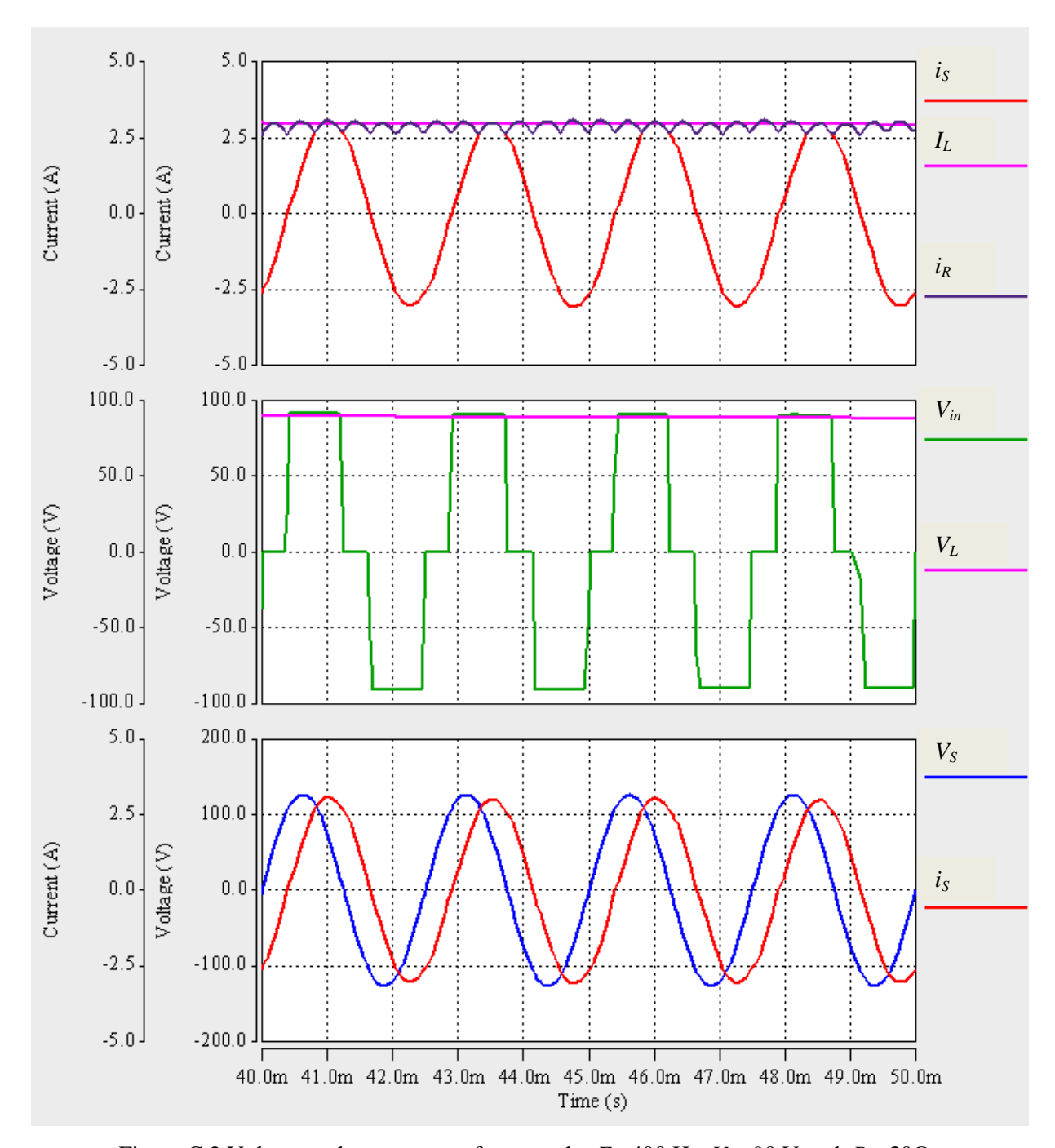


Figure C.2 Voltage and current waveforms under F_s =400 Hz, V_s = 90 V and R_L =30 Ω

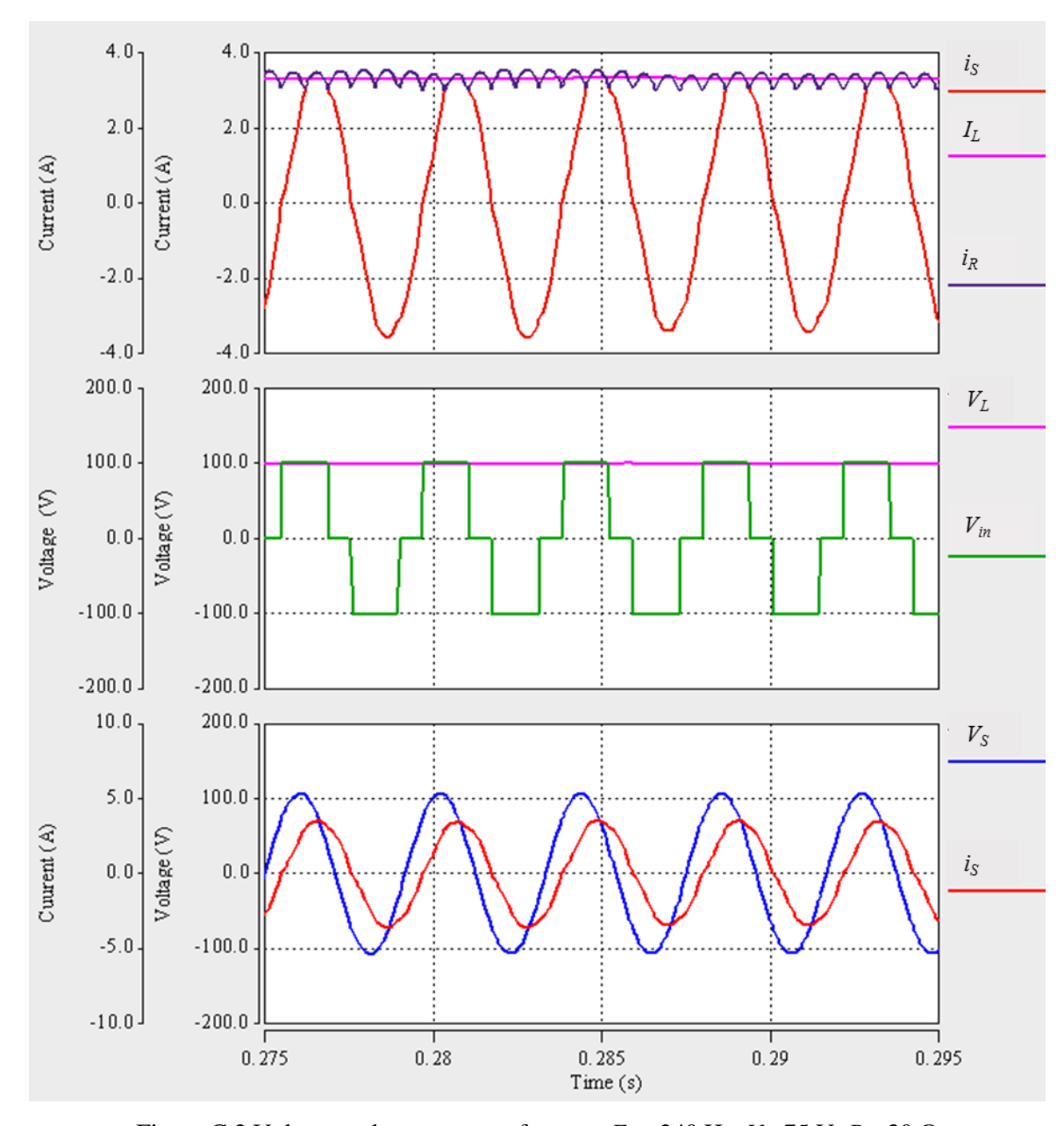


Figure C.3 Voltage and current waveforms at $F_s = 240$ Hz, $V_s = 75$ V, $R_L = 30$ Ω

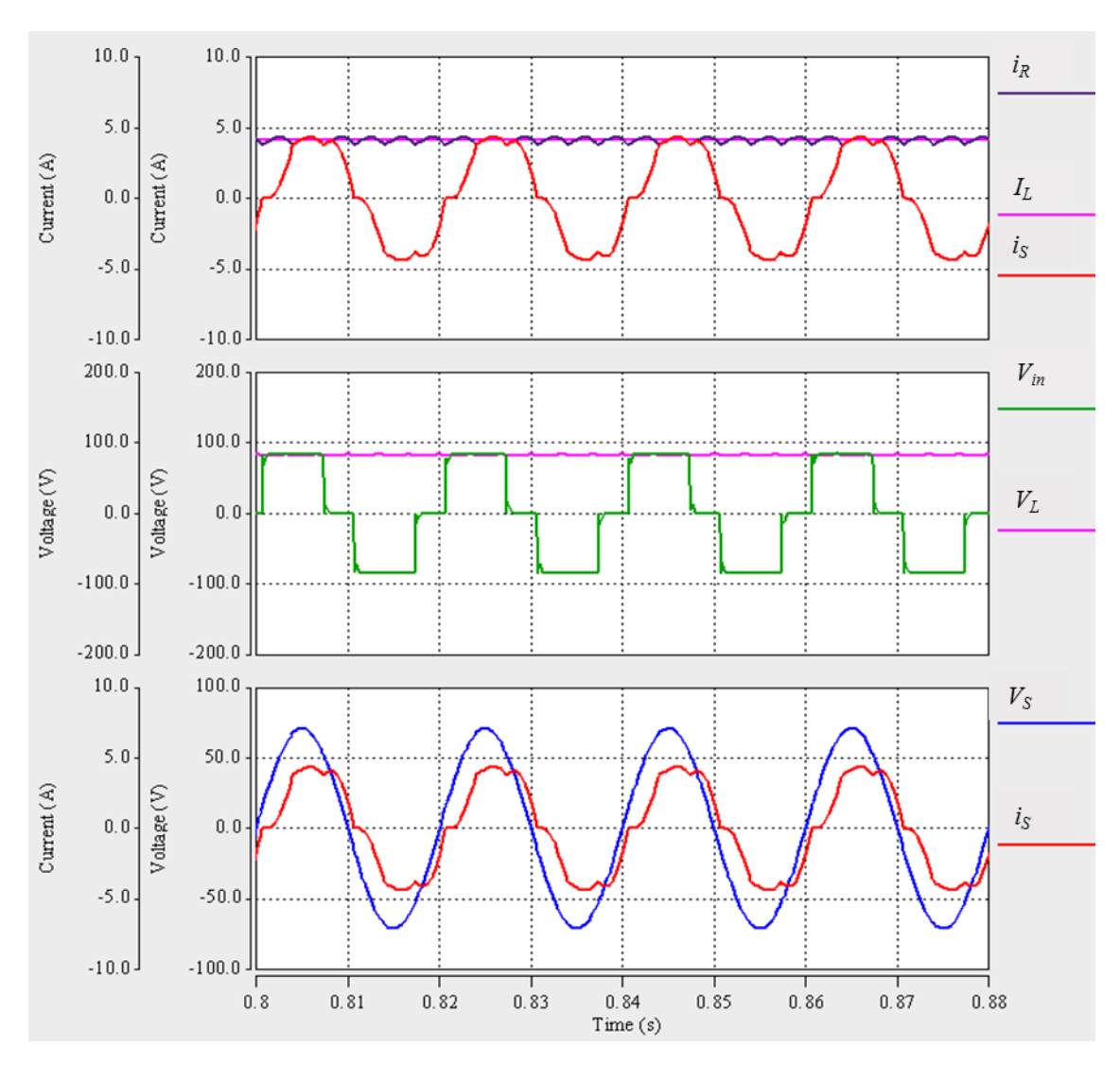


Figure C.4 Voltage and current waveforms at $F_s = 50$ Hz, $V_s = 50$ V, $R_L = 30$ Ω

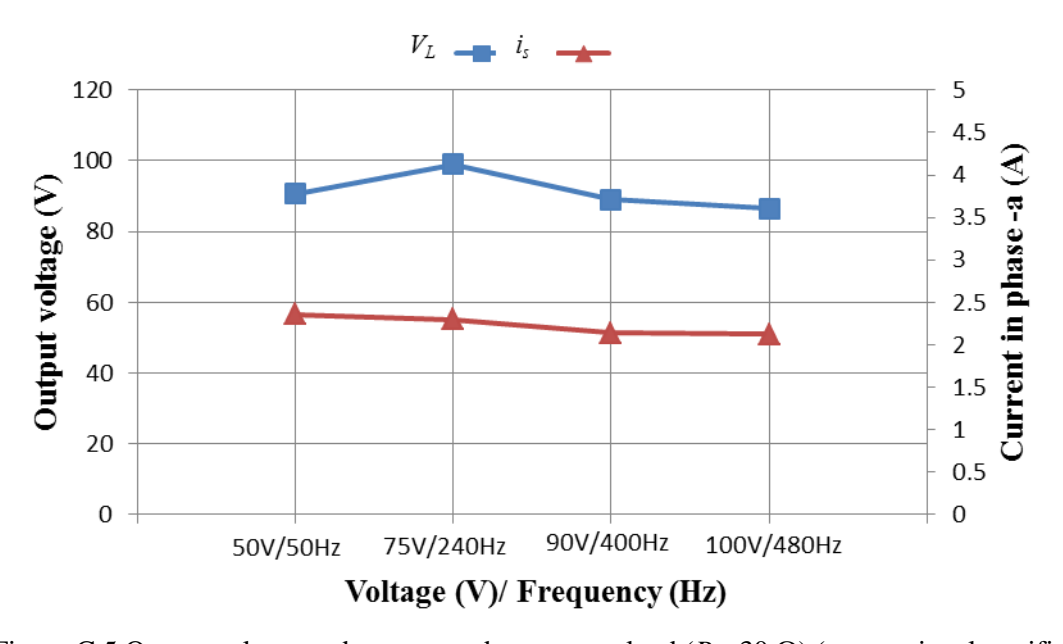


Figure C.5 Output voltage and current under constant load (R_L =30 Ω) (conventional rectifier)

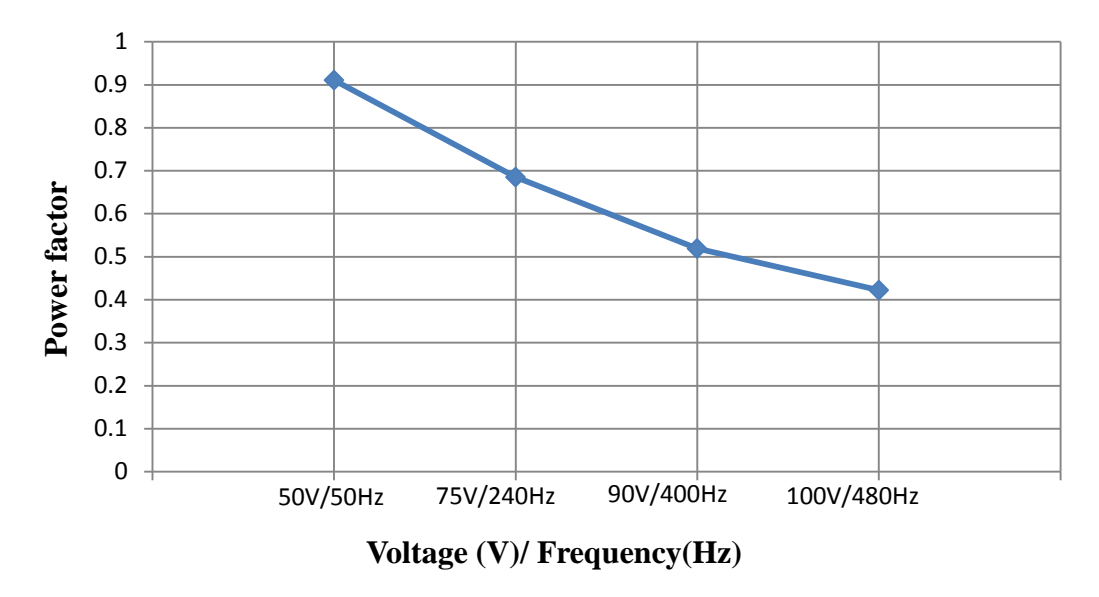


Figure C.6 Power factor under constant load (R_L =30 Ω)(conventional rectifier)

C.2 Three-Phase Diode Bridge Rectifier Operating with Variable Load

In this section, the behaviour of the three-phase rectifier is analysed numerically at various levels of load resistance in addition to various operating voltages and frequencies. The load resistance is varied between $10-30 \Omega$.

Figure C.7 shows how the output DC voltage is at its minimum level when the load resistance is at a minimum value of 10Ω . This is expected since the load is a parallel RC load and therefore it is governed by Ohm's Law. In addition, the average output voltage is increased when decreasing the supply voltage and frequency.

Conversely, the input AC current is reduced by increasing load resistance since the input current is a function of the load current which is reduced by increasing the load resistance as shown in Figure C.8. A significant current reduction occurs at the lower frequency of 50 Hz with a lower voltage value of 50 V.

The power factor is very poor at the high frequency of 480 Hz, with a value about 0.3 when the load resistance is at its lowest value of 10 Ω . Power factor values are improved gradually by increasing the load resistance, as shown in Figure C.9. However, a significantly high power factor is achieved at the lower frequency of 50 Hz. This explains the importance of replacing the conventional rectifier in any application with a variable frequency higher than 50 Hz.

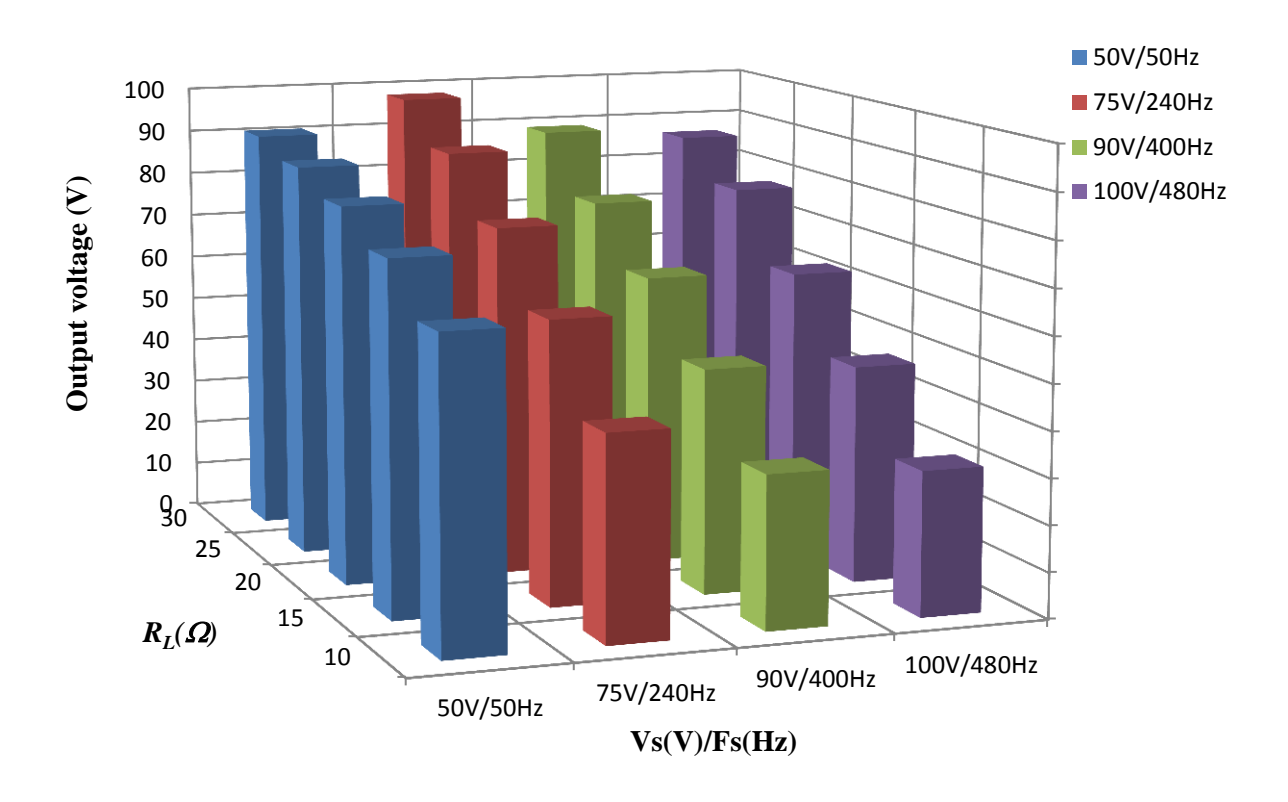


Figure C.7 DC output voltage as a function of supply voltage and frequency variations (conventional rectifier)

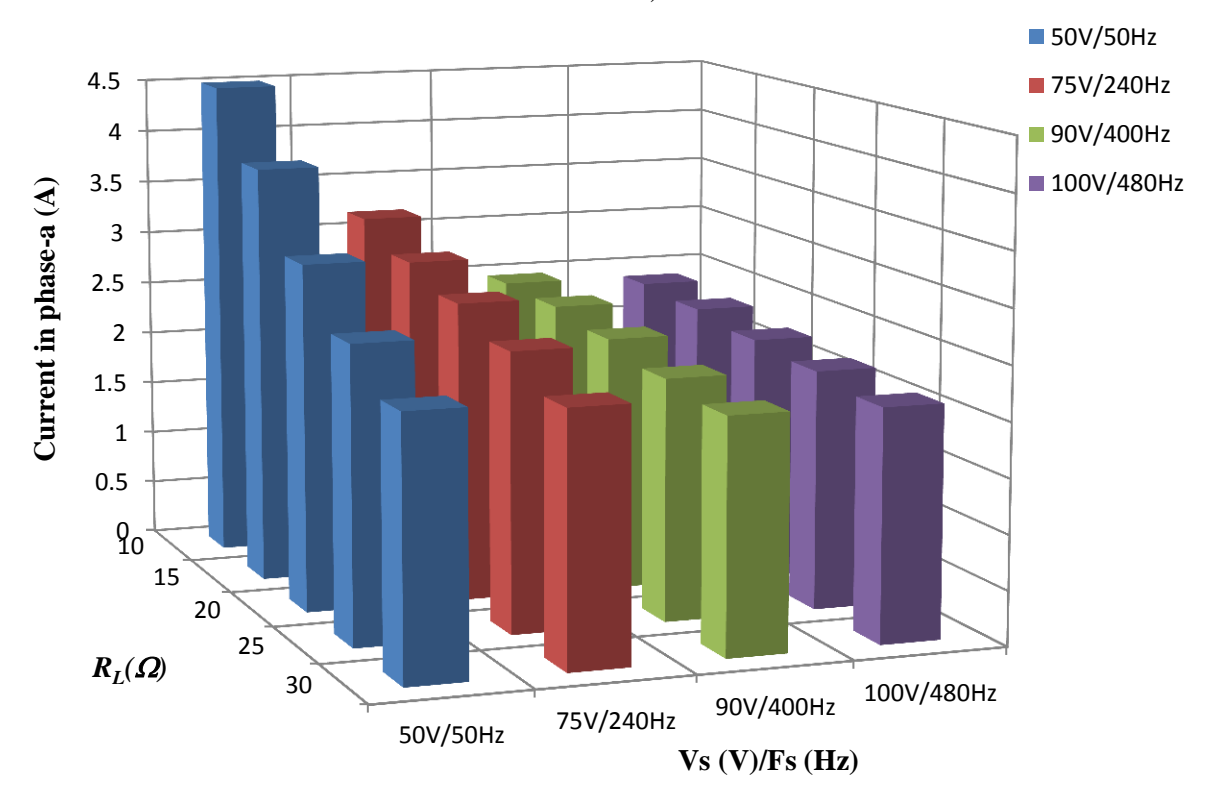


Figure C.8 Input current as a function of load resistance and supply voltage and frequency variations (conventional rectifier)

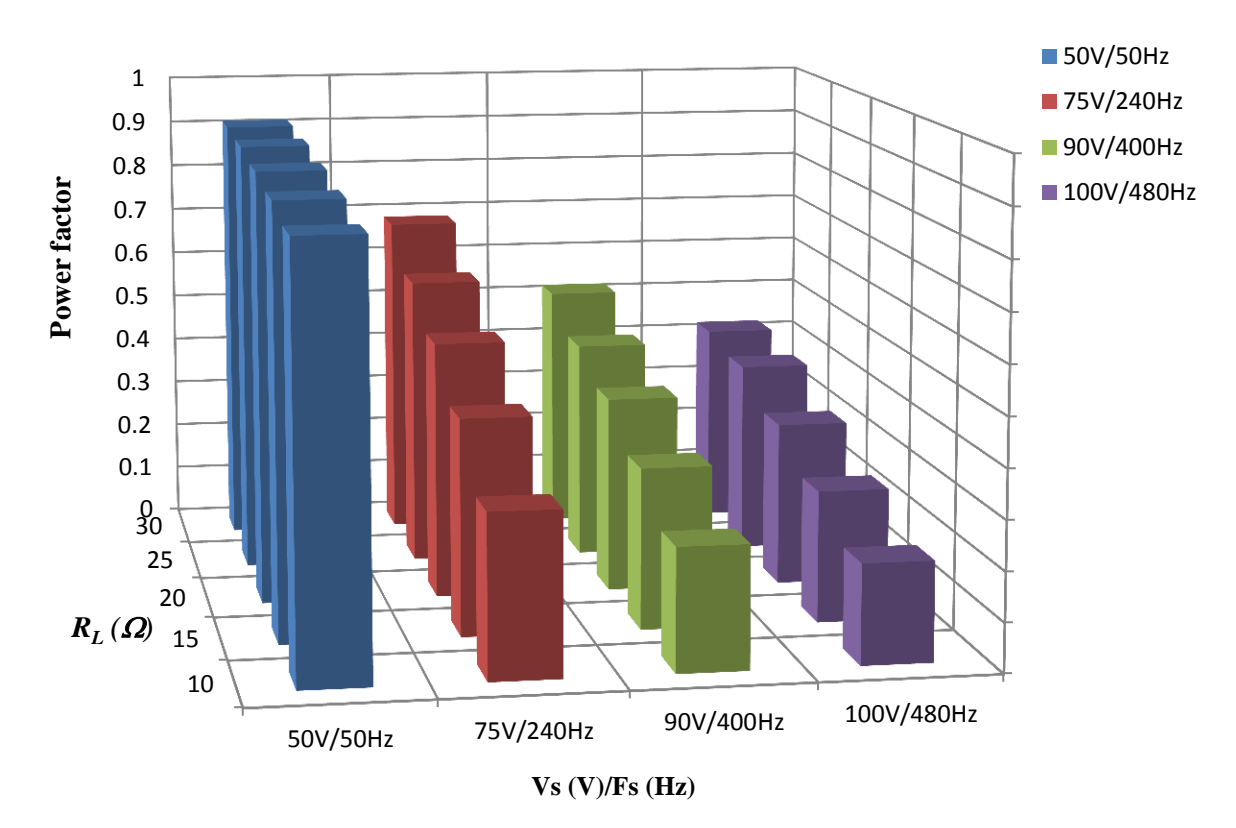


Figure C.9 Power factor as a function of load resistance and supply voltage and frequency variations (conventional rectifier)

Appendix D. Harmonic Analysis of the Programmable AC Power Source

The Behlman AC power supply unit used in this test suffers from distortion in its output voltages. Therefore, a harmonics analysis was carried out using FFT to calculate the most dominant harmonics in addition to the other harmonic components. The voltage waveforms were captured when the unit is running under no-load operating condition. A photograph of the unit is shown in Figure D.1. The voltage waveforms were captured for different voltage and frequency values and a fixed load of R_L =10 Ω .



Figure D.1 Programmable AC power source

By performing the FFT analysis in SABER, the harmonic components of the voltage waveform can be calculated.

Figure D.2 and Figure D.3 show clearly that the dominant harmonic is at approximately 20 kHz for frequencies of both 400 Hz and 200 Hz. Figure D.4 shows the harmonics components after the FFT analysis of the voltage waveforms operating at 100 Hz. The figure shows that different harmonics frequencies are available when operating at 100 Hz, including 20 kHz. This indicates that this power supply provides the most distorted waveform at lower frequencies in its operating frequency range. The harmonics components over the entire operating frequency ranges for line-to-neutral voltage (phase-a) are shown in Figure D.5 All the harmonics with amplitudes less than unity are ignored in this figure. The figure shows clearly that the most distorted phase voltage is the waveform recorded under the lowest frequency value of the spectrum (F_s =100 Hz), since it includes many harmonic components with different orders.

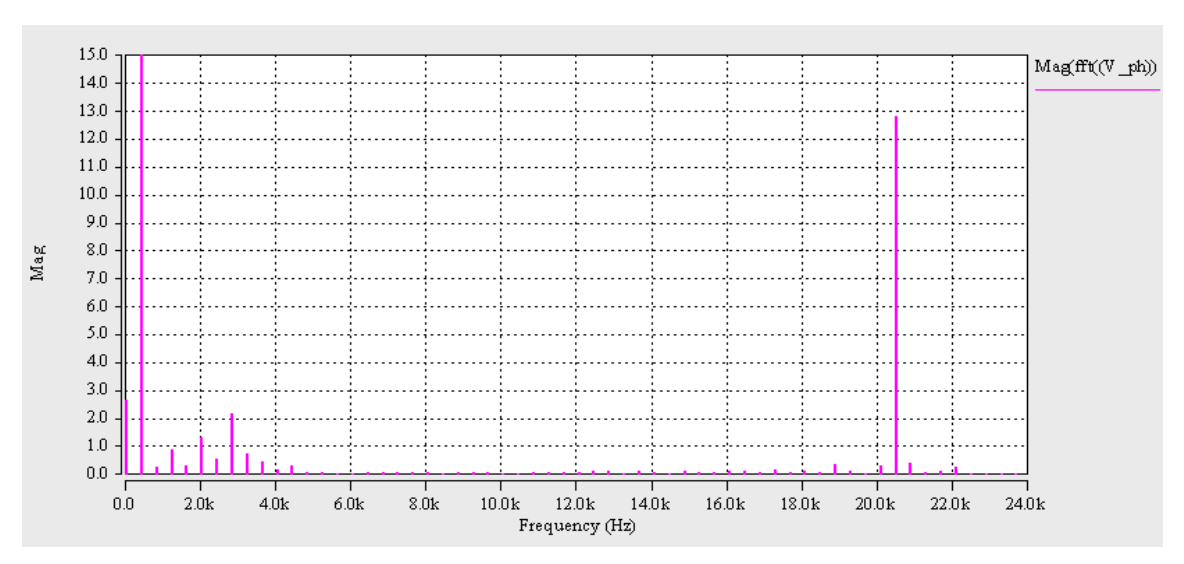


Figure D.2 Frequency spectra when operating at F_s =400 Hz, V_s =100, R_t =10

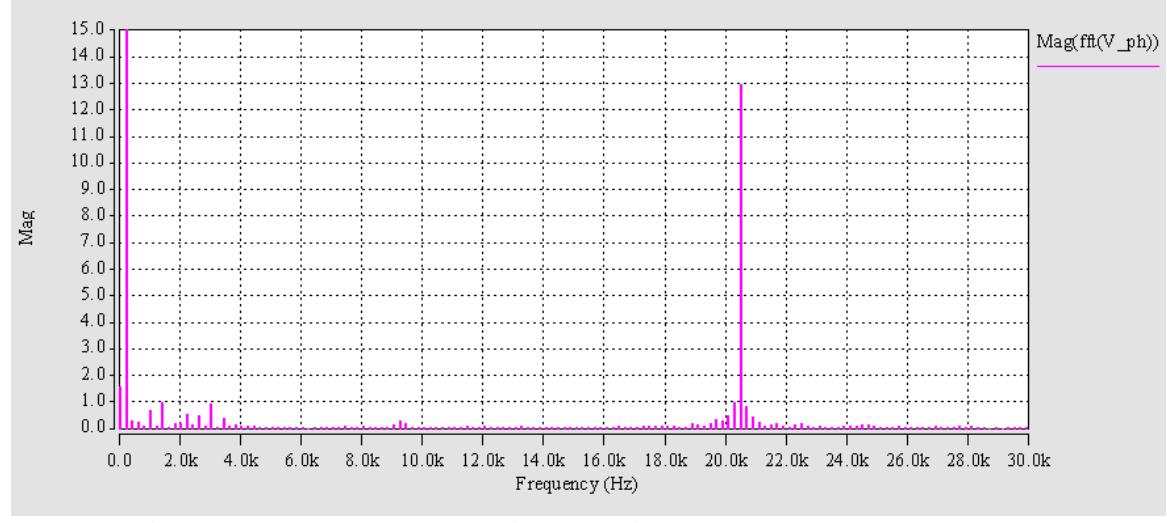


Figure D.3 Frequency spectra when operating at $F_s = 200$ Hz, $V_s = 70$ V, $R_L = 10$

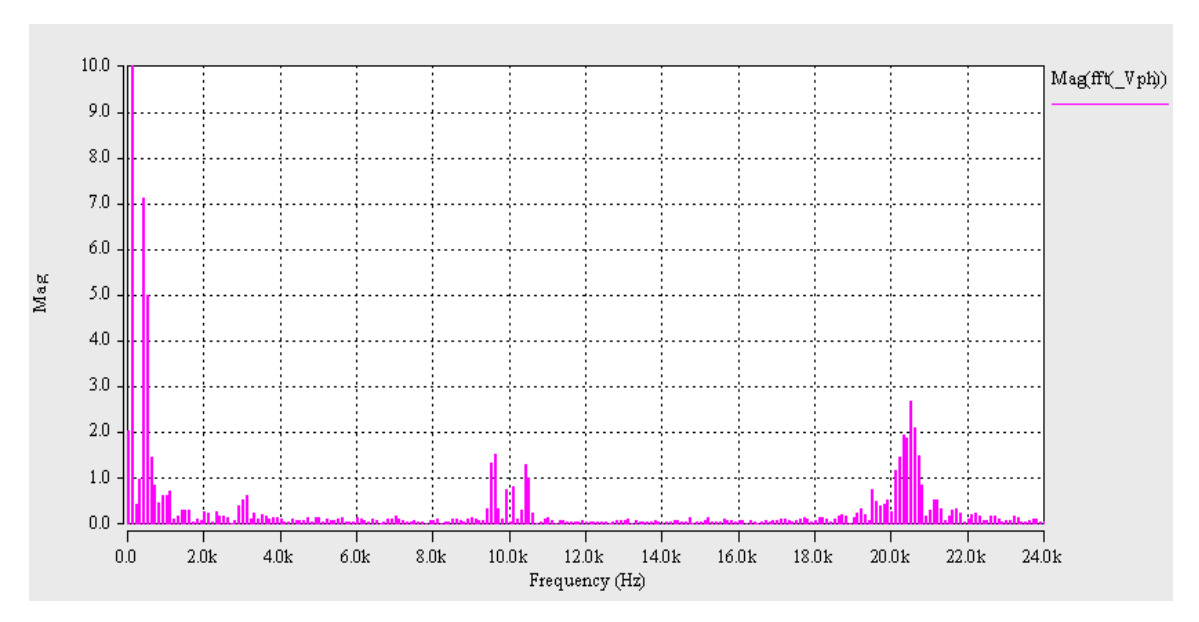


Figure D.4 Frequency spectra when operating at F_S =100, V_S =60, R_L =10

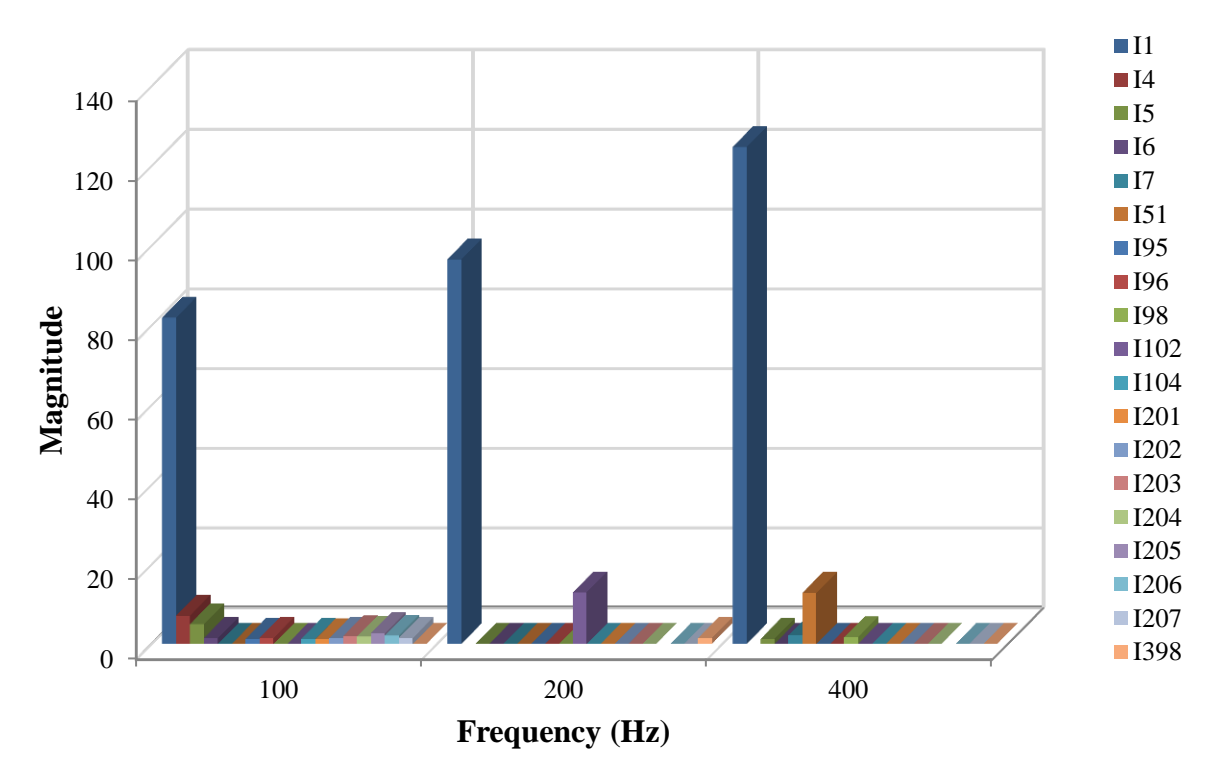


Figure D.5 Frequency spectra of AC supply voltage at different operating frequency ranges

Appendix E. Hardware Development

This appendix contains a detailed description of the test platform, along with the design and implementations of the system prototype, including the power converter, controller platform, and measurement circuits. The hardware position is also described in this Appendix. The hardware design and arrangements are described in detail and the hardware locations are also considered. A description of the general interface board for eZdsp Texas Instruments TMS320F28335 DSP is provided, while a detailed explanation of the peripherals utilised from the DSP is also included. The measurement units and load used to acquire the experimental results are also described and the procedure required to scale the sensed measurements down to meet the ADC channel requirements is included.

E.1 Hardware Set-up

The details of the hardware used to assemble the whole system are given in the following sections.

E.1.1 Electrical generator (PMA)

For the practical test, the permanent magnet alternator (PMA) is emulated by an equivalent circuit as presented previously in Chapter 4. Three main units were used for this emulation as given below:

1. Programmable AC power source

The Behlman PAC 2000 digital controller is a high power programmable AC power source/ frequency converter, which was used in this test to emulate the back EMF of the PMA generator. This power source is able to deliver 60 KVA of power with an output voltage between 0-132 V AC, 3-phase with a frequency range of 45-500 Hz. A photograph of the power supply unit is shown in Appendix D.

2. Internal reactor

To emulate the PMA inductance, two three-phase reactors were connected in series to achieve an inductance of 13.75 mH, as shown in Figure E.1. This figure shows that both reactors were

mounted in an enclosure for safety reasons. The first was a set of three-phase reactors, each with 750V/50 Hz and with an inductance value of 3.75 mH carrying a current of 16 A RMS. The second box also contained three reactors with three selectable values of inductance and with a maximum current of 15 A RMS/50 Hz. A value of 10mH was selected for each phase. By connecting both reactors in series, a three 13.75mH inductor set is achieved.



Figure E.1 A photograph of two sets of three-phase reactors connected in series

3. Internal resistor

Six potentiometers are used to perform the experimental test and these are divided into two groups of resistors. The first group included three sliding resistors used to represent the internal PMA generator resistance. One resistor was connected to each phase, with the resistance value capable of being varied to a maximum value of 10Ω (12A) for each phase as shown in Figure E.2. These resistors were located in the AC side of the three-phase FCSC circuit, or in other words between the power supply and the inductors. The second group of potentiometers are used to represent the load, as described in the next section.

E.1.2 Resistive load

The load is connected to the output of the three-phase rectifier (the DC side of the converter). The load was represented by three sliding resistors (similar type to the resistor in Figure E.2). These resistors are connected in series to provide variable resistance with a maximum value of 30 Ω . Each resistor has a value of 10 Ω (14 A).

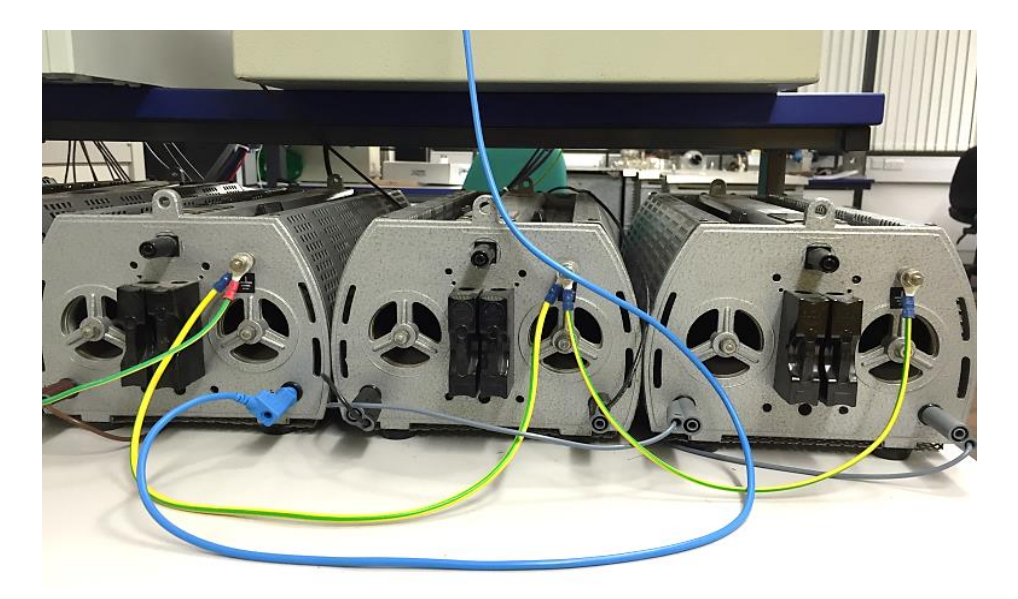


Figure E.2 Photograph of three sliding resistors in the AC side

E.1.3 Design and implementation of the three-phase FCSC converter

The design and selection of the three-phase FCSC converter is described as follows:

a) AC capacitor bank

Based on the principles of the symmetrical duty cycle control explained in Chapter 5, the maximum frequency in the frequency range was used to select the value of the required capacitors, which is able to cancel the effect of machine inductance. This means that the maximum frequency is considered to be equal to the resonant frequency in this work.

Based on the availability of this type of capacitor and using equation (E-1) [167], the capacitance value is calculated. Hence, three metallized film General Electric capacitors were chosen for use in this experimental set-up with a value of $8 \, \mu F / 660 \, V$ AC.

Since these capacitors are specifically designed for general purpose applications with a non-sinusoidal voltage waveform AC application, they were selected for the test due to advantages of their ability to handle high frequency currents, long-term reliability and safe operation; disadvantages of the metallized film capacitors such as large size and weight could be ignored.

However, with these capacitor values, the maximum frequency of the frequency spectrum was reduced from 500 Hz to 480 Hz as described earlier in Chapter 5.

$$f_{res} = \frac{1}{2\pi\sqrt{LC}} \tag{E-1}$$

where f_{res} represents resonance frequency.

The height of these capacitors is 4.74 inches with an oval base, and therefore they were mounted on a designed aluminium plate to hold them safely, as shown in Figure E.3.



Figure E.3 Photograph of AC capacitor

These capacitors are able to carry a maximum total RMS current of 15 A, which includes the fundamental current and harmonics. The equivalent series resistance (ESR) of each capacitor is 0.0657Ω . Equation (E-2) can be used to calculate loss in watts [168] as expressed below:

$$P_{loss}[W] = I_{RMS}^2 \times ESR \tag{E-2}$$

where P_{loss} represents the loss, and I_{RMS} is the total RMS current (fundamental and harmonics).

The power boards, which consist of the IGBT printed circuit board and the gate drive circuit PCB, were positioned very close to the AC capacitor to reduce noise and the EMI.

b) IGBT printed circuit board

Three identical PCBs were designed to house the switching device in the FCSC circuit.

The circuit was divided into three small boards because it is then easier to replace one board when failure occurs. Each board has two discrete IXYS IXDR 30N120 IGBTs with a voltage and current rating of 1200 V and 50 A respectively, and two International Rectifier

30CPF12PbF fast soft recovery diodes with a reverse recovery voltage V_{RRM} and current rating of 1200 V and 30 A respectively. Each diode was connected in series with one IGBT to ensure reverse blocking during the half-cycle of the operating voltage. A schematic diagram of the IGBT boards is presented in Figure E.4.

The IGBT switches and diodes were chosen to have high voltage and current to provide more flexibility to the experimental test, because they are connected across the AC capacitors which have a high voltage across them at certain values of operating voltage. All IGBT switches and diodes were fitted on a heat sink to reduce power dissipation during converter operation, and two small fans were fitted on the heat sink fins to improve the cooling process. These fans were supplied with +24 V DC from a TTi TSX3510 precision DC power supply. Figure E.5 shows a photograph of the three-phase FCSC converter.

c) Three-phase rectifier

An IXYS VU062-16NO7 three-phase bridge rectifier with 63 A and 1600 V was used to perform the AC to DC conversion. Each AC input of the rectifier was supplied by the capacitor terminal in each phase. The DC output terminals of the rectifier were connected to the load via a designed DC card.

d) DC card

This board mainly contains the pre-charged circuit components. Two Panasonic electrolytic type capacitors with 250 μ F and 450 V each were used as a smoothing capacitor in order to reduce the ripple in the output voltage.

These capacitors were connected in parallel to provide an equivalent capacitance of 500 μ F. In general, in the conventional three-phase diode bridge rectifier, it is always important to reduce the ripple in the output to a minimum value. This can be achieved by selecting an appropriate capacitor value as given by equation (E-3) [113]:

$$V_{r(pp)} = \frac{V_m}{f_r R_L C} \tag{E-3}$$

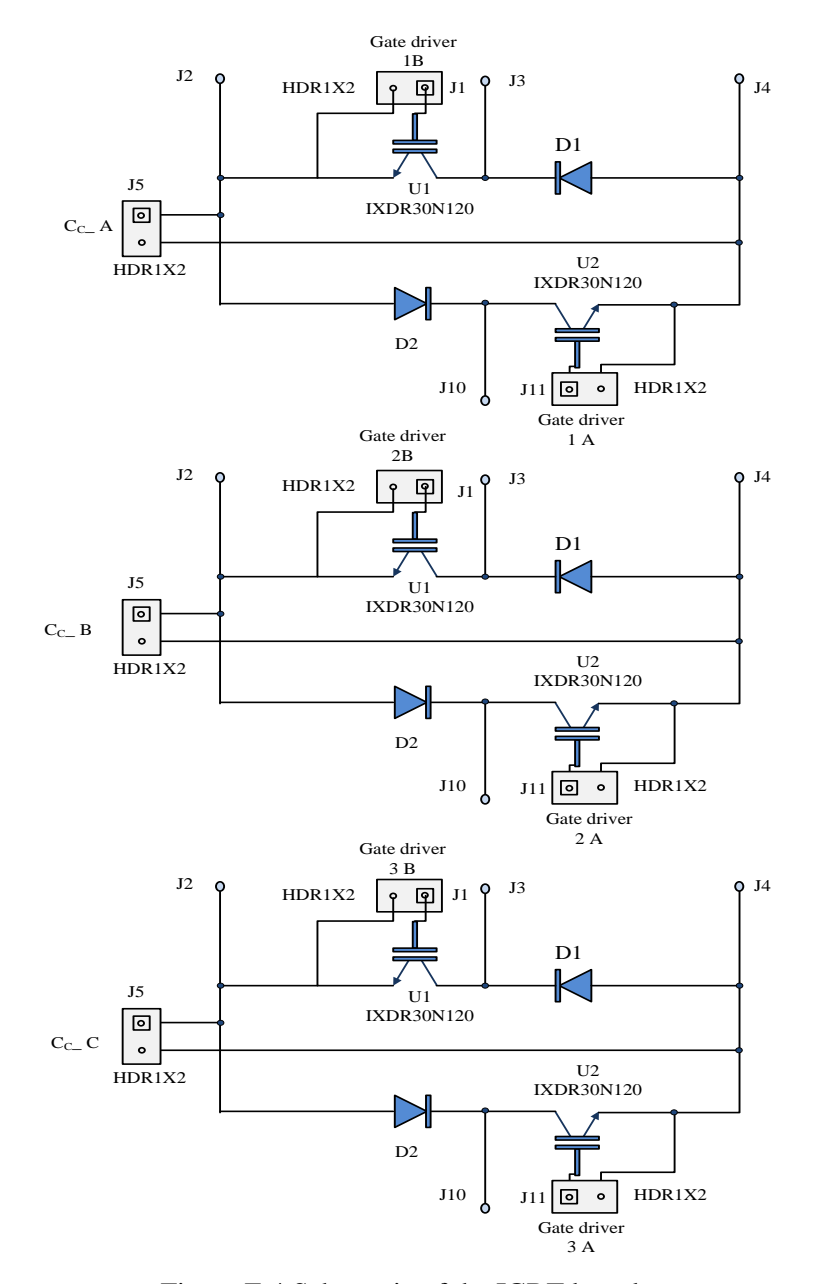


Figure E.4 Schematic of the IGBT boards

where $V_{r(PP)}$ represents the peak- to- peak ripple in the output voltage, which is required to be small. V_m is the maximum input voltage, f_r is the output ripple frequency which equals six times the supply frequency, and R_L is the load resistance.

In this project, the values of voltage and frequency were varied, and according to the above equation the maximum ripple will occur at the minimum frequency in the spectrum, which is 50 Hz. The selection of the smoothing capacitor value was achieved using the parameter sweep method via simulation. This value is equal to 500 μ F, and as a result the $V_{r(pp)}$ in the output is approximately 1 V at a frequency of 50 Hz.

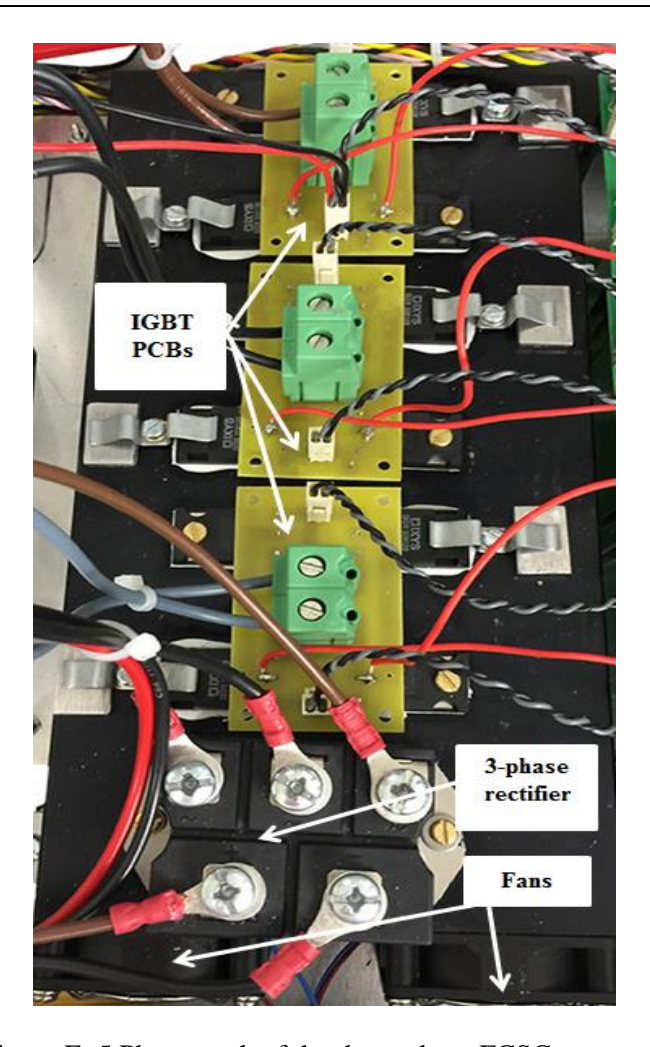


Figure E. 5 Photograph of the three-phase FCSC converter

In this experimental test, the smoothing capacitor should be charged first. Therefore, to avoid the risk of a high inrush current when the capacitor is connected to the AC supply for charging, an inrush current (pre-charge) resistor is inserted into the circuit during charging [114]. To short out the pre-charge resistor after the capacitor is fully charged, a double pole, double throw DPDT 10 A 24 V DC Finder PCB relay is used. The +24 V was supplied by an external DC power supply. This relay is controlled by the DSP relay, which is closed via a LabView control panel push-button named relay one, which controls the closing of the DSP relay manually after a certain capacitor charging time.

The charging time of the capacitor is typically considered to be five times the circuit time constant, as given below:

$$T = 5 R_L C_L \tag{E-4}$$

Since the load resistor is disconnected during the pre-charging interval using a ROCKER DPST SWITCH, the capacitor will be fully charged after a short time of approximately 32 ms.

It is worth noting that, in spite of the power dissipation, the full supply voltage is applied to the capacitor as calculated using equation (E-5) below:

$$P = \frac{V^2}{R} = 1 \text{ kW} \tag{E-5}$$

A wire bond resistor of 10Ω , 100 W is used, because the resistor is only connected for a very short time of 32 ms and therefore there is no difficulty using it even with a lower power rating. The photograph and a schematic of the DC board are shown in Figure E.6 and Figure E.7, respectively.



Figure E.6 Photograph of the designed DC card

E.1.4 The gate drivers

Three isolated dual gate drive cards developed at Newcastle University were used in this experimental test. Each card consists of two identical gate drive circuits named A and B, and they can operate either independently or as a complementary pair.

For this test, the two gate drives were configured to operate independently (non-complementary mode). A single 10-way ribbon cable is used to interface signals and power for both circuits. The gate drive circuit is based on an ACPL-332J opto-coupled driver device. The input signals to the gate drive PWM-A and PWM-B are routed to CD40106BT inverters to add more noise immunity.

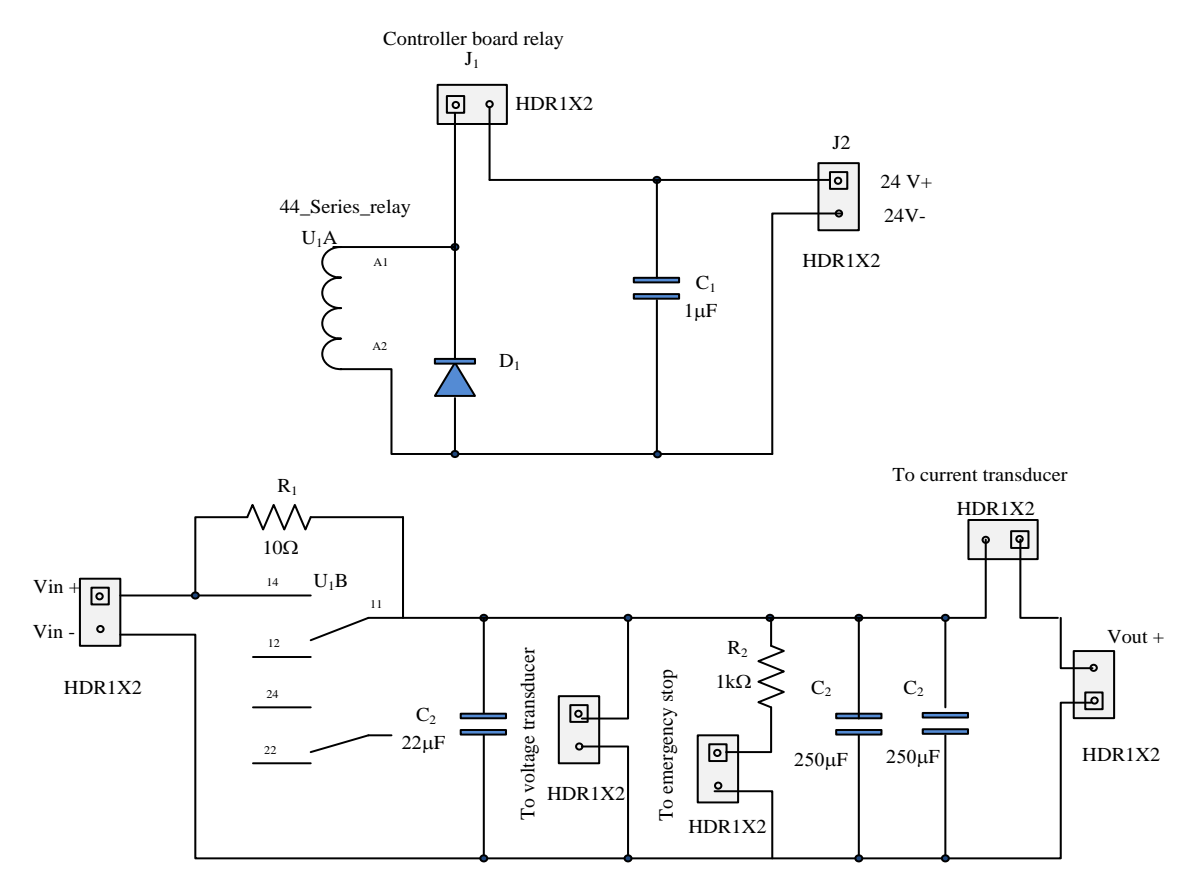


Figure E.7 Schematic of the DC board

Furthermore, the gate drives were not included in the general board to keep them close to the power converter. This is important to further reduce the noise level. To prevent transient overvoltage due to stray inductance, two back-to-back 18 V Zener diodes were provided between the gate and emitter on the isolated output side of ACPL-332J. Since the ACPL-332J has a built-in DESAT fault protection feature, a DESAT sensing circuit which includes a fast recovery diode connected to the collector (drain) of the IGBT/MOSFET terminal is used in this card. When the IGBT/MOSFET was turned OFF, this diode protects the driving circuit from high voltage. This gate driver is designed to drive a variety of IGBTs/ MOSFETs and therefore a flexible configuration is provided. A photograph of the three dual gate drivers is shown in Figure E.8.

E.1.5 Digital signal controller platform

In order to apply the symmetrical duty cycle control to the three-phase FCSC-rectifier and generate the required signal to drive the switching time of the IGBTs, a Spectrum Digital eZdsp TM F28335 evaluation board was used to programme the digital control scheme in this project, as shown in Figure E.9.

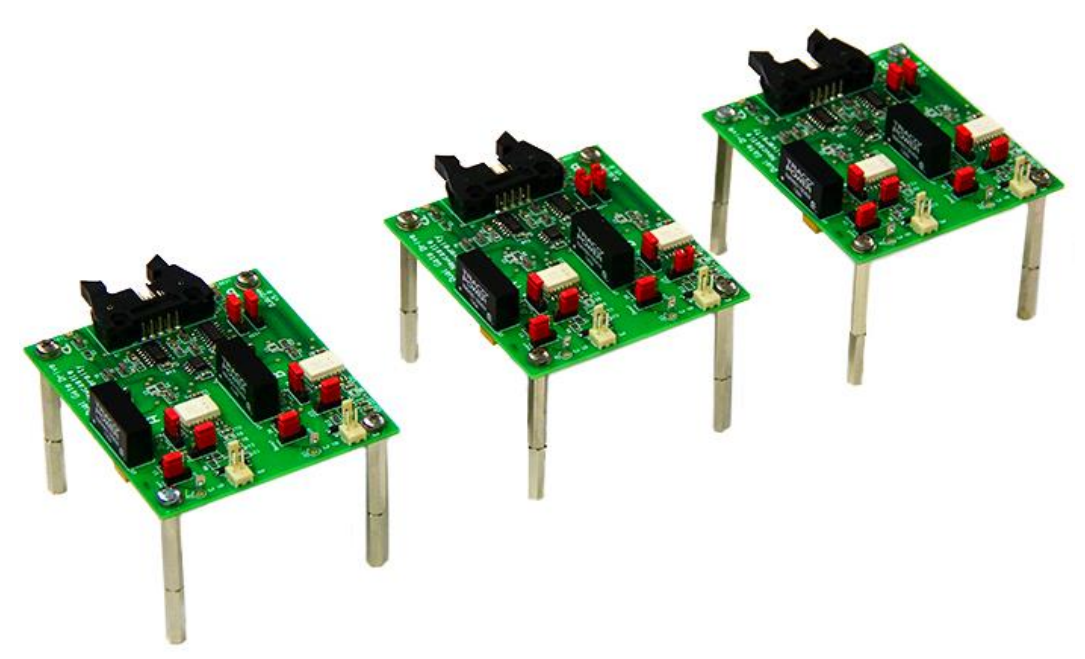


Figure E. 8 Photograph of three dual gate drivers

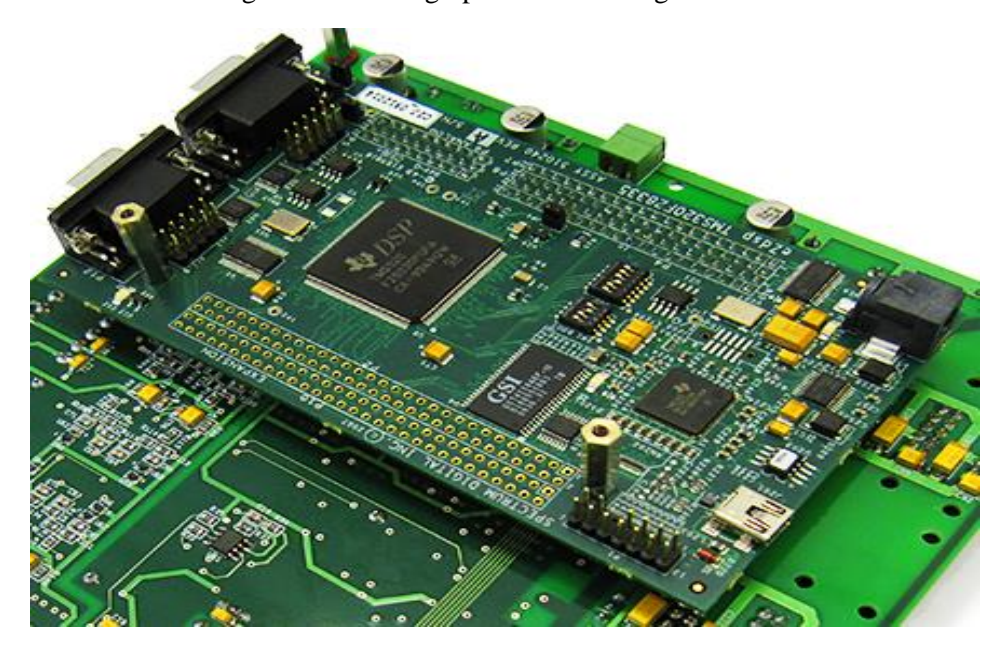


Figure E.9 Photograph of the Spectrum Digital eZdsp TM F28335

This board is based on the Texas Instruments TMS320F28335 digital signal controller (DSC), which is a single-precession 32-bit IEEE 754 floating point unit (FPU). This reduces the development time to perform a maths task efficiently. The Texas Instruments TMS320F28335 is a flexible controller with an operating speed of 150 MHz, and the hardware features control peripherals such as: six PWM modules able to generate independent/complementary PWM pulses and a 12-bit 16 channel analogue to digital converter (ADC) to digitise the sensed measurements. In addition, several serial communication peripherals are supported by this DSP, including: two enhanced controller area networks (eCANs), three serial communication

interfaces (SCIs) and one serial peripheral interface (SPI) in addition to three 32-bit CPU timers and 88 general purpose I/O pins which can be configured as input or output pins. The F28335 implements the standard IEEE 1149.1 JTAG (joint test action group) to enable real-time control mode, which means that the user can modify the content of the memory and peripherals during the code processing interval via the processor without stopping it.

Full details of the Spectrum Digital eZdspTMF28335 and microcontroller are available elsewhere [169, 170]. The aforementioned information shows that this controller can meet the requirement of this project. Code Composer Studio version 5.3 (CCS 5.3) from Texas Instruments was used as the integrated development environment for software development and debugging.

E.2 General purpose power interface board for eZdspTM F28335

An additional interface board was designed and developed by Electrical Power (EP) research group at Newcastle University to provide a flexible interface between the eZdspTM F28335 and power converters. This board is designed to be used for various power converter control applications, as shown in Figure E.10. The main functions of this board can be summarized as follows:

- Auxiliary power supply unit: on-board +15 V, -15 V, and +5 V auxiliary power supplies each with a choke are provided to energise all on-board devices. In addition, these power sources can be used to provide several off-board interfaces such as gate drivers or voltage and current sensors.
- Four small relays are provided which can be used for pre-charged circuits or protection to energise the contactor and relays coils, or they can be used directly with a low power circuit. In this project, one relay was employed to control the power relay used in the pre-charging circuit on the DC side of the rectifier.
- Six-pairs of gate drive interfaces are provided in this board to interface the PWM output pins of the eZdspTM F28335 with the external gate drive board. Each interface has two PWM signal pins, 5 V and 15 V pins for power requirement, and fault reset signal pins are also provided as these are required by some gate drive modules. This enables the microcontroller to monitor the gate drive circuit and perform suitable action during fault events. In this work, hardware modifications were implemented on

- the three-gate drive interfaces to comply with the pulses required for the IGBT switches as described in the next section.
- Ten flexible sensor interfaces from the 16-eZdsp analogue input are used to enable variety of voltage and current sensors to be interfaced with the microcontroller ADC input via four-pin connectors. These connectors have a supply pin which can be used to energise the external sensors with +15 or +5 V, -15 and 0. This can prevent the risk of a potential ground loop and noise which might be caused if using an external power supply. For this experiment, physical hardware modifications were performed in the voltage sensor interfaces to cope with the system requirements, as explained later. The other six sensor interfaces were connected to an out-of-range trip circuit to provide fast hardware overcurrent or overvoltage protection when required. It is worth mentioning that the ADC input ranges between 0-3 V. Hence, all sensed measurements, including voltages and currents, must be attenuated and scaled down by a certain factor to be compatible with the ADC scale.

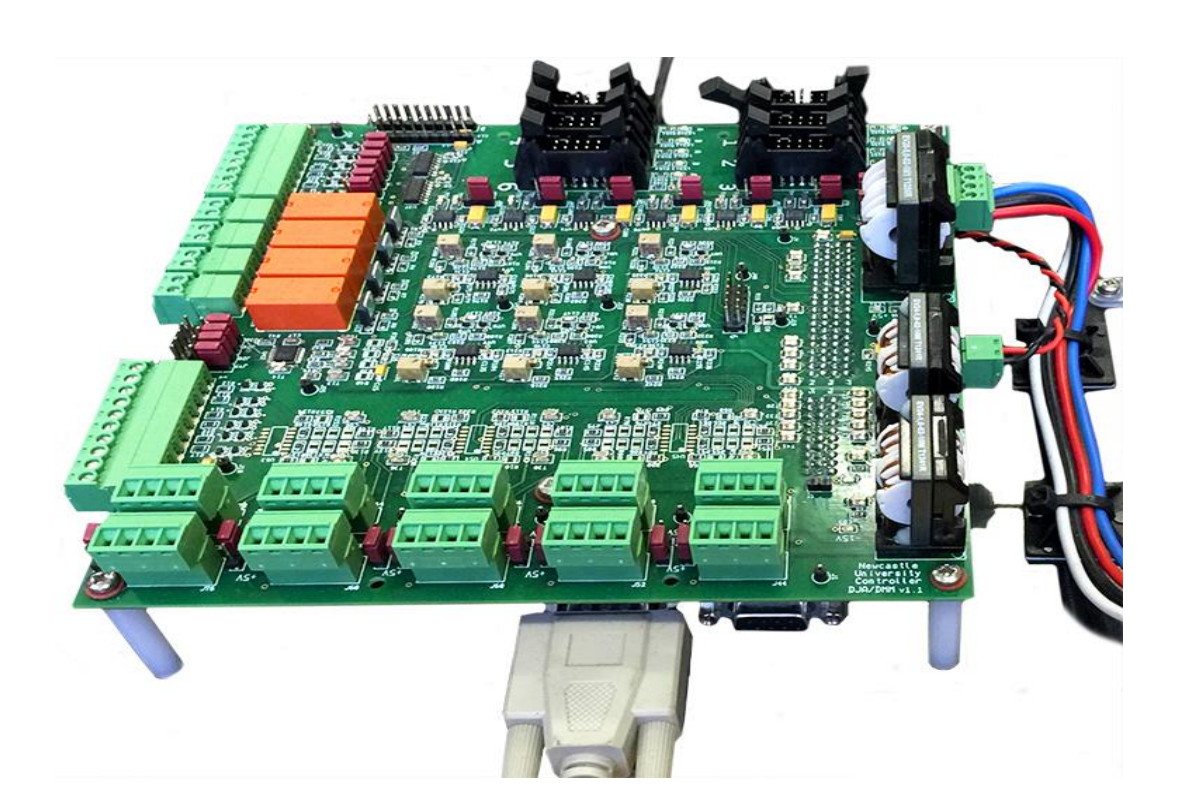


Figure E.10 Photograph of the general purpose power interface board

The board was designed to reduce the interference to a minimal level. Therefore, a board with four layers was used, where one layer was dedicated to be a common ground plane in addition to the use of decoupling capacitors in certain positions.

Additional functions are also available in this board, such as digital to analogue converters (DACs), shaft encoder interfaces, and general analogue interface. Details of these features are not included here because they were not used in this test.

E.3 Current sensors

In order to detect the input currents in all phases, three current transducers LEM CAS-15 NP Hall-effect with galvanic isolation were used in this test. The + 5 V power supply for the current transducers was provided by the ADC channels on the general interface board. The transducer output voltage was between 0.375V to 4.625V with a nominal voltage offset of 2.5 V when the current was zero, which is higher than the mid-point of the ADC input range of 0-3 V and therefore these voltages were scaled down via voltage resistor arrangements and two clamp diodes to comply with the ADC voltage range.

In addition, to ensure the accuracy of the transducer readings, a sensor calibration procedure was carried out to compensate for the differences reading via the software. Inaccurate sensor readings occurred because of the tolerance of component such as resistor tolerance. A photograph of three LEM CAS 15-NP current transducers is shown in Figure E.11.

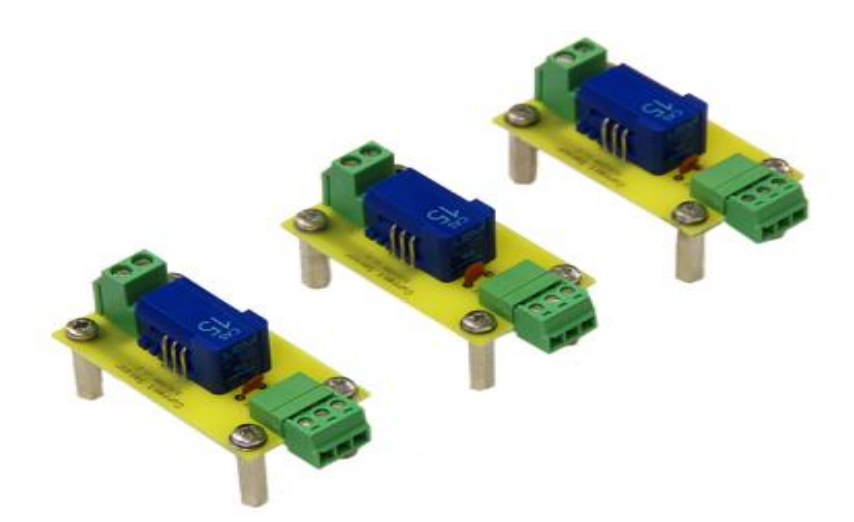


Figure E.11 Photograph of three LEM CAS 15-NP current transducers

E.4 Voltage sensors

Three LV 25-P 500V isolated voltage transducers were used in this test to measure the input voltage to the system, with the output of each transducer fed to one of the three input terminals of the zero crossing board (ZCD). The required \pm 15 V supplies for these transducers were provided by the \pm 15 V available on the ZCD board. Measuring resistors of 150 Ω were used in these boards.

As the converter works with a variable-voltage variable frequency supply, a 10 k Ω 25 W Arcol wirewound resistor was used in each card which represents the primary resistor R₁. The selection of R₁ was based on the maximum voltage in the range (100 V) [171]. A schematic and photograph of the voltage measurement unit are shown in Figure E.12 and Figure E.13, respectively.

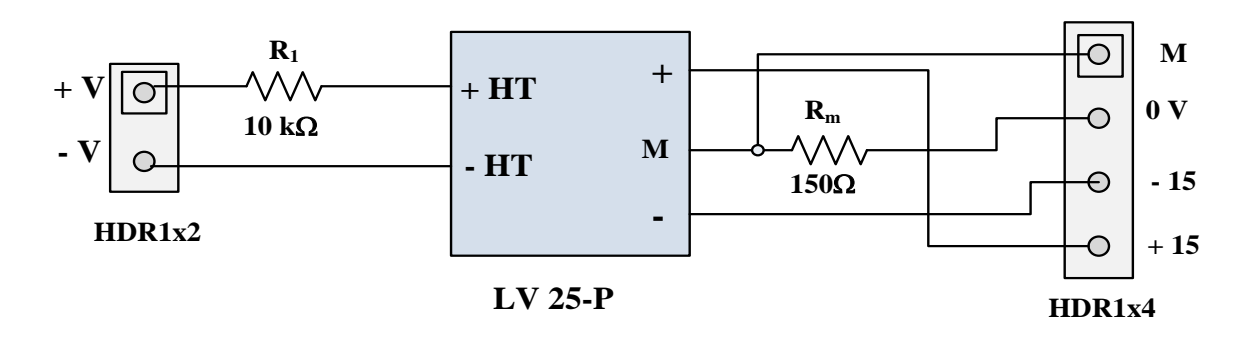


Figure E.12 Schematic of one voltage sensor circuit

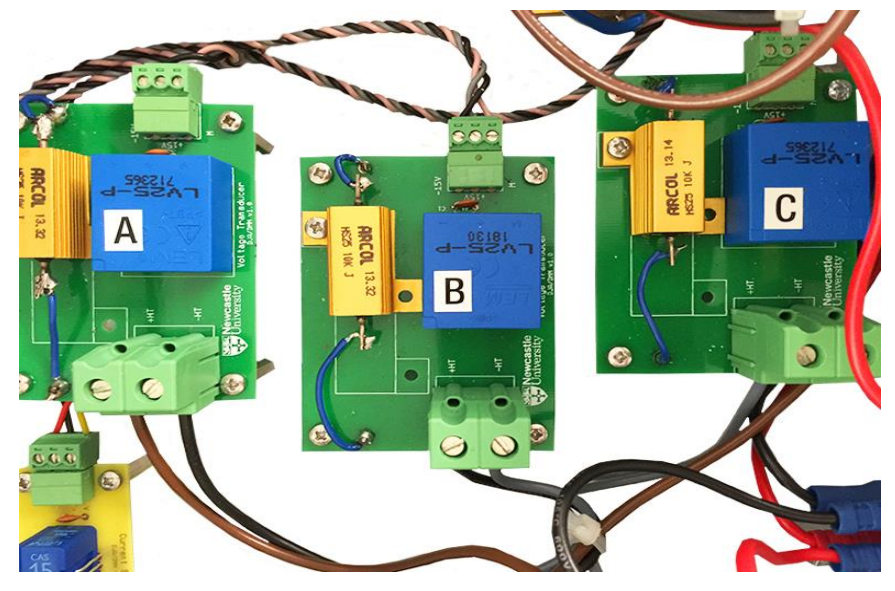


Figure E.13 Photograph of three LEM LV-25-P transducer

E.5 Design and construction of the zero crossing detection card

An LM393N comparator was used to produce the square wave output voltage signal by comparing the filtered voltage signal with a reference voltage to produce the square wave output. The output was then utilised by the ADC interface channels. The \pm 15 V were provided by the ADC channels from the general interface board. Similarly, voltage divider resistors were used in the general interface board to reduce the voltage level to the required voltage of 0-3 V.

The use of an RC filter causes a phase delay between the input and filtered voltages, which can be compensated for in the software. A 100 k Ω potentiometer was provided to adjust the pulse width as required. A schematic diagram of the constructed ZCD board and the voltage waveforms of the zero crossing detection board are shown in Figure E.14.

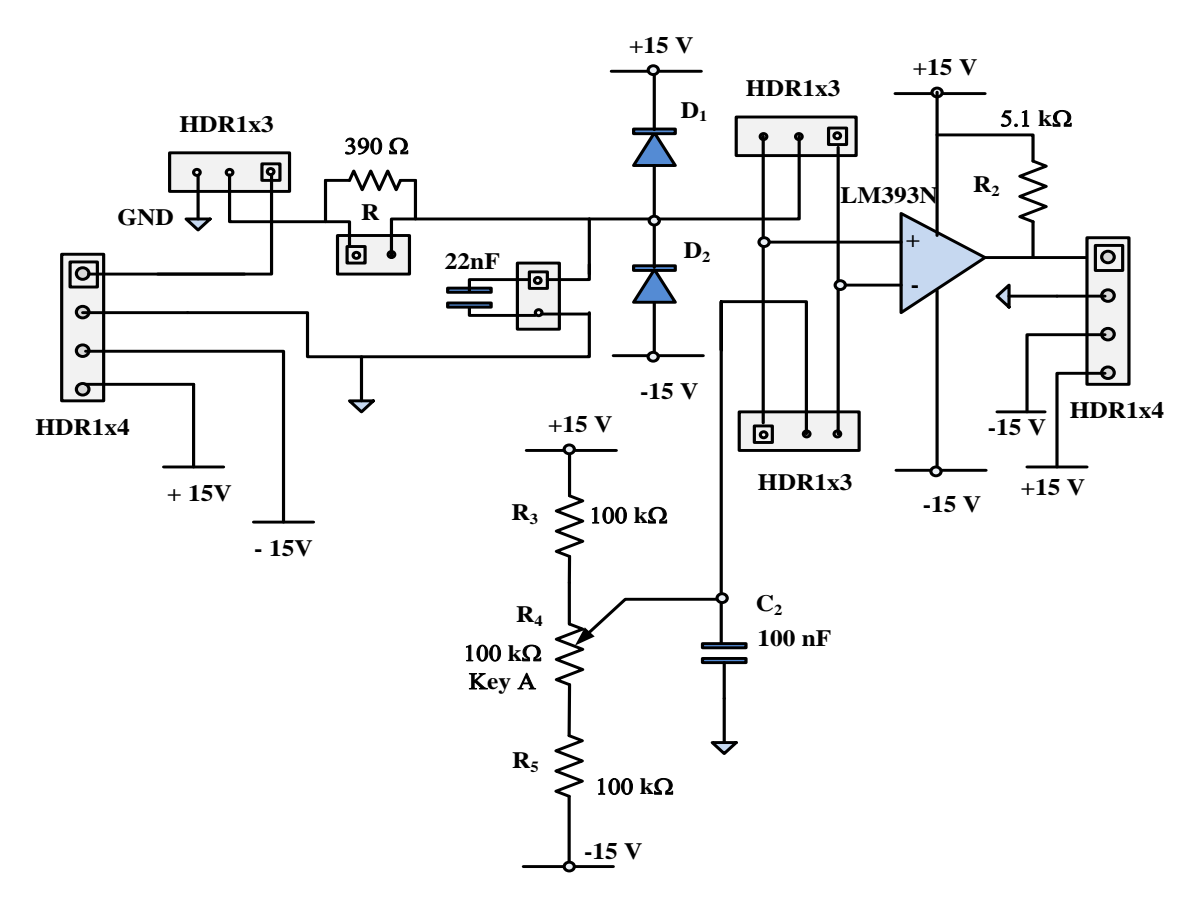


Figure E.14 Schematic diagram of the ZCD board

Moreover, the three-phase FCSC converter components were positioned in such a way as to provide appropriate physical locations to minimise the contamination of the control signal with noise. In addition, twisted-pair wires were used to transmit the signals supplied by the all PCB boards and especially the gate drivers, for the same purpose.

Furthermore, the general interface board was positioned very close to the driving circuit boards to keep the cable of the microcontroller PWM signal as short as possible, again for noise reduction purposes. The gate drives were kept very close to the power converter, which is important to reduce the noise level by minimising gate circuit inductance. A photograph of the arrangements and locations of the converter hardware components is shown in Figure E.15.

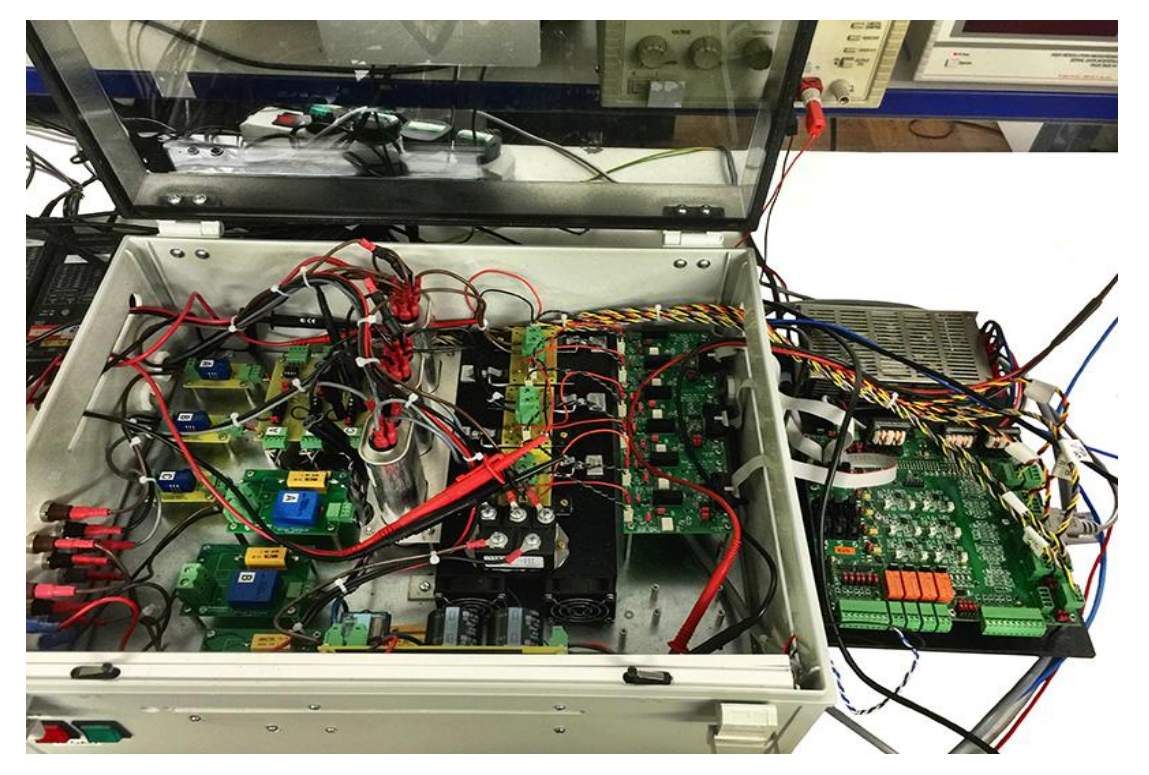


Figure E. 15 Photograph of the positioning of hardware components

E.6 Protective features and safety

The experimental test rig is designed with several personal and system safety features to protect the user and the system from any unexpected overcurrent or overvoltage during the experimental test.

- In order to prevent any risk of touching accidently live power, all of the connectors and conductors were carefully covered.
- All power circuits were fitted inside closed plastic enclosures which were earthed and configured so as to have no power when the lid was open, using two micro-switches which performed as an interlock mechanism.
- For over-current protection, a supply fuse of 15 A was provided.

- An arrangement with three switches was used, the first one of which was used to supply the power to the converter, with power ON (green). The second switch was used to shut power OFF (red), to ensure that the system was provided with power only after adjusting the output of the programmable power supply. The third switch was the emergency stop, allowing the power to be shut down in case of any abnormal operating conditions. The schematic of the protection circuit is shown below in Appendix F.
- Analogue multimeters were used for voltage and current measurements and monitoring.
- Bleed resistors were connected across all capacitors (AC and DC) to discharge the capacitor voltages to a safe voltage level when the power supply was disconnected from the system, either by normal shutting down or after activating the emergency stop button when a fault occurred. As the capacitors discharged exponentially, three 165 k Ω 2 W carbon resistors were connected across the AC capacitors to discharge the capacitor voltage (V_c) to a safe threshold voltage (V_t) within the discharge time (T_{dis}) as given by $R_{max} = \frac{-T_{dis}}{C \ln(V_t/V_c)}$ [172]. Therefore, the AC capacitors would be fully discharged within 7s. Similarly, a 1 k Ω 25 W wirewound resistor was connected across the DC side capacitor to discharge it within 2.5 s.
- A current limiting resistor was used to protect the converter from excessive current during the pre-charge capacitor process.
- Two contactors were used with 4NC and 3NO switches as the bleeder resistors were switched across the capacitors.

Appendix F. Schematic of the protection circuit

This appendix shows the schematic diagram of the protection circuit used in the experimental test.

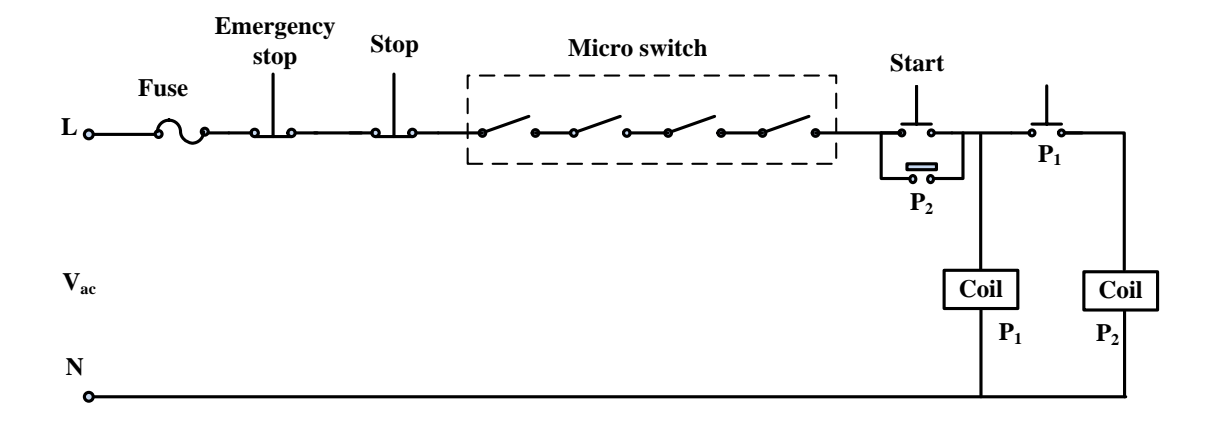


Figure F.1 Schematic of the protection circuit

Appendix G. Selective Experimental Results for a Three-Phase Rectifier Circuit under Variable-Voltage and Variable-Frequency

This appendix presents selective experimental results for the VVVF systems employing the three-phase diode bridge rectifier only. The voltage and current waveforms are shown under three operating frequencies in the range, including maximum, half of the maximum and the minimum frequencies.

Figure G.1 shows the voltage and current waveforms for the rectifier circuit at the maximum frequency value of 480 Hz. In this figure, the input current (i_s) is sinusoidal and lagging behind the voltage by 59.26°.

The RMS input voltage (V_s) is 100 V; however, the output voltage has dropped to 80 V as a DC voltage due to commutation overlap. The rectifier input voltage (V_{in}) is clamped by the load capacitor voltage (V_L) with a small voltage difference which represents the diode voltage drop.

At half of the frequency spectrum (i.e at F_s =240 Hz), the current is maintained as sinusoidal. However, the phase shift between the input voltage and current is reduced. The input current is lagging behind the input voltage by 44.76°. Similarly, less reduction in the output voltage occurs, since the RMS input voltage is 75 V and the output voltage is 89.7 V, as shown in Figure G.2.

At F_s =50 Hz, which represents the minimum frequency in the spectrum, Figure G.3 shows that by reducing the operating voltage and frequency, the current shape is non-sinusoidal which means that the harmonics components are higher at lower frequency. However, the phase-difference between the input voltage and current is reduced to 31.383°. In addition, the drop in the output voltage is reduced since the commutation overlap is less at the lower frequency.

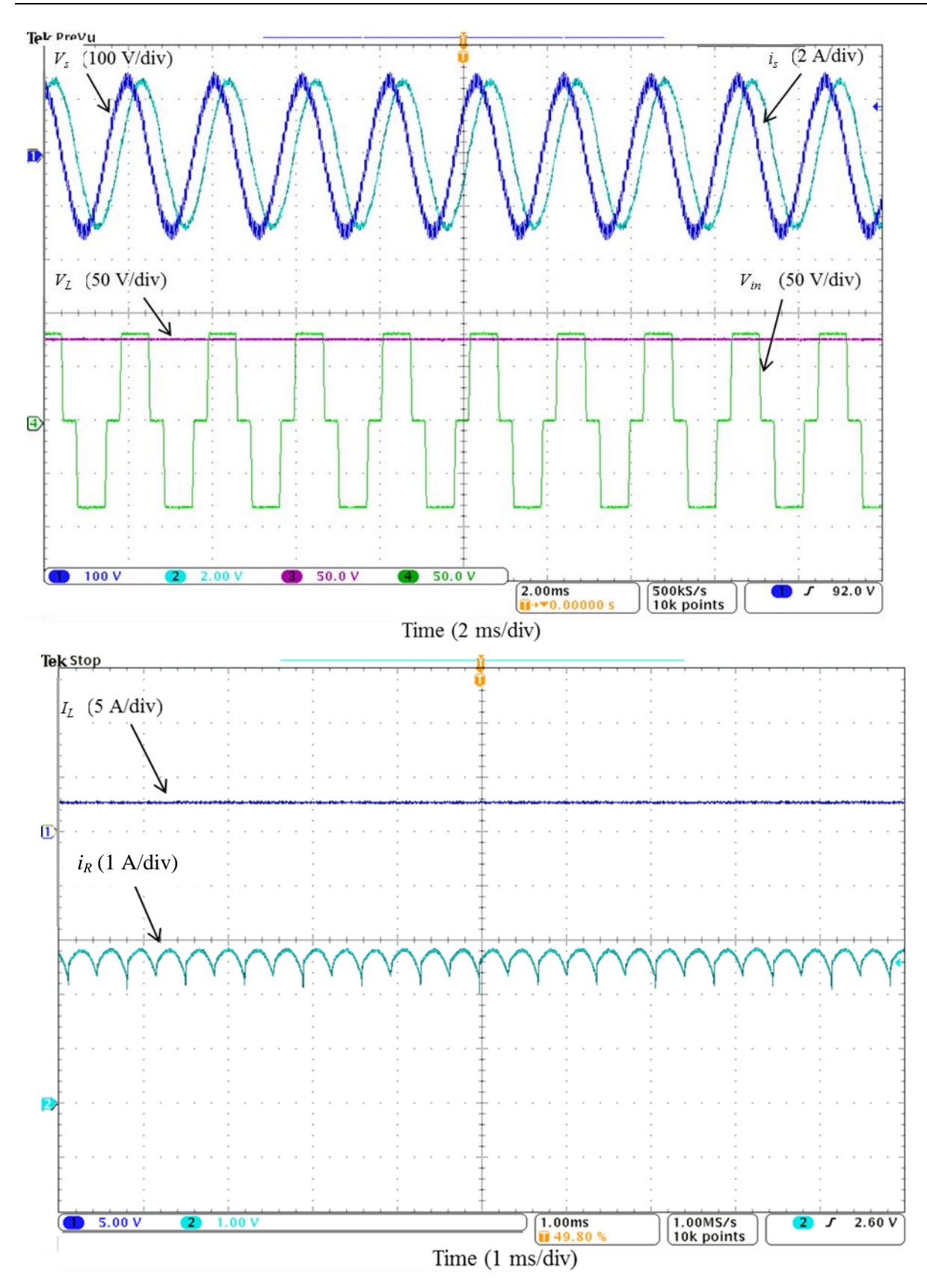


Figure G.1 Voltage and current waveforms under F_s =480 Hz, V_s = 100 V and R_L =30 Ω

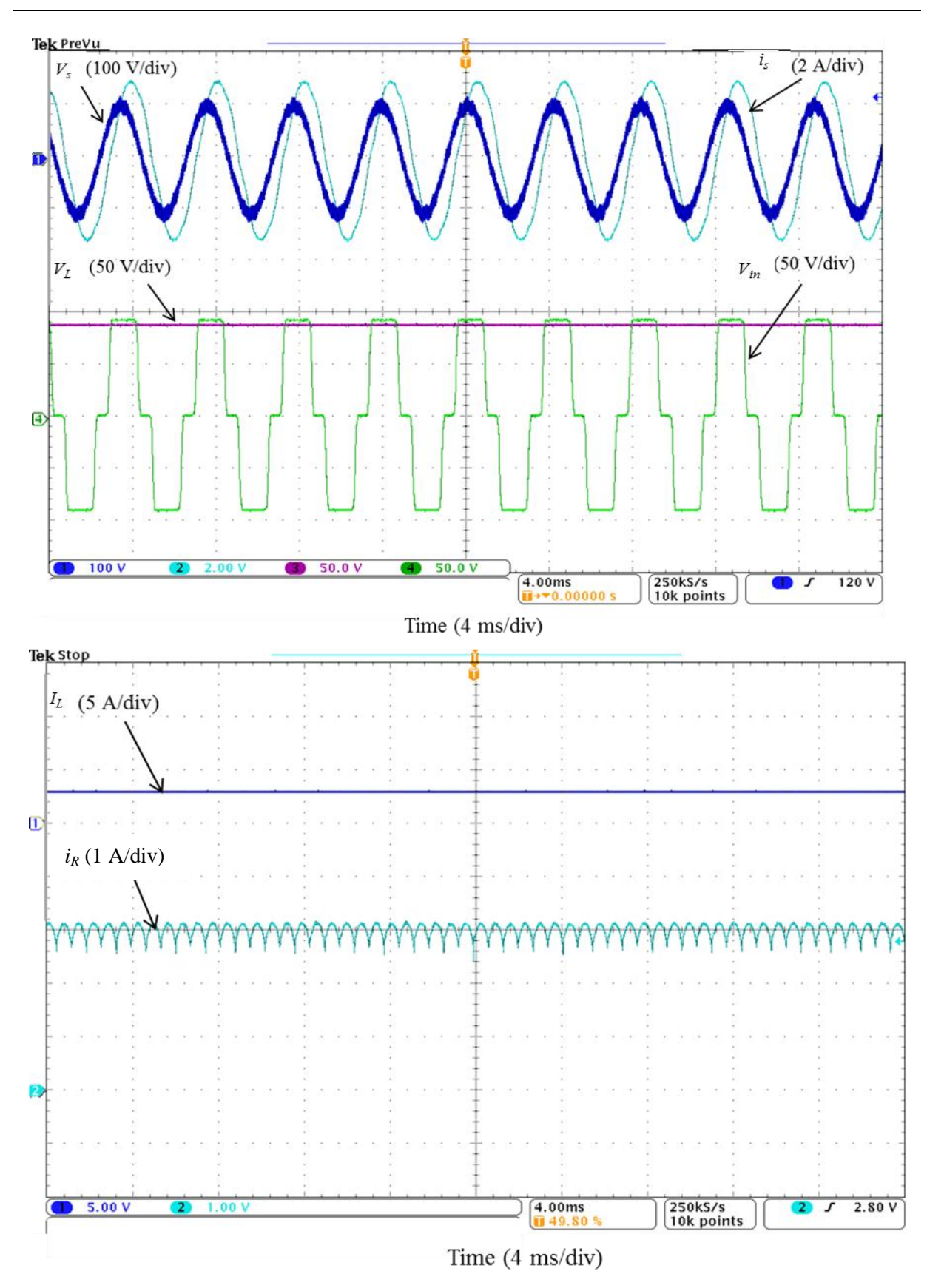


Figure G.2 Voltage and current waveforms at $F_s = 240$ Hz, $V_s = 75$ V, $R_L = 30$ Ω

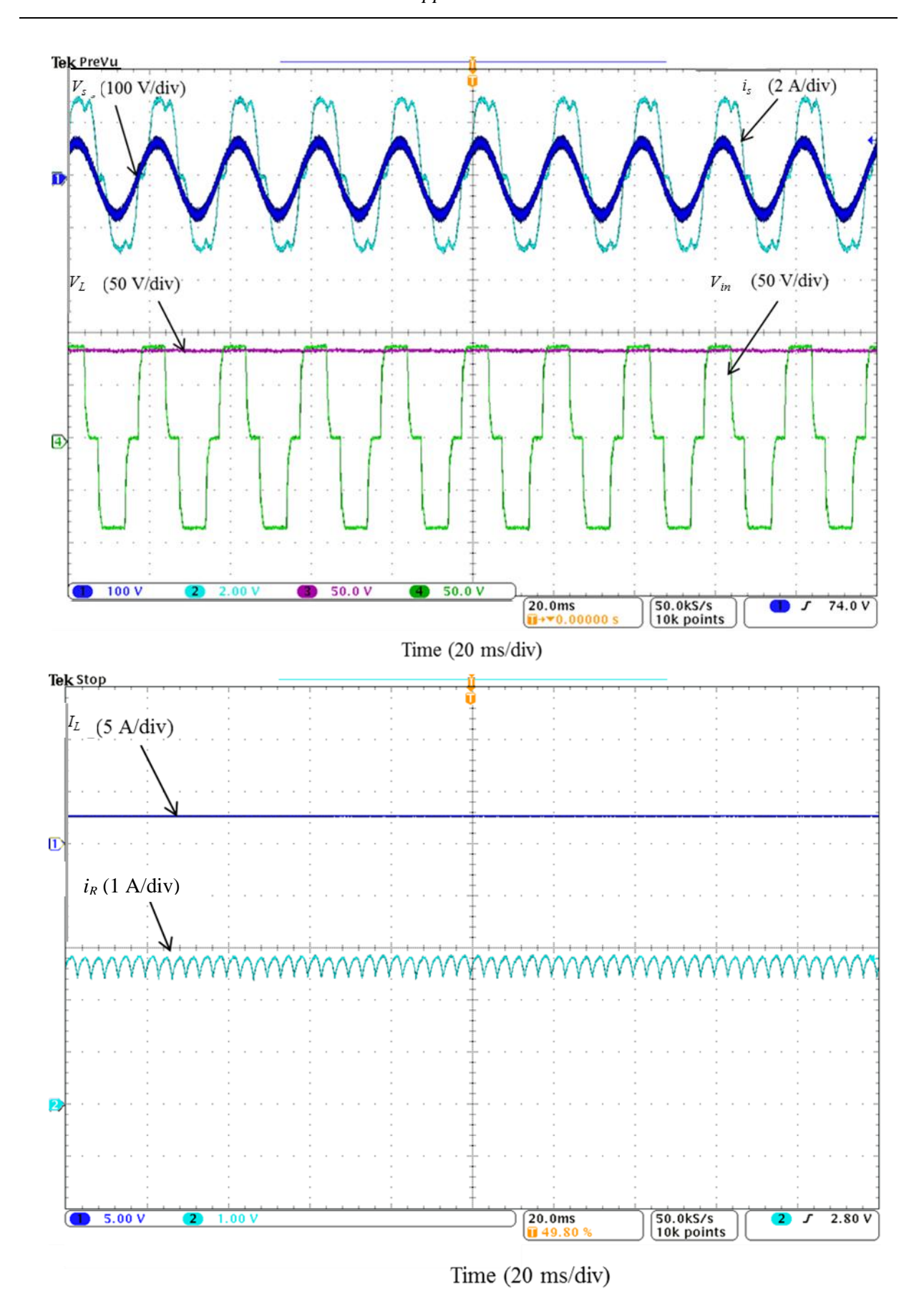


Figure G.3 Voltage and current waveforms at $F_s = 50$ Hz, $V_s = 50$ V, $R_L = 30$ Ω

Appendix H. Distorted Operating Voltages Impact on the system behaviour

This appendix demonstrates the impact of injecting the distorted voltages produced by the Behlman AC power supply unit used in this project to test the operation of the three-phase FCSC converter under variable voltage and variable frequency conditions.

From inputting the recorded distorted voltage waveforms in to SABER and simulating the circuit, a comparison of the load voltage developed using sinusoidal and distorted voltage supply at constant load with various frequencies is shown in Figure H.1. This figure shows that the distortion in the power supply unit reduces the output load voltage in comparison with the pure sinusoidal voltage source. This distortion causes a small error which is calculated to be around 4% at various frequencies with $R_L = 30 \Omega$. The impact of this distortion on the input current is also calculated and shown in Figure H.2.

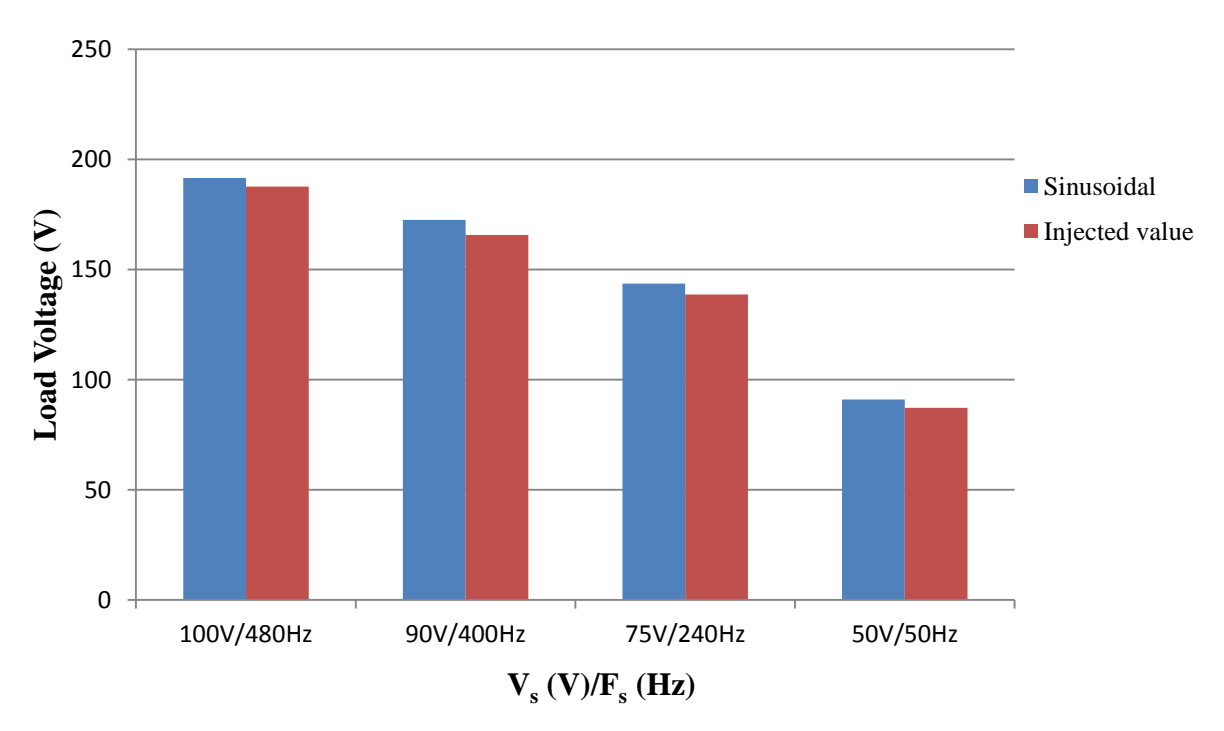


Figure H.1 Comparison between load voltage developed using sinusoidal and distorted supply voltage at various frequencies

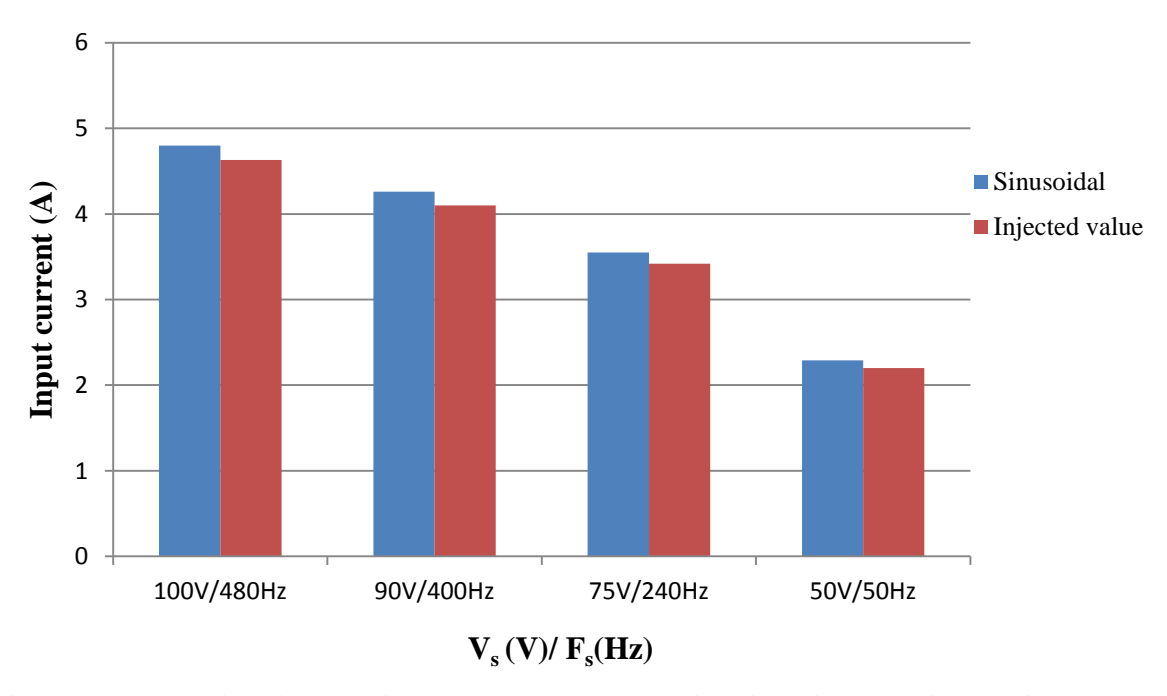


Figure H.2 Comparison between input current developed using sinusoidal and distorted input voltage at various frequencies

References

- [1] R. K. Pachauri and L. Meyer, "Climate Change 2014: Synthesis Report, Contribution of Working Groups I, II and III to the Fifth Assessment Report of the Intergovernmental Panel on Climate Change," IPCC, Geneva, Switzerland 2014.
- [2] European Renewable Energy Council (EREC). (17/04/2015). *Renewable energy*, the solution to climate change. Available: http://www.erec.org/renewable-energy/ocean-energy.html
- [3] B. Drew, A. Plummer and M. N. Sahinkaya, "A review of wave energy converter technology," *Proceedings of the Institution of Mechanical Engineers, Part A: Journal of Power and Energy*, vol. 223 (8), pp. 887-902, 2009.
- [4] D. Silva, E. Rusu and C. Soares, "Evaluation of Various Technologies for Wave Energy Conversion in the Portuguese Nearshore," *Energies*, vol. 6, pp. 1344-1364, 2013.
- [5] European Renewable Energy Council (EREC). (14/04/2015). *Ocean Energy Brochure*. Available: http://www.erec.org/renewable-energy/ocean-energy.html
- [6] H. Abu-Rub, M. Malinowski and K. Al-Haddad, *Power Electronics For Renewable Energy Systems, Transportation and Industrial Applications*: IEEE Press, Wiley, 2014.
- [7] M. H. Rashid, *Power Electronics : Circuits, Devices and Applications*, 3rd ed. London: Prentice Hall, 2004.
- [8] D. M. Vilathgamuwa and S. D. G. Jayasinghe, "Rectifier systems for variable speed wind generation a review," in *IEEE Int. Symp. on Industrial Electronics (ISIE)*, 2012, pp. 1058-1065.
- [9] J. W. Kolar and T. Friedli, "The essence of three-phase PFC rectifier systems," in 33rd Int. Telecommunications Energy Conference (INTELEC), Amsterdam, 2011, pp. 1-27.
- [10] J. Brombach, M. Jordan, F. Grumm and D. Schulz, "Converter topology analysis for aircraft application," in *Int. Symp. on Power Electronics Electrical Drives Automation and Motion (SPEEDAM)* 2012, pp. 446-451.
- [11] Abdelhafez A. A. and F. A. J., "A review of more electric aircraft," in 13th Int. Conf. on Aerospace Sciences and Aviation Technology (ASAT-13), Cairo, Egypt, 2009, pp. 1-13.
- [12] C. Jie and A. Wang, "New VF-power system architecture and evaluation for future aircraft," *IEEE Transactions on Aerospace and Electronic Systems*, vol. 42, pp. 527-539, 2006.
- [13] B. Sarlioglu, "Advances in AC-DC power conversion topologies for More Electric Aircraft," in *IEEE Transportation Electrification Conference and Expo (ITEC)*, MI,USA, 2012, pp. 1-6.
- [14] "Environmental conditions and test procedures for airbone equipment, DO-160E," ed. Washington,DC: RTCA,Inc, 2004.
- [15] B. Sarlioglu and C. T. Morris, "More Electric Aircraft: Review, Challenges, and Opportunities for Commercial Transport Aircraft," *IEEE Transactions on Transportation Electrification*, vol. 1, pp. 54-64, 2015.
- [16] G. Guanghai, M. L. Heldwein, U. Drofenik, J. Minibock, K. Mino, and J. W. Kolar, "Comparative evaluation of three-phase high-power-factor AC-DC converter concepts for application in future More Electric Aircraft," *IEEE Transactions on Industrial Electronics*, vol. 52, pp. 727-737, 2005.

- [17] X. Zhao, J. M. Guerrero and X. Wu, "Review of aircraft electric power systems and architectures," in *IEEE Int. Energy Conference (ENERGYCON)*, Dubrovnik, Croatia, 2014, pp. 949-953.
- [18] C. R. Avery, S. G. Burrow and P. H. Mellor, "Electrical generation and distribution for the more electric aircraft," in 42nd Int. Universities Power Engineering Conference (UPEC), 2007, pp. 1007-1012.
- [19] C. Zhong, L. Yingpeng, C. Miao, S. Lei and L. Jianxia, "Design and implementation of a high performance aeronautical active power filter," in 36th Annu. Conf. on IEEE Industrial Electronics Society (IECON), 2010, pp. 2032-2037.
- [20] A. Eid, H. El-Kishky, M. Abdel-Salam and M. T. El-Mohandes, "On power quality of variable-speed constant-frequency aircraft electric power systems," *IEEE Transactions on Power Delivery*, vol. 25, pp. 55-65, 2010.
- [21] H. El-Kishky, H. Ibrahimi, M. Abu Dakka, A. Eid and M. Abdel-Akher, "Modeling and characterization of VSCF aircraft electric power systems with nonlinear loading," in *IEEE Pulsed Power Conference (PPC)*, 2011, pp. 1482-1485.
- [22] J. F. Guerreiro, J. A. Pomilio and T. D. C. Busarello, "Design and implementation of a multilevel active power filter for more electric aircraft variable frequency systems," in *Power Electronics Conference (COBEP)*, 2013, pp. 1001-1007.
- [23] S. Jian, "On the zero-crossing distortion in single-phase PFC converters," *IEEE Transactions on Power Electronics*, vol. 19, pp. 685-692, 2004.
- [24] S. Jian, "Analysis and design of single-phase PFC converters for airborne systems," in 29th Annu. Conf. of the IEEE Industrial Electronics Society (IECON), 2003, pp. 1101-1109.
- [25] Z. Yan, L. Jinjun and Z. Chaoyi, "A simple switched capacitor compensator to minimize zero-crossing distortion in single-phase PFC converters," in *IEEE* 8th Int. Conf. on Power Electronics and ECCE Asia (ICPE & ECCE), 2011, pp. 749-755.
- [26] S. Jian, M. Chen and K. J. Karimi, "Aircraft power system harmonics involving single-phase PFC converters," *IEEE Transactions on Aerospace and Electronic Systems*, vol. 44, pp. 217-226, 2008.
- [27] N. G. Hingorani and L. Gyugyi, *Understanding FACTS: concepts and technology of flexible AC transmission system.* New York: IEEE Press, 2000.
- [28] X.-P. Zhang, C. Rehtanz and B. Pal, *Flexible AC transmission systems modelling and control*, 2nd ed. Berlin; New York: Springer, 2012.
- [29] D. Kalpaktsoglou, A. Al-Busaidi and V. Pickert, "Evaluation of generator-sets with power factor correction circuits," in 13th European Conference on Power Electronics and Applications (EPE), 2009, pp. 1-10.
- [30] V. Pickert, B. Zahawi and D. Kalpoktsoglou, "Forced commutation controlled series capacitor (FCSC) circuit applied to stand-alone wave energy conversion buoys," *Proceedings of IMarEST - Part A - Journal of Marine Engineering and Technology*, vol. 10, pp. 15-23, 2011.
- [31] S. Sivanagaraju and S. Satyanarayana, *Electric Power Transmission and Distribution*. India: Pearson/Dorling Kindersley, 2008.
- [32] E. Acha, V. Agelidis, O. Anaya and Ebooks Corporation., *Power Electronic Control in Electrical Systems*. Burlington: Elsevier, 2002.
- [33] M. Noroozian, L. Angquist, M. Ghandhari and G. Andersson, "Improving power system dynamics by series-connected FACTS devices," *IEEE Transactions on Power Delivery*, vol. 12, pp. 1635-1641, 1997.
- [34] Y. H. Song and A. T. Johns, *Flexible ac transmission systems (FACTS)*. London: Institution of Electrical Engineering, 1999.

- [35] N. N. Joshi and N. Mohan, "Application of TCSC in wind farm application," in *Int. Symp. on Power Electronics, Electrical Drives, Automation and Motion (SPEEDAM)*, 2006, pp. 1196-1200.
- [36] L. Kejun, S. Ying, L. Wei-Jen and C. Jintao, "Impedance Control of Thyristor Controlled Series Capacitor to Improve the Transfer Capability of Remote Wind Farms," in *IEEE Industry Applications Society Annual Meeting (IAS)* 2010, pp. 1-6.
- [37] R. K. Varma, S. Auddy and Y. Semsedini, "Mitigation of Subsynchronous Resonance in a Series-Compensated Wind Farm Using FACTS Controllers," *IEEE Transactions on Power Delivery*, vol. 23, pp. 1645-1654, 2008.
- [38] H. A. Mohammadpour, S. Yong-June and E. Santi, "SSR analysis of a DFIG-based wind farm interfaced with a gate-controlled series capacitor," in 29th IEEE Annu. Applied Power Electronics Conference and Exposition (APEC), 2014, pp. 3110-3117.
- [39] H. A. Mohammadpour and E. Santi, "SSR Damping Controller Design and Optimal Placement in Rotor-Side and Grid-Side Converters of Series-Compensated DFIG-Based Wind Farm," *IEEE Transactions on Sustainable Energy*, vol. 6, pp. 388-399, 2015.
- [40] H. A. Mohammadpour and E. Santi, "Modeling and Control of Gate-Controlled Series Capacitor Interfaced with a DFIG-based Wind Farm," *IEEE Transactions on Industrial Electronics*, vol. 62, pp. 1022-1033, 2015.
- [41] L. Piyasinghe, Z. Miao, J. Khazaei and L. Fan, "Impedance Model-Based SSR Analysis for TCSC Compensated Type-3 Wind Energy Delivery Systems," *IEEE Transactions on Sustainable Energy*, vol. 6, pp. 179-189, 2015.
- [42] D. Kalpaktsoglou, "Power Factor Correction for Stand-alone Wave Energy Conversion Buoys," PhD., School of Electrical, Electronic and Computer Engineering, University of Newcastle upon Tyne, Newcastle University, 2010.
- [43] D. Kalpaktsoglou and V. Pickert, "Controlled series capacitor converters applied to wave energy conversion buoys a simulation study," in 4th IET Conf. on Power Electronics, Machines and Drives (PEMD) York, 2008, pp. 396-400.
- [44] K. R. Padiyar. (2007). Facts Controllers in Power Transmission and Distribution. Available: http://NCL.eblib.com/patron/FullRecord.aspx?p=418812
- [45] P. M. Anderson, B. L. Agrawal and J. E. Van Ness, *Subsynchronous Resonance in Power Systems*: John Wiley & Sons, 1999.
- [46] J. W. Ballance and S. Goldberg, "Subsynchronous Resonance in Series Compensated Transmission Lines," *IEEE Transactions on Power Apparatus and Systems* vol. PAS-92, pp. 1649-1658, 1973.
- [47] R. G. Farmer, A. L. Schwalb and E. Katz, "Navajo project report on subsynchronous resonance analysis and solutions," *IEEE Transactions on Power Apparatus and Systems*, vol. 96, pp. 1226-1232, 1977.
- [48] N. Johansson, L. Angquist and H. P. Nee, "An Adaptive Controller for Power System Stability Improvement and Power Flow Control by Means of a Thyristor Switched Series Capacitor (TSSC)," *IEEE Transactions on Power Systems*, vol. 25, pp. 381-391, 2010.
- [49] J. J. Vithayathil, C. Taylor, M. Klinger and W. Mittelstadt, "Case studies of conventional and novel methods of reactive power control on AC transmission systems," in *CIGRE SC 38-02*, Paris, 1988.
- [50] J. J. Vithayathil, "Scheme for rapid adjustment of network impedance," US 5032738 1991.
- [51] K. Clark, B. Fardanesh and R. Adapa, "Thyristor controlled series compensation application study-control interaction considerations," *IEEE Transactions on Power Delivery*, vol. 10, pp. 1031-1037, 1995.

- [52] F. C. Jusan, S. Gomes and G. N. Taranto, "Study on the influence of TCSC structure and control on SSR damping using an improved s-domain model," in *IEEE Transmission and Distribution Conference and Exposition: Latin America (T&D-LA)*, 2010, pp. 13-21.
- [53] L. L. Grigsby, *Power System Stability and Control*, 3rd ed.: Taylor & Francis, 2012.
- [54] E. Acha, Power Electronic Control in Electrical Systems: Newnes, 2002.
- [55] D. P. Subramanian and R. P. K. Devi, "Application of TCSC Power Oscillation Damping controller to enhance power system dynamic performance," in *Joint Int. Conf. on Power Electronics, Drives and Energy Systems (PEDES)*, India, 2010, pp. 1-5.
- [56] D. Jovcic and G. N. Pillai, "Analytical modeling of TCSC dynamics," *IEEE Transactions on Power Delivery*, vol. 20, pp. 1097-1104, 2005.
- [57] A. D. Del Rosso, C. A. Canizares and V. M. Dona, "A study of TCSC controller design for power system stability improvement," *IEEE Transactions on Power Systems* vol. 18, pp. 1487-1496, 2003.
- [58] C. Weindl and G. Herold, "Development of an analytic state-space description of power systems including thyristor controlled series compensation," in 9th Int. Conf. on Harmonics and Quality of Power, 2000, pp. 961-966
- [59] H. Hak-Guhn, P. Jong-Keun and L. Byung-Ha, "Analysis of thyristor controlled series compensator dynamics using the state variable approach of a periodic system model," *IEEE Transactions on Power Delivery*, vol. 12, pp. 1744-1750, 1997.
- [60] V. Mahajan, "Thyristor Controlled Series Compensator," in *IEEE Int. Conf. on Industrial Technology (ICIT)*, Mumbai, India, 2006, pp. 182-187.
- [61] S. Meikandasivam, R. K. Nema and S. K. Jain, "Selection of TCSC parameters: Capacitor and inductor," in *Int. Conf. on Power Electronics (IICPE)*, India 2011, pp. 1-5.
- [62] E. W. Kimbark, "Improvement of system stability by switched series capacitors," *IEEE Transactions on Power Apparatus and Systems*, vol. PAS-85, pp. 180-188, 1966.
- [63] S. A. Zulkifli, C. Kok Boon, M. Z. Ahmad, R. Hamdan and N. A. Ibrahim, "Study of poles and zeros arrangement method for PID controller on TCSC," in *13th Int. Conf. on Harmonics and Quality of Power (ICHQP)*, 2008, pp. 1-5.
- [64] M. Khederzadeh, "Application of TCSC to enhance power quality," in 42nd Int. Universities Power Engineering Conference (UPEC) 2007, pp. 607-612.
- [65] S. O. Faried, R. Billinton and M. Fotuhi-Firuzabad, "Impact of thyristor controlled series capacitor on power system reliability," in *Int. Conf. on Electric Power Engineering*, Budapest 1999, p. 151.
- [66] D. H. Baker, G. E. Boukarim, R. D'Aquila and R. J. Piwko, "Subsynchronous resonance studies and mitigation methods for series capacitor applications," in *Power Engineering Society Inaugural Conference and Exposition in Africa*, Africa, 2005, pp. 386-392.
- [67] Z. Xiang, X. Zheng and Z. Jing, "A supplementary damping controller of TCSC for mitigating SSR," in *IEEE Power & Energy Society General Meeting*, *PES '09*, 2009, pp. 1-5.
- [68] X. Lombard and P. G. Therond, "Series compensation and subsynchronous resonance details analysis of the phenomenon and of its damping by a Tcsc," in 6th Int. Conf. on AC and DC Power Transmission, 1996, pp. 321-328.
- [69] N. Kakimoto and A. Phongphanphanee, "Subsynchronous resonance damping control of thyristor-controlled series capacitor," *IEEE Transactions on Power Delivery*, vol. 18, pp. 1051-1059, 2003.

- [70] L. A. S. Pilotto, A. Bianco, W. F. Long and A. Edris, "Impact of TCSC control methodologies on subsynchronous oscillations," *IEEE Transactions on Power Delivery*, vol. 18, pp. 243-252, 2003.
- [71] "First benchmark model for computer simulation of subsynchronous resonance," *IEEE Transactions on power Apparatus and Systems* vol. 96, pp. 1565-1572, 1977.
- [72] L. Wenlei, L. Shirong, J. Gangyi and G. M. Dimirovski, "Nonlinear adaptive robust control for thyristor controlled series compensation," in 6th World Congress on Intelligent Control and Automation (WCICA) 2006, pp. 7434-7438.
- [73] W. Yan, J. Yuanwei and Z. Weilun, "Adaptive robust control of thyristor controlled series compensation," in *Chinese Control and Decision Conference (CCDC)*, China, 2011, pp. 4139-4143.
- [74] M. Monge, N. Johansson, L. Angquist and H. P. Nee, "Adaptive control for power oscillation damping by means of a Thyristor Controlled Series Capacitor (TCSC)," in 43rd Int. Universities Power Engineering Conference (UPEC) 2008, pp. 1-5.
- [75] S. Mahapatra and A. N. Jha, "Modeling and simulation of TCSC based controller in a multi machine power system," in *Students Conference on Engineering and Systems* (SCES), 2014, pp. 1-6.
- [76] V. Pickert, D. Kalpaktsoglou and A. Al-Busaidi, "Controlled series capacitor converters applied in generators for SHEV's," in 24th Int. Battery, Hybrid and Fuel Cell Electric Vehicle Symposium and Exhibition (EVS), Stavanger, Norway, 2009.
- [77] L. F. W. De Souza, E. H. Watanabe and M. Aredes, "GTO controlled series capacitors: multi-module and multi-pulse arrangements," *IEEE Transactions on Power Delivery* vol. 15, pp. 725-731, 2000.
- [78] E. H. Watanabe, M. Aredes, L. F. W. De Souza and M. D. Bellar, "Series connection of power switches for very high-power applications and zero-voltage switching," *IEEE Transactions on Power Electronics*, vol. 15, pp. 44-50, 2000.
- [79] L. F. W. de Souza, E. H. Watanabe and J. E. da Rocha Alves, "Thyristor and Gate-Controlled Series Capacitors: A Comparison of Components Rating," *IEEE Transactions on Power Delivery*, vol. 23, pp. 899-906, 2008.
- [80] G. G. Karady, T. H. Ortmeyer, B. R. Pilvelait and D. Maratukulam, "Continuously regulated series capacitor," *IEEE Transactions on Power Delivery*, vol. 8, pp. 1348-1355, 1993.
- [81] M. M. Nejad and T. H. Ortmeyer, "GTO thyristor controlled series capacitor switch performance," *IEEE Transactions on Power Delivery*, vol. 13, pp. 615-621, 1998.
- [82] F. D. De Jesus, E. H. Watanabe, L. F. W. Souza and J. E. R. Alves, "SSR mitigation using gate-controlled series capacitors," in *IEEE Power Engineering Society General Meeting*, Montreal, Que, 2006, pp. 1-7.
- [83] F. D. de Jesus, Watanabe, E. H., de Souza, L. F. W., and Alves, J. E. R., "SSR and Power Oscillation Damping Using Gate-Controlled Series Capacitors (GCSC)," *IEEE Transactions on Power Delivery*, vol. 22, pp. 1806-1812, 2007.
- [84] B. S. Umre, J. B. Helonde, J. P. Modak and S. Renkey, "Application of gate-controlled series capacitors (GCSC) for reducing stresses due to sub-synchronous resonance in turbine-generator shaft," in *IEEE Energy Conversion Congress and Exposition(ECCE)*, 2010, pp. 2300-2305.
- [85] S. Ray, G. K. Venayagamoorthy and E. H. Watanabe, "A Computational Approach to Optimal Damping Controller Design for a GCSC," *IEEE Transactions on Power Delivery*, vol. 23, pp. 1673-1681, 2008.
- [86] H. A. Mohammadpour, M. Pahlavani and A. Shoulaie, "On control of gate controlled series capacitor for SSR and power oscillation damping," in *Compatibility and Power Electronics(CPE)* 2009, pp. 196-203.

- [87] M. R. Alizadeh Pahlavani and H. A. Mohammadpour, "Damping of sub-synchronous resonance and low-frequency power oscillation in a series-compensated transmission line using gate-controlled series capacitor," *Electric Power Systems Research*, vol. 81, pp. 308-317, 2011.
- [88] A. Safari and N. Rezaei, "Towards an extended power system stability: An optimized GCSC-based inter-area damping controller proposal," *International Journal of Electrical Power & Energy Systems*, vol. 56, pp. 316-324, 2014.
- [89] A. Safari and N. Rezaei, "Design of multi-objective damping controller for gate-controlled series capacitor," *Sadhana*, vol. 39, pp. 363-376, 2014.
- [90] A. Cichocki and R. Unbehauen, "Appllication of switched-capacitor self-oscillating circuits to the conversion of RLC parameters into a frequency or digital signal," *Sensors and Actuators A: Physical*, vol. 24, pp. 129-137, 1990.
- [91] T. Miyasaka, K. Yamazaki, J. Tsuchiya, T. Shimizu, G. Kimura, and M. Shioya, "Improved operating characteristics of linear pulse motor using resonant current," in *Int. Conf. on Industrial Electronics Control and Instrumentation (IECON)*, 1993, pp. 896-901
- [92] A. Al-Busaidi, D. Kalpaktsoglou and V. Pickert, "Comparison of power factor correction techniques for generator-sets for SHEVs," in *Ecologic vehicles Renewable energies*, Monaco, 2009.
- [93] T. Takaku, G. Homma, T. Isobe, S. Igarashi, Y. Uchida, and R. Shimada, "Improved wind power conversion system using magnetic energy recovery switch (MERS)," in 14th Industry Applications Conference, Annual Meeting, 2005, pp. 2007-2012.
- [94] J. A. Wiik, T. Isobe, T. Takaku, F. D. Wijaya, K. Usuki, N. Arai, and R. Shimada, "Feasible series compensation applications using Magnetic Energy Recovery Switch (MERS)," in *European Conference on Power Electronics and Applications*, 2007, pp. 1-9.
- [95] J. A. Wiik, T. Takaku, F. D. Wijaya, T. Kitahara and R. Shimada, "Improvement of Synchronous Generator Charateristics Using Bi-directional Current Phase Control Switch," in 12th Int. Power Electronics and Motion Control Conference (EPE-PEMC) 2006, pp. 1506-1511.
- [96] J. A. Wiik, O. J. Fønstelien and R. Shimada, "A MERS type series FACTS controller for low voltage ride through of induction generators in wind farms," in 13th European Conference on Power Electronics and Applications (EPE), Barcelona, 2009, pp. 1-10.
- [97] T. Takaku, T. Isobe, J. Narushima and R. Shimada, "Power supply for pulsed magnets with magnetic energy recovery current switch," *IEEE Transactions on Applied Superconductivity*, vol. 14, pp. 1794-1797, 2004.
- [98] A. K. Ramasamy, R. Krishnan Iyer, V. K. Ramachandaramuthy and R. N. Mukerjee, "Dynamic Voltage Restorer For Voltage Sag Compensation," in *Int. Conf. on Power Electronics and Drives Systems (PEDS)* 2005, pp. 1289-1294.
- [99] J. G. Nielsen, M. Newman, H. Nielsen and F. Blaabjerg, "Control and testing of a dynamic voltage restorer (DVR) at medium voltage level," *IEEE Transactions on Power Electronics* vol. 19, pp. 806-813, 2004.
- [100] J. G. Nielsen, F. Blaabjerg and N. Mohan, "Control strategies for dynamic voltage restorer compensating voltage sags with phase jump," in 16th IEEE Applied Power Electronics Conference and Exposition (APEC) 2001, pp. 1267-1273
- [101] A. M. Rauf and V. Khadkikar, "An Enhanced Voltage Sag Compensation Scheme for Dynamic Voltage Restorer," *IEEE Transactions on Industrial Electronics*, vol. 62, pp. 2683-2692, 2015.
- [102] G. A. de Almeida Carlos, E. Cipriano dos Santos, C. Brandao Jacobina and J. P. Ramos Agra Mello, "Dynamic Voltage Restorer Based on Three-Phase Inverters

- Cascaded Through an Open-End Winding Transformer," *IEEE Transactions on Power Electronics*, vol. 31, pp. 188-199, 2016.
- [103] F. Badrkhani Ajaei, S. Afsharnia, A. Kahrobaeian and S. Farhangi, "A Fast and Effective Control Scheme for the Dynamic Voltage Restorer," *IEEE Transactions on Power Delivery*, vol. 26, pp. 2398-2406, 2011.
- [104] M. A. Bhaskar, S. S. Dash, C. Subramani, M. J. Kumar, P. R. Giresh, and M. V. Kumar, "Voltage Quality Improvement Using DVR," in *Int. Conf. on Recent Trends in Information, Telecommunication and Computing (ITC)*, 2010, pp. 378-380.
- [105] F. M. Mahdianpoor, R. A. Hooshmand and M. Ataei, "A new approach to multifunctional Dynamic Voltage Restorer implementation for emergency control in distribution systems," *IEEE Transactions on Power Delivery*, vol. 26, pp. 882-890, 2011.
- [106] L. Gyugyi, C. D. Schauder and K. K. Sen, "Static synchronous series compensator: a solid-state approach to the series compensation of transmission lines," *IEEE Transactions on Power Delivery*, vol. 12, pp. 406-417, 1997.
- [107] K. K. Sen, "SSSC-static synchronous series compensator: theory, modeling, and application," *IEEE Transactions on Power Delivery*, vol. 13, pp. 241-246, 1998.
- [108] M. Bongiorno, J. Svensson and L. Angquist, "On control of static synchronous series compensator for SSR mitigation," *IEEE Transactions on Power Electronics*, vol. 23, pp. 735-743, 2008.
- [109] R. Thirumalaivasan, M. Janaki and N. Prabhu, "Damping of SSR using subsynchronous current suppressor with SSSC," *IEEE Transactions on Power Systems*, vol. 28, pp. 64-74, 2013.
- [110] W. Li and V. Quang-Son, "Power flow control and stability improvement of connecting an offshore wind farm to a one-machine infinite-bus system using a Static Synchronous Series Compensator," *IEEE Transactions on Sustainable Energy*, vol. 4, pp. 358-369, 2013.
- [111] N. Mohan, *Power Electronics: A First course*. United States of America: John Wiley & Sons, 2012.
- [112] R. W. Erickson and D. Maksimovic, *Fundamentals of Power Electronics*. Massachusetts, United states of America: Kluwer Academic Puplishers, 2001.
- [113] M. Rashid, Power Electronics Handbook. MA, USA: Elsevier, 2010.
- [114] N. Mohan, T. M. Undeland and W. P. Robbins, *Power electronics : converters, applications, and design*, 3rd ed. Hoboken, N.J.: J. Wiley, 2003.
- [115] T. A. Kneschke, "Distortion and power factor of nonlinear loads," in *Joint ASME/IEEE Railroad Conference* 1999, pp. 47-54.
- [116] J. E. Mitchell, "Distortion factor: the `new' problem of power factor," in 14th Int. Telecommunications Energy Conference (INTELEC), 1992, pp. 514-516.
- [117] C. Sankaran and Ebooks Corporation., *Power Quality*. Hoboken: CRC Press, 2001.
- [118] D. L. O'Sullivan and A. W. Lewis, "Generator selection and comparative performance in offshore oscillating water column ocean wave energy converters," *IEEE Transactions on Energy Conversion*, vol. 26, pp. 603-614, 2011.
- [119] M. A. Mueller, H. Polinder and N. Baker, "Current and Novel Electrical Generator Technology for Wave Energy Converters," in *IEEE International Electric Machines & Drives Conference, IEMDC '07*, 2007, pp. 1401-1406.
- [120] H. Polinder, M. E. C. Damen and F. Gardner, "Linear PM Generator system for wave energy conversion in the AWS," *IEEE Transactions on Energy Conversion*, vol. 19, pp. 583-589, 2004.

- [121] R. Henderson, "Design, simulation, and testing of a novel hydraulic power take-off system for the Pelamis wave energy converter," *Renewable Energy*, vol. 31, pp. 271-283, 2006.
- [122] J. P. Kofoed, P. Frigaard, E. Friis-Madsen and H. C. Sørensen, "Prototype testing of the wave energy converter wave dragon," *Renewable Energy*, vol. 31, pp. 181-189, 2006.
- [123] H. Polinder, B. C. Mecrow, A. G. Jack, P. Dickinson and M. A. Mueller, "Linear generators for direct-drive wave energy conversion," in *IEEE Int. Electric Machines and Drives Conference*, 2003, pp. 798-804
- [124] M. A. Mueller, "Electrical generators for direct drive wave energy converters," *IEE Proceedings- Generation, Transmission and Distribution*, vol. 149, pp. 446-456, 2002.
- [125] Y. Zhao and J. Chai, "Power factor analysis of transverse flux permanent machines," in 8th Int. Conf. on Electrical Machines and Systems (ICEMS), 2005, pp. 450-459
- [126] Z. Chen, E. Spooner, W. T. Norris and A. C. Williamson, "Capacitor-assisted excitation of permanent-magnet generators," *IEE Proceedings-Electric Power Applications*, vol. 145, pp. 497-508, 1998.
- [127] A. S. Al-Busaidi, "A generator-set for series hybrid electric vehicles operating at high output voltage," PhD, School of Electrical, Electronic and Computer Engineering, Newcastle University, United Kingdom, 2011.
- [128] L. Ran, P. J. Tavner, M. A. Mueller, N. J. Baker and S. McDonald, "Power conversion and control for a low speed permanent magnet direct-drive wave energy converter," in 3rd IET Int. Conf. on Power Electronics, Machines and Drives (PEMD), 2006, pp. 17-21.
- [129] J. N. Ross, *The Essence of Power Electronics*. Hertfordshire, UK.: Printic Hall Europe, 1997.
- [130] T. Al-Mhana, V. Pickert and B. Zahawi, "Impact of load variations on the operating PF of an FCSC converter applied to wave energy systems," in *2013 IEEE Energytech* 2013, pp. 1-6.
- [131] A. Emadi and M. Ehsani, "More-Electric Vehicles," in *The Power Electronics Handbook*, T. L. Skvarenina, Ed., ed: CRC Press, 2001.
- [132] J. P. Noon and D. Dalal, "Practical design issues for PFC circuits," in 12th Applied Power Electronics Conference and Exposition(APEC) 1997, pp. 51-58
- [133] Q. Xiaohui and R. Xinbo, "A scheme for improving input current zero-crossing distortion of single-phase power factor correction converters," in 37th IEEE Power Electronics Specialists Conference(PESC), 2006, pp. 1-6.
- [134] T. Wildi, Electrical Machines, Drives, and Power Systems: Pearson Education, 2013.
- [135] S. J. Chapman, *Electric machinery and power system fundamentals*: McGraw-Hill, 2002.
- [136] J. Vithayathil, *Power electronics principles and applications*. United States of America: McGraw-Hill, 1995.
- [137] K. L. Lian, B. K. Perkins and P. W. Lehn, "Harmonic analysis of a three-phase diode bridge rectifier based on sampled-data model," *IEEE Transactions on Power Delivery*, vol. 23, pp. 1088-1096, 2008.
- [138] J. A. M. Bleijs, "Continuous conduction mode operation of three-phase diode bridge rectifier with constant load voltage," *IEE Proceedings Electric Power Applications*, vol. 152, pp. 359-368, 2005.
- [139] B. K. Bose, *Power Electronics And Motor Drives: Advances and Trends*: Elsevier Science, 2010.
- [140] N. Backer. (2014, 03/12). Permanent Magnet Alternator (PMA) Development. Available: http://www.ncl.ac.uk/eee/research/project/4427

- [141] D. F. Peelo, *Current Interruption Transients Calculation*. Chichester, United Kingdom: John Wiley & Sons Ltd, 2014.
- [142] M. M. Radmanesh, *The Gateway to Understanding: Electrons to Waves and Beyond*: AuthorHouse, 2005.
- [143] A. O. Monroy, L.-H. Hoang and C. Lavoie, "Modeling and simulation of a 24-pulse Transformer Rectifier Unit for more electric aircraft power system," in *Electrical Systems for Aircraft, Railway and Ship Propulsion (ESARS)*, 2012, pp. 1-5.
- [144] T. Al-Mhana, V. Pickert and B. Zahawi, "FCSC converter with symmetrical short duty cycle for variable frequency applications," in 7th IET International Conference on Power Electronics, Machines and Drives (PEMD), 2014, pp. 1-5.
- [145] T. Al-Mhana, B. Zahawi and V. Pickert, "Symmetrical duty cycle control for FCSC converter for wave energy applications," in 9th Int. Symposium on Communication Systems, Networks & Digital Signal Processing (CSNDSP), 2014, pp. 56-60.
- [146] R. W. Wall, "Simple methods for detecting zero crossing," in 29th IEEE Industrial Electronics Society (IECON) 2003, pp. 2477-2481
- [147] M. Ciobotaru, R. Teodorescu and F. Blaabjerg, "A new single-phase PLL structure based on second order generalized integrator," in 37th IEEE Power Electronics Specialists Conference (PESC) 2006, pp. 1-6.
- [148] G. H. Tomlinson, *Electrical networks and filters: theory and design*: Prentice Hall, 1991.
- [149] S. Winder, Analog and Digital Filter Design, 2nd ed. Woburn: Newnes 2002.
- [150] A. I. Pressman, K. Billings and T. Morey, *Switching power supply design*, Third ed. United States: The McGraw-Hill Companies, 2009.
- [151] W. T. McLyman, *Transformer and Inductor Design Handbook*, Third ed. New York, U.S.A: Marcel Dekker, Inc., 2004.
- [152] L. Jinjun, T. G. Wilson, R. C. Wong, R. Wunderlich and F. C. Lee, "A method for inductor core loss estimation in power factor correction applications," in 17th IEEE Applied Power Electronics Conference and Exposition (APEC) 2002, pp. 439-445
- [153] K. Rhinefrank, A. Schacher, J. Prudell, T. K. A. Brekken, C. Stillinger, J. Z. Yen, S. G. Ernst, A. von Jouanne, E. Amon, R. Paasch, A. Brown, and A. Yokochi, "Comparison of direct-drive power takeoff systems for ocean wave energy applications," *IEEE Journal of Oceanic Engineering* vol. 37, pp. 35-44, 2012.
- [154] H. Titah-Benbouzid and M. Benbouzid, "Ocean wave energy extraction: Up-to-date technologies review and evaluation," in *Int. Electronics and Application Conference and Exposition (PEAC)*, 2014, pp. 338-342.
- [155] I. López, J. Andreu, S. Ceballos, I. Martínez de Alegría and I. Kortabarria, "Review of wave energy technologies and the necessary power-equipment," *Renewable and Sustainable Energy Reviews*, vol. 27, pp. 413-434, 2013.
- [156] M. Karimirad, Offshore Energy Structures For Wind Power, Wave Energy and Hybrid Marine Platforms. Switzerland: Springer, 2014.
- [157] O. Farrok and M. M. Ali, "A new technique to improve the linear generator designed for oceanic wave energy conversion," in *Int. Conf. on Electrical and Computer Engineering (ICECE)* 2014, pp. 714-717.
- [158] J. A. Rosero, J. A. Ortega, E. Aldabas and L. Romeral, "Moving towards a more electric aircraft," *IEEE Aerospace and Electronic Systems Magazine*, vol. 22, pp. 3-9, 2007.
- [159] M. J. J. Cronin, "The all-electric aircraft," *IEE Review*, vol. 36, pp. 309-311, 1990.
- [160] I. Moir, "The all-electric aircraft-major challenges," in *IEE Colloquium on All Electric Aircraft* London, 1998, pp. 2/1-2/6.

- [161] R. I. Jones, "The More Electric Aircraft: the past and the future?," in *IEE Colloquium on Electrical Machines and Systems for the More Electric Aircraft*,, 1999, pp. 1/1-1/4.
- [162] R. T. Naayagi, "A review of more electric aircraft technology," in *Int. Conf. on Energy Efficient Technologies for Sustainability (ICEETS)* 2013, pp. 750-753.
- [163] A. Wechsler, "Improving fault Tolerant Drives For Aerospace Applications," EngD thesis, School of Electrical, Electronic Engineering, Newcastle University, 2013.
- [164] D. R. a. m. center. The Power Optimised Aircraft Project [Online]. Available: http://www.dlr.de/rmc/rm/en/desktopdefault.aspx/tabid-3837/5985_read-8790/
- [165] C. W. Lander, *Power Electronics*, 2nd ed. London; New York: McGraw-Hill, 1987.
- [166] V. R. Moorthi, *Power Electronics: Devices, Circuits and Industrial Applications*. Oxford: Oxford University Press, 2005.
- [167] B. Visvesvara Rao, K. Raja Rajeswari, P. Chalam Raju Pantula and K. B. R. Murty, *Electronic Circuit Analysis*: Pearson Education India, 2012.
- [168] G. Capacitors. Capacitors for AC and DC General Purpose Applications [Online]. Available: http://www.farnell.com/datasheets/1582131.pdf
- [169] D. Spectrum, "eZdsp TM F28335 Technical reference," 2007.
- [170] Texas and Instruments. (2010, 10/03/2014). TMS320F28335,TMS320F28334,TMS320F28332,TMS320F28235,TMS320F28234,T MS320F28232,Digital signal controller(DSCs). Available: http://www.ti.com/product/tms320f28335
- [171] LEM. Voltage transducer LV 25-P [Online]. Available: http://www.lem.com/docs/products/lv%2025-p.pdf
- [172] T. electronics. Resistors for high voltage applications [Online]. Available: http://www.digikey.co.uk/Web%20Export/Supplier%20Content/tt-electronics-welwyn-985/pdf/welwyn-an-resistors-for-hi-voltage.pdf?redirected=1